Tracing Environmental Processes using Cold Dust with The Herschel Space Observatory

by

Christopher J. E. Fuller

A Thesis submitted to Cardiff University
for the degree of Doctor of Philosophy

November 2014

Declaration

This work has not been submitted in substance for any other degree or award at this or any other university or place of learning, nor is being submitted concurrently in candidature for any degree or other award.

Signed: ____________________ (candidate) **Date:** __________

Statement 1

This thesis is being submitted in the partial fulfillment of the requirements for the degree of PhD.

Signed: ____________________ (candidate) **Date:** __________

Statement 2

This thesis is the result of my own independant work/investigation, except where otherwise stated. Other sources are acknowledged giving explicit references. The views expressed are my own.

Signed: ____________________ (candidate) **Date:** __________

Statement 3

I hereby give consent for my thesis, if accepted, to be available for photocopying and for inter-library loan, and for the title and summary to be available to outside organisations.

Signed: ____________________ (candidate) **Date:** __________

Statement 4: Previously Approved Bar on Access

I hearby give consent for my thesis, if accepted, to be available for photocopying and for inter-library loans **after expiry of a bar on access previously approved by the Academic Standards & Quality Committee**

Signed: ____________________ (candidate) **Date:** __________

"In the beginning God created the heavens and the earth."

Genesis 1

Acknowledgements

A PhD is more than 3 years and far more than one person. In my case it has been a 28 year endeavour with the help from many friends, family, teachers and lecturers. I have tried my hardest to recognise you all. However, for every person mentioned here by name, there are 10 more I could have included.

As you have been with me on this journey from the very beginning it seems fitting to start with my family. Mum, Dad and Louisa I am forever indebted to you. There have been many times I have stumbled. You have always been there to pick me back up again and again. I have failed more tests and exams than most have ever sat. If it had not been for your constant encouragement I doubt I would have even got out of school with a single GCSE. As it stands I only got out with 5.

I wasn't a high achiever at school by any considerable stretch of the imagination (see above). This was despite the considerable efforts of many of my teachers namely; Richard Brown, Roger Cheeseman and Penny Mariote.

Leaving college I made my way to Cardiff University to begin my undergraduate degree. I would like to make special mention of Derek Ward-Thompson, Steve Eales and Hugh Lang who supervised my 3rd year undergraduate project, giving me my first taste of research.

After this I applied to study for a PhD at Cardiff University. A little known fact for those that haven't studied a PhD is that a prospective PhD student indicates which supervisor he would like to study with and that supervisor has the final choice of whom they accept. In this way both a student and supervisor choose each other and thus only have each other to blame if things go wrong! With the latter in mind, Jon Davies accepted me to be a student and I am extremely grateful that he did. Jon has contributed massively to this thesis. Those 6 hour meetings fighting through thousands of lines of indigestible prose paid off. I genuinely dread to think of the amount of times Jon has read this thesis. I am very grateful that you have taken the time to not only 'get-me-through' my PhD, but also to fundamentally change the way I see the universe around me.

During my PhD I have spent more or less my entire time in the 'Galaxies' office with Robbie Auld, Matthew Allen, Tom Bakx, Christopher Clark, Olivia Keenan, George Ford, Andreas Papageorgiou, Ezzy Pearson, Simon Schofield, Matthew Smith, and Elisabetta Valiante. Office rugby and golf are personal highlights, not to mention secret santa. I would like to make special mention of Matthew Smith and Robbie Auld. Both of you have taken a great deal of your time to help me develop many of the practical and statistical skills needed to complete a PhD. Furthermore, the entire galaxy group and postgraduate community have been fantastic people to be around for the last 3 years.

I have been lucky to be part of some great collaborations HeViCS and H-ATLAS have been those I have spent most of my PhD working within. I would like to make special mention of the PI's, Jon Davies and Steve Eales as well as Maarten Baes, Simone Bianchi, Marco Bocchio, Alessandro Boselli, Marcel Clemens, Tim Davies, Ilse De Looze, Marco Grossi, and Sebastien Viaene. A massive thanks to Tom Hughes and Paolo Serra who both took time to correct the horrendous english in the Fornax paper before its re-submission.

Outside of University I have some great friends and I would like to make special mention of Jon and Rohanna Roberts, Katie and Oli Salisbury, Dan and Anna Ralph, James Drake, Guy Thallon and Geraint Probert. You have all kept me sane and remained so yourselves. Your support, encouragement and friendship have been a joy.

Lastly - but in no way least - my wife, Esther. Your enduring love and support has been vital throughout my PhD. Thank you for your patience when I have worked evenings and weekends or 'had' to disappear to the other side of the world leaving you alone. Thank you for helping my dreams become reality.

Abstract

This thesis presents an investigation into the effect of environment on a galaxy's ISM. I have used new data from the *Herschel Space Observatory*, which detects the peak of far-infrared (FIR) emission from cold dust ($\sim$20 K) in nearby galaxies. Using data from the *Herschel* Fornax Cluster Survey (HeFoCS) and the *Herschel* Astrophysical Large Area Terahertz Survey (H-ATLAS) I have measured the FIR fluxes of galaxies in the nearby Fornax cluster and Coma region. In order to measure these FIR fluxes I used the optical shape and size of galaxies as a starting point. In the case of Fornax there was already a high quality optical catalogue, the Fornax Cluster Catalogue (FCC; Ferguson, 1989). However, in the case of the Coma cluster and filament I created my own using data from the SDSS spectroscopic survey, selecting galaxies based on position and velocity. Thus, creating the Coma Cluster Catalogue (CCC) and Coma Filament Catalogue (CFC).

For galaxies detected in at least 3 and 5 *Herschel* bands for the HeFoCS and H-ATLAS galaxies, respectively, I fitted a modified blackbody with a fixed beta emissivity index of 2, yielding dust masses and temperatures for 22 and 198 HeFoCS and H-ATLAS galaxies, respectively. All Early-type galaxies showed a lower mean dust mass and hotter temperature than found for late-types. When comparing early-type galaxies across all sampled environments, their FIR properties are found to be statistically identical. I only find a significant difference in dust-to-stellar mass for late-type galaxies between the filament and a field sample. This may suggest that the effect of the cluster and filament is more subtle than previously thought and that the evolution of the ISM components has mostly taken place well before the cluster was assembled.

I use a method to compare multiple parameters for the Coma cluster and filament galaxies and how each is affected by local environmental density. Late types show a moderate change in most parameters with the exception of gas-to-stars, which is strongly affected by environmental density. I suggest that late-types' lower sSFRs and higher stellar masses in the cluster when compared to the filament indicate that the galaxies in the cluster formed earlier and are hence more evolved.

In order to understand how the baryonic components of the galaxies change as a whole between the cluster and filament I have created mass functions. Using Schechter function fits to stellar, gas and dust mass density ratios for the Coma cluster and filament I calculated the ratio of gas-to-stellar and dust-to-stellar mass densities for each environment finding that Virgo, Fornax, Coma and the filament were gas deficient when compared to the field, but all their dust mass functions appeared identical. This further demonstrates that dust is largely invariant to environment, whereas, gas is affected well before entry into the cluster.

Contents

List of Tables

List of Figures

Chapter 1
Introduction

"All you really need to know for the moment is that the universe is a lot more complicated than you might think, even if you start from a position of thinking it as pretty damn complicated in the first place…The chances of finding out whats really going on in the universe are so remote, the only thing to do is hang the sense of it and keep yourself occupied."

Douglas Adams

1.1 Galaxies Evolving over Cosmic Time

1.1.1 Beginnings

Mankind has looked out into the night sky and seen what we now know as the 'Milky Way' (MW) for many thousands of years (see Figure 1.1). It was the Greek philosopher Democritus ($\sim$400 BC) who first proposed that the bright band in the night sky could possibly be composed of individual stars (Plutarch, 2006). However, it was much later ($\sim$1620) that Galileo Galilei used the first telescope to show observationally that the MW was composed of many faint stars. Building on the work of Thomas Wright, Immanuel Kant in 1755 was the first to propose that the MW was a gravitationally bound system and that nebulae observed were other such 'Island Universes'. However, Kant lacked observational evidence sufficient to verify his hypotheses.

The dawn of extragalactic study was marked by the 'Great Debate' between Harlow Shapley and Heber Curtis. The debate focused on the nature of so called 'spiral nebulae' and whether

Figure 1.1. The Milky Way as seen from ATCA - Australia. Dust lanes can be seen running parallel to the plane of the Milky Way.

they resided within our MW or were 'Island Universes' of their own. This was eventually resolved by the observations of Edwin Hubble (Hubble, 1925) who used Cepheid variable stars to show the Andromeda galaxy was well outside the MW. And thus, the study of extragalactic astronomy was born. Almost 90 years later it is still a vibrant field of study, and we are still grappling with unanswered questions asked by its original pioneers.

1.1.2 Galaxy Evolution

The current paradigm of galaxy evolution fits within the so called ΛCDM framework. In this paradigm the Universe is dominated by cold dark matter (CDM) and at the latest times expansion is accelerated by dark energy (Λ) which acts as a negative pressure. In the moments immediately following the big bang it is hypothesised that quantum fluctuations produced regions of over-density which provide the seeds for the formation of structure. As the Universe expanded it cooled allowing the first atoms (mostly atomic hydrogen) to form.

Small regions of over-density attracted nearby matter and thus grew even denser until a critical point when the density of gas was high enough to form the first stars and thus simultaneously the first galaxies were born. These galaxies are thought to grow hierarchically merging to form larger and larger galaxies. These galaxies likewise hierarchically group together to form the largest structures in the universe. This network of large-scale structure is known as the 'cosmic web' as it resembles a spider's web of interconnected filaments. At the junctions of filaments the densest large-scale structures are found - cluster of galaxies. The left most panel in Figure 1.2 shows the dark matter distribution of a recent computer simulation showing the growth of the 'cosmic web' (Vogelsberger et al., 2014).

The density a galaxy resides in can span several orders of magnitude, from $0.2\rho_0$ in voids

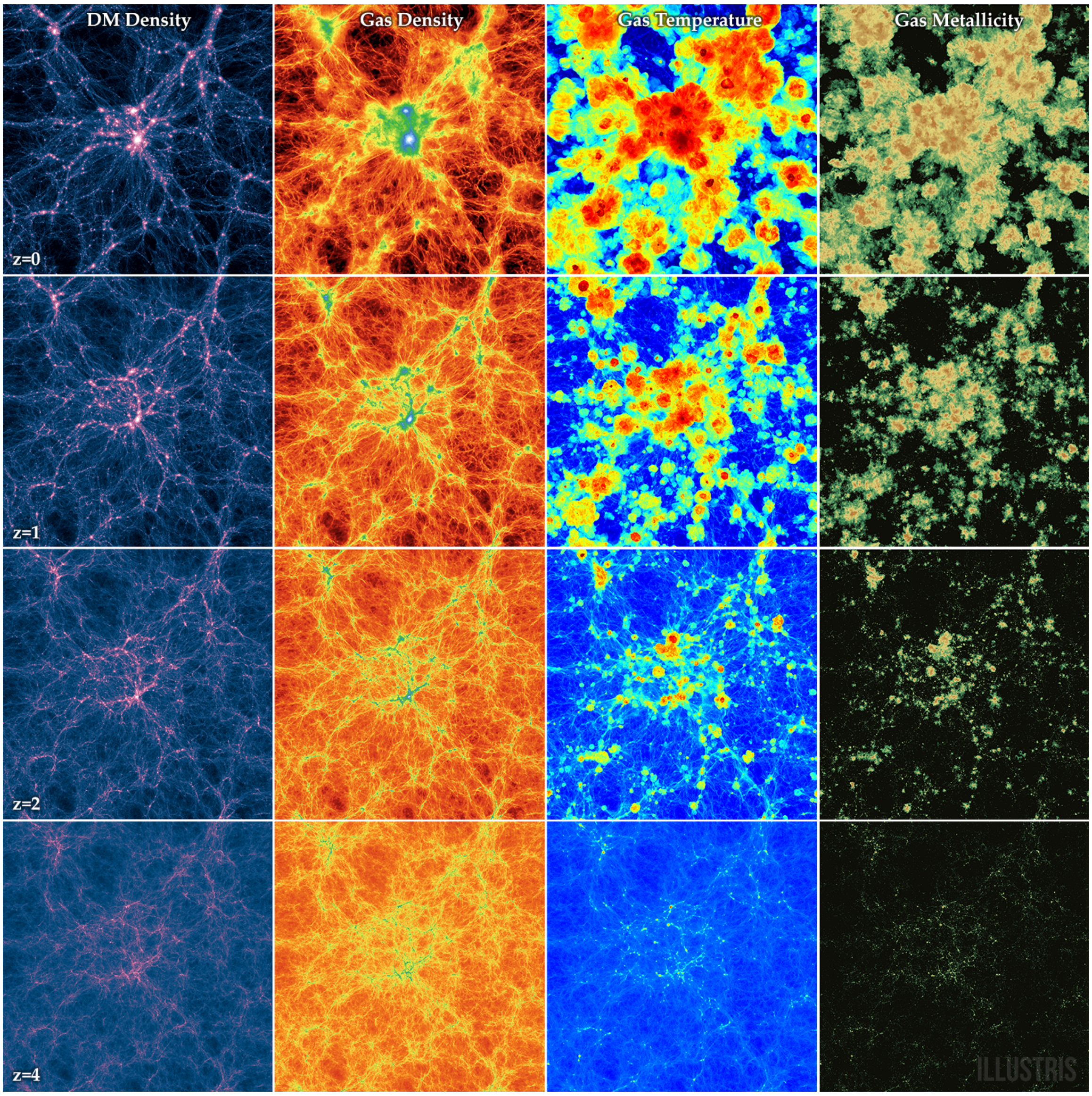

Figure 1.2. Slices through the recent Illustrius simulation. The sub-panels increase from z=4 to z=0 (bottom to top) and show four projections: dark matter density, gas density, gas temperature, and gas metallicity (left to right). Credit: Illustris Collaboration

to $5\rho_0$ in filaments feeding clusters where the density can exceed $100\rho_0$. ρ_0 is the mean density of the 'field' (Ramella et al., 1989). Nearby examples of clusters are Virgo, Coma and Fornax. Although, all three represent high density environments they are very different in themselves. Coma is the most massive with over 10000 estimated members, whereas Fornax has only ∼300. Coma and Fornax are very centrally concentrated, whereas, Virgo is far more 'clumpy' and thus likely represents a dynamically younger example of a cluster.

Galaxies come in two broad morphological groups[1], spirals and ellipticals. Spirals have flat disks actively forming stars leading to a blue optical colour whereas ellipticals are tri-axially symmetric with little active star formation leading to a redder optical colour.

Morphology and local environment are two quantities that appear strongly linked (Hubble & Humason, 1931; Morgan, 1961; Abell, 1965; Oemler, 1974). Dressler (1980) analysed 55 nearby clusters and showed that the fraction of late-type galaxies in the field is ∼80 % reducing to almost zero in the centre of clusters and showed the reverse to be true for early-type galaxies. This is known as the *morphology-density* relation. Using the *Hubble Space Telescope* (HST) Dressler et al. (1997) remeasured the morphology-density relation in 10 intermediate-redshift clusters (z∼0.5), finding the fraction of elliptical galaxies unchanged, however, the S0 fraction was 2/3 times less with a proportional increase in the spiral fraction. Dressler et al. (1997) suggested that this shows that elliptical galaxies predate the formation of rich clusters and S0 type galaxies are formed by interaction within the cluster environment. Whether a galaxy is shaped by nature or nurture or some proportion of both is still an open question.

Here 'nature' refers to galaxies forming earlier in the highest density regions of the young universe and are hence more evolved and thus naturally redder (Bower et al., 1998; Thomas et al., 2005). 'Nurture' refers to physical processes that are related to environment that can affect a galaxy's physical properties (see below).

The challenge of studying galaxy evolution is that at z=0.5 even with instruments like HST morphological classification is ambiguous due to the lack of physical resolution. With the advent of the 30m optical/near infrared telescopes in the near future this may be improved significantly.

However, we can use another mode of investigation to complement the study of galaxies at high redshift. We can study nearby galaxies across a range of environments in exquisite detail both in terms of physical resolution and by the use of multi-wavelength data. Using this very detailed data we can become 'galaxy archaeologists' looking for clues to their past evolutionary history.

[1]In this thesis we will use the terms spiral and late-type interchangeably. When we use the term early-type we include both ellipticals and lenticulars.

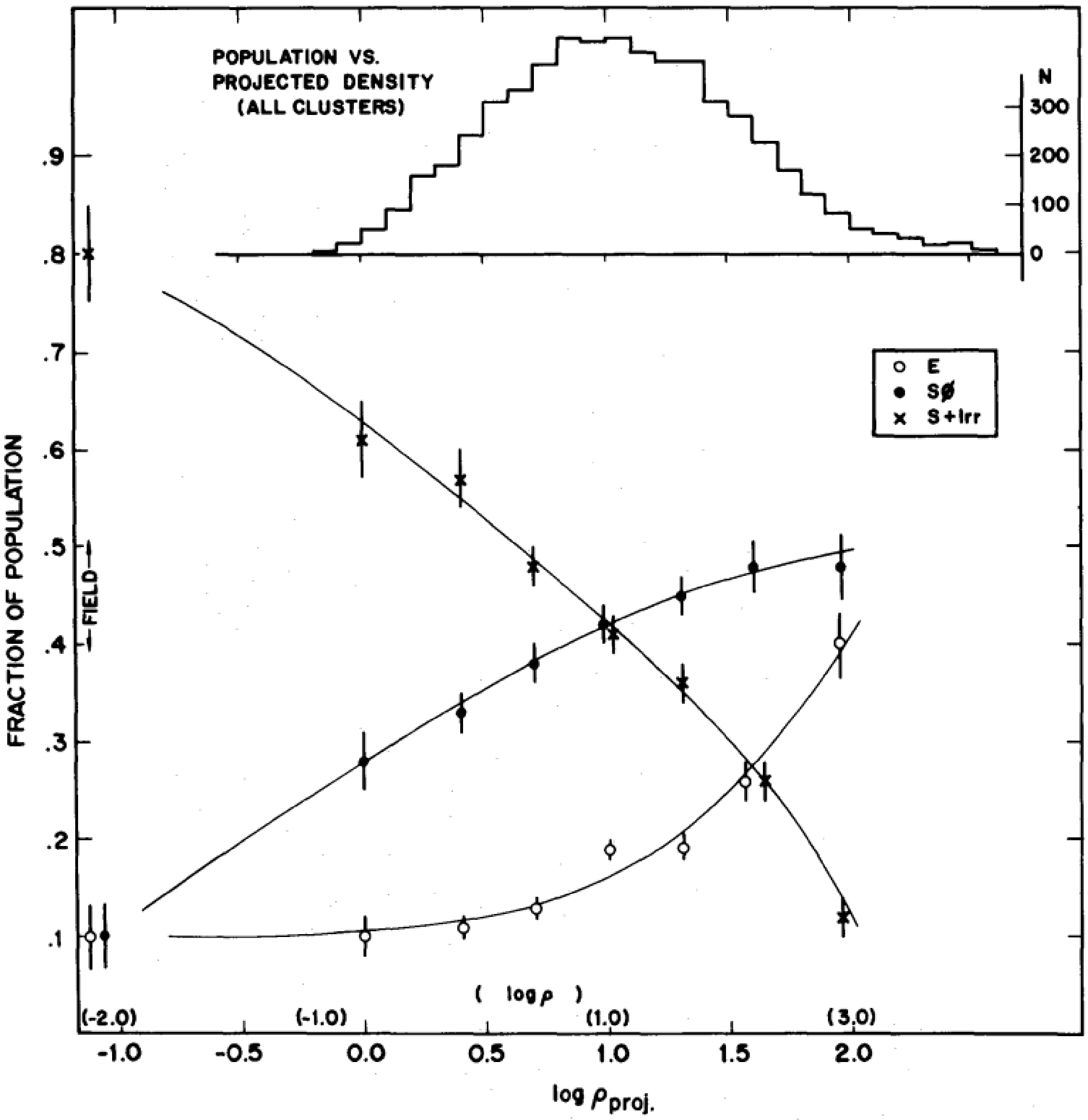

Figure 1.3. Figure 4 from Dressler (1980) showing the fraction of elliptical, lenticular and spiral galaxies as a function of projected density (Mpc^{-2}). The upper histogram shows the distribution of the sample across all measured projected densities.

1.1.3 The Interstellar Medium

A galaxy's ISM has a typical density of 10^6 atoms m^{-3} and represents $\sim$20 % of the overall mass of a normal spiral galaxy (Yin et al., 2009) and less than $\sim$1 % (excluding hot gas) in an elliptical (di Serego Alighieri et al., 2007; Grossi et al., 2009). The ISM is 99 % composed of gas (hydrogen and helium) with around 1 % from dust (see below) (Ferrière, 2001). The gas is mostly primordial with its ratio of hydrogen to helium determined by nucleosynthesis in the hot early universe, whereas the heavier elements have been processed in the core of stars or in the hot envelopes of supernovae.

The gaseous part of the ISM is key in the life cycle of a normal late-type galaxy. Where HI is dense and cool it can condense to form clouds of molecular hydrogen (H_2). These clouds of molecular hydrogen collapse to form stars. Kennicutt (1998) showed that the surface density of molecular hydrogen is directly proportional to the surface density of star formation.

In normal (late-type), isolated galaxies the HI can be found well outside a galaxy's optical disk (Grossi et al., 2008). However, as atomic hydrogen is the least bound component of the ISM, it is most strongly affected by environment. Haynes & Giovanelli (1984) measured the HI masses of a sample of isolated galaxies covering all Hubble-types effectively defining an 'HI-normal' sample. In a later paper Haynes et al. (1984) showed that in higher density regions galaxies had less HI when compared to the HI-normal sample, this difference is commonly referred to as HI-deficiency. More latterly Gavazzi et al. (2006) and Taylor et al. (2012) have found that galaxies in the cluster environment were HI deficient to $\sim 1.5\times$ the cluster's virial radii, and most HI deficient at the cluster centre. Molecular gas is difficult to remove as it sits much deeper in a galaxy's potential well (Kenney & Young, 1989; Rengarajan & Iyengar, 1992). However, if HI is removed by the cluster environment it could prove catastrophic for star formation. As Larson et al. (1980) proposed a galaxy requires inflow of gas from an extended gas reservoir, because on a time scale of a few Gyrs star formation would exhaust the available gas and thus shut down star formation. Larson et al. (1980) proposed that this method could make spiral structure far less pronounced and thus in time a 'red-and-dead' lenticular/early-type galaxy would form. This physical mechanism is aptly referred to as 'Starvation'.

In fact many physical processes have been proposed to remove a galaxy's ISM or stop the gas within it collapsing to form stars. These physical process can be split into two broad types; gravitational/tidal (galaxy-galaxy and galaxy-cluster) and hydrodynamic (ram pressure stripping, viscous stripping and thermal evaporation) as well as hybrid process (starvation and preprocessing). For a full review of physical processes in nearby clusters see Boselli & Gavazzi (2006).

Any gaseous ISM remaining in early-type galaxies has been shown to be very different to that of late-type galaxies. Davis et al. (2013) shows that unlike a typical late-type galaxy, early-types have an extremely depleted gaseous ISM. Krajnović et al. (2011) showed that gas (including molecular and atomic) in early-types is often kinematically miss-aligned with its stellar component - suggesting an external origin from a merger event.

1.2 Dust

Dust, the other major component of the ISM, contains approximately half of the metals not locked up in stars, and plays a key role in the life cycle of a galaxy. Molecular hydrogen forms on the surface of dust grains, making it crucial for star formation (Hollenbach & Salpeter, 1971). Dust - like HI - is not as gravitationally bound as the stars of a galaxy, but it is still unclear if or how strongly dust is affected by environment.

Dust attenuates light from the ultra-violet (UV) through to the infrared (IR), which can be seen by the naked eye in the 'dust lanes' running parallel to the plane of the MW as shown in Figure 1.1. The light that is attenuated by dust is then reprocessed and emitted at longer wavelengths. Figure 1.4 shows a typical late-type galaxy's spectral energy distribution (SED) from the UV to sub-millimetre (sub-mm). Emission from dust is expected from 5 μm to 1mm (Beichman, 1987; Soifer et al., 1987; Driver et al., 2008), however, in the near-infrared (NIR, 1 - 5 μm) and mid-infrared (MIR, 5 - 20 μm) emission from a galaxy is dominated by the old stellar population and complex molecular line emission, respectively, while the far-infrared (FIR, 20 - 500 μm) and sub-mm regime (500 - 1000 μm) are dominated by dust emitting as a modified blackbody. By studying dust we obtain another window into the inner workings of a galaxy and by covering the entire SED of a galaxy we can understand the amount of light that truly escapes.

The dust component can be further divided into two components, warm and cold at T$\sim$60 and 20 K, respectively. Cold dust is heated by the interstellar radiation field (ISRF), whereas, warm dust is heated by UV photons from young hot stars (de Jong et al., 1984; Cox & Mezger, 1987). The emission from the two components roughly peaks at 60 and 200 μm, respectively. However, due to the observational challenges associated with the FIR and sub-millimetre wavebands cold dust is one of the least understood components of the ISM.

1.2.1 Previous FIR and Sub-Millimetre Observatories

Although there are a few small windows in the earth's atmosphere, most of the infrared spectrum is absorbed and is either impractical or not possible to observe from the ground, so the infrared wavelength regime is best studied from space-based observatories.

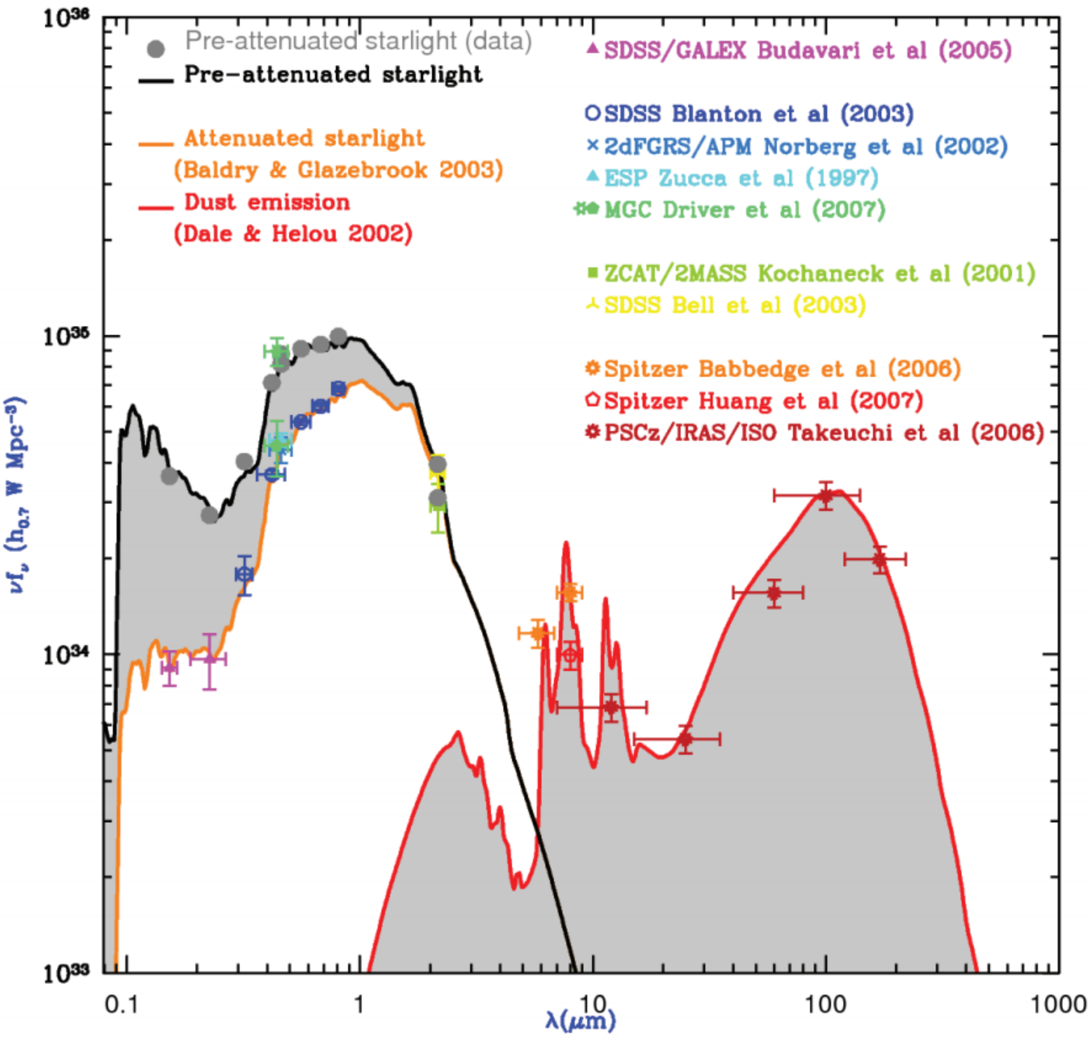

Figure 1.4. Figure 4 from Driver et al. (2008) showing data from nearby galaxies over the enitre wavelenght range a galaxies emitts in. The left-hand peak is light emitted from stars, the right-hand peak is emission from dust. The shaded area is energy attunated by dust and then reprocessed and emmited in the IR. As the shaded areas are equal it is possible to caculate the amount of light before it is attunated.

The first FIR space mission, IRAS (Neugebauer et al., 1984) (10 - 100 μm) was an all sky survey launched in 1983 for a 10 month mission. IRAS detected over 10^4 IR sources many of which were thought to be distant starburst galaxies (Aaronson & Olszewski, 1984). In the local universe late-type galaxies were well detected by IRAS, whereas early-type galaxies were detected very infrequently (de Jong et al., 1984). Leggett et al. (1987b) studied late-type galaxies in the nearby Virgo cluster and suggested that their MIR/FIR properties were identical to a sample of field galaxies. In a later paper again using IRAS data Leggett et al. (1987a) further showed that if separated by HI-deficiency rather than by environment there was still no difference in MIR/FIR properties. However, this latter result was disputed by Doyon & Joseph (1989) and Bicay & Giovanelli (1987) who found HI deficient galaxies to have 'cooler' dust temperatures and less IR luminosity.

The next FIR space mission, ISO (Kessler et al., 1996) (2.5 - 240 μm) was launched in 1995 with a mission length of just under 29 months far longer than its predecessor. ISO tentatively made the first discovery of dust in the intracluster medium (ICM) (Stickel et al., 2002). Contursi et al. (2001) targeted 18 late-type galaxies in the Coma cluster; performing deep observations, they found that even though the galaxies were interacting with the cluster, their dust properties were bizarrely un-affected. ISO's longer wavelength range helped reveal a previously unseen cold dust component ($\sim$ 20K) that could only be poorly constrained by ISO's photometric points. Contursi et al. (2001) further showed that the near infrared (NIR) traced stellar mass where as MIR, and especially far infrared (FIR), was not coincident with NIR emission and was more extended tracing a colder dust component.

The *Spitzer Space Telescope* (Werner et al., 2004) (3 - 160 μm) was launched in 2003, and it was the next generation of IR space based observatory. It exhausted its supply of cryogenic coolant in 2009, but two NIR bands are still operational (3.6 and 4.5 μm). Again *Spitzer* lacked the long wavelength coverage to detect cold dust less than $\sim$20 K (Bendo et al., 2003). Edwards & Fadda (2011) observed multiple fields covering the Coma cluster with a total survey footprint of $\sim 3\,\mathrm{deg}^2$ approximately 1/3 of the area traced by the virial radius. This survey confirmed that star formation was strongly suppressed in late-type galaxies in the core of the cluster.

These instruments allowed the study of warm dust and in a narrow sense cold dust as well; but they were limited in constraining cold dust as they could not cover the Rayleigh-Jeans tail of blackbody emission. The ratio of cold-to-warm dust mass can reach values in excess of $\sim$ 1000 (Vlahakis et al., 2005) - to this point we had only seen the tip of the iceberg.

In the above sections I hope to have demonstrated how important studying nearby galaxies across a range of environments is in an attempt to solve the 'nature vs nurture' question. Furthermore, the benefit of understanding the effect environment has on the ISM, specifically, the least understood major component - cold dust.

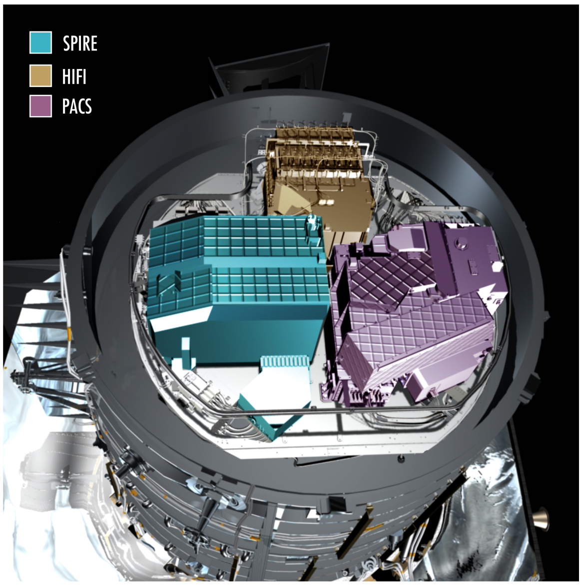

Figure 1.5. An artist's impression of the *Herschel Space Observatory* and its onboard instruments left and right-hand panels, respectivly. Credits: ESA (Image by AOES Medialab); background: Hubble Space Telescope, NASA/ ESA/ STScI and ESA for left and right-hand pannels, respectively.

1.3 The Herschel Space Observatory

In order to study cold dust in nearby galaxies - the primary focus of this thesis - an instrument was required that could cover these technically demanding and previously unseen wavebands (see above). And so on the 14^{th} of May 2009 the *Herschel Space Observatory* (Pilbratt et al., 2010) (see Figure 1.5) was launched into an orbit about the second Lagrange point of the Sun-Earth system (L2). With a 3.5 metre primary mirror *Herschel* possesses the largest mirror in space, and will only be surpassed by the *James Webb Space Telescope* at the end of this decade. It has three instruments onboard (described below) cooled to near absolute zero which offer coverage from 51 to 671 μm in unparalleled resolution and sensitivity. *Herschel* data (PACS and SPIRE) are used extensively in this work and as such I will briefly outline the instrumentation and capability of the observatory.

- **HIFI (Heterodyne Instrument for the Far Infrared):** HIFI is a high resolution hetrodyne spectrometer that operates from 157-625 μm. See de Graauw et al. (2010) for full details.

- **PACS (Photodetector Array Camera and Spectrometer):** PACS an imaging photometer and medium resolution grating spectrometer. PACS performs spectroscopy between 51 and 220 μm. In imaging dual-band photometry mode, PACS operates in three possible bands 70, 100, and 160 μm. See Poglitsch et al. (2010) for full details.

- **SPIRE (Spectral and Photometric Imaging Receiver):** SPIRE is an imaging photometer and an imaging Fourier transform spectrometer. SPIRE performs spectroscopy between 194 and 671 μm. In imaging photometry mode, SPIRE operates in three bands simultaneously these bring 250, 350 and 500 μm. See Griffin et al. (2010) for full details.

The lifetime of *Herschel* was limited by the supply of helium used to cool the three instruments. The nominal lifetime was 3 years, however, *Herschel* managed to operate for almost 4 years until the 29^{th} of April 2013. *Herschel* has revolutionised the way we understand the dusty ISM.

1.3.1 Related Herschel Surveys

In this section I will outline the *Herschel* surveys that are either related to or the direct context for this work.

The HeViCS

The *Herschel* Virgo Cluster Survey (HeViCS) was an Open Time Key Program. The HeViCS covers 84 deg^2 of the nearby (17 Mpc) Virgo cluster, however, only 55 deg^2 are at the full depth. The survey's full depth is 8 scans in SPIRE and PACS parallel mode giving deep FIR coverage in 5 FIR bands (100, 160, 250, 350, 500 μm) as shown in Figure 1.6. The main aims of this survey are:

- The detection of dust in the intra-cluster medium;
- Extended cold dust around galaxies;
- FIR-submm luminosity functions;
- The UV to sub-mm spectral energy distribution of galaxies of various morphological types; and
- The detection of dust in dwarf and giant elliptical galaxies.

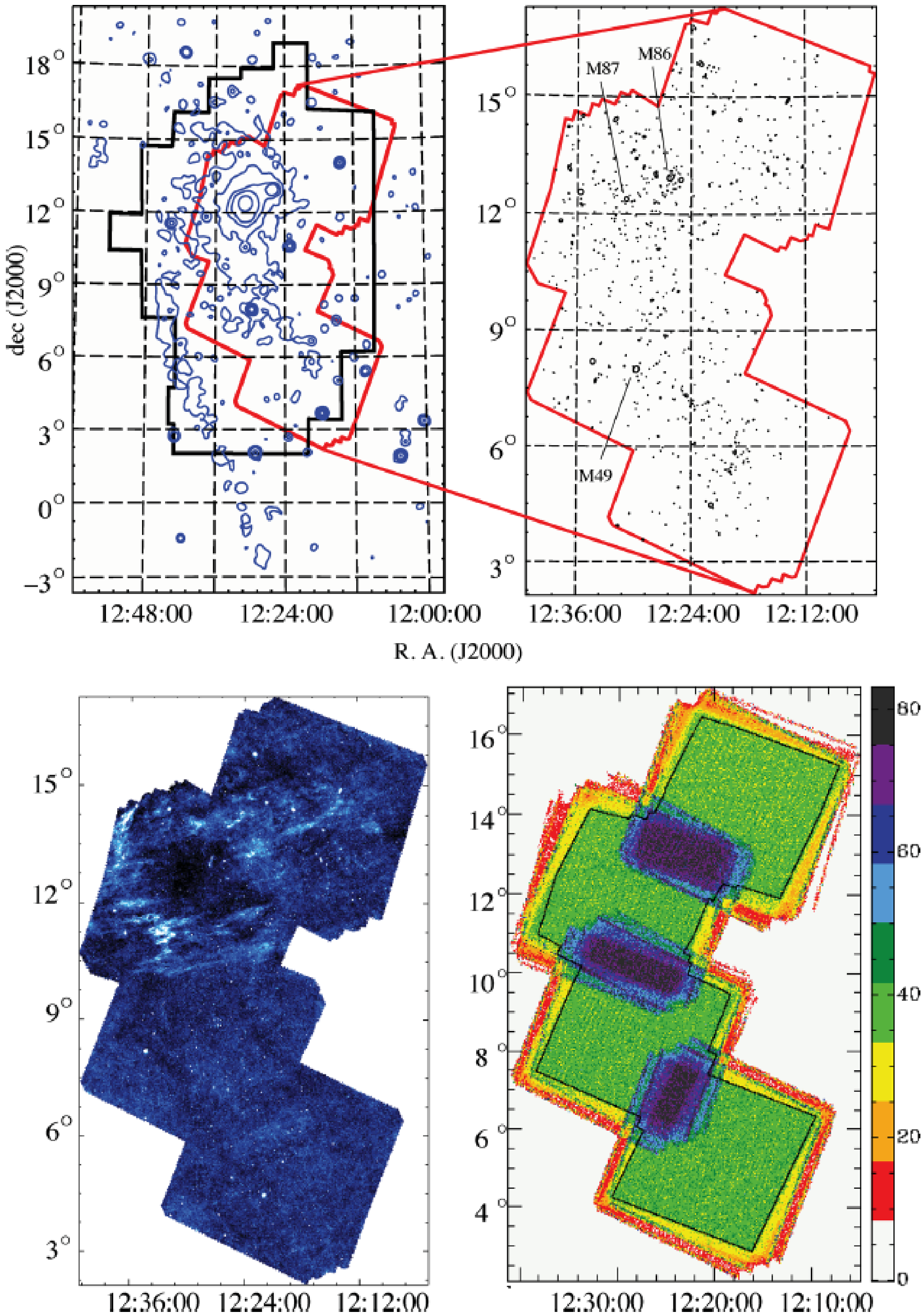

Figure 1.6. Figure 1 with caption from Auld et al. (2013) Top left: the Virgo cluster region. X-ray contours from Boehringer et al. are shown in blue. The VCC survey region is outlined in solid black and the full extent of HeViCS is outlined in red. Top right: the HeViCS survey region with black ellipses representing the VCC optical discs measured to D_{25}. The dominant cluster galaxies have been labelled and their positions correspond to the peaks in X-ray emission. Bottom left: Herschel-SPIRE 250 μm image of the full survey. Even in this small image it is possible to identify the VCC galaxies with the strongest FIR emission and the large swathes of Galactic dust cirrus. Bottom right: survey depth, measured in samples per pixel, from the 250 μm data. The inner region, covered by eight scans with PACS and SPIRE, is shown by the black outline. In the overlap region between tiles the coverage rises to 16 scans.

The HeViCS has studied dust in the largest local cluster, and has published a series of papers which are the direct context for this work. The publications are as follows: Paper I (Davies et al., 2010) examined the FIR properties of galaxies in the Virgo cluster core; Paper II (Cortese et al., 2010b) studied the truncation of dust disks in Virgo cluster galaxies; Paper III (Clemens et al., 2010) constrained the lifetime of dust in early-type galaxies; Paper IV (Smith et al., 2010) investigated the distribution of dust mass and temperature in Virgo's spirals; Paper V (Grossi et al., 2010) examined the FIR properties of Virgo's metal-poor, dwarf galaxies; Paper VI (Baes et al., 2010) presents a FIR view of M87; Paper VII (De Looze et al., 2010) detected dust in dwarf elliptical galaxies in the Virgo cluster; Paper VIII (Davies et al., 2012b) presented an analysis of the brightest FIR galaxies in the Virgo cluster; Paper IX (Magrini et al., 2011) examined the metallicity dependence of the molecular gas conversion factor; Paper X (Corbelli et al., 2012) investigated the effect of interactions on the dust in late-type Virgo galaxies; Paper XI (Pappalardo et al., 2012) studied the effect of environment on dust and molecular gas in Virgo's spiral galaxies; Paper XII (Auld et al., 2013) examined the FIR properties of an optically selected sample of Virgo cluster galaxies; Paper XIII (Di Serego Alighieri et al., 2013) investigated the FIR properties of early-type galaxies in the Virgo cluster; Paper XIV (De Looze et al., 2013) studied Virgo's transition-type dwarfs and Paper XVI (Davies et al., 2014) presented an analysis of metals, stars, and gas in the Virgo cluster. Six further papers (Boselli et al., 2010; Cortese et al., 2012b; Boquien et al., 2012; Ciesla et al., 2012; Smith et al., 2012; Eales et al., 2012) discuss the HeViCS galaxies along with other galaxies observed as part of the Herschel Reference Survey (HRS).

The HeFoCS

After the success of the HeViCS the next logical step was to extend the study to the nearby (19 Mpc) Fornax cluster. Fornax is more dynamically relaxed and therefore more evolved offering an interesting and highly complementary comparison to Virgo.

The *Herschel* Fornax Cluster Survey (HeFoCS) is an Open Time Key Program that was proposed by the members of the HeViCS. The HeFoCS covers 12 deg^2 of the Fornax cluster in SPIRE and PACS parallel mode giving deep FIR coverage in 5 FIR bands (100, 160, 250, 350, 500 μm) with comparable depth to the 8 scan HeViCS data as both are effectively confusion limited (see Chapter 2). The main aims of this survey are very similar to the HeViCS (see above). To date only two papers have been published: Paper I (Davies et al., 2012a) presented an analysis of the brightest FIR galaxies in the Fornax cluster and Paper II (Fuller et al., 2014) examined the FIR properties of an optically selected sample of Fornax galaxies. The full exploitation of the HeFoCS data is central to this thesis.

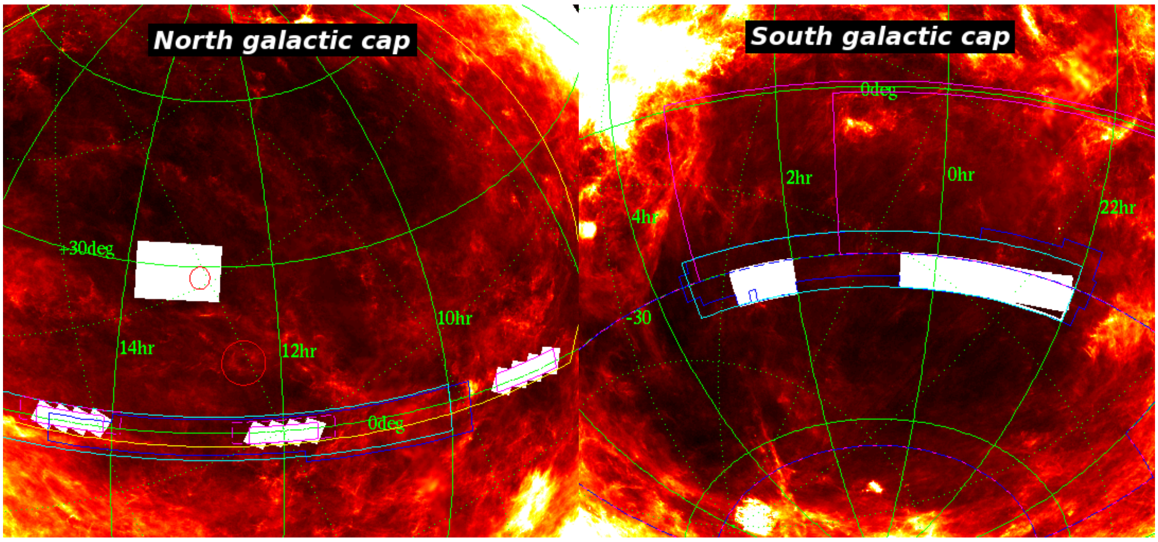

Figure 1.7. Left: This figure shows the northern and equatorial survey fields. The North Galactic Pole (NGP) is the uppermost and the red circle is the virial radius of the Coma cluster. The three equatorial survey fields are known as the GAMA fields. Right: This figure shows the two southern fields also known as the South Galactic Pole (SGP) fields. Credit: H−ATLAS.

The H−ATLAS

The Herschel Astrophysical Terahertz Large Area Survey (H-ATLAS) (Eales et al., 2010) is currently the largest FIR extra-galactic survey covering 570 deg^2 using the *Herschel* Space Observatory as shown in Figure 1.7. The H-ATLAS observations cover this large area with 5 Herschel bands (100, 160, 250, 350 and 500 μm).

The fields are located in areas of low galactic cirrus; the Northern Galactic Pole (NGP) includes the nearby Coma cluster (100 Mpc), as well as wide spatial coverage of the surrounding area. This not only allows a study of the Coma cluster, but gives good coverage of the filament it resides in, the so called 'Great wall' of galaxies that lies at 100 Mpc connecting Coma and Abell1367, thus allowing us to extend our study of nearby environments.

1.4 Organisation of this thesis

The main aim of this thesis is to study 3 nearby environments; Fornax, Coma and the Coma filament and compare and contrast these to the Virgo cluster and nearby field galaxy samples. Our secondary objectives are to understand the origin of dust in galaxies as well as use the plethora of auxiliary data that is available in our study of the Coma region to understand the wider effect of environment on the physical properties of galaxies. The chapters are as follows:

- Chapter 2: Outlines the data used in this thesis with detailed descriptions of its reduction and measurement.
- Chapter 3: Further outlines the auxiliary data used to study the Coma region.
- Chapter 4: Examines the FIR properties of optically selected Fornax cluster galaxies.
- Chapter 5: Studies the FIR properties of optically selected Coma cluster and filament galaxies.
- Chapter 6: Explores the auxiliary data to more fully understand the galaxies' evolution in the Coma region, thus examining the effect of environment on key parameters.
- Chapter 7: Uses mass functions to understand the relative abundance of gas, dust and stars in the Coma cluster and filament.
- Chapter 8: Summarises the main results from this thesis as well as the overall conclusions and implications of this work.

Parts of Chapters 2 and 4 have been published in Monthly Notices of the Royal Astronomical Society (Fuller et al., 2014).

Part I

Data

Chapter 2
FIR and Optical Data

"Experts often possess more data than judgment."

Colin Powell

In this thesis we will use the methodology of Auld et al. (2013) to fully exploit the H-ATLAS NGP and HeFoCS datasets and present the FIR properties of our optical-selected samples. Auld et al. (2013) wrote software that uses the optical positions, sizes and shapes as a starting point from which to fit an aperture and measure the FIR emission for each galaxy. We have used this software (fully described below) with modifications appropriate for each dataset.

2.1 Optical Catalogues

As optical catalogues are the starting point for our source measurement process we will define the origins and properties of each.

2.1.1 Fornax

The Fornax Cluster Catalogue (FCC; Ferguson, 1989), was created from visual inspection of photographic plates taken with the Du Pont 2.5m reflector at the Las Campanas Observatory. It is complete to $m_{BT} \sim 18$, and contains members down to $m_{BT} \sim 20$. Although this catalogue is 20 years old it is still the best optical catalogue available. It is equivalent to the Virgo Cluster Catalogue (VCC; Binggeli et al., 1985) used by Auld et al. (2013) and so enables a good comparison between the two clusters. Ferguson (1989) assigned cluster membership mainly based on morphology and the detail that could be observed in the images. There are now 104 radial velocity measurements of FCC galaxies which indicate that 5 of them are outside the cluster, (FCC 97, 141, 189, 257, and 287 with velocities of 16582, 16831, 31044, 50391, and 68474 $\mathrm{km\,s^{-1}}$). These were removed from our sample.

2.1.2 Coma

Defining a sample of galaxies at the distance of Coma ($\sim 100\,\mathrm{Mpc}$) is non-trivial. The FCC and VCC surveys were conducted on photographic plates, and then galaxies included or excluded on morphological grounds with some velocity data. Godwin & Peach (1977) conducted a similar survey in the direction of the Coma Cluster, however Coma is ~5x further away and as such morphological classification for fainter members becomes ambiguous. This leads to foreground/background contamination. Redshift surveys also exist for the Coma region, (Kent & Gunn, 1982; Colless & Dunn, 1996; Geller et al., 1999; Castander et al., 2001; Mobasher et al., 2001). However the lack of homogeneity precludes the generation of a unified redshift selected Coma cluster catalogue suitable for our purposes.

Castander et al. (2001), the most recent addition to redshift surveys of the region, was used for commissioning the Sloan Digital Sky Survey's (SDSS) spectrograph. When their paper was written the SDSS photometric survey had not yet covered Coma. They selected cluster galaxies at random from the relevant superCOSMOS fields within a 1.5° radius of the cluster centre. The region of the sky is now covered by both the spectroscopic and photometric SDSS surveys, and thus allows us to select a clearly defined optical catalogue with secure redshift distances. The Coma Cluster Catalogue (CCC) I have produced will hopefully be as useful as those previously used for Virgo (VCC) and Fornax (FCC).

The SDSS spectroscopic survey selected its Main Galaxy Sample (MGS) according to the criteria discussed extensively in Strauss et al. (2002). Briefly, objects are selected as having a 5σ detection in the r band, galaxies are then separated from stars by testing if they are a point or extended source in the r band ($r_{psf} - r_{model} \geq 0.3$), also stipulating that it cannot have the flags SATURATED, BRIGHT, or BLENDED. Finally galaxies must have an r band apparent magnitude brighter than $m_r \leq 17.77$.

The SDSS spectrograph has the physical limitation that two fibres cannot be closer than 55" or 26 kpc at the distance of Coma. If this occurs one will be chosen at random. This is unlikely to be a problem for the Coma cluster and will only affect higher redshift clusters.

Our sample is selected from the MGS, isolating the cluster and filament in both spatial and velocity extent. When drawing our sample, we select it from SDSS DR10 using only galaxies with a secure spectroscopic redshift.

Our rough initial selection was all galaxies within a velocity range 3000km s^{-1} to 11000km s^{-1}, with a spatial selection over the area of the NGP. These were selected to be roughly symmetrical about the current value for Coma's mean velocity as listed in the Nasa Extra-Galactic Database[1] (NED) of $\sim 7000\,\mathrm{km\ s^{-1}}$.

For a galaxy to be truly a member of a cluster we must argue that it is virialised. Firstly many clusters are far from a virial equilibrium, meaning a selection like R_{200}, the radius at which the density drops to 1/200 of the critical density, is more appropriate. Coma however is a dynamically mature cluster, making the virial radius a more realistic definition. A cluster in perfect virial equilibrium would have a velocity distribution perfectly traced by a Gaussian function. Figure 2.1 show's this is a good approximation for the Coma cluster.

Cluster

We define the centre of the cluster by the peak X-ray emission (Colless & Dunn, 1995). This X-ray emitting gas is a much more reliable indicator of the mass distribution of the cluster than the optical surface density of galaxies, as it better traces the total mass distribution. The centre of the Coma cluster is thus; RA: 12h59m48.7s, DEC: +27h58m50.0s (J2000). The spatial extent of the cluster is 3.1Mpc, which is a mean value from the 4 seminal measurements of the virial radius using 4 different methods (Kubo et al., 2007; Geller et al., 1999; Hughes, 1989; The & White, 1986).

We define a velocity selection similar to the VCC's (Binggeli et al., 1985) using the velocity dispersion (σ) of a Gaussian function fitted to galaxies within the projected virial radius. However, the velocity dispersion is sensitive to the initial rough velocity selection (see above). In order to overcome the former stated problem we have used an iterative method. The method involves fitting a Gaussian function, then removing galaxies outside of 3σ and re-fitting a Gaussian function until the value for σ converged.

Figure 2.1 & 2.2 indicates that this is an appropriate method, due both to the Gaussian's goodness of fit to the histogram of Coma cluster galaxies, $\chi^2_{dof=23} = 30.1$ (where $\chi^2_{dof=23} = 35.2$ is equivalent to a 95 % confidence interval) and the low number of galaxies outside the derived range. Both in front of and behind the cluster there are natural voids, suggesting the cluster has cleared its immediate surroundings. There are doubtless galaxies that are inside this velocity range projected into it by an extreme peculiar velocity. However without a more complex cluster selection method, introducing further assumptions, these cannot be identified. Table 2.1 shows the limits in which we have defined the extent of the Coma cluster. There are 754 SDSS galaxies spectroscopically confirmed within these limits which are henceforth referred to as the CCC.

[1] http://ned.ipac.caltech.edu

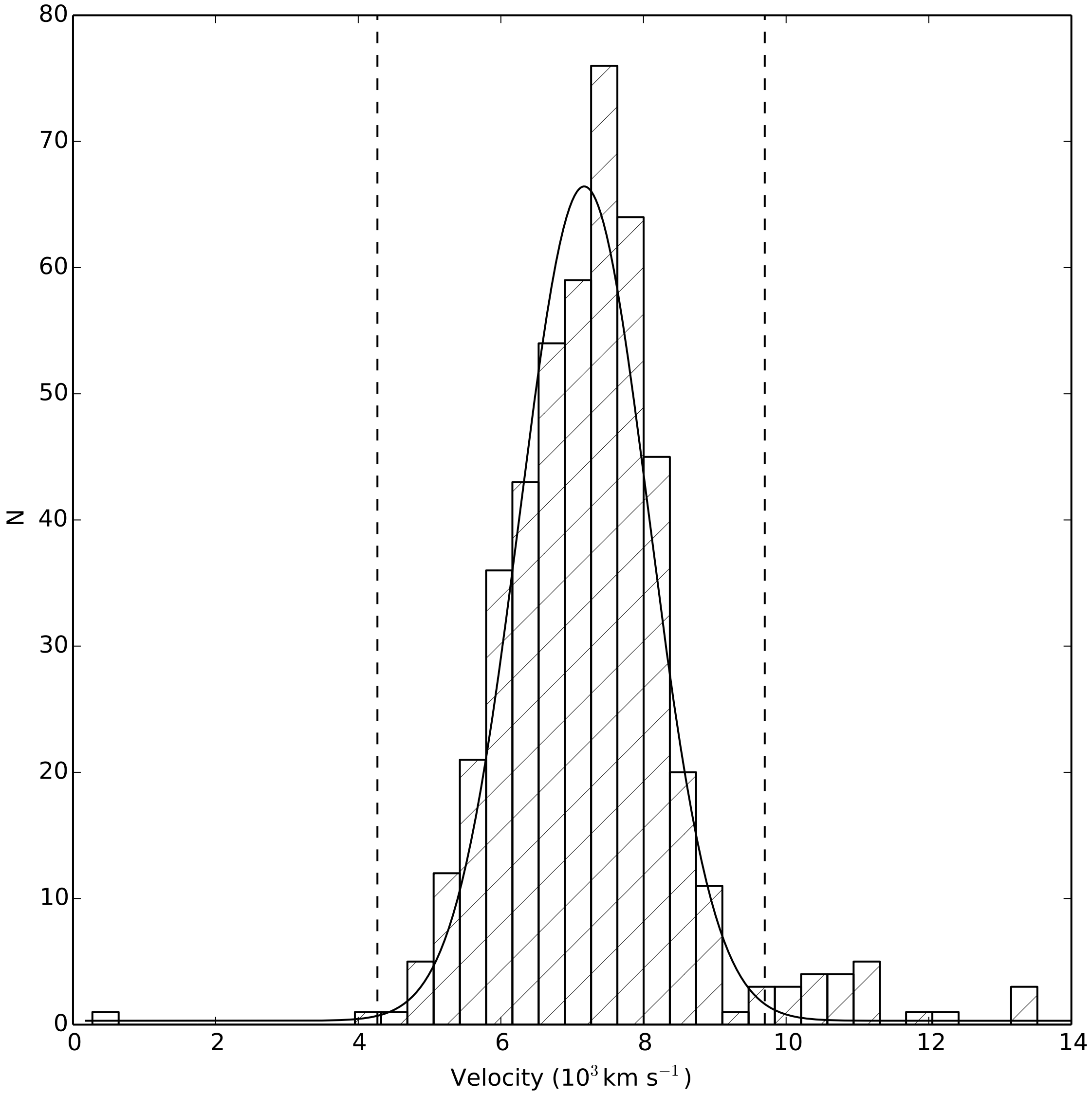

Figure 2.1. The velocity distribution of the CCC galaxies, showing a clearly relaxed system. The vertical dashed lines represent the 3σ velocity dispersion of the fitted Gaussian function.

Virial Radius	3.1 Mpc
Velocity Dispersion, σ	905.2 km s^{-1}
Mean Cluster velocity, μ	6984.5 km s^{-1}
Minimum velocity limit, $\mu - 3\sigma$	4268.8 km s^{-1}
Maximum velocity limit, $\mu + 3\sigma$	9700.2 km s^{-1}

Table 2.1. The key parameters of the Coma cluster as derived using the stated method.

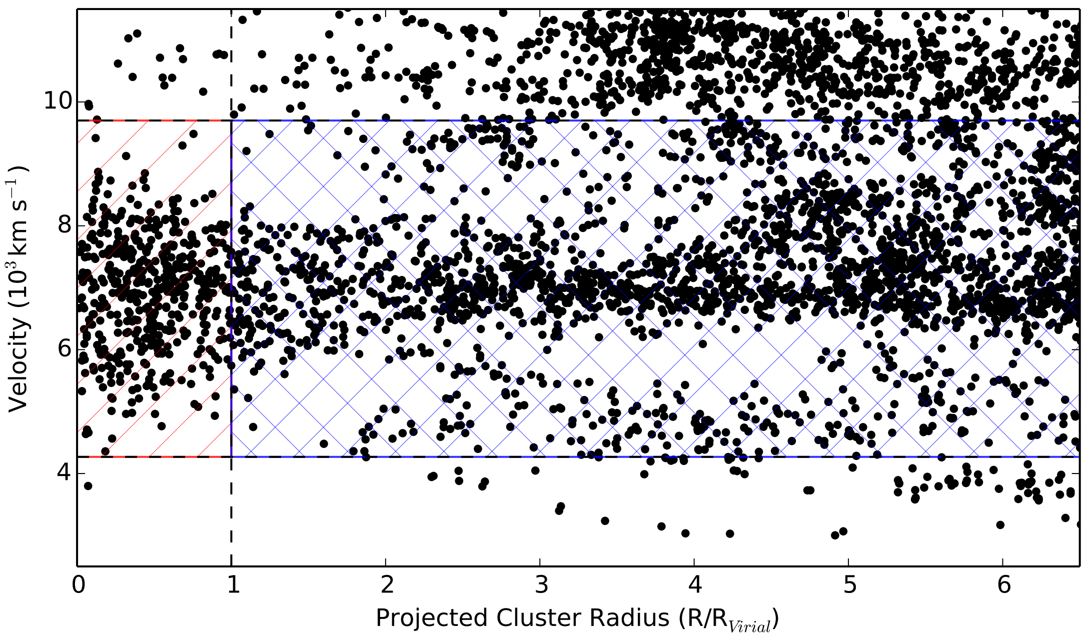

Figure 2.2. This plot shows the galaxies in the Coma cluster region in velocity and distance from the Coma cluster X-ray centre. The red diagaonally-hatched box is a visual representation of the cluster selection, and the blue cross-hatched box is shows the selection of the filament sample. The cluster has a clear gravitational influence out and past 6× the virial radius, as well as voids in front and behind.

Filament

The Coma cluster sits within the 'great wall', an over-density of galaxies that connects it with A1367. Defining a 'filament' sample is non-trivial as it is clearly a non-virialised structure. Within the filament also there are several loose groups, making it an interesting dynamical region to compare to the cluster sample. Figure 2.2 shows clearly the filament that the cluster sits in, the over density at $\sim$7000kms^{-1} extending well beyond 18 Mpc. These are galaxies at the same recessional velocity as Coma and are highly likely to be in-falling through the filament into the cluster.

We are defining the filament sample as any galaxy that falls within the bounds of the NGP survey area and outside the virial radius of Coma. We use the same velocity selection as the cluster (see Table 2.1). This yields 951 filament galaxies and is thus the Coma Filament Catalogue (CFC).

2.2 FIR Data

We have outlined above optical catalogues used as starting points for our source measurement program. In this section we outline the FIR data that is used in this thesis. The FIR maps used in this work were made as described below by Matthew Smith.

2.2.1 Fornax

The HeFoCS observations cover a $4^\circ \times 4^\circ$ tile centred on NGC 1399 [$\alpha = 03^h38^m29.8^s, \delta = -35^o27'2.7"$ (J2000)], the central elliptical galaxy. This is an area of apparently low Galactic cirrus when compared to the Virgo cluster field (Davies et al., 2012a). The region contains $\sim 70\,\%$ of the area covered by the FCC catalogue (see Figure 2.3). It should be noted that there is an unavoidable misalignment between SPIRE and PACS due to their respective locations on the *Herschel* focal plane. This misalignment leads to a loss of 30 galaxies that are not in the PACS maps, and are only observable by SPIRE. In total 60 % of the FCC cluster galaxies are observed in all 5 bands (100, 160, 250, 350 & 500 μm).

A full description of the data reduction for the HeFoCS is available in Davies et al. (2012a). Briefly, the HeFoCS observations are taken using PACS (100 & 160 μm) (Poglitsch et al., 2010) and SPIRE (250 , 350, & 500 μm) (Griffin et al., 2010) in parallel mode with a fast scan rate (60 arcsec s^{-1}), and our final maps consist of 4 scans (2×2 orthogonal cross-linking scans).

PACS data were taken from level 0 to level 1 using the standard pipeline, then the 4 scans were combined with the *Scanamorphous* map maker (Roussel, 2013).

SPIRE data were processed with a customised pipeline from level 0 to level 1, which is very similar to the official pipeline. The difference was the use of a method called BriGAdE (Smith et al., in preparation), in place of the standard *temperatureDriftCorrection*. BriGAdE effectively corrects all the bolometers for thermal drift without removing large extended structures like Galactic cirrus. These scans are then combined using the naïve mapper in the standard pipeline.

The final HeFoCS maps have pixel sizes of 2, 3, 6, 8 and 12 arc seconds and 1σ noise over the entire image of 0.5, 0.7, 0.7, 0.8 and 0.9 mJy pixel^{-1} for 100, 160, 250, 350 and 500 μm, respectively.

The approximate Full Width Half Maximum (FWHM) of the *Herschel* beam is 11, 14, 18, 25 & 36 arc seconds, at 100, 160, 250, 350 & 500 μm, respectively. At the distance of Fornax 10 arc seconds $\simeq 1$ kpc giving us the potential to resolve many Fornax galaxies. For example, the three biggest galaxies in the cluster are NGC 1365, 1399, and 1380 with optical diameters of 5.5, 3.8, and 2.7 arc minutes, respectively.

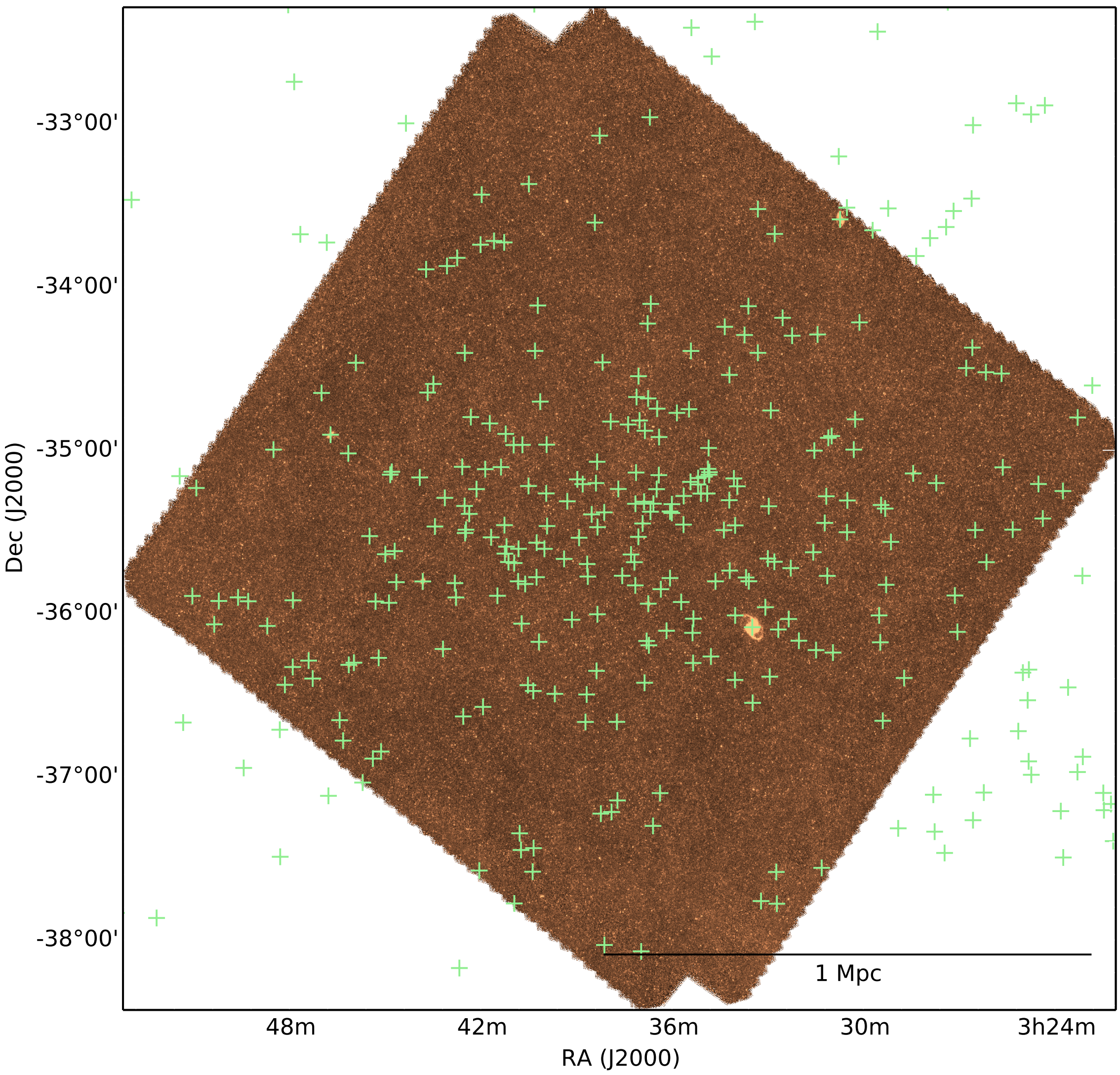

Figure 2.3. The HeFoCS 250 μm image, with a green cross marking the position of every galaxy from the optical FCC catalogue. The *Herschel* data miss galaxies in the outskirts of the cluster. A scale bar of 1 Mpc is marked in the lower right hand corner, assuming a distance to the cluster of 17.2 Mpc.

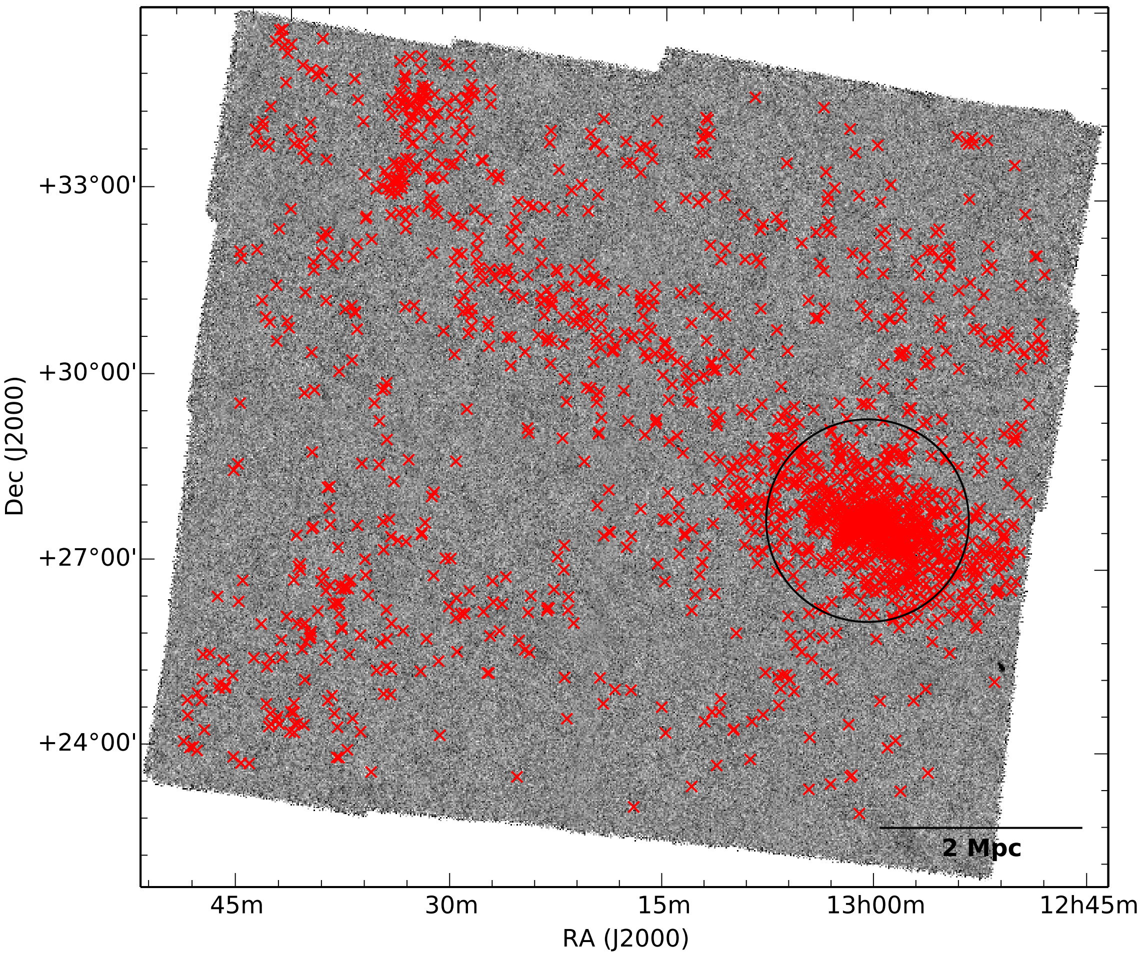

Figure 2.4. The H-ATLAS NGP map, with a red cross marking every galaxy in both our cluster and filament samples. The black circle marks the 1.67° or 3.1 Mpc virial radius of the cluster.

2.2.2 Coma

The North Galactic Pole (NGP) is part of the H-ATLAS survey covering $15^\circ \times 10^\circ$, centred at $\alpha = 13^h 18^m 00.0^s$, $\delta = 29^\circ 00' \, 00.0''$ (J2000). This is an area of low Galactic cirrus as shown in Figure 2.4 in which the Coma cluster and a large amount of the filament are illustrated.

The data reduction of the NGP maps are identical to those of the HeFoCS and HeViCS with the exception of the NGP being composed of 2 scans (1×1 orthogonal cross-linking scans).

The final NGP maps have pixel sizes of 3, 4, 6, 8 and 12 arc seconds and 1σ noise over the entire image of 0.8, 1.1, 0.9, 0.9 and 1.1 mJy pixel^{-1} for 100, 160, 250, 350 and 500 μm, respectively. At the distance of Coma 10 arc seconds $\simeq 5$ kpc giving us the potential to resolve some Coma galaxies. For example, the three biggest galaxies in our sample are NGC 4839, 4889, and 5127 with optical diameters of 3.6, 3.3, and 2.3 arc minutes, respectively.

NGP Complete Source Catalogue

H-ATLAS NGP source catalogue (Valiante et al. in preparation), henceforth referred to as the NGPSC, will be a catalogue of all FIR sources in the NGP maps. Currently, it exists only for the three SPIRE bands and only for point-sources. We use it for flux verification and to remove contaminating galaxies from the background.

2.2.3 Comparison with HeViCS

As much of this thesis is based on a comparison between Fornax, Virgo and Coma it is therefore worthwhile to examine the difference between the HeFoCS, HeViCS and NGP data. The FIR maps of all three surveys are created using identical data reduction techniques. However, they differ with respect to depth and spatial coverage of the clusters.

First we consider the depth of the surveys. The HeViCS maps consist of 8 scans (4×4 orthogonal cross-linking scans), 2 and 4 times as many as the HeFoCS and NGP maps leading to a $\sim\sqrt{2}$ and $\sim\sqrt{4}$ increase in instrumental noise in the later two surveys, respectively. Auld et al. (2013) calculated instrumental and confusion noise, showing that the HeViCS SPIRE bands were effectively confusion noise limited (70 % of the overall noise is from the confusion noise at 250 μm). Consequently, when planning the HeFoCS we requested 4 scans as this offered almost confusion limited maps with half the time required for a single HeViCS tile. The NGP was designed to cover as much area as possible with very low depth and subsequently is only composed of a scan and cross-scan.

In order to assess the ratio of the global noise in the HeViCS, HeFoCS and NGP maps, we measure the pixel-pixel fluctuations and apply an iterative 3σ clip to remove bright sources. The global noise in the HeViCS, HeFoCS and NGP at 250 μm is thus, 7.5, 8.9 and 11.3 mJy beam^{-1}, respectively, yielding ratios between the HeViCS-HeFoCS and HeViCS-NGP of 1.2 and 1.5, respectively. These ratios are significantly less than one would expect from a simple $\sqrt{2}$ and $\sqrt{4}$ increase in depth if the maps were purely instrumental noise limited, thus showing that the surveys are reasonably well suited for comparison.

Second we consider the coverage of the HeViCS, HeFoCS and NGP FIR maps of their respective clusters. The Coma cluster is covered well beyond the virial radius, however calculating the coverage for the other surveys is less straightforward. The clusters have very different physical sizes and states of relaxation - Virgo is far more 'clumpy' than Fornax or Coma. The irregular shape of Virgo leads to the HeViCS FIR maps comprising of 4 tiles ($4^\circ \times 4^\circ$) running North to South, whereas the HeFoCS is only a single tile ($4^\circ \times 4^\circ$). A possible solution is to use the fraction of the VCC and FCC galaxies that lie inside the boundary of each FIR survey, which is incidentally $\frac{2}{3}$ for both, showing again that the HeViCS and HeFoCS are well suited for a FIR comparison of the two clusters.

2.3 Source Measurement

2.3.1 General approach

I have used a semi-automated source measurement program written in IDL, to measure the FIR flux density of each galaxy. This program was written by Robbie Auld and is fully described and extensively tested in Auld et al. (2013). I use his software with a few changes that are described below as it was shown to produce reliable fluxes for HeViCS galaxies in the local universe.

Of the FCC galaxies, 237 fall into the SPIRE maps and 201 fall into both the PACS and SPIRE maps. Of the CCC/CFC galaxies, 1725 fall into both the PACS and SPIRE maps. The optical parameters (position, eccentricity, optical diameter D_{25} and position angle[2]) from the optical catalogues were used to make an initial estimate of the shape and size of the FIR emission. Previous studies (Cortese et al., 2010b; Pohlen et al., 2010) show that FIR emission is well traced by the optical parameters of late-type galaxies, whereas early-type galaxies typically show more compact dust emission (Smith et al., 2012). The optical parameters are only used to make an initial estimate for creating masks. The program then

[2]Position angle and eccentricity are not listed in the FCC but were obtained using the online database *Hyperleda* (Paturel et al., 2003).

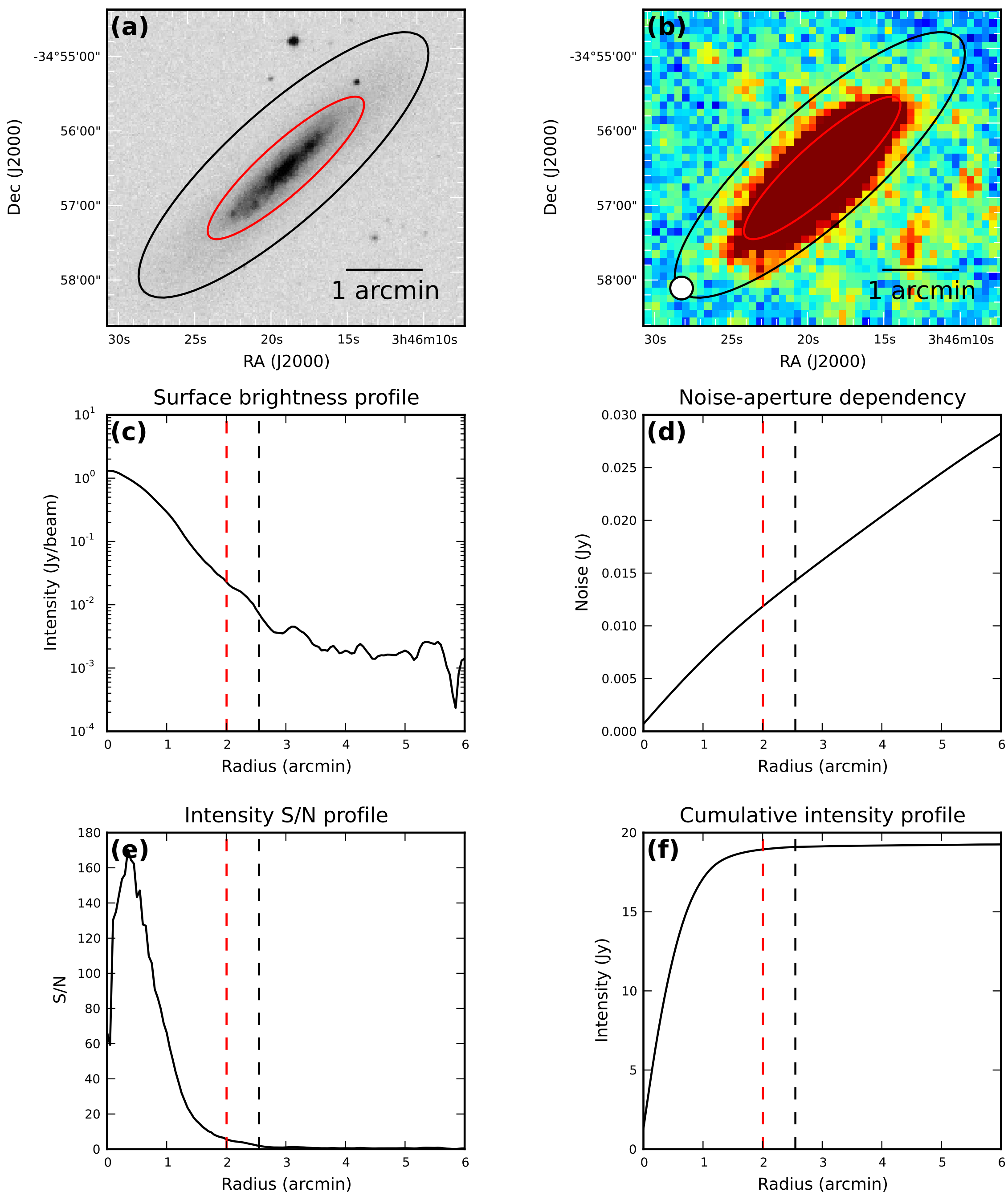

Figure 2.5. This is the postscript output generated for FCC312. Excluding the upper left-hand panel, all panels refer to the *Herschel* 250 μm band. (a) An optical image of the galaxy, the red and black ellipses show the optical D_{25} and the FIR extent of the galaxy (see text for definition). (b) The raw sub-image cutout of the FIR map. The beam size is shown in the lower left-hand corner. (c) The surface brightness profile. (d) Noise for an equivalent sized circular aperture (see text for definition). (e) S/N per annuli. This shows the cut off when S/N$\leq$2. (f) A cumulative intensity profile. The red and black dashed lines show the optical and FIR extents, respectively.

iterates, to create masks and apertures that best match the diameter and ellipticity of the FIR emission. For the following explanation, it may serve the reader to consult Figure 2.5.

The flux measurement process starts by extracting a 200×200 pixel sub-image from the raw map as shown in Figure 2.5b. To measure the background of the sub-image, all nearby galaxies including the galaxy being measured are initially masked at $1.5 \times \mathrm{D}_{25}$. If the optical extent of the galaxy is such that this sub-image is not large enough to give an accurate background estimation, then the program will increase the size of the sub-image, up to 600×600 pixels for SPIRE and 1200×1200 for PACS.

The background estimation has to deal with the near confusion limited SPIRE maps and instrumental noise in the PACS maps. This program was originally written for use in the HeViCS maps where Galactic cirrus was also a major problem. In order to remove bright background galaxies and Galactic cirrus Auld et al. (2013) used a 98% flux clip and then fitted the remaining pixels with a 2D polynomial. The flux clip removes bright background galaxies by masking out the brightest 2% of pixels, which ensures that the 2D polynomial is only fitting the Galactic cirrus. Cirrus is not obviously present in the HeFoCS or NGP maps and as such the 98% clip has been retained and then the median pixel value of the masked sub-image taken as the background value.

We measured total flux, surface brightness, aperture noise (fully described in Section 2.3.2) and signal to noise (S/N) along annuli of increasing radius centred on the galaxy's optical centre. The shape of the annuli is based on the galaxy's optical parameters convolved with the appropriate point spread function (PSF). We plot the corresponding radial profiles in Figure 2.5 c, e & f, respectively. The FIR diameter[3] D_{FIR} is defined where the S/N profile drops below 2. This D_{FIR} is used to replace the $1.5 \times D_{25}$ used to make the initial mask. The process iterates until the mask and the D_{FIR} value converge.

If the total S/N value was less than 3, the sub-image was then searched optimally for a point source. After convolving with the relevant PSF, the maximum value within the FWHM of the PSF centred on the optical position was taken as the flux. The noise was calculated according to Marsden et al. (2009) and Chapin et al. (2011), which involved plotting a histogram of all the pixels in the PSF-convolved sub-image and fitting a Gaussian function to the negative tail. The FWHM of this Gaussian is then used to estimate the combined instrumental and confusion noise. This has been summed in quadrature with the calibration uncertainty (see below) to obtain a value for the total noise. If the S/N was still less than 3 we consider the object undetected and set an upper limit on the flux equal to 3 times the noise in the PSF-convolved sub-image. This marked the end of the automatic source measurement process. The output is in the form of postscript files for each galaxy, as shown in Figure 2.5.

[3]As some galaxies are not resolved D_{FIR} in some cases will be defined by the PSF of the *Herschel* beam and will not be representative of the extend of dust in the galaxy.

2.3.2 Total uncertainty estimate

The total uncertainty is estimated from the calibration uncertainty, σ_{cal} and aperture uncertainty, σ_{aper}, summed in quadrature.

For SPIRE, σ_{cal} is based on single scans of Neptune and on an assumed model of its emission. The final error for each band is estimated to include 4% correlated and 1.5% from random variation in repeated measurements, as well as 4 % due to uncertainty in the beam area. The SPIRE observer's manual[4] suggests that these should be added together, leading to a SPIRE σ_{cal} of 9.5%.

For PACS, σ_{cal} is based on multiple sources with different models of emission. The PACS observer's manual[5] lists the uncorrelated uncertainties as 3 % & 4 % for 100 and 160 μm, respectively, and the correlated uncertainty is given for point sources as 2.2 %. However, the data used for calculating these uncertainties were reduced and analysed in a different way than the HeViCS, HeFoCS and NGP PACS data. Here we use the same value for total error as in Auld et al. (2013), i.e. 12 %.

To calculate the aperture uncertainty (σ_{aper}) a large number of apertures of a fixed size were placed randomly on each sub-image. We measure the total flux in each aperture, then by applying an iterative 3σ clipping procedure use σ as the uncertainty for that size of aperture. Repeating this for a range of aperture sizes allows us to estimate the aperture uncertainty as a function of size (Ibar et al., 2010). This method takes into account both confusion noise and instrumental noise. Figure 2.5d shows such a plot of aperture uncertainty against radial distance for FCC312 (a detected HeFoCS galaxy). Auld et al. (2013) tested this method over an entire 4° x 4° tile in the southern region of Virgo and compared it to the results obtained on the sub-images. They found very good agreement between the two, within the typical radii of FIR emission for Virgo galaxies. At larger radii this relationship broke down, which was attributed to large scale structure in the HeViCS maps.

2.4 Dealing with Blending and Contamination

Herschel's comparatively large FWHM can lead to unavoidable contamination by FIR background sources, which could be falsely identified as target galaxies. The level of this contamination is estimated below. However, due to the very different samples we have used two very different approaches. Fornax, like Virgo has a small number of point-sources and is relatively nearby therefore (as described and tested below) we can reject galaxies using a 'by-eye' method. Coma is too distant for a simple 'by-eye' method, however, the CCC/CFC

[4]http://herschel.esac.esa.int/Docs/SPIRE/html/spire_om.html
[5]http://herschel.esac.esa.int/Docs/PACS/html/pacs_om.html

Flux bin (mJy)	N_a	N_r	N_p ($\deg^{-2}$)	N_c
20-45	9	17	516	9
45-100	5	1	297	5
100+	3	1	59	1

Table 2.2. Estimates of the contamination from background galaxies in the HeFoCS 250 μm SPIRE band. N_a is the number of sources accepted in each flux bin, N_r is the number of sources that were rejected from the catalogue in each flux bin. N_p is the source number density (see text). N_c is the expected number of spurious contaminating sources.

have many more galaxies and thus it is possible to use a 'Monte Carlo' modelling method (fully described below) to estimate background contamination and reject sources on this basis.

2.4.1 Fornax

We have plotted the 250 μm map as contours over a superCOSMOS (Hambly et al., 2001) image of each galaxy and its immediate environment. As shown in Figure 2.6, if a galaxy could not be clearly separated from a nearby or background galaxy we removed it from our catalogue. Figure 2.6a shows a FIR source that is clearly coincident with a Fornax galaxy. Figure 2.6b shows a background source that is brighter than the 3σ noise limit and has been registered as a detection by our program. Figure 2.6c may be a detection, however, we cannot separate it from another apparent detection, so it was also removed. For galaxies that have been eliminated from our final catalogue through this process we set an upper limit on their flux density equal to the 3σ noise from the PSF-convolved map. As in Auld et al. (2013) we impose a strict criterion that a galaxy must be detected at 250 μm as this provides the best combination of sensitivity and resolution.

In order to show our source rejection process has been successful we examine the source counts. We assume that if extended FIR emission is found coincident with a Fornax galaxy it is reliable, and thus only concern ourselves with the point source population.

We assume that the background sources are distributed randomly and uniformly across the sky with no cosmic variance. The number of contaminating sources is estimated using the number counts from the HeFoCS data (as described in Section 2.1) and then calculating the probability of a chance alignment with the 250 μm SPIRE beam. We limit this analysis to the 250 μm SPIRE band, as this was the band in which we made our by-eye inspection. It should also be noted that while the SPIRE bands are near confusion noise limited, the PACS bands are limited by instrumental noise. Consequently, PACS fluxes are far less likely

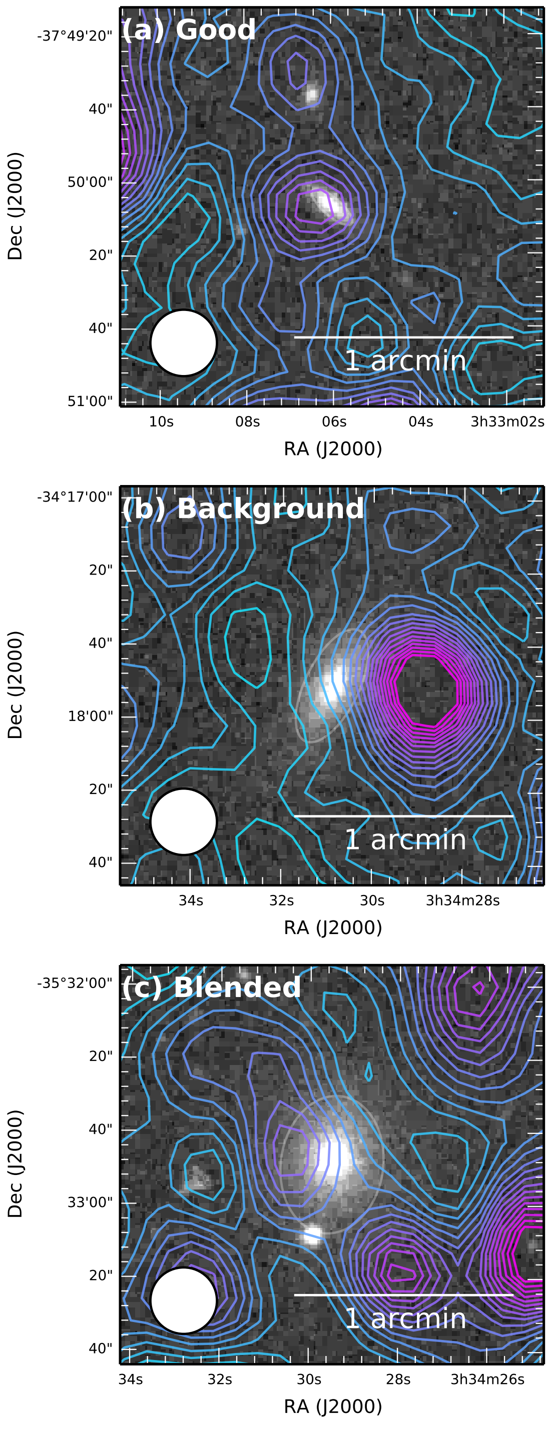

Figure 2.6. The SPIRE 250 μm contour map, plotted over the superCOSMOS r-band image of FCC 117, 135 and 136 for sub-figures (a), (b) and (c) respectively. The beam size is shown in the lower left hand corner. The white ellipses indicate the optical (D_{25}) extent of each galaxy. (a) a galaxy that by-eye we flagged as a good detection as it is coincident with the FIR contours. (b) this galaxy was removed as it is clearly a bright background source that does not appear in the optical image. (c) the FIR source cannot be uniquely identified; it looks to be comprised of more than one source and as such was removed.

to be contaminated by a background source.

The contamination has been calculated within various flux intervals, as shown in Table 2.2. If done correctly we would expect the number of rejected galaxies to be roughly equivalent to the number of expected contaminating sources within the sum of the total area of apertures used. Table 2.2 clearly shows that we have been over zealous in our rejection of sources in the 20 - 45 mJy bin, however, in the 45 - 100 mJy bin we have not rejected as many contaminating sources as the number counts predict. Overall we accept 17, reject 19 and estimate there are 15 contaminating galaxies at 250 μm. If we assume Poisson root N errors, then these small numbers are within 3σ.

2.4.2 Coma

The Coma sample is too distant to use the 'by-eye' inspection of sources to reject background sources as used in the HeViCS and HeFoCS (see above). However, the comparatively large sample allows us to use 'Monte Carlo' modelling of the background source population to calculate our expected contamination for a given FIR-optical source distance (fully detailed below).

We again assume that if extended emission is detected at the location of a optical Coma galaxy it is a reliable detection. Consequently, the following discussion is only regarding the point-source populations (60 % of the total detections at 250 μm are point-sources).

As in Fornax and Virgo we impose a strict criterion that a galaxy must be detected at 250 μm as this provides the best combination of sensitivity and resolution (see below). Thus, we estimate the contamination at 250 μm. We have done this by comparing the separation between the optical galaxy and its FIR counterpart, then repeating this for a random catalogue of equal size and then comparing this histogram with a randomly generated one.

We have computed the distance to the nearest FIR neighbour from the NGPSC[6] for each optical CCC/CFC galaxy, the white diagonally hatched histogram in the upper panel of Figure 2.7 shows this distribution of CCC/CFC galaxies to NGPSC galaxies in the 250 μm band. We then repeat this process, inputting a catalogue of equal length to the CCC/CFC with random positions on the sky inside our survey area, and again find the nearest FIR neighbour from the NGPSC for each galaxy. In order to minimise the error in this latter step we repeat this random catalogue generation and cross-match many ($\sim 10^6$) times taking the average of all these distributions. The random-NGPSC mean distribution is shown in the blue histogram in the upper panel of Figure 2.7. The lower panel of Figure 2.7 shows the percentage contamination in our catalogue for each bin of angular separation in arc

[6]The NGPSC (Valiante et al. in preparation), fit a gaussian to each point source to determine an accurate centre for each FIR detection in the entire NGP map.

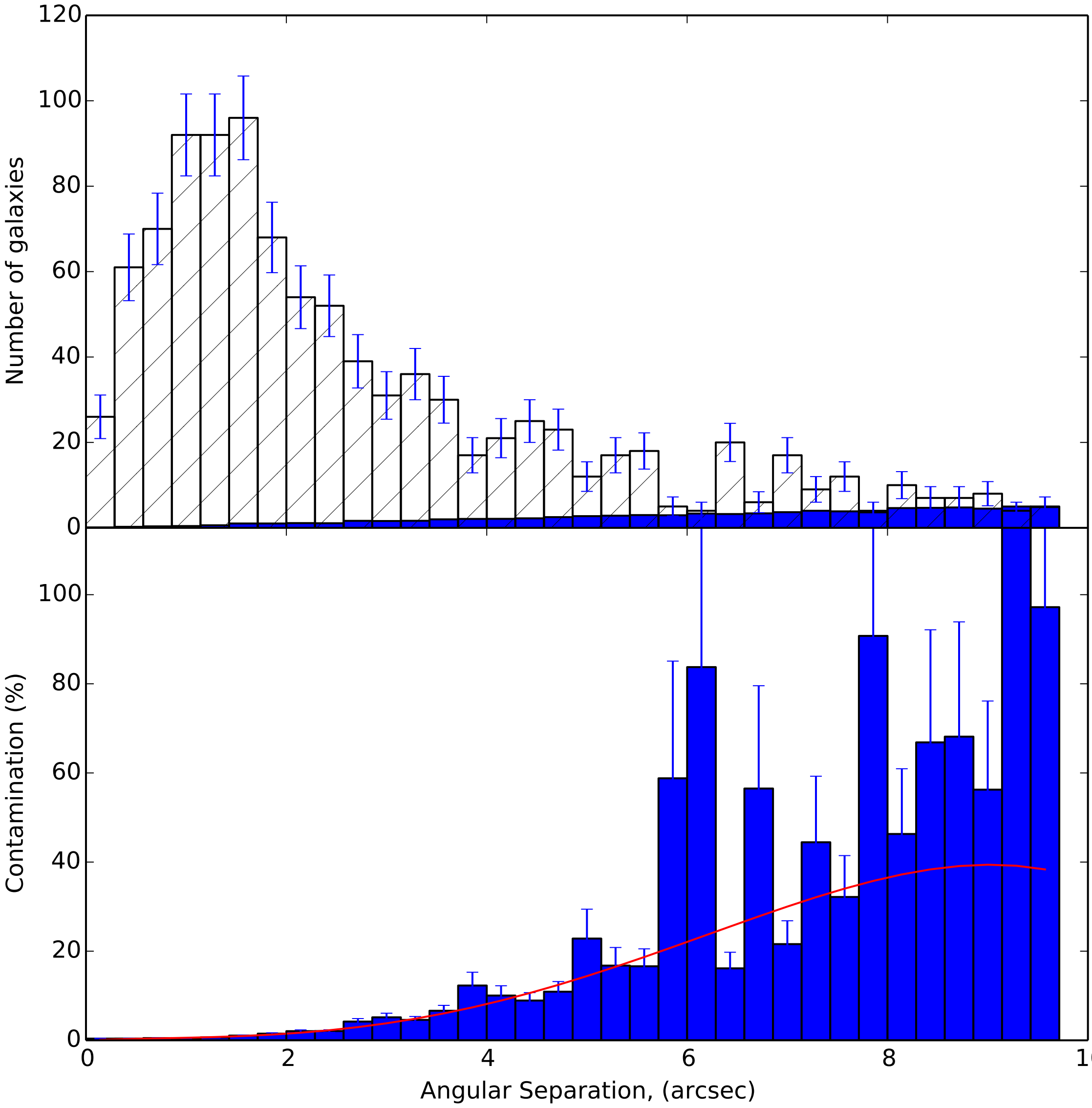

Figure 2.7. This figure shows the results of our simulations and our method for estimating angular contamination at 250 μm in the CCC/CFC. The clear hatched histogram in the upper panel shows the distribution of angular separations of CCC/CFC galaxies thier nearest FIR neighbour. The blue histogram in the upper panel shows the mean distribution of our simulations of a random catalogue of galaxies (see text). The lower panel shows the contamination for each bin of angular separation. The red line is a third order polynomial fitted to the data using a χ^2 minimisation technique.

Band μm	Gradient, M	Intercept, C
100	0.992 ± 0.025	0.007 ± 0.151
160	0.938 ± 0.018	0.054 ± 0.113
250	1.015 ± 0.015	-0.011 ± 0.055
350	1.024 ± 0.015	-0.001 ± 0.024
500	0.963 ± 0.033	0.003 ± 0.021

Table 2.3. The parameters of the straight line fit shown in Figure 2.8 for the HeFoCS.

seconds. We fit a third order polynomial using a χ^2 minimisation technique, then calculate the angular separation where contamination is equal to 5 % and we find this to be at 3.5 arc seconds.

As such we set a limit of 3.5 arc seconds between a CCC/CFC galaxy and a FIR point-source at 250 μm. For galaxies that have been eliminated from our final catalogue through this process we set an upper limit on their flux density equal to the 3σ noise from the PSF-convolved map.

2.5 Flux Verification

In order to verify our automated FIR source measurement process we cross match and compare our measured fluxes with FIR data in the literature for both Fornax and Coma.

2.5.1 Fornax

We have compared our measured fluxes with the Fornax Bright Galaxy Sample (BGS) (Davies et al., 2012a), as shown in Figure 2.8, and tabulated the gradients and intercepts in Table 2.3. Davies et al. (2012a) matched 10 galaxies with IRAS (Helou & Walker, 1988; Conrow et al., 1993) and 5 with PLANCK (López-Caniego, 2014) sources finding good agreement in both cases. Table 2.3 shows overall that the results are consistent with a gradient of 1 and an intercept of 0.

2.5.2 Coma

We have compared our CCC/CFC fluxes with those found in the literature, as shown in Figure 2.9, and tabulated the gradients and intercepts in Table 2.4. We matched our catalogue with the IRAS point source catalogue (Helou & Walker, 1988), the IRAS faint source catalogue (Conrow et al., 1993), Hickinbottom et al. (2014) a deep *Herschel*-PACS

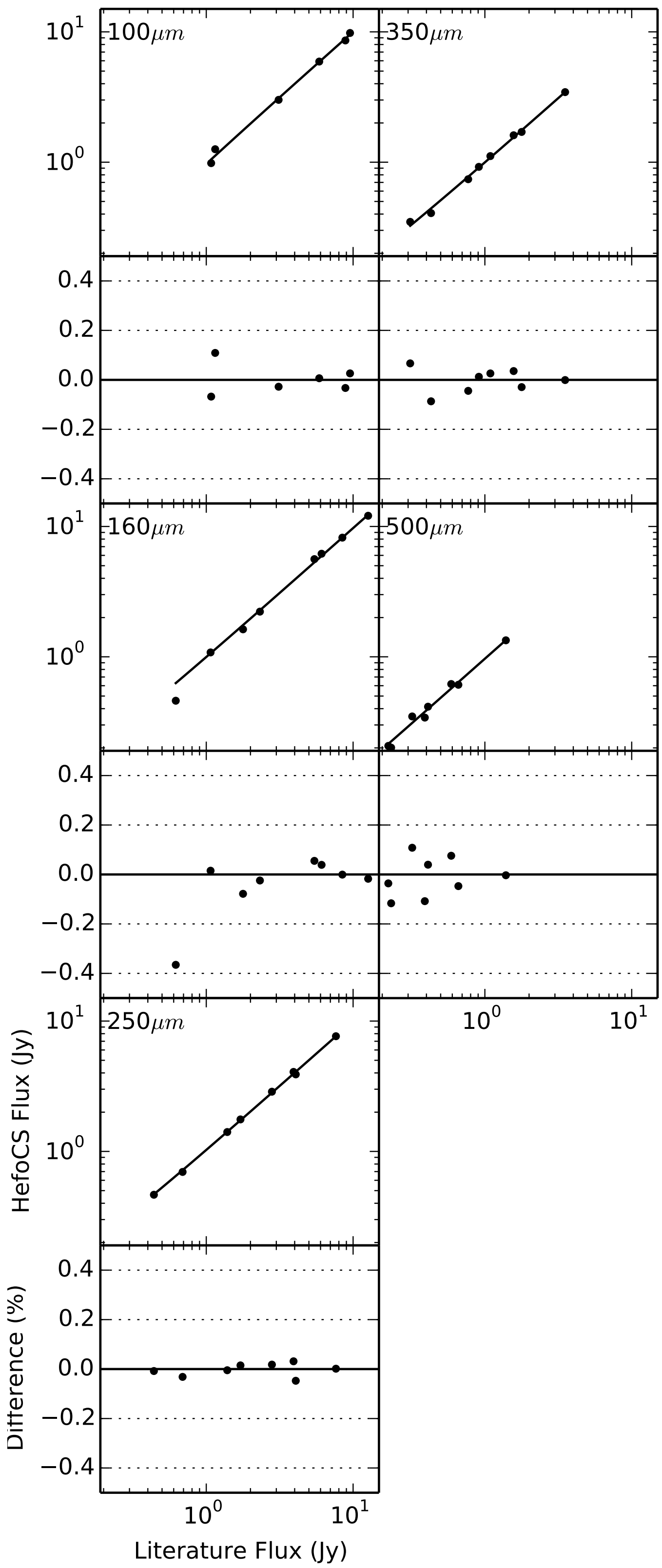

Figure 2.8. The HeFoCS fluxes plotted against the Davies et al. (2013) values for the bright galaxy sample. The residual plot below shows the percentage deviation from the fitted line.

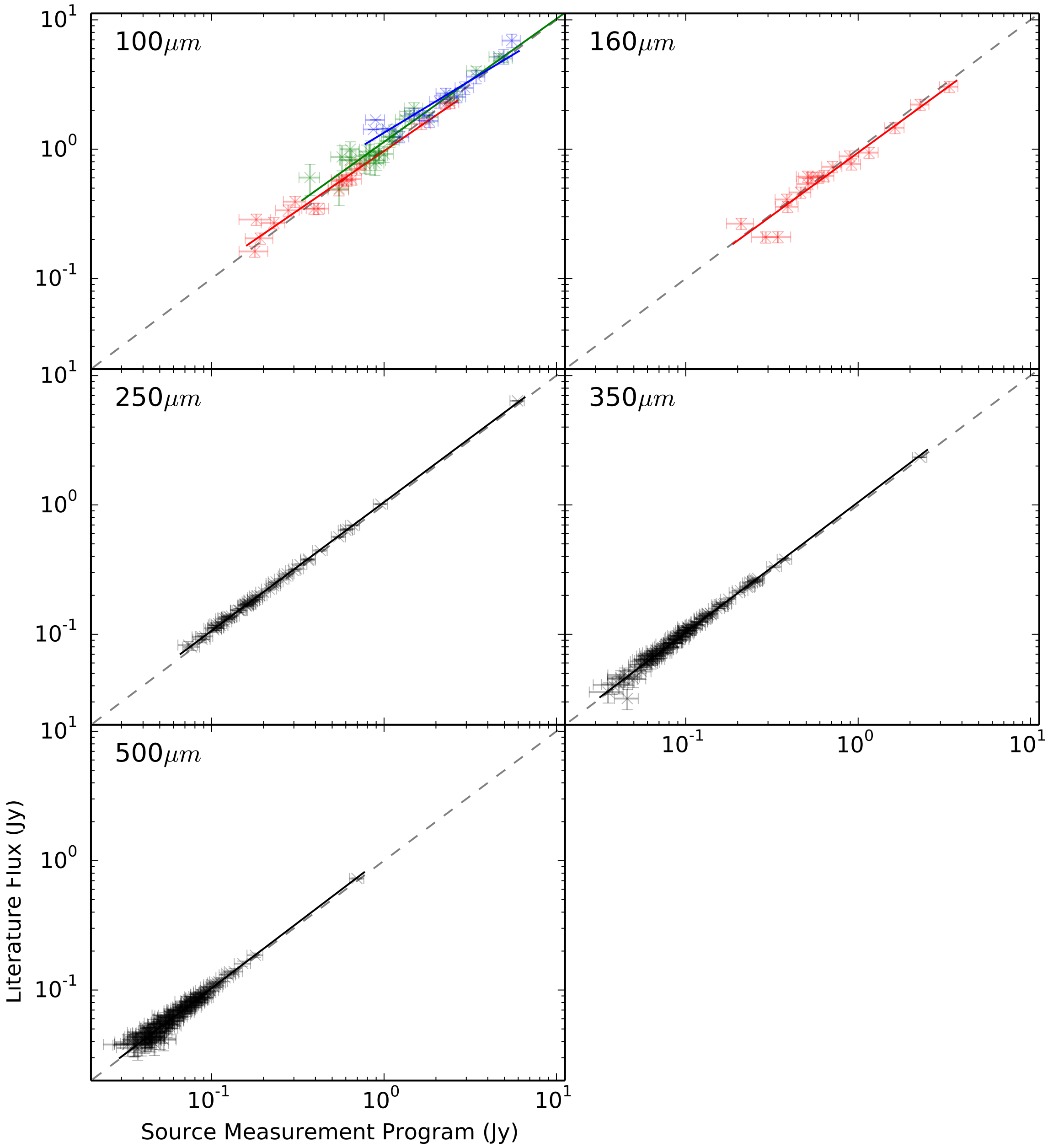

Figure 2.9. The FIR CCC/CFC fluxes plotted against other measured values. Markers are as follows; IRAS faint source catalogue (Conrow et al., 1993), green; IRAS point source catalogue (Helou & Walker, 1988), blue; deep PACS (Hickinbottom et al., 2014), red; and NGPSC, black. The gray diagonal dash line represents a linear one-to-one relation ($y = mx = c$, where $m = 1$ and $c = 0$).

Band μm	Gradient, M	Intercept, C
100^a	1.060 ± 0.009	0.074 ± 0.041
100^b	1.093 ± 0.077	0.108 ± 0.211
100^c	0.915 ± 0.057	0.033 ± 0.020
160^c	0.952 ± 0.083	0.024 ± 0.040
250^d	1.073 ± 0.001	-0.011 ± 0.055
350^d	1.024 ± 0.015	-0.001 ± 0.024
500^d	0.963 ± 0.033	0.003 ± 0.021

a - IRAS FSC - Conrow et al. (1993)
b - IRAS PSC - Helou & Walker (1988)
c - Deep PACS - Hickinbottom et al. (2014)
d - NGPSC

Table 2.4. The parameters of the straight line fits shown in Figure 2.9 for the CCC/CFC-NGP galaxies.

survey of the cluster core, and with the NGPSC. For IRAS and NGPSC sources we find good agreement. Table 2.4 shows overall that the results are consistent with a gradient of 1 and an intercept of 0. However, the faintest (<50 mJy) matched sources from Hickinbottom et al. (2014) appeared brighter than the flux recorded at 100 and 160 μm in our catalogue. These sources were all recorded at fluxes below the 3σ global noise limit of the NGP PACS maps. After extensive testing by both ourselves and Hickinbottom et al. (2014) we place a further stipulation for a source to be detected in the PACS bands thus, requiring all PACS sources to have a flux density greater than $3\times$ the global measured noise in the NGP PACS maps. My pacs fluxes could have had higher values than the Hickinbottom et al. (2014) fluxes due to a phenomenon known as 'Eddington bias'. The variability of our measured flux can randomly fluctuate and as as we set a firm signal to noise threshold for detection only sources where this random fluctuation adds to the flux will be detected and where it lowers the flux they will not be detected in the FIR. Thus, artificially increasing the fluxes of our galaxies.

2.5.3 Missing FIR sources

By using optical catalogues we run the risk of missing a population of FIR sources not detected in the optical. Conversely we could make our selection in the FIR, but then there is no way of determining which sources are in the clusters.

Below, we show that a large population of cluster FIR sources without optical counterparts is unlikely to exist. We do this by comparing the number counts of sources in the HeViCS, HeFoCS and NGP 250 μm maps with data extracted from the north-east quadrant of the

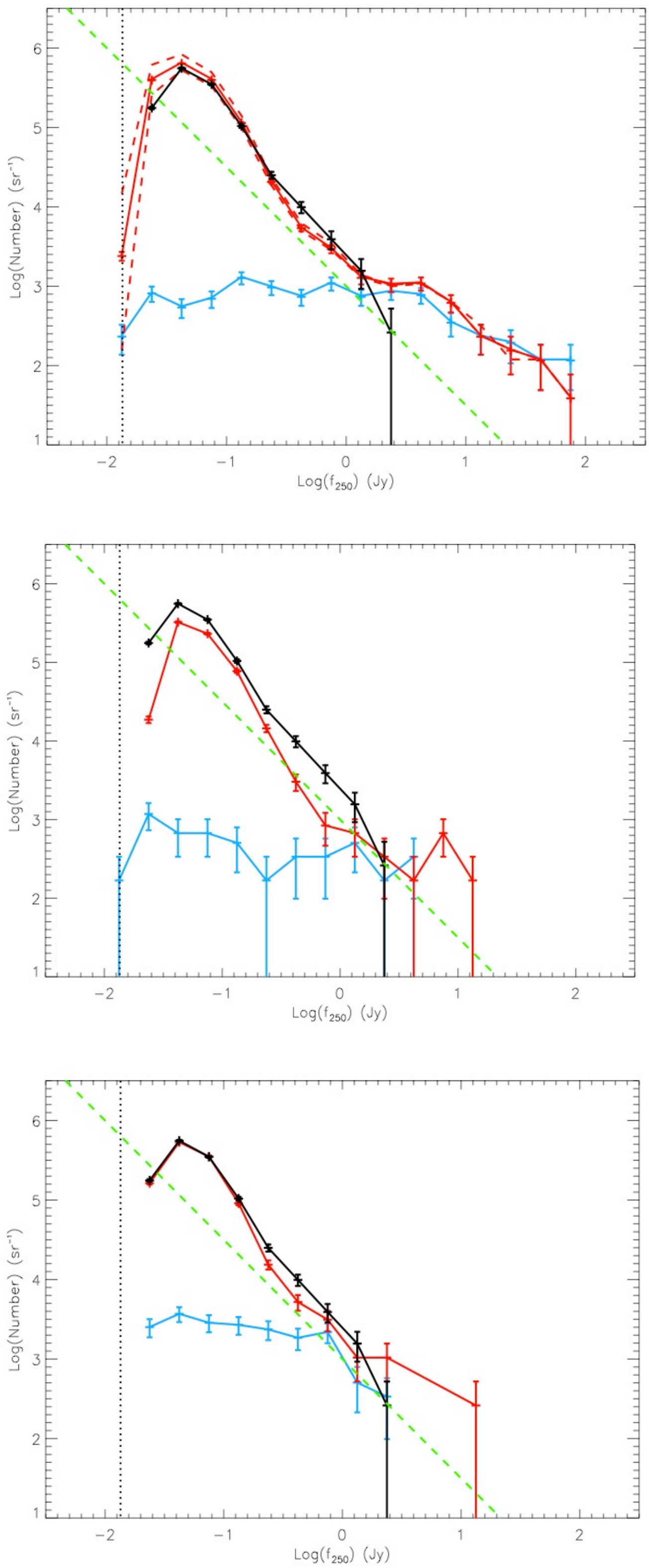

Figure 2.10. Histograms of the 250 μm flux density of galaxies against number per steradian. The black lines are the NGP (north-east quadrant, see text for more details). The red lines represent the HeViCS, HeFoCS and NGP fields in the upper, middle and bottom panels, respectively. The cyan dashed lines represents the FIR detected galaxies from the optical catalogues in each cluster. The errors are simply $\sqrt{N}$. The vertical dashed lines mark the minimum flux density detectable.

NGP as it has the lowest foreground galaxy density (see Figure 2.4). By comparing histograms of number counts in these fields, one 'looking' through the clusters and the other a purely background reference, we can look for evidence of a FIR excess of sources in the clusters.

We only use the 250 μm band to do this, as we impose a selection in our FIR catalogue such that each galaxy must be detected at 250 μm (see below). We use the software, *SExtractor* to measure the flux density of all the sources in each map. *SExtractor* 'grids up' each map and calculates the noise in each sub-grid. The parameter that controls this is 'meshsize', which we fix at 100 arcmin^2 as this is much greater than the size of any of our foreground galaxies. The detection threshold was set at 1.6σ above the local background for all maps. Another requirement was that the detection size of a source was greater than the SPIRE beam area at 250 μm (450 arcsec^2).

Figure 2.10 shows the number counts generated from using the above approach for each survey (HeViCS, HeFoCS and NGP are shown in the upper, middle and lower panels, respectively). The black lines are the NGP (north-east cluster free quadrant). The red lines represent the HeViCS, HeFoCS and NGP fields in the upper, middle and bottom panels, respectively. The cyan dashed lines represents the FIR detected galaxies from the optical catalogues in each cluster. The black and red lines trace each other very well within the $\sqrt{N}$ errors below about 1 Jy, brighter than this there is a small excess due to the presence of cluster galaxies. In conclusion we find no evidence for a significant excess population of FIR sources that are not associated with the optical sources in our three optical catalogues.

2.6 SED FITTING

After producing a FIR flux catalogue (see above) Matt Smith fitted a modified blackbody to every galaxy detected in at least 3 and 5 $Herschel$ bands for Fornax and Coma, respectively. The requirement in the HeViCS was 5 $Herschel$ bands, however, we lowered this in the case of the HeFoCS to increase our sample size. Using the SED fit we estimate dust mass and temperature. The fit is based on the equation:

$$S_\lambda = \frac{\kappa_{abs} M_{dust} B(\lambda, T_{dust})}{D^2} \tag{2.1}$$

where S_λ is the flux density, M_{dust} is the dust mass, T_{dust} is the dust temperature, $B(\lambda, T_{dust})$ is the Planck function, D is the distance to the cluster and κ_{abs} is the dust absorption coefficient. The latter follows a power law modified by an emissivity (β), such that:

$$\kappa_{abs} = \kappa_{abs}(\lambda_0) \times \left(\frac{\lambda_0}{\lambda}\right)^\beta \tag{2.2}$$

We assume that emission at these wavelengths is purely thermal and from dust at a single temperature with a fixed $\beta = 2$ emissivity. We use $\kappa_{abs}(350\,\mu\mathrm{m}) = 0.192\,\mathrm{m}^2\,\mathrm{kg}^{-1}$ according to Draine (2003). The above function is fitted using a χ^2 minimisation technique.

Although this is most likely an overly simplistic analysis, this approach has been used in previous works (Davies et al., 2010, 2012a; Smith et al., 2012; Auld et al., 2013; Verstappen et al., 2013) and shown to fit the data very well in the FIR/sub-mm regime. Bianchi (2013) showed that using a single component modified blackbody returns equivalent results to more complex models such as Draine & Li (2007).

Chapter 3
Auxiliary Data

"In our world, said Eustace, a star is a huge ball of flaming gas. Even in your world, my son, that is not what a star is, but only what it is made of."

C S Lewis - The Voyage of the Dawn Treader

In this chapter I will outline the auxiliary data available for each region. With regards to the HeFoCS, very little other data exists for this region. Conversely, the NGP region is covered with SDSS spectroscopic and photometric surveys which offer not only the positions, sizes and shapes as used in the previous chapter, but also SFR, stellar mass and metallicity. We also take advantage of the atomic gas data in the well observed Coma region as detailed below.

3.1 Fornax

3.1.1 Stellar masses

Only 35 galaxies in the FCC have both a $(B-V)$ colour and K-band flux listed in *Hyperleda* and we have used this to calculate stellar masses using the prescription of Bell et al. (2003):

$$\log_{10}\left(\frac{M_{Star}}{\mathrm{M}_{\odot}}\right) = -0.206 + 0.135(B-V) + \log_{10}\left(\frac{L_K}{\mathrm{L}_{\odot}}\right) \quad (3.1)$$

Based on these 35 galaxies we find the following best-fitting linear relation between m_{BT} and stellar mass as shown in Figure 3.1:

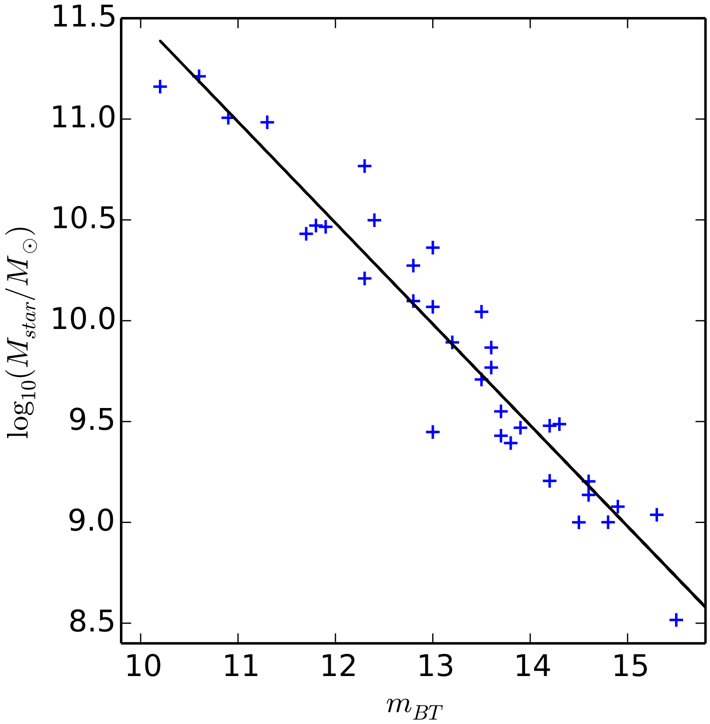

Figure 3.1. Calculated stellar mass plotted against total blue magnitude for the FCC galaxies. The blue points are galaxies with stellar masses calculated from their $(B-V)$ colour and K band fluxes and the black line is a best fit line to these data.

$$\log_{10}\left(\frac{M_{Star}}{\mathrm{M}_{\odot}}\right) = -0.51\, m_{BT} + 16.6 \tag{3.2}$$

We use this relation and the m_{BT} value listed in *Hyperleda* to estimate the stellar mass of all remaining galaxies in the FCC.

3.2 Coma

3.2.1 Stellar Mass, Star Formation Rate and Metallicity

Kauffmann et al. (2003), Brinchmann et al. (2004) and Tremonti et al. (2004) have used the SDSS spectra and optical colours to calculate stellar mass[1], SFR and gas phase metallicities, respectively. Kauffmann et al. (2003), Brinchmann et al. (2004) and Tremonti et al. (2004) designate a galaxy as either having emission lines or not. For galaxies without emission lines, stellar mass and SFR are calculated using the optical colours and the 4000 $\AA$ break in the SDSS spectra. However, for galaxies without emission lines metallicities cannot be measured this way. In Table 3.1 we have shown the number of galaxies in the CCC/CFC with and without measured metallicities.

3.2.2 Atomic Hydrogen

We have cross-matched the CCC/CFC with data collected from Gavazzi et al. (2006) and galaxies from the Arecibo Legacy Fast Arecibo L-band Feed Array Survey (ALFALFA) (Haynes et al., 2011). Gavazzi et al. (2006) used the Arecibo radio telescope to detect 35 spiral galaxies in the Coma supercluster. They also added all the data available in the literature, yielding 92 galaxies that appear in both catalogues. We use the ALFALFA 0.4α data (Haynes et al., 2011) adding a further 138 galaxies. In total we have atomic hydrogen data for 230 CCC/CFC galaxies. Where we have a measurement from the literature and from ALFALFA we have taken the value from the ALFALFA 0.4α, however, in all cases any difference is inside a $1\,\sigma$ uncertainty. In Table 3.1 I have shown the number of galaxies detected of each morphological type (see below) in the cluster and filament.

[1] In order to make the stellar masses in Coma consistent with Fornax and Virgo we have adjusted the SDSS stellar masses by +0.15 dex to converted fom the Kroupa IMF (Kroupa, 2002) to a “diet” Salpeter IMF (Bell et al., 2003) as per the recipes in Brinchmann et al. (2004).

3.2.3 Morphology

The large distance of the Coma cluster makes morphological classification far more ambiguous, especially for the fainter members of the CCC/CFC. The Galaxy Zoo project (Lintott et al., 2008) covers the majority of the SDSS DR7 galaxies that are included in the spectroscopic sample. They invite members of the general public to decide if a galaxy is either an elliptical or spiral. Based on these votes each galaxy can then be assigned a probability of being elliptical $p(E)$ or spiral $p(S)$. This allows us to define 3 morphological categories; early, $p(E)>0.8$; late, $p(S)>0.8$ and uncertain where $p(E)<0.8$ and $p(S)<0.8$. We will discuss the significance of these morphological categories below.

The *Goldmine* database[2] provides multi-wavelength data from an number of sources, with varying levels of completeness. As part of the *Goldmine* database Gavazzi & Boselli (1996) catalogued galaxies in the Coma region. They are complete for galaxies brighter than $m_B = 15.5$, covering a large - although not total - fraction of the NGP survey area. They visually classify galaxy morphologies into the more familiar Hubble types (E through to Sd). However the lack of optical depth, and area coverage means only 256 (15 %) galaxies are in both *Goldmine* and our SDSS catalogue.

The Galaxy Zoo catalogue has been shown to be consistent with classifications of the same galaxies by professional astronomers (Lintott et al., 2008). However, Lintott et al. (2008) also show that fainter galaxies are harder to classify and more likely to be classified as an early-type or uncertain-type. In order to understand our 3 morphological groups based upon the selection above, we have plotted a histogram for each of our morphological groups in Figure 3.2.

Figure 3.2 clearly shows that at the distance of Coma, Galaxy Zoo is a good predictor of morphology when compared to *Goldmine*. Early-types with a 0.8 likely-hood selection are mainly composed of E and S0s ($\sim$ 98 %), with only one early-type is in the S0/Sa bin. Late-type galaxies are mainly composed of Sa to Scs types. However, 8 galaxies are classified late-type by Galaxy Zoo and early-type by goldmine. In order to understand this we have visually inspected these galaxies (see Figure 3.3). Four of these galaxies (CCC 232, CCC 513, CFC 57, and CFC 344) are clearly edge-on galaxies, and as such morphological classification is always ambiguous. The remaining four galaxies are clearly late-types and are likely misclassified in *Goldmine*.

Figure 3.2 also helps understand the morphological make up of the uncertain-type galaxies(see above for definition). The uncertain-type covers a range of morphologies from E to Sc, however, it is mostly made up of S0 and S0/Sa galaxies. Goldmine is selected from the brightest galaxies in our sample where morphological classification is relatively

[2] http://goldmine.mib.infn.it

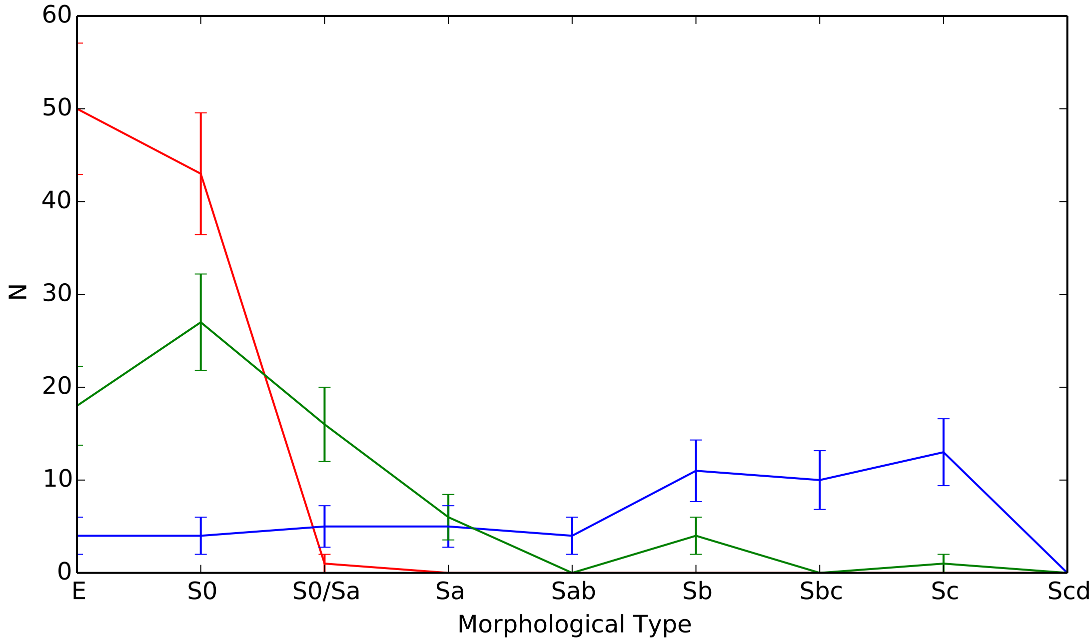

Figure 3.2. This plot shows three histograms of the three morphological groups; early, uncertain and late, as red, green and blue, respectivley. See text for definition of the three morphological groups. The categories on the x-axis are as per the *Goldmine* database. The error bars are simple root N errors.

Figure 3.3. This figure shows 8 galaxies that are classified as early by the *Goldmine* database, however, Galaxy Zoo gives them a greater than 80 % likelihood of being a late-type. The upper row are classfied as E, and the lower are classfied as S0. The images are colour images genorated from g, r and i SDSS bands. The galaxies are sorted left-to-right with galaxies on the right having the highest likelihood of being edge on.

Sample	N_{late}	$N_{uncert.}$	N_{early}	N_{total}
SDSS (full)	474 (100 %)	963 (100 %)	288 (100 %)	1725 (100 %)
SDSS (+Metallicity)	285 (60 %)	295 (30 %)	5 (1 %)	585 (33 %)
HI	119 (25 %)	81 (8 %)	8 (2 %)	208 (12 %)

Sample	Cluster			Filament		
	N_{late}	$N_{uncert.}$	N_{early}	N_{late}	$N_{uncert.}$	N_{early}
SDSS (full)	83	504	187	391	459	101
SDSS (+Metallicity)	25	53	1	260	242	4
HI	24	21	7	95	60	1

Table 3.1. The above table shows the availability of data for the CCC/CFC. The optical (SDSS) sample is the catalogue from which all other sub-samples are drawn. The persentage in brackets refers to the percentage of that galaxy for a given morphological type. See text for a definition of each sample.

clear. As Lintott et al. (2008) caution against inferring the uncertain-type is some form of intermediate-type (a galaxy midway through some kind of morphological transformation) we will include them in our analysis with this strict caveat in mind.

3.2.4 Local density

In order to examine the effect of local structure in comparison to global structure such as the cluster and filament we use the familiar N^{th} nearest neighbour statistic (Σ_N) as defined by the equation:

$$\Sigma_N = \frac{N}{\pi D_N^2} \tag{3.3}$$

Where D_N is the distance in Mpc to the Nth nearest neighbour. Generally this is used for galaxies within some velocity range. As we assume that all our galaxies are approximately at 100 Mpc we effectively 'collapse' our catalogue of cluster and filament into a 2D plane and measure distances on the sky[3].

We have calculated this Σ_N for the 1^{st}, 5^{th} and 10^{th} nearest neighbours for each galaxy. In order to avoid edge effects we have drawn a sample from the SDSS DR 10 spectroscopic

[3]This assumption is a reasonable one close to the cluster. However, as Figure 2.2 shows this may not be accurate at the edges of our sample in radial space. The benefits of having a velocity selection for these few galaxies eg of within 1000 km s^{-1}, would bias the determination of local density for cluster galaxies as the 1σ velocity dispersion is $\sim$ 1000 km s^{-1}. Thus for this work it is a reasonable comprise to 'collapse' the sample into a 2D plane assumed to lie at 100 Mpc.

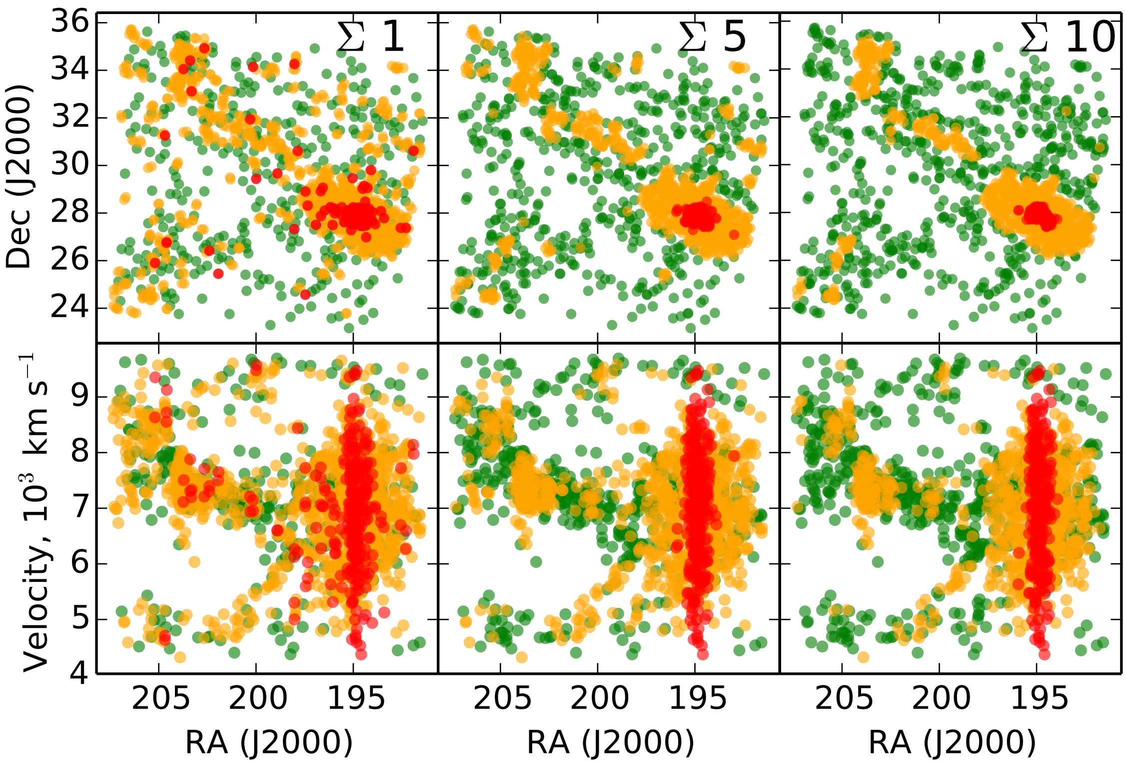

Figure 3.4. This series of plots demonstrates Σ_N for the 1^{st}, 5^{th} and 10^{th} nearest neighbours in our sample. The upper three plots are spatial plots in RA and Dec. The lower three plots show velocity and RA. Each plot has been divided into 3 bins, where green, amber, and red indicate lower, medium, and high density regions.

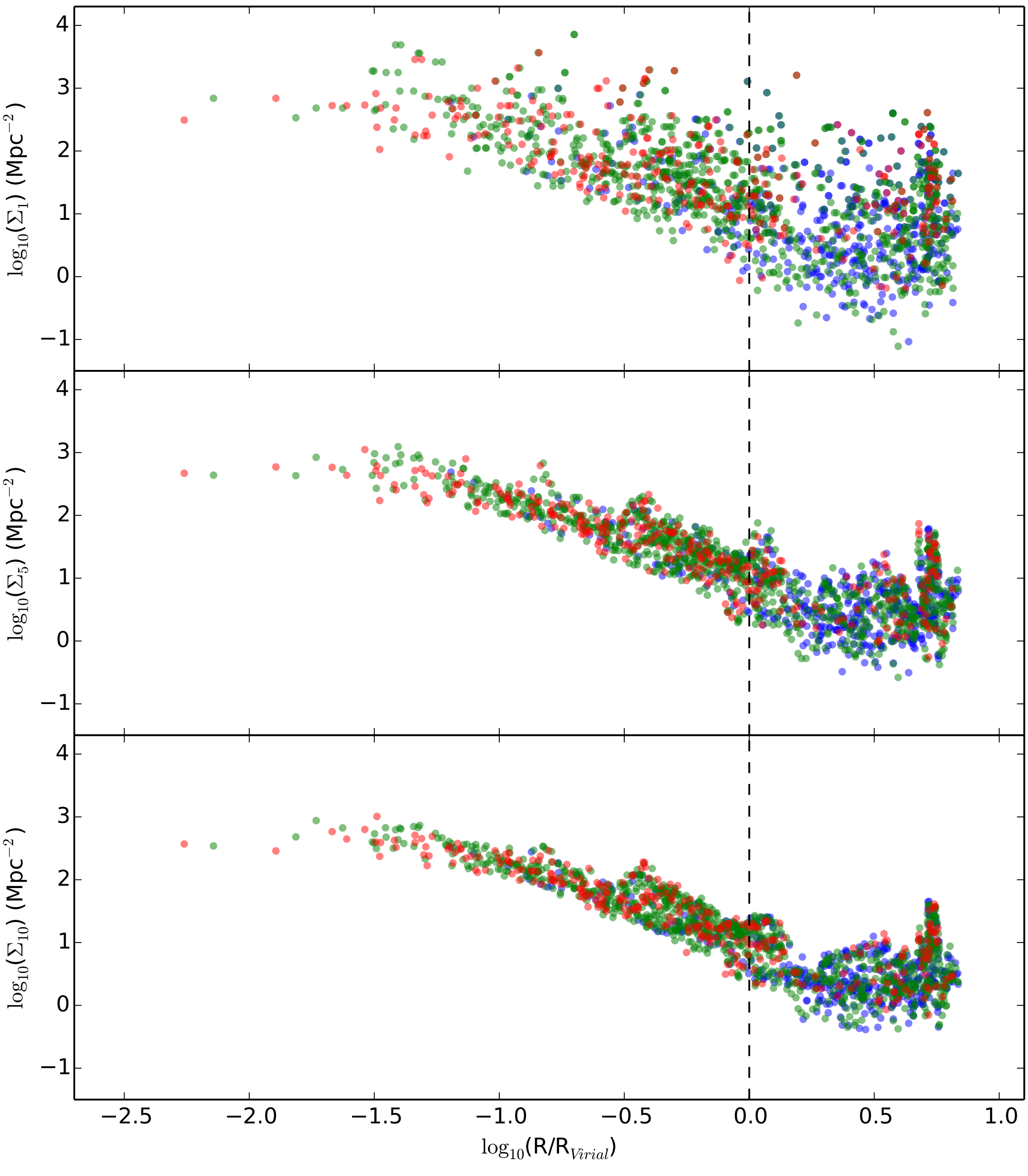

Figure 3.5. The three tracers of local density Σ_1, Σ_5 and Σ_{10} against projected cluster radius. Red, green and blue markers represent early, uncertain and late-type galaxies. The vertical dashed line marks Coma's virial radius (3.01 Mpc).

sample with our original velocity selection for the cluster and filament samples but to a greater spatial area.

Figure 3.4 shows the merit of each Σ_N statistic and what scale of environment it traces. Σ_{10} effectively smoothes over the largest spatial scale and is sensitive to the largest scale structures. Conversely, Σ_1 and Σ_5 are sensitive to a galaxy's immediate environment such as pairs and loose groups, respectively. Naturally, all Σ_N statistics are highest in the cluster core. However, Figures 3.4 and 3.5 show that within the filament there are a number of higher density regions that are group like. These groups are most likely in-falling into the cluster.

Part II

Fornax

Chapter 4
FIR properties of optically-selected Fornax cluster galaxies

"Without precise calculations, we'd fly right through a star, bounce too close to a supernova, and that'd end your trip real quick, wouldn't it?"

Han Solo

4.1 Introduction

The Fornax cluster is a nearby example of a poor but relatively relaxed cluster. It has a recession velocity of 1379 km s^{-1} and a distance of 17.2 Mpc, a mass of $7{\times}10^{13}$ $M_{\odot}$ and virial radius of 0.7 Mpc (Drinkwater et al., 2001). It is located away from the Galactic plane with a Galactic latitude of $-53.6°$ in an area of relatively low Galactic cirrus. This makes it ideal for study at all wavelengths.

Drinkwater et al. (2001) showed that despite Fornax's apparent state of relaxation, it still contains substructure, e.g. a small, in-falling group centred on NGC 1316, 3° to the southwest. However, compared to the Virgo cluster, Fornax is very centrally concentrated and probably formed at an earlier time. This is also suggested by the strong morphological segregation that has taken place, leaving the cluster almost entirely composed of early-type galaxies. Drinkwater et al. (2001) also noted that there exist two different populations, suggesting that while the giant galaxies are virialised, the dwarf population is still in-falling. Morphological segregation is not the only indicator of evolution in the cluster; the interstellar medium (ISM) of the galaxies also seems to have been affected by the cluster environment. Schröder et al. (2001) found that 35 Fornax cluster galaxies were extremely

H I -deficient in comparison to a field sample. H I is generally loosely bound to galaxies and as such is a good indicator of the effects of environmental processes.

In contrast to Virgo, Fornax has only very weak X-ray emission (Eckert et al., 2011; Shang & Scharf, 2009), which traces the hot intra-cluster gas. Compared to Virgo, this lack of an intra-cluster medium (ICM) along with a lower velocity dispersion ($\sim 300\,\mathrm{km\,s^{-1}}$) reduces the efficiency of mechanisms such as ram pressure stripping. We can estimate the efficiency of ram pressure stripping using $E \propto t_{cross} \delta v^2 \rho_{gas}$ (Gunn & Gott, 1972), where (E) is the stripping efficiency of a cluster, with a velocity dispersion (δv), central gas density (ρ_{gas}) and a crossing time t_{cross}. Both Virgo and Fornax have a similar crossing time, $t_{cross} \sim 10^9$ yr which is much less than their relaxation time $t_{relax} \sim 10^{10}$ yr (Boselli & Gavazzi, 2006). Virgo has a velocity dispersion which is $\sim 4\times$ greater and an ICM $\sim 2\times$ as dense as Fornax (Chen et al., 2007; Boselli & Gavazzi, 2006), indicating that Fornax may be $\sim 32\times$ less efficient than Virgo in removing a galaxy's ISM via ram pressure stripping.

Fornax's higher galaxy density, lower ICM density and lower velocity dispersion suggest that galaxy-galaxy tidal interactions will play a more important role than in a more massive cluster like Virgo (Combes et al., 1988; Kenney et al., 1995).

Dust, another constituent of the ISM, is also affected by the environment. Cortese et al. (2010b,a) showed that within a cluster like Virgo, dust can be stripped from the outskirts of a galaxy, truncating the dust disk. Dust is crucial for the lifecycle of a galaxy, as it allows atomic hydrogen to transform on its surface into molecular hydrogen and is thus essential for star formation. Around half the energy emitted from a galaxy is first emitted by stars, then reprocessed by dust, and re-emitted from 1 μm to 1 mm (Driver et al., 2008). Thus, to better understand the physical processes affecting galaxies it is crucial that we observe and understand the complete 'stellar' spectral energy distribution (SED). In 1983, the *IRAS* (Neugebauer et al., 1984) (10 - 100 μm) all-sky survey opened up the extragalactic infrared sky for the first time. Of particular interest to us is the first detection of FIR sources associated with the Fornax cluster. Wang et al. (1991) found 5 *IRAS* sources matching known Fornax galaxies inside the bounds of our survey and located preferentially towards the outskirts of the cluster. Since *IRAS*, very little further study has been undertaken of the Fornax cluster in the MIR or FIR (more detail about FIR results from other nearby clusters can be found in Chapter 1).

All FIR instruments to-date including IRAS lacked photometric coverage at wavelengths needed to constrain the temperature and mass of cold dust (T<20K). The *Herschel* Space Observatory (Pilbratt et al., 2010) rectified this problem as it was able to survey large areas of sky at longer FIR wavelengths and with superior resolution and sensitivity. This chapter uses the HeFoCS data to study cold dust in the Fornax cluster to understand the problems discussed above.

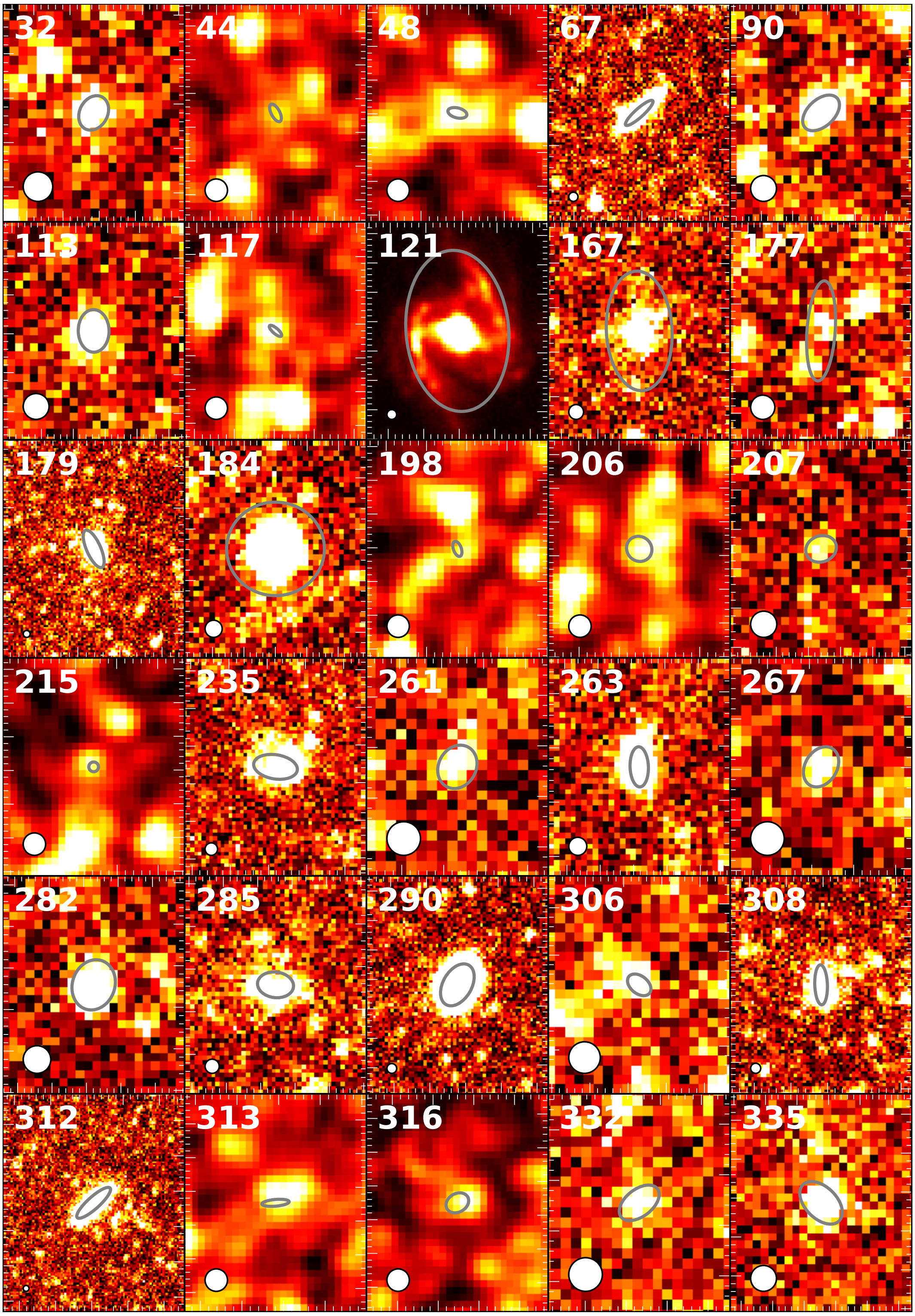

Figure 4.1. The 30 HeFoCS galaxies detected at 250 μm. The beam size is shown in the lower left hand corner. The grey ellipses indicate the optical extent (D_{25}) of each galaxy. Each 250 μm sub-image is resized to display the FIR source optimally and does not represent the overall size of the sub-image in the source measurement process.

Band (μm)	Number of detections (N)	Detection rate (%)
100	19	9
160	18	8
250	30	13
350	28	12
500	21	9

Table 4.1. Detection rates of all the FCC galaxies in the *Herschel* bands. 237 FCC galaxies fall into the SPIRE maps and 200 fall into both PACS and SPIRE in total.

Morphological		Virgo			Fornax	
Type	Total	Detected	%	Total	Detected	%
dE/dS0	314	14	4 ± 1	185	11	6 ± 2
E/S0	86	29	34 ± 6	29	6	21 ± 8
Sa/Sb/Sc/Sd	152	138	91 ± 8	10	9	90 ± 30
BCD/Sm/Im/dS	157	74	47 ± 5	13	4	31 ± 15

Table 4.2. A comparison of detection rates in the SPIRE 250 μm band, between the Virgo and Fornax clusters. Errors are simply root N. The galaxies have been split into dwarf (dE / dS0), early (E / S0), late (Sa / Sb/ Sc/ Sd), and irregular (BCD / Sm / Im /dS).

In this chapter we describe the HeFoCS detection rate in each *Herschel* band and compare our results to those obtained for galaxies in Virgo by Auld et al. (2013). We then investigate the location of FIR detected and undetected galaxies within the cluster. Every HeFoCS galaxy detected at 250 μm is shown in Figure 4.1, where the grey ellipse shows the extent and location of the optical counterpart.

4.2 Detection rates

Figure 4.2 shows the distribution of optical magnitudes m_{bt} of all (black) and detected (blue) FCC galaxies. Except for one faint galaxy (discussed separately in Section 4.2.1), no galaxies are detected in the FIR below $m_{bt} = 18.2$. Therefore, we do not expect that a deeper optical catalogue would increase the number of FIR detections in our current data.

Table 4.1 indicates how many galaxies were recovered in each band above a 3σ noise level in the FIR maps. The SPIRE bands have higher detection rates than the PACS bands, and 250 μm has the highest detection rate of all. This is due to a combination of its sensitivity and the typical shape of the FIR SED. Consequently, we use the 250 μm band to compare Fornax and Virgo. At 250 μm we detect 30 of 237 (13 %) FCC galaxies. This is significantly less than in Virgo, where 254 of 750 (34 %) VCC galaxies are detected (Auld et al., 2013).

In order to investigate the source of the lower global detection rates in Fornax in comparison

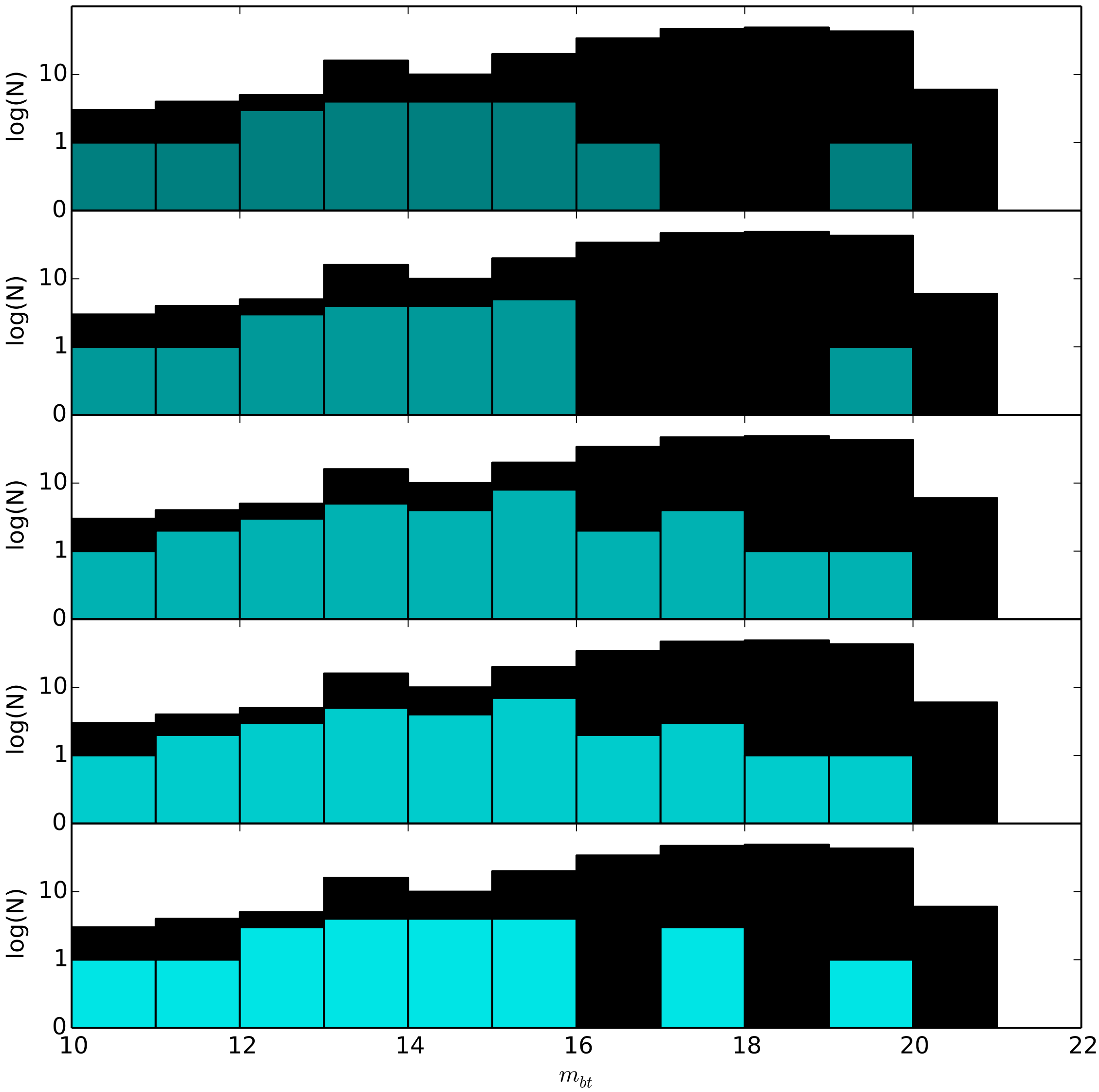

Figure 4.2. A histogram of optical magnitude m_{bt} of the FCC galaxies. The black and cyan bars are the total and FIR detected galaxies respectively.

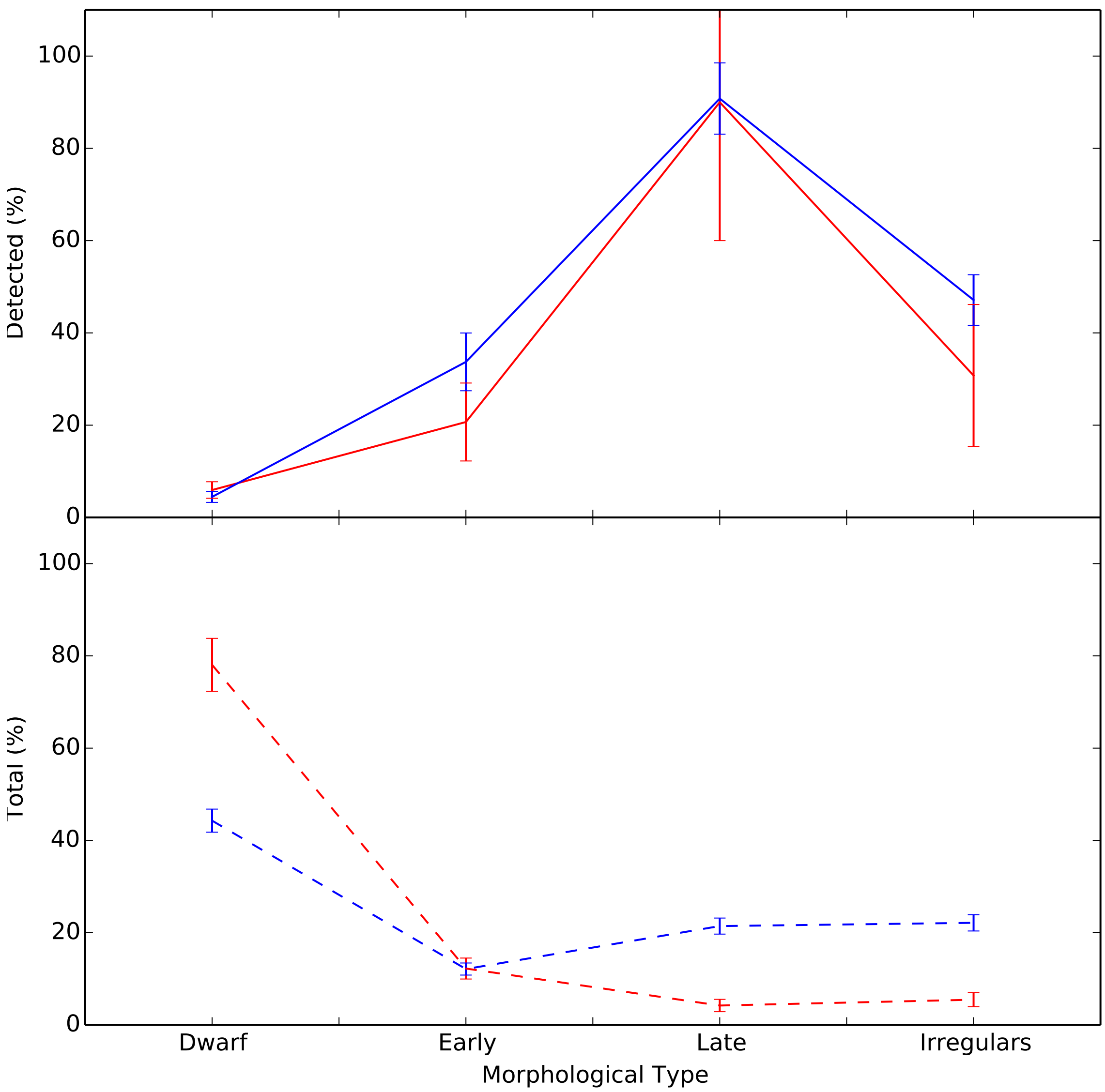

Figure 4.3. The morphologies of the Fornax and Virgo galaxies in red and blue, respectively. The upper panel represents the percentage detected in SPIRE 250 μm band. The lower panel shows the overall morphological make up of each cluster. The bins are as follows; dwarf (dE / dS0), early (E / S0), late (Sa / Sb/ Sc/ Sd), and irregulars (BCD / Sm / Im /dS).

to Virgo, we examine the morphological make up of each cluster and the detection rates therein. We separate the galaxies into 1 of 4 morphological groups; dwarf (dE /dS0), early (E / S0), late (Sa / Sb/ Sc / Sd), and irregular (BCD / Sm / Im / dS). The upper panel in Figure 4.3 shows the fraction of galaxies detected in each morphological group, while the lower panel shows the overall morphological make up of each cluster (tabulated in Table 4.2). Dwarf galaxies are the most numerous in both clusters, however, only 4 % and 6 % are recovered at 250 μm for Virgo and Fornax, respectively. Early, late[1], and irregular-type galaxies are detected at 21 %, 90 %, and 31 % in Fornax and 34 %, 91 %, and 47 % in Virgo, respectively. The lower panel of Figure 4.3 shows that Fornax has a far higher fraction of dwarf galaxies, with the lowest detection rate, and far fewer late and irregular-type type galaxies with the highest detection rate. Furthermore Figure 4.3 shows the fraction of early-type galaxies is the same in both clusters, having no effect on the global detection rate. What is remarkable, is that within the errors the two clusters match each other very closely with respect to the fraction of detected galaxies in each morphological group. The above implies that the lower global detection rates in Fornax are tracing the morphological make up of the cluster.

In order to better understand the limits of our data we estimate the limiting dust mass required for a detection at 250 μm. The lowest detected 250 μm flux in our FIR catalogue is $\sim$15 mJy. Assuming a dust temperature of 20 K the corresponding limiting dust mass is $\log(M_{Dust}/\mathrm{M}_{\odot}) = 5.1$. If we assume that early and late-type galaxies typically have dust-to-stellar mass ratios of approximately, $\log(M_{Dust}/M_{Stars}) = -5$ and -3, respectively (Cortese, 2012; Smith et al., 2012), then we should detect galaxies with stellar masses of $\log(M_{Stars}/\mathrm{M}_{\odot}) \geq 10.1$ and 8.1, respectively. We can see this more clearly in Figure 4.4. The 4 left-hand panels display the distribution of stellar mass in the 4 morphological groups described above, with black and coloured histograms showing galaxies undetected and detected at 250 μm, respectively. The dashed lines indicate the stellar mass above which we expect to detect galaxies with a dust-to-stellar mass ratio of $\log(M_{Dust}/M_{Stars}) = -5$ and -3, respectively.

The dwarf galaxies are the most challenging morphological group to detect in the FIR, due to their low stellar masses, thus requiring a substantially higher dust-to-stellar mass ratio for their detection. 6%(11) of dwarf galaxies are detected, whereas we would expect to detect 18%(33) of the dwarf galaxies if they had dust-to-stellar mass ratios of $\log(M_{Dust}/M_{Stars}) = -3$ similar to a typical late-type galaxy. The righthand panel of Figure 4.4, shows where these galaxies are projected spatially in the cluster. The FIR detected dwarf galaxies generally appear on the outskirts of the cluster. To quantify this, Table 4.3 lists the average

[1]FCC 176 was originally classified as Sa by Ferguson (1989), however, we did not detect this galaxy in any *Herschel* bands. Upon further inspection it has a very red colour, $B - V = 0.88$ (Prugniel & Heraudeau, 1998), placing it well within the red sequence, it has also been reclassified S0, more latterly by De Vaucouleurs et al. (1991), we have adopted this reclassification.

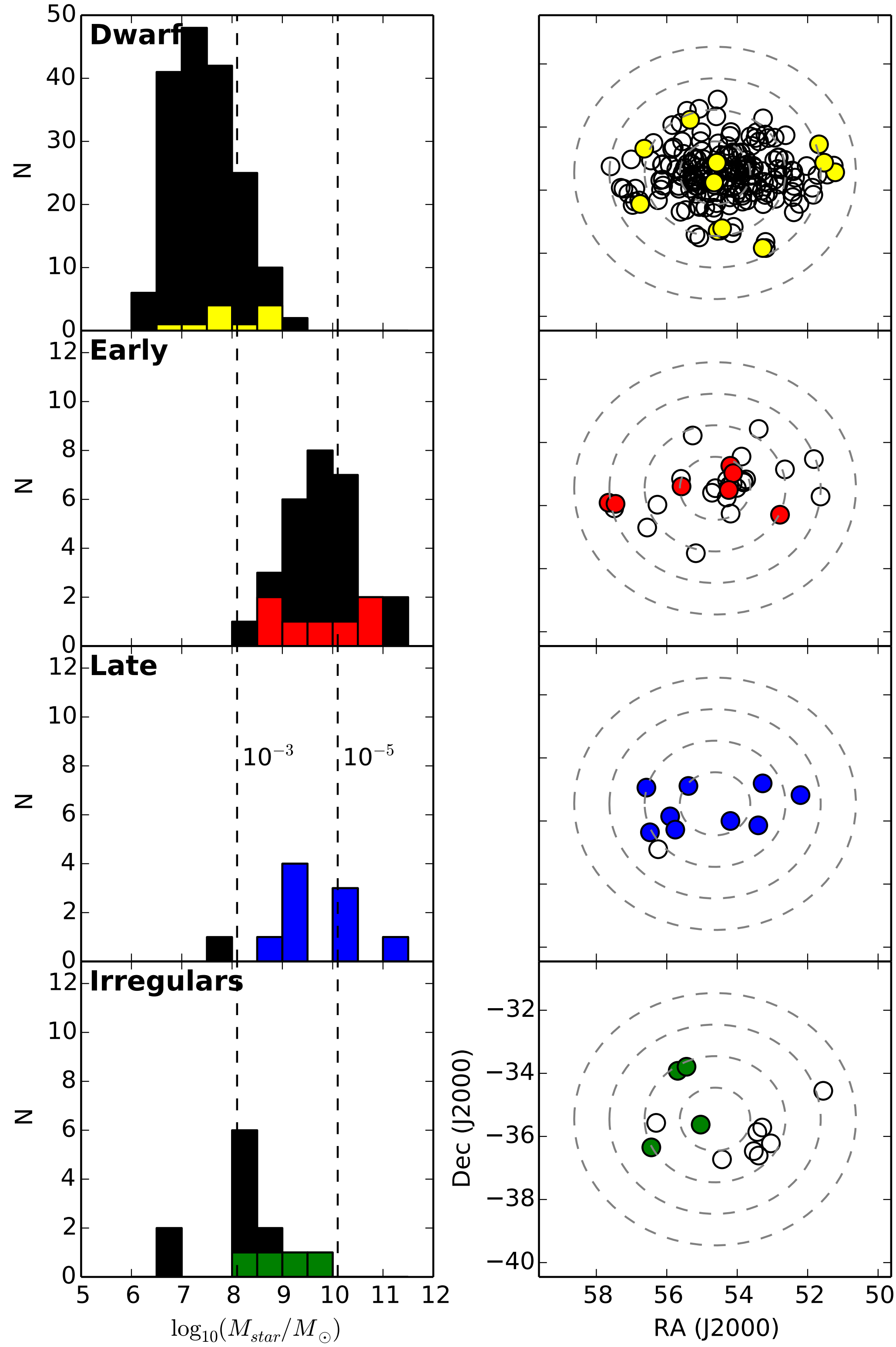

Figure 4.4. Histograms of stellar mass for 4 morphological types; dwarf (dE / dS0), early (E / S0), late (Sa / Sb/ Sc / Sd), and irregular (BCD / Sm / Im / dS). The black and coloured histograms are for undetected and detected galaxies at 250 μm, respectively. The vertical dashed lines represent our estimated stellar mass detection limits for the indicated dust-to-stars mass ratio. Note the change in the Y-scale for the dwarf galaxies panel. The adjacent plots show the locations within the cluster of the undetected and detected galaxies, with empty and filled markers respectively.

Morphological Type	$< R_{detected} >$ (R/R_{virial})	$< R_{undetected} >$ (R/R_{virial})
Dwarf	0.84 ± 0.04	0.50 ± 0.01
Early	0.56 ± 0.05	0.50 ± 0.02
Late	0.56 ± 0.02	0.83
Irregulars	0.61 ± 0.06	0.57 ± 0.01

Table 4.3. A comparison of galaxies detected and undetected in the SPIRE 250 μm band. Projected radii are given as a fraction of the Fornax cluster virial radius of 0.7 Mpc (Drinkwater et al., 2001).

projected cluster centric radius as a fraction of the virial radius (R_{virial} =0.7 Mpc) for FIR detected and undetected galaxies. On average detected dwarf galaxies are found at a 0.84 R_{virial}, whereas undetected are at 0.50 R_{virial}. These detected dwarf galaxies are found on the outskirts of the cluster in a similar position to the transition dwarfs identified in the Virgo cluster by De Looze et al. (2013).

Only 21 % of all early-type galaxies are detected by *Herschel* at 250 μm, with some of the extremely dust deficient early types having dust-to-stars ratios of below $\log(M_{Dust}/M_{Stars}) = -6.6$. Early-type galaxies appear very centrally concentrated when compared to the dwarf and irregular-type galaxies. However, both detected and undetected galaxies are found at an average projected cluster centric radius of $\sim 0.5 R_{virial}$. It would appear that cluster centric radius has no perceivable effect on whether or not an early-type galaxy is detected by *Herschel*.

There are nine late-type galaxies in the Fornax cluster and they are all detected except for FCC 299. In order to be detected at 250 μm, the latter would require a dust-to-stars ratio greater than $\log(M_{Dust}/M_{Stars}) = -3$ due to its low stellar mass of $\log(M_{Stars}/M_\odot) = 7.8$. The detected galaxies have a mean projected cluster centric radius of $\sim 0.56 R_{virial}$ and no late-type galaxy it at a radius less than 0.3 R_{virial}.

The majority of irregular-type galaxies would be detected at 250 μm if they had dust-to-stars ratios of $\log(M_{Dust}/M_{Stars}) = -3$. Instead, approximately 31 % of the irregular-type galaxies are detected, preferentially with higher stellar masses. There is no obvious trend to where they are located in the cluster, both detected and undetected galaxies having a mean projected radius of $\sim 0.6 R_{virial}$.

4.2.1 FCC 215

From 185 dwarf galaxies identified in the FCC, only 11 were detected in the 250 μm band, and only FCC 215 was detected in 3 or more *Herschel* bands. FCC 215 has a very high dust-to-stars ratio (approximately $\log(M_{Dust}/M_{Stars}) = -1$) and a very faint optical magnitude

($m_{bt} \sim 19$), making it an interesting object worthy of further inspection.

FCC 215 has a dust mass of $\log_{10}(M_{dust}/M_{\odot}) = 5.2$ and a stellar mass of $\log_{10}(M_{stars}/M_{\odot}) = 6.5$. It is just detected in the 3 SPIRE bands at S/N ≤ 5. The SED fit is quite poor with $\chi^2_{dof=3} = 9.94$. The SED appears very flat, which may indicate it is a background galaxy with a synchrotron component. However, it is listed in NED as having a velocity of 1964 km s^{-1}, which places it inside the cluster. Its optical colour is very blue, B-R = 0.36, suggesting that the galaxy is undergoing/has undergone an episode of recent star formation. Assuming that this is a bonafide detection, how could it have such a high dust-to-stars ratio? Is it possible for a galaxy to produce this much dust? Using a closed box model of a galaxy, i.e. no inflow or outflow of material, Edmunds & Eales (1998) derive; $\Delta_{max,f} = \eta p f \log(1/f)$, where $\Delta_{max,f}$ is the maximum mass of dust a galaxy could possess with a gas fraction f, a fraction of metals in the dust η and a stellar yield p. The stellar yield is the fraction of metals produced per unit mass of gas freshly formed in nucleosynthesis. Its value has been estimated to lie between 0.004 and 0.0012 (Vila-Costas & Edmunds, 1992). The fraction of metals in the dust η has been estimated by Meyer et al. (1998) and more latterly by Davies et al. (2014) as 0.5. The gas fraction is $f = M_{gas}/(M_{stars} + M_{dust} + M_{gas})$, so using the equation above we can estimate the gas mass required, for FCC 215 to have a dust-to-stars ratio of $\log(M_{Dust}/M_{Stars}) = -1.5$. The gas-to-stars ratio would have to be 1 and thus a gas mass of $\log_{10}(M_{gas}/\mathrm{M}_{\odot}) = 6.5$, making it also very gas rich. Currently the only 21cm survey that covers this region of sky is the H I Parks All Sky Survey (HIPASS) (Barnes et al., 2001). HIPASS does not detect FCC 215, yet their estimated rms noise of ~15 mJy beam^{-1} approximately corresponds to an H I gas mass $\log_{10}(M_{HI}/\mathrm{M}_{\odot}) = 8$ at the distance of Fornax, meaning that HIPASS would be unable to detect FCC 215 even if all the gas content was locked up in H I. The HeFoCS has secured time to map the Fornax cluster, using the Australia Telescope Compact Array. The estimated survey detection limit is $\mathrm{M}_{HI} \simeq 10^7$ $\mathrm{M}_{\odot}$ at the distance of Fornax, very close to our predicted upper estimate of the gas mass of FCC 215.

4.3 Analysis of SED fits, dust masses & temperatures

4.3.1 Environmental effects on dust in galaxies

For the following analysis we split the sample into early and late-type galaxies and initially consider only the 22 galaxies detected in at least 3 *Herschel* bands. ‘Early’ was classified as anything earlier than Sa and ‘late’ as anything later than (and including) Sa. The SED of all galaxies was fitted with a single temperature modified blackbody with $\beta = 2$. Only two

Sample 1	Sample 2	$\mu_1(\sigma_1)$	$\mu_2(\sigma_2)$	K-S test		Sample Size	
				Value	P_{value}	N_1	N_2
Dust Mass (log($M_{Dust}/M_{\odot}$))							
Virgo Early	Virgo Late	6.18(0.12)	6.68(0.06)	0.488	0.011	11	103
Fornax Early	Fornax Late	5.82(0.2)	6.54(0.19)	0.571	0.113	5	14
Virgo Early	Fornax Early	6.18(0.12)	5.82(0.2)	0.6	0.102	11	5
Virgo Late	Fornax Late	6.68(0.06)	6.54(0.19)	0.179	0.784	103	14
Stellar Mass / Dust Mass (log($M_{Stellar}/M_{\odot}$) - log($M_{Dust}/M_{\odot}$))							
Virgo Early	Virgo Late	3.62(0.19)	2.76(0.04)	0.611	0.001	11	103
Fornax Early	Fornax Late	3.89(0.27)	2.94(0.08)	0.929	0.001	5	14
Virgo Early	Fornax Early	3.62(0.19)	3.89(0.27)	0.364	0.645	11	5
Virgo Late	Fornax Late	2.76(0.04)	2.94(0.08)	0.332	0.104	103	14
Dust Temp. (K)							
Virgo Early	Virgo Late	21.65(0.94)	19.27(0.24)	0.442	0.028	11	103
Fornax Early	Fornax Late	20.82(1.77)	17.47(0.96)	0.443	0.355	5	14
Virgo Early	Fornax Early	21.65(0.94)	20.82(1.77)	0.236	0.975	11	5
Virgo Late	Fornax Late	19.27(0.24)	17.47(0.96)	0.4	0.027	103	14

Table 4.4. A statistical comparison of Fornax and Virgo galaxies using dust mass, dust-to-stellar mass, and dust temperature. Early types include E and S0, while all other galaxy types are classified as 'late'.

galaxies, FCC 215 (discussed above) and FCC 306, were poorly fitted using this emissivity, with $\chi^2_{dof=3} = 9.94$ and 18.65. The average for the entire sample was, $< \chi^2_{dof=3} >= 2.92$. If FCC 215 and 306 are removed, then the average for the sample falls to $< \chi^2_{dof=3} >= 1.78$. In Table A.1 we include all galaxies with measured dust mass and temperature. Figure 4.5 shows the SED fits for each galaxy.

Detected late-type galaxies have dust masses ranging from $\log_{10}(M_{dust}/\mathrm{M}_\odot) = 5.5$ to 8.2 and temperatures of 11.2 to 23.7 K, with mean values $\log_{10}(M_{dust}/\mathrm{M}_\odot) = 6.5$ and 17.5 K. By contrast, detected early types have a narrower range of dust masses of $\log_{10}(M_{dust}/\mathrm{M}_\odot) = 5.4$ to 6.6 and temperatures of 14.9 to 25.8 K, with mean values $\log_{10}(M_{dust}/\mathrm{M}_\odot) = 5.8$ and 19.3 K. Detected Fornax galaxies have mean dust-to-stellar mass ratios of $\log_{10}(M_{dust}/M_{stars}) =$ -3.87 and -2.93, for early and late-types, respectively. As expected from our previous results for Virgo, late-types have a richer and cooler dust reservoir, and early-types have a relatively depleted and warmer ISM.

In Table 4.4 we use the Kolmogorov-Smirnov two sample test (KS) to make a more quantitative comparison between Virgo and Fornax's early and late-type galaxy populations with respect to dust mass, dust-to-stars ratio, and dust temperature. Here we use 140 of the Auld et al. (2013) galaxies that had SEDs modelled identically to our sample using a single temperature component with a fixed $\beta = 2$ emissivity. For Virgo we use stellar masses calculated using H band magnitudes and SDSS g-r colours from Davies et al. (2014). Virgo, like Fornax, has early types that have lower dust masses and higher temperatures than its late types. However, a KS test shows that for a given morphological type the FIR properties of galaxies in Fornax and Virgo are statistically identical (with the caveat that we are only sampling the massive galaxies, $\log_{10}(M_{star}/\mathrm{M}_\odot) \geq 8.2$). The above results suggest that the different cluster environments have had very little effect on the dust properties of early or late-type galaxies.

Auld et al. (2013) compared the Virgo cluster to the Herschel Reference Survey (HRS; Boselli et al., 2010; Cortese et al., 2012b; Smith et al., 2012). The HRS is a volume limited ($15 \leq$ D ≤ 25 Mpc), K band ($K \geq 8.7$) selected sample. It covers a range of environments from the field to the core of the Virgo cluster, making it an ideal comparison sample. Auld et al. (2013) showed that early-type galaxies in the Virgo cluster and HRS field have very similar dust properties. However, late-type galaxies typically have larger dust masses in the field. Auld et al. (2013) concluded that the difference in dust mass between field and cluster late-type galaxies was due to dust removal in the cluster environment. The implication of this result as well as the results presented in this chapter, is that early-type galaxies appear identical in their FIR properties irrespective of what environment they originated from. Furthermore, the larger dust reservoirs of late-type galaxies in the field and the lack of difference in FIR properties between Fornax and Virgo, suggests that this change in dust mass likely occurred before they entered the cluster environment.

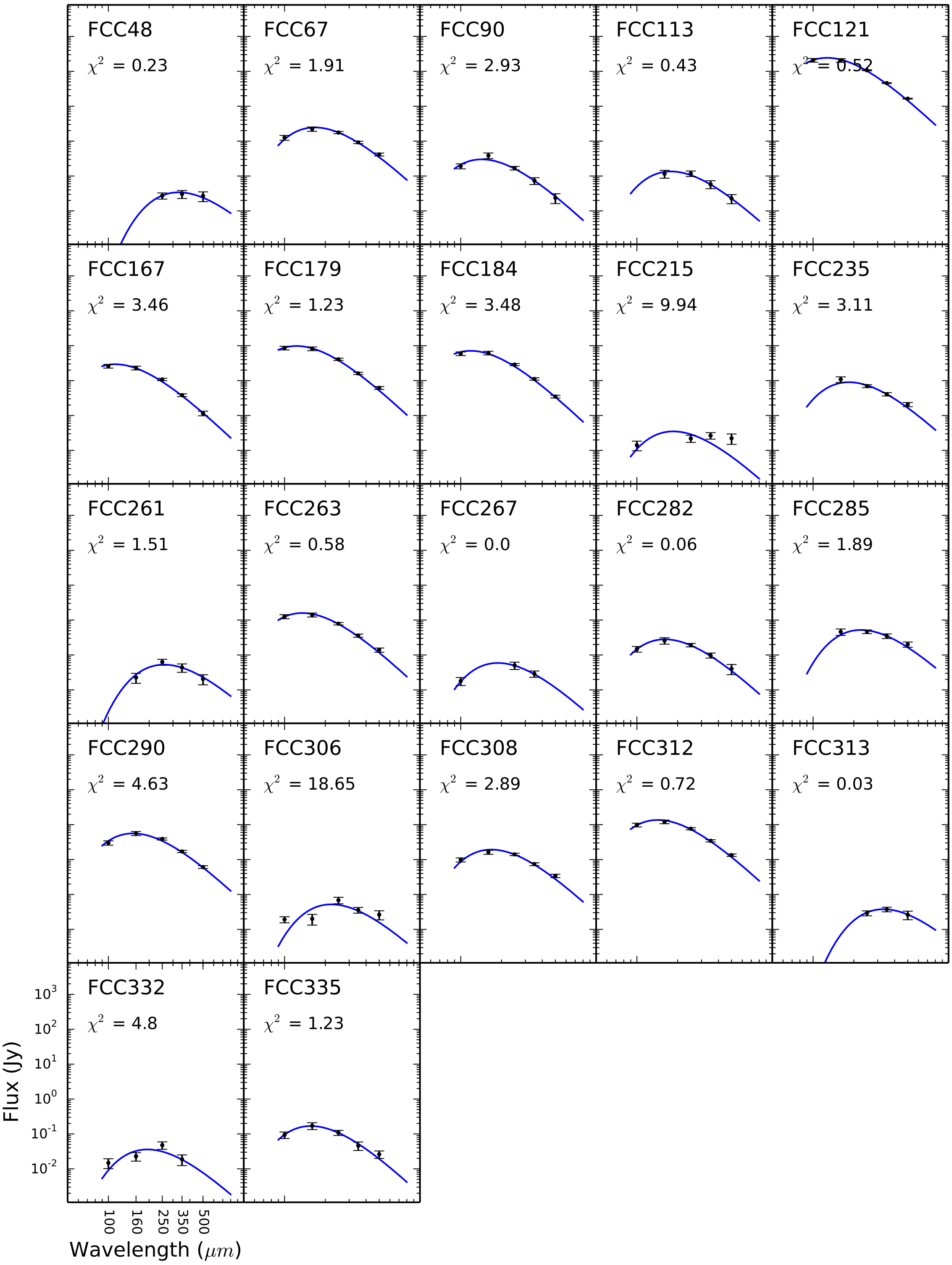

Figure 4.5. Modified blackbody fits to 22 HeFoCS galaxies. The blue line represents a single temperature $\beta = 2$ fit to the data. We have only used galaxies with at least 3 *Herschel* bands.

It is worth noting that 'global' environment on its own may not be the best tracer of the action of physical processes. A quantity more sensitive to direct interaction with the cluster environment is the H I-deficiency. Cortese et al. (2012b) compare the FIR properties of galaxies, separated in both H I-deficiency and global environment. They found an $\sim 8\sigma$ difference in $\log(M_{Dust}/M_{Stars})$ when comparing H I-normal and H I-deficient galaxies, whereas only a $\sim 3\sigma$ difference is found between samples separated based on the environment (i.e. field and cluster members).

4.3.2 Origin of dust in galaxies

In order to extend our analysis of dust and stellar mass to lower limits, and to study how the dust-to-stars ratio changes with lower dust and stellar masses (Figure 4.6), an additional 9 galaxies were included in the analysis. These galaxies had insufficient SED data to be fitted by a modified blackbody and so the 250 μm flux density was used as a proxy for dust mass by assuming a dust temperature of 20 K. The diagonal dashed line in Figure 4.6 indicates the minimum dust-to-stellar mass detected, given our previous estimate of a minimum detectable dust mass of $\log_{10}(M_{dust}/\mathrm{M}_{\odot}) = 5.1$ (Section 4.2). The same morphological categories are used - 'early' was classified as anything earlier than Sa and 'late' as anything later than, and including, Sa.

Figure 4.6 shows early and late-type galaxies designated by red and blue markers, respectively, from both clusters. Fornax galaxies are indicated by a marker set onto a black square. We have measured the correlation between M_{dust} and M_{star} using the Pearson correlation coefficient (PCC). Late-type galaxies have a PCC of 0.84, early-type galaxies have a PCC of 0.43. The correlation between dust and stellar mass in late-type galaxies may find its origins in the mass-metallicity relation (Lequeux et al., 1979; Tremonti et al., 2004; Lara-López et al., 2010; Hughes et al., 2013). These authors have shown that gas phase metallicity correlates with stellar mass and so we might also expect this to be true for the metals in the dust. They have also shown that at larger stellar masses the mass-metallicity relation flattens out (ie m $\rightarrow$ 0). This flattening in the mass-metallicity relation may explain why our relation between dust-to-stars and stellar mass is not flat ie m=0.

Early-type galaxies in Fornax and Virgo have a very large range of dust-to-stellar mass ratios, $-1.3 \geq \log_{10}(M_{star}/M_{dust}) \geq -6.2$, and the weak correlation of dust to stellar mass could be due to the imposed limiting dust mass, artificially creating a correlation, as shown in Figure 4.6. However, the PCC for early-type galaxies is far lower than we found for late-type galaxies, implying that stellar mass is far less if at all correlated with dust mass in early-type galaxies.

A clue about the origin of these two different correlations may lie in the distribution of the

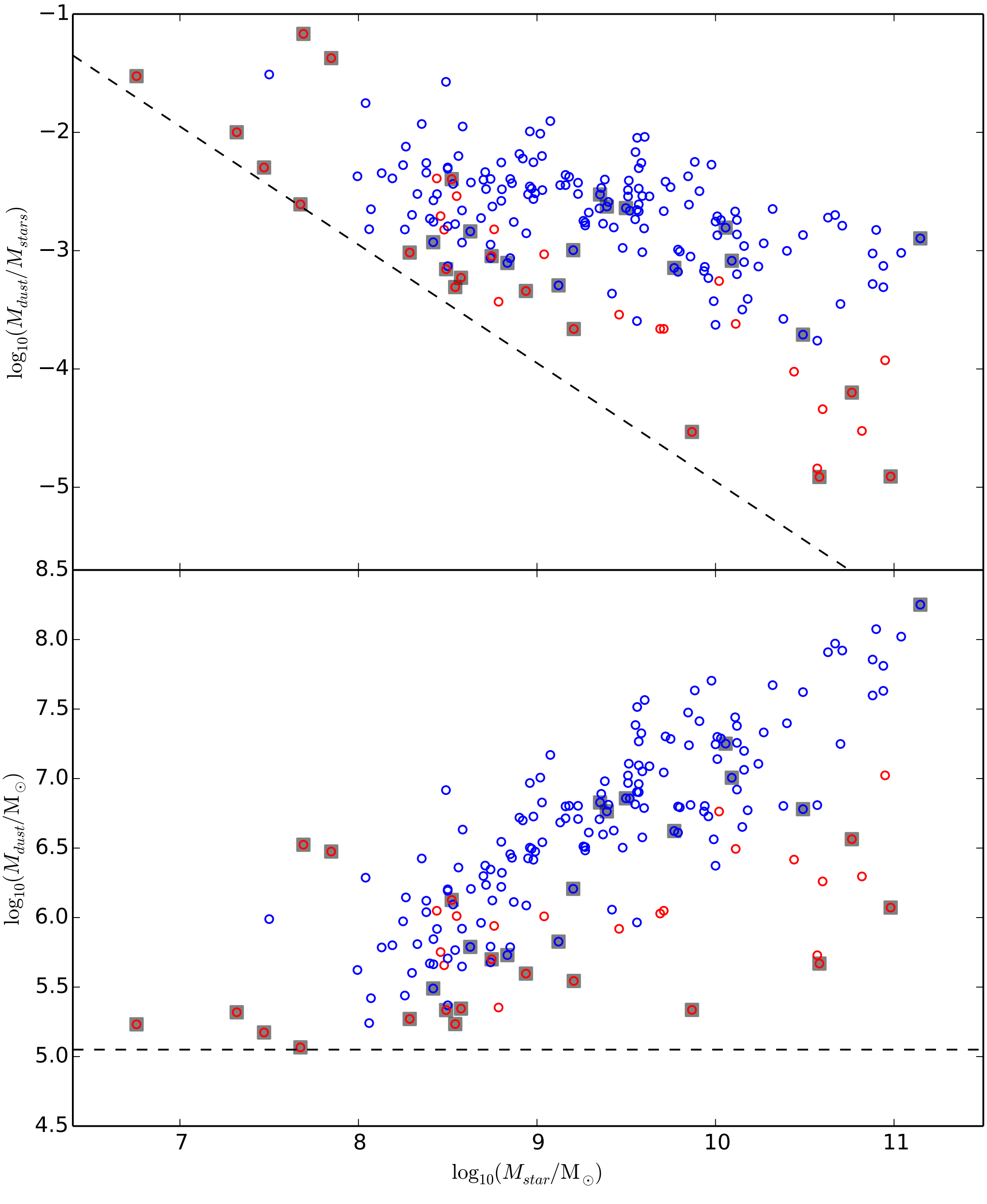

Figure 4.6. The upper panel shows stellar mass against dust-to-stars ratio, the lower panel shows stellar against dust mass, for both Virgo and Fornax, where the latter are designated by a marker set onto a black square. Early and late-type galaxies are shown as red and blue markers, respectively. The dashed line represents the minimum dust mass and dust-to-stellar mass we can detect for a given stellar mass, for the lower and upper panels, respectively.

dust within early and late-type galaxies. We have calculated the ratio of the FIR to optical size for Fornax cluster galaxies, where this ratio is defined as the FIR diameter of emission D_{FIR} as defined in Chapter 2 divided by the optical diameter D_{25}. We will use the FIR diameter as measured at 250 μm, and thus we will for the rest of this section refer to D_{FIR} as D_{250}. Only 1 of 7 early and 2 of 13 late types have FIR emission that is smaller than the FWHM of the *Herschel* 250 μm beam, and are thus measured as point sources with a D_{250} equal to the 250 μm beam size. As the majority have D_{250} greater than the PSF FWHM, we can use them to measure the distribution of the dust in comparison to the stars. The mean FIR/optical size ratio is 0.464 and 0.903, for early and late-type galaxies, respectively. In order to further test the effect of the *Herschel* beam we restricted the sample to galaxies with an optical diameter greater than 3 times the 250 μm beam FWHM. This results in a mean FIR/optical size ratio of 0.305 and 0.917 for early and late-type galaxies, respectively, thus showing that the beam size has a limited effect on the overall result. This shows that dust in early-type galaxies is very centrally concentrated in comparison to late-type galaxies. This has been demonstrated previously for early-type galaxies by Smith et al. (2012) and Di Serego Alighieri et al. (2013). Cortese et al. (2010b) showed that H I-deficient galaxies in the cluster environment also had smaller FIR/optical size ratios, suggesting that dust had been stripped from these galaxies, this would affect the late-type galaxies far more than early-type galaxies, as the above shows that dust in late-type galaxies is held less deeply in their potential wells.

Davis et al. (2013) and Helfer et al. (2003) measure the extent of molecular hydrogen in early-type and late-type galaxies. They find the size ratio of molecular gas to optical radius as ~ 0.25 in both cases. In the case of late-types, the spatial extent of molecular gas is much less than of the dust, whereas early-type galaxies have molecular gas and dust that appear spatially coincident. This suggests that the origin of dust in early-types may be the same as that of molecular gas (see below), whereas dust in late-types is coincident with the stellar population, and as shown above, dust mass is regulated by stellar mass (i.e. mass-metallicity relation), suggesting an internal origin.

Dust in early-type galaxies has two possible origins, either internally produced in the atmospheres of evolved stars (Whittet, 1992) and supernovae remnants (Morgan & Edmunds, 2003), or externally obtained from mergers with other galaxies. The strongest prediction for dust created internally is that the mass of dust and stars should be spatially correlated. Figure 4.6 shows that this is clearly not the case for early-type galaxies. The stellar population must produce dust, but Clemens et al. (2010) show that it is destroyed on a short timescale of <50 Myrs. They argue that this is far shorter than the dust-transfer timescale, and thus dust created in outer regions of a galaxy is effectively destroyed "on-the-spot". However, the dust destruction timescale can be greatly extended if the dust is embedded in a cloud of molecular hydrogen, leading to lifetimes of a few 100 Myrs (Jones & Nuth, 2011).

This indicates that dust created internally cannot be the main source of dust in early-type galaxies.

If the dominant source of dust is not internal, Smith et al. (2012) argue that it may have an external origin such as mergers with dust rich galaxies. Mergers of different dust masses at different times would explain the large range of dust-to-stars ratios seen in early-type galaxies as well as the $\sim 75\%$ of systems which we do not detect with *Herschel*. However, as shown above, the FIR properties of early-type galaxies do not change between Virgo and Fornax (Table 4.4) or the HRS field (Auld et al., 2013), suggesting that the flow of dust into and out of these systems must be invariant with environment. Since Clemens et al. (2010) show that the destruction time in early-type galaxies is determined by thermal sputtering, and thus is largely independent of the environment, our findings would imply that the merger rate is roughly the same in all three environments. This is at odds with the idea that the merger rate depends on environment. For example, Mihos (2004) shows that mergers are far less common in clusters than in groups or in the field - thus there is a dilemma.

The mystery deepens if we compare our FIR results for early-types to the molecular gas component of the ISM. Davis et al. (2011) show that the detection rate of the molecular ISM and the molecular gas-to-stars ratios for early-type galaxies are invariant to environment, mirroring the FIR results presented in this chapter. However, they discovered that the gas kinematics inside and outside of clusters is different. They found one third of galaxies outside of clusters had gas kinematically misaligned to their stars, supporting an external origin. Interestingly, this was not seen in early-types inside the cluster.

4.4 Summary

We have undertaken the deepest FIR survey of the Fornax cluster using the *Herschel* Space Observatory. Our survey covers over 16 deg^2 in 5 bands and extends to the virial radius of the cluster, including 237 of the 340 FCC galaxies. We have used the optical positions and parameters of these FCC galaxies to fit appropriate apertures to measure FIR emission. We have detected 30 of 237 (13 %) cluster galaxies in the SPIRE 250 μm band, a significantly lower detection rate than in the Virgo cluster (34 %; see Auld et al., 2013).

In order to better understand the global detection rate we separated Fornax and Virgo galaxies into 4 morphological categories: dwarf (dE / dS0), early (E / S0), late (Sa / Sb / Sc / Sd), and irregular (BCD / Sm / Im / dS). We examined the detection rate for each morphological group in the 250 μm band as it has the highest detection rate of all the *Herschel* bands. In Fornax we detect 6%, 21%, 90%, and 31% of dwarf, early, late, and irregular, respectively. These results agrees with the fraction of detected galaxies in each morphological category in the Virgo cluster, indicating that the lower global detection rate in Fornax is due to its lower fraction of late-type galaxies.

For galaxies detected in at least 3 bands we fit a modified blackbody with a fixed beta emissivity index of 2, giving dust masses and temperatures for 22 Fornax galaxies. Fornax's early-type galaxies show lower dust masses and hotter temperatures than late-type galaxies. When comparing early-type galaxies from the Fornax cluster to their counter-parts in the Virgo cluster, their FIR properties are statistically identical. The same is true for the late-type galaxies. This may suggest that the effect of the cluster is more subtle than previously thought and that the evolution of the ISM components has mostly taken place before the cluster was assembled.

We observe dust mass to be well correlated to stellar mass for late-type galaxies. We suggest that this correlation has its origins in the mass-metallicity relation (Lequeux et al., 1979; Tremonti et al., 2004; Lara-López et al., 2010; Hughes et al., 2013), as the ratio between the mass of metals in the dust and the gas has been found to be 0.5 (Meyer et al., 1998; Davies et al., 2014). It therefore follows that any correlation with gas phase metallicity should also be observed between stellar and dust mass.

We find early-type galaxies to have a very large range of dust-to-stars ratios, $-1.3 \geq \log_{10}(M_{star}/M_{dust}) \geq -6.2$. We argue that this supports a scenario where the dust in early-type galaxies is from an external origin, as has been previously suggested by other authors (Smith et al., 2012). As FIR properties are statistically identical between environments, therefore so must the balance between dust input/creation and removal/destruction. However, this conclusion is perplexing as mergers are thought to be far less common in clusters when compared to groups or the field (Mihos, 2004), and dust destruction is largely regulated internally (Clemens et al., 2010), thus invariant with respect to environment.

Part III

Coma

Chapter 5
FIR properties of optically-selected Coma cluster and Filament galaxies

"The word adventure has gotten overused. For me, when everything goes wrong - thats when adventure starts"
Yvon Chouinard

5.1 Introduction

The Coma cluster is a local example of a giant relaxed structure, located at a distance of $\sim 100\,\mathrm{Mpc}$, with a mass $\sim 10^{15}\,M_{\odot}$ and a large virial radius $\sim 3\,\mathrm{Mpc}$ (Boselli & Gavazzi, 2006). It sits in a large filamentary structure, the 'great wall', an over-density of galaxies linking it with A1367. The cluster has a high Galactic latitude of $b = 88.0^{o}$, making it an ideal location for extra-galactic studies at all wavelengths. It was first observed by the 48 inch reflector on Mount Wilson (Zwicky, 1951) and more latterly by Godwin & Peach (1977) who created the seminal optical catalogue of galaxies. Godwin & Peach (1977) found over 6000 galaxies in the region of the Coma cluster, although not all of these are members. This compares to the Virgo cluster, which has about 1300 cluster members. Coma in contrast to other less relaxed clusters like Virgo, is far richer and probably formed at an earlier time.

In comparison to Virgo, Coma has a much more centrally concentrated distribution of galaxies. This can be seen in the X-ray emitting gas (Colless & Dunn, 1995). This gas is thought to be stripped from galaxies and heated by the gravitational potential of the cluster. It shows a mostly smooth, centrally concentrated distribution of mass, although a small in-falling group 40 arc minutes south west of the cluster centre is also clearly observed in the X-ray emission. This small in-falling group centred on NGC4839 has already or is about to pass through the cluster core. Hot X-ray emitting gas has a strong effect on the galaxies as they are plunging through the cluster at high velocities ($1000\,\mathrm{km\,s^{-1}} \geq$). Ram pressure stripping (Gunn & Gott, 1972) and thermal evaporation (Cowie & McKee, 1977) act to remove atomic hydrogen from a typical L_* galaxy in about 40 Myr and 1 Gyr in Coma and Virgo, respectively (Boselli & Gavazzi, 2006). Studying Coma we can further probe these physical mechanisms in the most extreme density environment, in which these processes act.

Strong morphological segregation is shown in the Coma cluster - an overwhelming proportion of its members are early-type galaxies. It is clear that the inter-stellar medium (ISM) of the cluster late-type galaxies has also been affected. Gavazzi et al. (2006) found that Coma galaxies were HI-deficient to $\sim 1.5\times$ the cluster's virial radius, and most HI deficient at the X-ray centre of the cluster.

Dust, the other major component of the ISM is detectable by its emission in the FIR and sub-mm wavebands (see Chapter 1). As mentioned previously the technical difficulties with observing FIR/sub-mm wavebands has limited the study of dust in Coma galaxies to space-based observatories. The first space mission, IRAS (Neugebauer et al., 1984) (10 - 100 μm), an all sky survey, detected 41 sources in Coma (Wang et al., 1991), almost entirely composed of late type galaxies at the edge of the cluster. They found that there was a weak correlation of dust where gas had been previously found. Using ISO (Kessler et al., 1996) (2.5 - 240 μm) Contursi et al. (2001) targeted 11 Coma galaxies performing deep observations, and they found that even though the galaxies were interacting with the cluster, their dust properties seemed to be bizarrely unaffected. ISO's longer wavelength range helped reveal a previously unseen cold dust component (~ 10K) that could only be poorly constrained with ISO's photometric points. Using the Spitzer Space Telescope (Werner et al., 2004) (3 - 160 μm), Edwards & Fadda (2011) observed multiple fields covering a total area of $\sim 3\,\mathrm{deg}^2$ approximately 1/3 of the area traced by the virial radius. They confirmed that star formation was strongly suppressed in Coma's core and observed some starburst galaxies in the south west in-fall region. These instruments allowed the study of warm dust (T$\sim$ 60K) and in a narrow sense cold dust (T$\sim$ 20K) as well, but they were limited in constraining cold dust as they could not cover the Rayleigh-Jeans tail of blackbody emission which peaks at $\sim$160 μm.

The *Herschel* Astrophysical Terahertz Large Area Survey (H-ATLAS) (Eales et al., 2010) is the largest FIR extra-galactic survey to date covering $570\,\mathrm{deg}^2$. The H-ATLAS observations cover this large area with 5 *Herschel* bands (100, 160, 250, 350 and 500 μm). The fields are located in areas of low Galactic cirrus. The Northern Galactic Pole (NGP) field includes the Coma cluster, as well as wide spatial coverage of the surrounding area. This not only allows a study of the Coma cluster, but gives good coverage of the filament it resides in

Band	Cluster		Filament	
(μm)	Number of detections (N)	Detection rate (%)	Number of detections (N)	Detection rate (%)
100	60	7	187	19
160	55	7	210	22
250	99	12	422	44
350	80	10	355	37
500	54	6	247	25

Table 5.1. These are the detection rate for each *Herschel* band in the cluster and the filament. In total there are 744 and 951 galaxies in the cluster and filament, respectively.

Morphological Type	Cluster N$\pm$ σN (% $\pm$ σ%)	Filament N$\pm$ σN (% $\pm$ σ%)	Difference
late	37 ± 6 (44 ± 7)	239 ± 15 (61 ± 3)	$2\,\sigma$
uncertain	47 ± 6 (9 ± 1)	164 ± 12 (35 ± 2)	$9\,\sigma$
early	15 ± 3 (8 ± 2)	19 ± 4 (18 ± 4)	$2\,\sigma$

Table 5.2. The detection rate for each morphological type in the cluster and filament. Errors are calculated as simple $\sqrt{N}$ errors.

leaving us with a large sample of galaxies in small groups, filament, and the cluster.

We use the H-ATLAS NGP data to extend the analysis performed in the previous chapter to the Coma cluster and surrounding filamentary region. The FIR data and source measurement is fully described in Chapter 2. Furthermore, the auxiliary data (optical magnitudes, stellar masses, SFRs, gas masses and metallicities) are detailed in Chapter 3.

In this chapter we describe the detection rate in each *Herschel* band, in both the cluster and filament sample (See Chapter 3 for a full description of our optical catalogue for the Coma cluster and surrounding filament). We then examine the location and velocity of FIR detected and undetected galaxies. Using the FIR properties (dust mass, dust-to-stars and dust temperature) calculated from the modified blackbody fit in Chapter 2 we compare the cluster and filament with Virgo and Fornax as well as a field sample.

5.2 Detection rates

Every CCC and CFC galaxy detected at 250 μm is shown in Figure B.-5, where the grey ellipse shows the extent and location of the optical counterpart.

Figure 5.1 shows the distribution of optical magnitudes in the SDSS r band of all CCC/CFC (black) and detected (blue) galaxies. We do not detect any galaxies fainter than, r = 17.7, which is the completeness limit of our optical selection. Therefore we do not expect that a

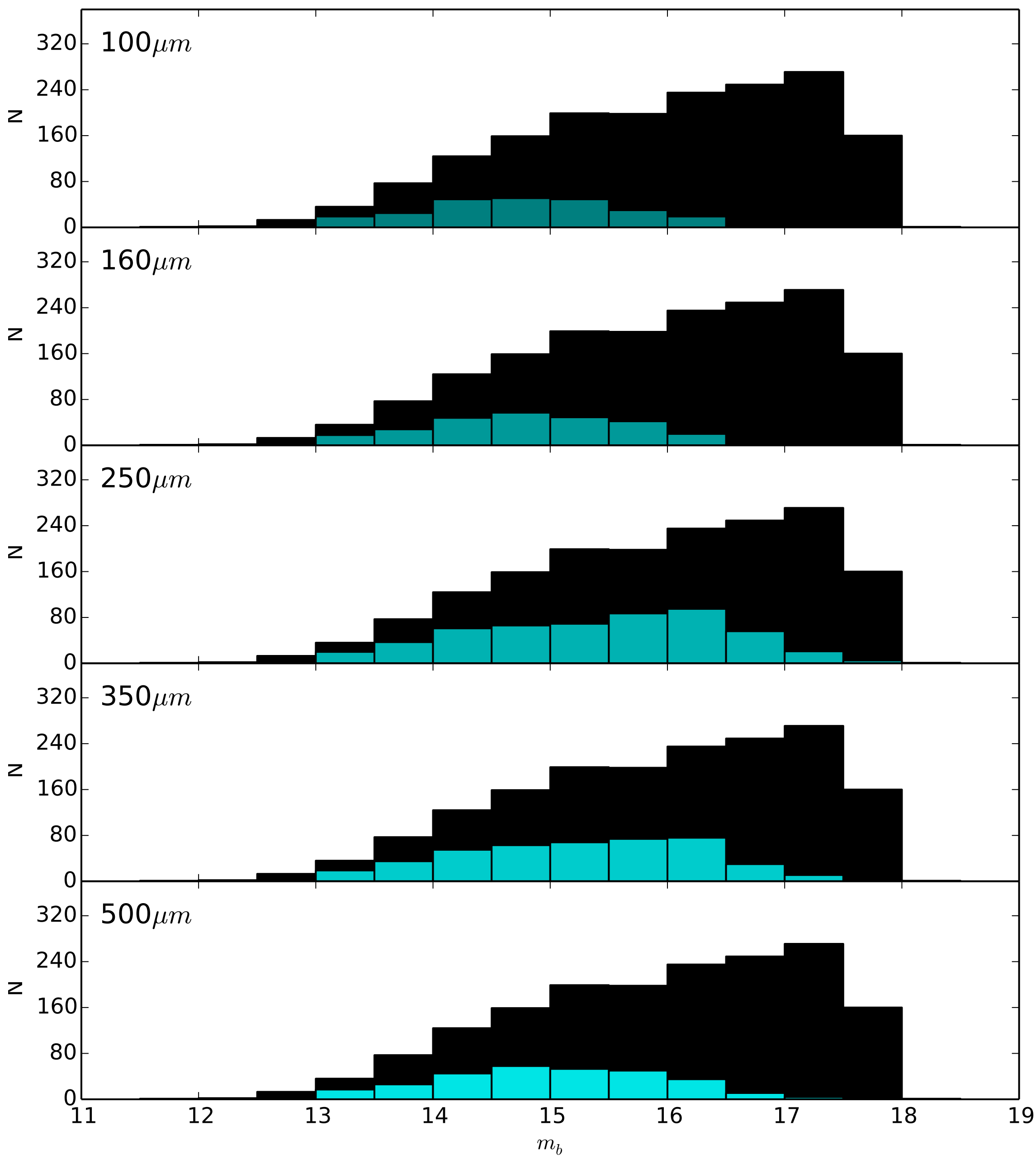

Figure 5.1. A histogram of optical magnitude m_b of the CCC/CFC galaxies - the black and cyan bars are the total and FIR detected galaxies respectively.

deeper optical catalogue would significantly increase the number of FIR detections in our current data. This shows that not only is the CCC well suited for our purposes - adding the FIR data to existing optical and gas data to study the Coma region - but it is also the current state-of-the-art optical catalogue for the Coma cluster.

Table 5.1 indicates how many galaxies were recovered in each band above a 3σ noise level in the FIR maps in both the cluster and filament. The SPIRE 250 μm band has the highest detection rate, as has been seen previously by Auld et al. (2013) and Fuller et al. (2014) in Virgo and Fornax, respectively. This is due to a combination of its sensitivity and the typical shape of the FIR SED. Consequently, we use the 250 μm band to compare the cluster and filament. At 250 μm we detect 99 of 744 (12 %) galaxies in the cluster and 422 of 951 (44 %) galaxies in the filament.

In order to better understand the limits of our data we estimate the limiting dust mass required for a detection at 250 μm. The lowest detected 250 μm flux in our FIR catalogue is $\sim$15 mJy. Assuming a dust temperature of 20 K the corresponding limiting dust mass is $\log_{10}(M_{dust}/\mathrm{M}_{\odot}) = 6.1$. If we now assume that a typical late-type galaxy has a dust-to-stellar mass ratio of $\log_{10}(M_{dust}/M_{stars}) = -3$ (Cortese, 2012), we should detect all late-type galaxies with a stellar mass of $\log_{10}(M_{stars}/\mathrm{M}_{\odot}) > 9.1$.

Table 5.2 shows the detection rate of each morphological type between the cluster and filament. Late-type galaxies have the highest detection rate ($\sim$53 %). Early-type galaxies conversely have the lowest detection rate ($\sim$12 %). Both early and late-type galaxies' detection rates are statically identical between the two samples, whereas, uncertain-type galaxies have far lower detection rates inside the cluster environment (9 % and 35 % for the cluster and filament, respectively).

Thus, initially showing that there is little if any difference between the cluster and filament for early and late-type galaxies. This result mirrors the comparison in the previous chapter between the Virgo and Fornax clusters.

For each morphological group we have examined the FIR detected and undetected galaxies' positions and velocities in the cluster as shown in Figure 5.2. The left panel's black and coloured markers represent the spatial position of each galaxy. The dashed black line in the right-hand panel marks the virial radius of the cluster. The right-hand panels show histograms of radial velocity. For each histogram of velocity dispersion we have fitted a Gaussian using a χ^2 minimisation technique, where errors are $\sqrt{N}$ galaxies per bin. The purple and grey histograms represent fits to the detected and undetected galaxies respectively. We have listed the average projected cluster radius for detected and undetected galaxies in the cluster as well as the derived velocity dispersions in Table 5.3.

All three morphological types have velocity dispersions that are statistically identical for FIR detected and undetected galaxies. All the velocity dispersion are also statistically identical

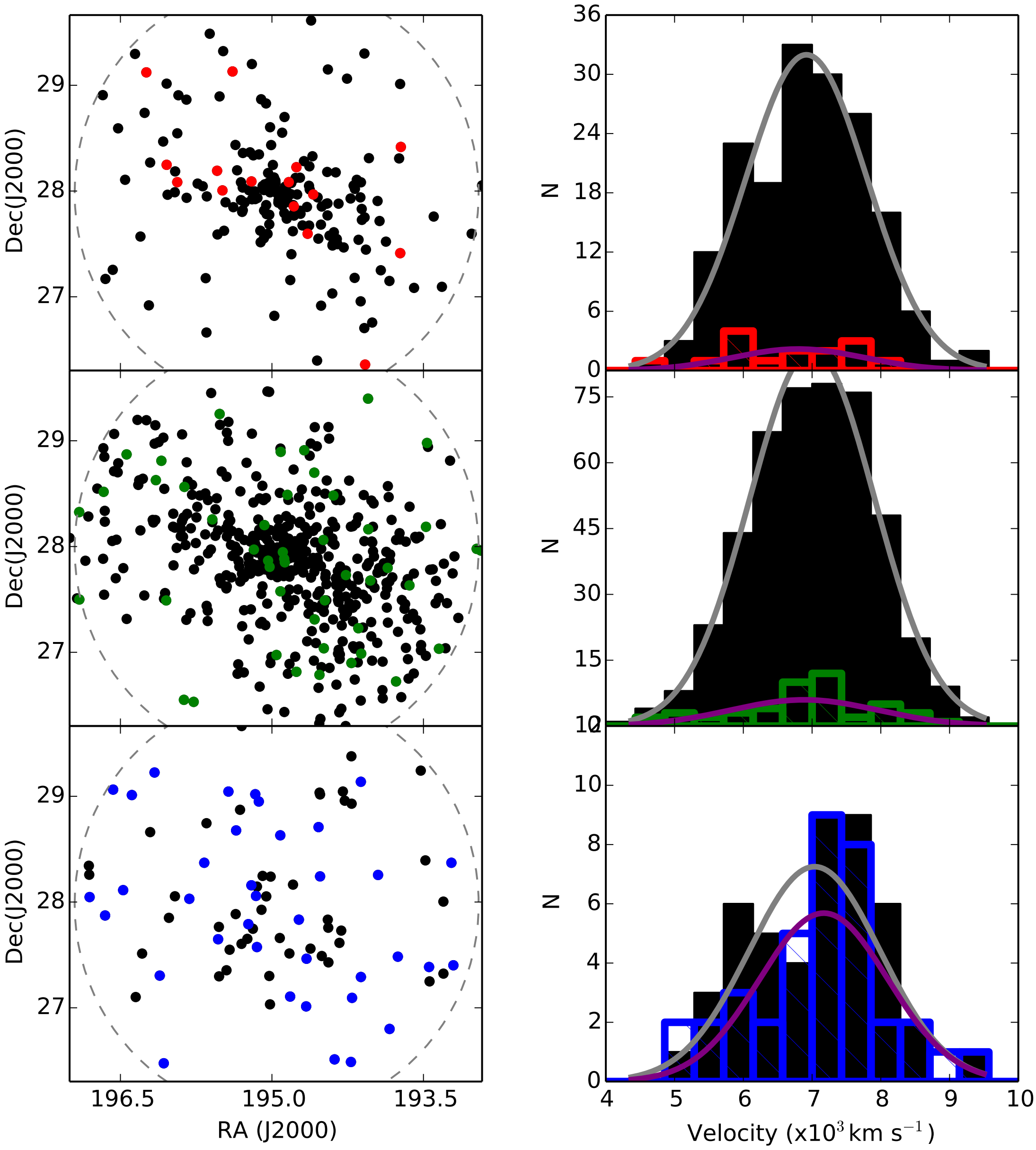

Figure 5.2. The above figure show the locations and velocities of galaxies inside the cluster. Coloured and black markers and histograms designate FIR-detected and undetected galaxies, respectively. The three morphological types are shown from top to bottom in red, green and blue representing early, uncertain and late-type galaxies, respectively. The left-hand panels represent the location in RA and Dec of each galaxy. The right-hand panels show histograms of radial velocity, where for each histogram of velocity dispersion we have fitted a gaussian using a χ^2 minimisation technique, where errors are $\sqrt{N}$. The purple and grey histograms represent fits to the detected and undetected galaxies, respectively.

Morphological Type	Radius, (R/R$_{virial}$) <R>		Difference	Velocity Dispersion, (km s^{-1}) σ ($\chi^2_{reduced}$)		Difference
	Detected	Undetected		Detected	Undetected	
late	0.48±0.04	0.59±0.04	1.9 σ	935±154 (0.5)	956±117 (0.56)	0.1 σ
uncertain	0.42±0.01	0.57±0.04	3.6 σ	1070±206 (0.9)	906±20 (0.37)	0.8 σ
early	0.43±0.07	0.36±0.02	1.0 σ	951±206 (0.29)	884±46 (0.67)	0.3 σ

Table 5.3. This table contains information relating to Figure 5.2 for the cluster. The radius refers to the average projected cluster centric radius for either FIR detected or undetected galaxies of each morphological type. In the far right hand panels of Figure 5.2 velocity dispersions have been fitted by a Gaussian function; this table includes the velocity dispersion (σ) of each fit as well as the $\chi^2_{reduced}$ value.

to the overall velocity dispersion($\sim$ 900 km s^{-1}). If any of the morphological populations had a velocity dispersion that was greater than that of the cluster as a whole it would imply that it was less relaxed and thus probably far later in joining the cluster. The fact that all our morphological types show no evidence of a different velocity dispersion implies that they have been in the cluster longer than a crossing time (1 Gyr), which is over 25$\times$ the stripping timescale (40 Myr).

Late-type galaxies have the largest average projected cluster radius (0.6 R$_{virial}$). Early-type galaxies conversely have the smallest average projected cluster radius (0.4 R$_{virial}$). Both late and early-type galaxies show no difference in mean radius between FIR detected and undetected galaxies (<2σ). Uncertain-type galaxies are the only sample that shows any significant difference by FIR selection (0.4 and 0.6 R$_{virial}$ for detected and undetected galaxies, respectively). This further implies that galaxies' locations within the cluster are largely unaffected for FIR detected and undetected galaxies of a given morphological type.

5.3 Analysis of SED fits, dust masses & temperatures

The SED of all galaxies detected in all 5 *Herschel* bands were fitted with a single temperature modified blackbody with $\beta = 2$ (198 galaxies). The average χ^2 goodness of fit value for the entire sample was, $< \chi^2_{dof=3} >= 2.7$ (where $\chi^2_{dof=3} < 7.8$, corresponds with a confidence level of 95 %) indicating that for the majority of the sample the SED was well fitted. 7 galaxies have $\chi^2_{dof=3} > 7.8$ indicating that a single temperature component may not be sufficient to model their FIR emission. In Tables B.3 and B.4 we include all galaxies with measured dust masses and temperatures for the cluster and filament, respectively. Figure B.1 shows the SED fits for each galaxy. Figure 5.3 shows histograms of the dust masses, dust-to-stellar masses and dust temperatures produced from the SED fitting process.

Figure 5.3 shows that late-type galaxies have dust masses ranging from $\log_{10}(M_{dust}/\mathrm{M}_{\odot}) =$

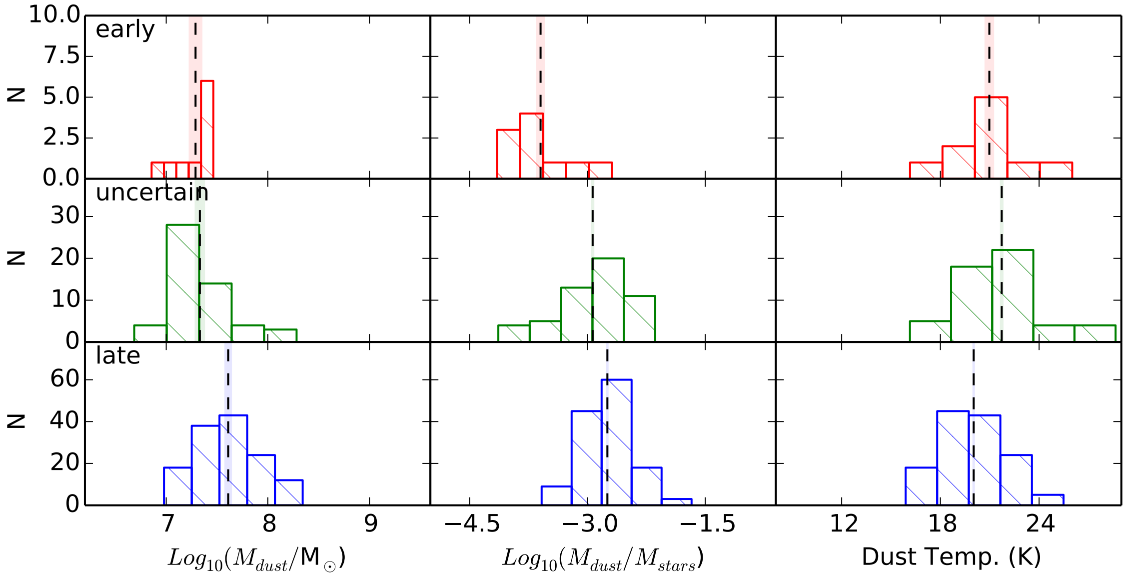

Figure 5.3. Histograms of dust mass (lefthand panels), dust-to-stellar mass (centre panels) and dust tempreture (righthand panels) caculated from galaxies detected in 5 *Herschel* bands and fitted with a modfied black body (see text). These are plotted for early, uncertain and late-type galaxies in red, green and blue, respectivly. The vertical dashed line and shaded region either side of it refere to the mean and uncerantiy, respectivly of each sample.

7.0 to 8.3 and temperatures of 16.0 to 25.5 K, with mean values of $\log_{10}(M_{dust}/\mathrm{M}_\odot) = 7.63 \pm 0.02$ and 20.0 ± 0.1 K. Uncertain-type galaxies have dust masses ranging from $\log_{10}(M_{dust}/\mathrm{M}_\odot) = 6.7$ to 8.3 and temperatures of 16.2 to 28.7 K, with mean values of $\log_{10}(M_{dust}/\mathrm{M}_\odot) = 7.33 \pm 0.04$ and 21.7 ± 0.5 K. Early-types have a narrower range of dust masses of $\log_{10}(M_{dust}/\mathrm{M}_\odot) = 6.9$ to 7.5 and temperatures of 16.2 to 26.0 K, with mean values of $\log_{10}(M_{dust}/\mathrm{M}_\odot) = 7.3 \pm 0.04$ and 21.0 ± 0.2 K.

CCC/CFC galaxies have mean dust-to-stellar mass ratios of $\log_{10}(M_{dust}/M_{stars})$ = -3.6 $\pm$ 0.04, -2.93 $\pm$ 0.01 and -2.75 $\pm$ 0.01 for early, uncertain and late-types, respectively. As expected from our previous results for Virgo and Fornax (Auld et al., 2013; Fuller et al., 2014), late-types have a richer and cooler dust reservoirs, and early-types have a relatively depleted and warmer ISM.

In Table 5.4 we use the Kolmogorov-Smirnov two sample test (KS) to make a more quantitative comparison between the cluster and filament's early, uncertain and late-type galaxy populations with respect to dust mass, dust-to-stars ratio, and dust temperature. A KS test shows that for a given morphological type the FIR properties of galaxies in the cluster and filament are statistically identical with the exception of dust temperature, where early-types have slightly warmer dust temperatures in the cluster environment. The above results suggest that the different environments have had very little effect on the dust mass or dust-to-stars ratio of early or late-type galaxies.

Sample 1	Sample 2	$\mu_1(\sigma_1)$	$\mu_2(\sigma_2)$	K-S test		Sample Size	
				Value	P_{value}	N_1	N_2
Dust Mass (log($M_{Dust}/M_\odot$))							
Cluster Early	Filament Early	7.25(0.09)	7.35(0.05)	0.333	0.89	6	4
Cluster Uncertain	Filament Uncertain	7.33(0.07)	7.33(0.05)	0.14	0.974	15	38
Cluster Late	Filament Late	7.66(0.06)	7.6(0.03)	0.12	0.914	25	110
HI-Normal	HI-Deficient	7.64(0.06)	7.72(0.05)	0.317	0.5	7	41
Dust Mass / Stellar Mass (log($M_{Stellar}/M_\odot$) - log($M_{Dust}/M_\odot$))							
Cluster Early	Filament Early	-3.74(0.14)	-3.39(0.23)	0.583	0.254	6	4
Cluster Uncertain	Filament Uncertain	-3.05(0.14)	-2.89(0.07)	0.168	0.892	15	38
Cluster Late	Filament Late	-2.78(0.06)	-2.74(0.03)	0.144	0.762	25	110
HI-Normal	HI-Deficient	-2.98(0.11)	-2.65(0.04)	0.544	0.036	7	41
Dust Temp. (K)							
Cluster Early	Filament Early	22.12(0.77)	19.25(0.9)	0.833	0.03	6	4
Cluster Uncertain	Filament Uncertain	21.51(0.49)	21.81(0.43)	0.179	0.845	15	38
Cluster Late	Filament Late	20.66(0.44)	19.88(0.18)	0.229	0.205	25	110
HI-Normal	HI-Deficient	20.46(0.99)	20.37(0.32)	0.213	0.918	7	41

Table 5.4. A statistical comparison of environment (cluster and filament) and H I-deficiency comparing dust mass, dust-to-stellar mass, and dust temperature.

In addition, we have used the H I-deficiency values calculated for 70 galaxies from Gavazzi et al. (2006) to compare galaxies that are H I-normal (H I-def. ≥ 0.5) with H I-deficient (H I-def. < 0.5) these galaxies are exclusively late-type. A KS test shows that H I-normal and H I-deficient galaxies are statistically identical with respect to dust mass and temperature. However, a KS test shows that with respect to dust-to-stellar mass ratio H I-normal and H I-deficient galaxies are significantly different, whereby H I-normal galaxies have more dust per unit mass of stars than the H I-deficient sample. Gavazzi et al. (2006) showed that H I-deficiently decreases with cluster centric distance and are most H I-deficient in the centre of the cluster. H I-deficiency traces galaxies most strongly interacting with the cluster environment. The above result - that galaxies have lower dust-to-stellar mass ratios when separated by H I-deficiency - shows that physical processes can affect the FIR properties of late-types. This has been shown previously by Cortese et al. (2012b) using the HRS sample spanning both the cluster and field environments. Cortese et al. (2012b) showed that radial extent of dust was truncated for H I-deficient galaxies. Our results would imply that galaxies interacting with the cluster environment can have dust removed. However, crucially even with the increased ram stripping power of Coma, when compared to Virgo, dust is still not completely removed. Our spatial resolution at the distance of Coma precludes us from accurately measuring the physical extent of dust in late-types in the cluster and filament to see if the dust disks are truncated.

We have extended the above statistical comparison in Table 5.5 to compare Coma to Virgo and Fornax as well as the Filament to a field sample. In Table 5.5 we have restricted our

Sample 1	Sample 2	$\mu_1(\sigma_1)$	$\mu_2(\sigma_2)$	K-S test		Sample Size	
				Value	P_{value}	N_1	N_2
Dust Mass / Stellar Mass ($\log(M_{dust}/M_{stellar})$)							
Coma Early	Virgo Early	-3.63(0.13)	-3.62(0.19)	0.273	0.883	6	11
Coma Early	Fornax Early	-3.63(0.13)	-3.89(0.27)	0.4	0.652	6	5
Coma Late	Virgo Late	-2.74(0.07)	-2.76(0.04)	0.087	0.997	25	103
Coma Late	Fornax Late	-2.74(0.07)	-2.94(0.08)	0.323	0.251	25	14
Filament Late	HRS Late	-2.75(0.03)	-2.3(0.04)	0.594	5.310^{-17}	110	99
Filament Early	HRS Early	-3.45(0.16)	-3.68(0.2)	0.25	0.98	4	10

Table 5.5. A statistical comparison of Virgo, Fornax, Coma, the Filament, and the HRS comparing dust-to-stellar mass.

comparison to dust-to-stellar mass only. We have used the HRS galaxies that are outside of the Virgo cluster as a 'Field' sample[1] (Boselli et al., 2010; Smith et al., 2012; Cortese et al., 2012b).

The key question is if late-type galaxies' FIR properties are affected by environment? On what density scale does this effect take place? Using Table 5.5 it is clear that a KS test indicates this transition takes place between the field and filament environment. Suggesting that late-types are affected well before entry into the cluster environment. Furthermore, the FIR properties of late-types are invariant with respect to Virgo, Coma and Fornax - three very different cluster environments. Furthermore, Table 5.5 shows that early-types dust-to-stars ratios appear identical regardless of environment.

5.4 Chemical Evolution

In this section we examine the chemical evolution of cluster and filament galaxies. The simplest approach is to use a closed box model ie no inflow or outflow of material. Although a closed box model is unlikely to reflect the reality of these galaxies as it is well known that there is inflow and outflow of materials in galaxies. However, it is still instructive to compare various parameters (derived below) between our two samples. In order to model

[1] We have used updated values for dust mass by Cortese et al. (2014) where HRS galaxies have had FIR properties caculated using the identical method used here (ie $\beta = 2$). We have used stellar masses from Cortese et al. (2012a) and in order to make the stellar masses in the HRS consistent with our other samples we have adjusted the HRS stellar masses by +0.36 dex to converted fom the Chabrier IMF (Chabrier, 2003) to a "diet" Salpeter IMF Bell et al. (2003) as per the recipes in Chabrier (2003).

these galaxies we need several parameters that we have not measured thus far, namely total gas mass (M_{Gas}^{Tot}) and total metallicity (z_{total}). We define both below using the data outlined in Chapters 2 and 3. As mentioned previously dust as well as gas phase metallicity gives a 'complete' picture of the metals in the ISM in our galaxies.

To extend our analysis of dust mass to lower limits we have included an additional 323 galaxies. These galaxies had insufficient data to be fitted by a modified blackbody (ie detected in less than 5 *Herschel* bands with measured fluxes) and so for galaxies detected in the 250 μm band we use this flux density as a proxy for dust mass by assuming a dust temperature of 20 K.

5.4.1 Total Gas Mass

In Chapter 3 we discuss the origin and extend of our atomic gas data. In order to calculate the total gas mass of each galaxy we must take account of all the other major gas phases; molecular hydrogen, helium and the gas in the warm and hot components. Davies et al. (2014) estimate that $M_{Gas}^{Total} = 2.5 M_{H\,I}$ for galaxies in the Virgo cluster. We use the former relation to adjust our H I masses to take account of all phases of the gaseous ISM.

5.4.2 Total Metallicity

From the SDSS spectroscopic data we have the gas phase metallicity in the form of oxygen abundance ($12.0 + \log_{10}(O/H)$) for SDSS galaxies with emission lines (see Chapter 3). Asplund & García Pérez (2001) give the solar oxygen abundance as $12.0 + \log_{10}(\mathrm{O/H})_{\odot} = 8.69$ and $z_{\odot} = 0.014$, thus allowing us to convert oxygen abundance (O/H) to total metallicity in the gas phase (z_{gas}) using the relation z_{gas}= 29.2(O/H). The mass of metals in the cold gas is then $z_{gas} M_{H\,I}$. However, the former does not account for the metals in the warm and hot phases of the ISM. Davies et al. (2014) use the work of Gupta et al. (2012) and estimate that the mass of metals in the hot and warm phases of the ISM to be $0.2 z_{gas} M_{H\,I}$, giving $M_{Metals} = 1.2 z_{gas} M_{H\,I}$. The 'total' metallicity (z_{total}) is then calculated from both the gaseous and dusty ISM, defined as; $z_{total} = (M_{Metals} + M_{Dust})/M_{Gas}^{Total}$.

5.4.3 Mass Fraction of Metals in Dust and Gas

We can independently calculate the fraction of metals by mass in the dust to gas, η. I find the fraction of metals in the dust as 0.4 ± 0.1, which agrees with previous estimates of 0.5 by Meyer et al. (1998); Whittet (1992). Davies et al. (2014) performed the same analysis in the Virgo cluster and found $\eta = 0.5$. This further shows that two very different clusters have no statically significant effect on how the metals in a galaxy are distributed within the ISM.

5.4.4 Chemical Evolution Modeling

Using the above derived parameters we can examine our galaxies within the framework of the simple closed boxed model. Edmunds (1990) show that the total metallicity (see above) can be related to the gas fraction (f) by a parameter p the stellar yield using the equation $z_{total} = pln(1/f)$. The gas fraction is $f = M_{gas}/(M_{stars} + M_{dust} + M_{gas})$. The stellar yield p is the mass fraction of metals released back into the ISM per unit mass of material that goes into star formation. The above equation holds for a closed box model ie where there are no inflows or outflows of gas. Edmunds (1990) defines the effective yield as $p_{eff} = \frac{z_{total}}{ln(1/f)}$ regardless of inflow or outflow. They show that $p_{eff} \leq p$. Simply put, that a model with inflow or outflow can never outperform the simple closed boxed model and that effective yield will always be less than the simple model.

In the upper panel of Figure 5.4 we plot total metallicity (see above) against the logarithm of the reciprocal of the gas fraction (ln(1/f)). The red and blue markers and lines represent cluster and filament galaxies, respectively. We fit a linear relation with a y-axis intercept of 0, the gradient is the effective yield (p_{eff}). The effective yield of the cluster and filament are 0.017 ± 0.01 and 0.019 ± 0.01, respectively. Thus the two are statistically identical. The black line is a fit to all the galaxies and gives an effective yield of 0.018 ± 0.01. The galaxies appear well fitted by a linear relation. This is a familiar theme in this chapter, again in terms of a chemical evolution model galaxies in the cluster appear identical to galaxies in the filament, implying that if there has been inflow or outflow it has occurred before these galaxies entered the cluster or the filament environment.

Edmunds & Eales (1998) derive; $\Delta_{max,f} = \eta p_{eff} f \log(1/f)$, where $\Delta_{max,f}$ is the maximum dust mass per unit total mass a galaxy could possess with a gas fraction f, a fraction of metals in the dust η and a effective yield p_{eff}.

The lower panel of Figure 5.4 we have plotted dust-to-total mass against 1-f. Again, as in the upper plot red and blue markers refer to cluster and filament galaxies, respectively. Using the values for $\eta = 0.4$ and $p_{eff} = 0.018$ as calculated using total metallicity above we can plot the maximum dust mass per unit total mass using the equation $\Delta_{max,f} = \eta p_{eff} f \log(1/f)$ from Edmunds & Eales (1998) in black. Almost all galaxies in the filament and the cluster have lower $\Delta_{max,f}$ for a given gas fraction. The latter may imply that as shown in Table 5.5 dust-to-stellar mass has been depleted in these galaxies compared to a field sample. However, this effect occurred before entry into the cluster or filament

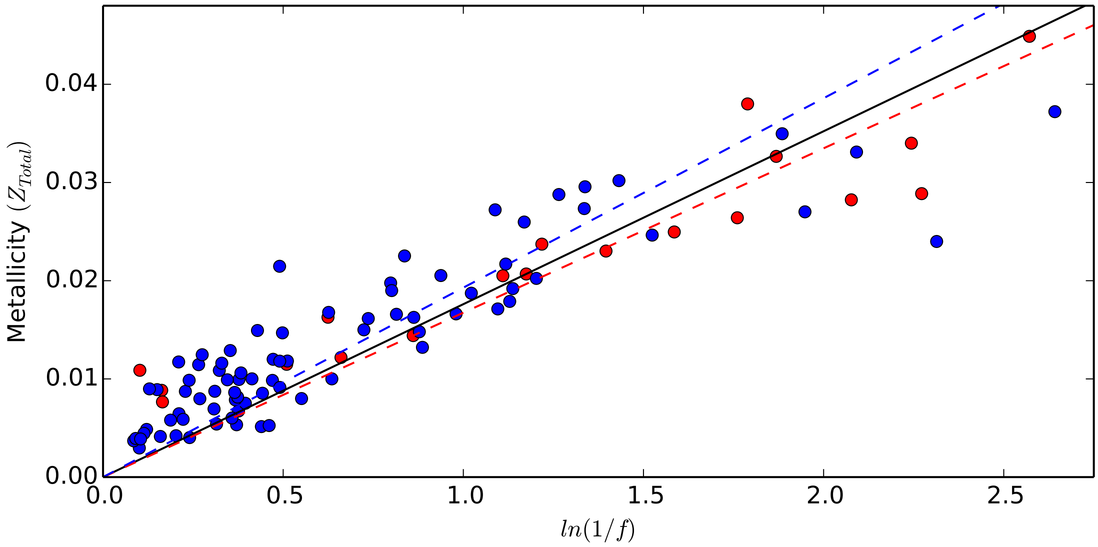

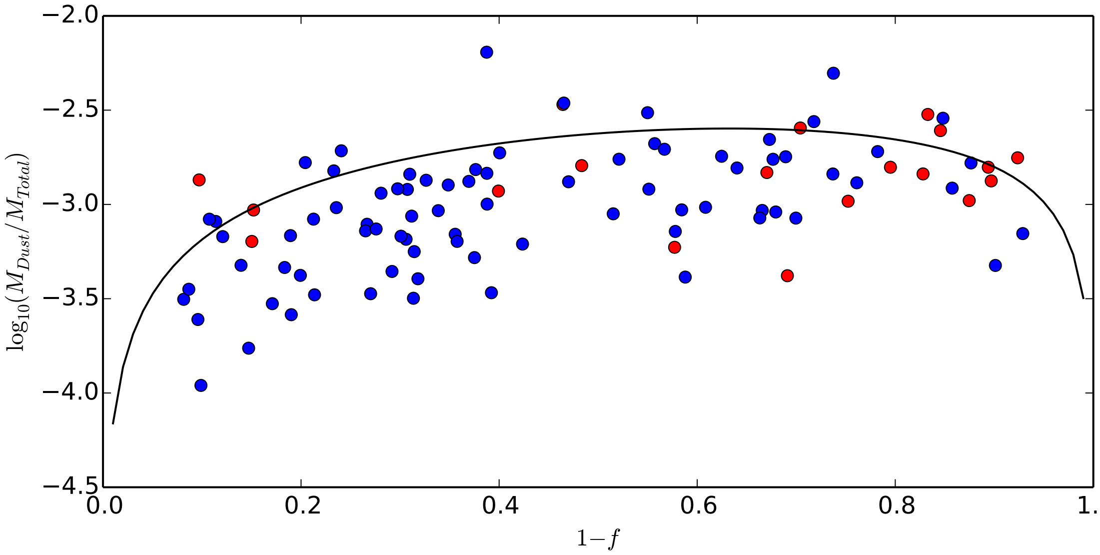

Figure 5.4. The upper plot shows the derived metallicity (taking account of both metals in dust and the gaseous phases of the ISM) against ln(1/f), f is the gas fraction (see text). The red and blue markers are used for cluster and filament galaxies, respectively. The red, blue and black lines are fitted to the cluster, filament and overall samples, respectively. Their gradients are equal to the effective yield, p_{eff} (see text). The lower plot shows dust-to-total mass ratio against 1-f. The markers on the lower plot are the same as in the upper plot. The values of p_{eff} (derived in the upper plot) are used to plot the maximum dust-to-total mass ratio expected given the assumption of a closed box model.

environments.

5.5 Summary

We have undertaken the deepest FIR survey of the entire Coma cluster and filament using the *Herschel* Space Observatory[2]. Our survey covers over 150 deg^2 in 5 bands and extends to well beyond the virial radius of the cluster and covers the filament also known as the 'Great Wall' it sits within. We have used the SDSS spectroscopic survey to define a redshift selected sample of the Coma cluster, the Coma Cluster Catalogue (CCC). Using our velocity selection and our area coverage we select 744 and 951 galaxies in the cluster and filament, respectively.

We have used the optical positions and parameters of these CCC galaxies to fit appropriate apertures to measure FIR emission. We have detected 99 of 744 (12 %) and 422 of 951 (44 %) cluster and filament galaxies in the SPIRE 250 μm band, respectively.

In order to better understand the global detection rate we separated the cluster and filament galaxies into 3 morphological categories using the Galaxy Zoo data: early, $p(E)>0.8$; late, $p(S)>0.8$ and uncertain where $p(E)<0.8$ and $p(S)<0.8$. We examined the detection rate for each morphological group in the 250 μm band as it has the highest detection rate of all the *Herschel* bands. Early and late-type galaxies have the same detection rates in the cluster and filament, indicating that the lower global detection rate in the cluster are due to its lower fraction of late-type galaxies.

We compare the velocity dispersions of detected and undetected late and early-types. We found that all morphological types have velocity dispersions statistically identical to the cluster's overall velocity dispersion. The former implies that all morphological types have been in the cluster longer than a crossing time and 25$\times$ as long as the timescale for viscous stripping.

For galaxies detected in at least 5 bands we fit a modified blackbody with a fixed beta emissivity index of 2, giving dust masses and temperatures for 198 galaxies. Early-type galaxies show lower dust masses and hotter temperatures than late-type galaxies. When comparing early-type galaxies from the Coma cluster with other nearby clusters (Virgo and Fornax) and the filament, their FIR properties are statistically identical. The same is true for the late-type galaxies. We only show a significant difference in dust-to-stellar mass for late-type galaxies between the filament and field sample of nearby galaxies. This may suggest that the effect of the cluster and filament is more subtle than previously thought

[2] Hickinbottom et al. (2014) have conducted a deeper study using the PACS instrument, however, the former survey covers the cluster core and SW infall region, whereas ours covers the cluster and filament it resides in.

and that the evolution of the ISM components has mostly taken place well before the cluster was assembled.

We use recipes to estimate the total gas mass as well as the metallicity taking account of both metals in the gas and dust. Using these we estimate the effective yield and find that galaxies in the cluster and filament again appear statistically identical. We use simple models to estimate the amount of dust per total mass a galaxy could have for a given gas fraction. We find that almost all cluster and filament galaxies have less dust than expected.

Chapter 6
Trends with density

"The heavens declare the glory of God;
the skies proclaim the work of his hands.
Day after day they pour forth speech;
night after night they reveal knowledge,
They have no speech, they use no words;
no sound is heard from them.
Yet their voice goes out into all the earth,
their words to the ends of the world."

Psalm 19: 1 - 3

6.1 Introduction

In this work so far we have largely used FIR data and made global comparisons (eg cluster vs filament) for several FIR parameters (dust mass, temperature and dust-to-stars ratio). In this chapter we will examine other parameters (dust-to-stars, sSFR, morphology, and gas-to-stars) and how each is affected by environmental density (Σ_1, Σ_5, Σ_{10}, and projected cluster radius see Chapter 3 for the definition of these parameters) for galaxies in the Coma region. The Σ_{10} and Σ_1 parameters trace large and small scale structure, respectively which allows us to examine how these parameters change on a more 'local' scale. As I described in the main introduction to this work, the field, group and cluster paradigm is a somewhat redundant way of examining the cosmic web - which appears to be far more complex.

The method that I have used below is (as far as i'm aware) a unique way of measuring a change in a given physical parameter for a population of galaxies across environment. The method is not without its limitations (discussed below). However, it overcomes the problem of comparing the relative change with density in several parameters with different units. My

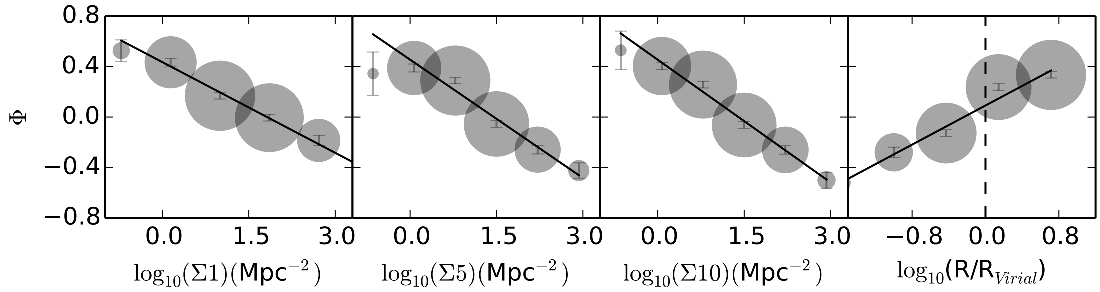

Figure 6.1. This plot shows how morphology (ϕ - see text) changes with environmental density traced using Σ_1, Σ_5, Σ_{10}, and projected cluster radius (right to left). Σ_1, Σ_5, Σ_{10} are given in units of galaxies per Mpc^2, and projected cluster radius is given in units of the cluster's virial radius (3.01 Mpc). Each marker represents a given density bin's mean value, and its size represents the number of galaxies in each bin. Each line is fitted using a χ^2 minimisation technique(see text). The trend for all galaxies is shown with black markers and lines fitted.

initial expectation when conducting the analysis detailed in this chapter was comparing the strength of change in each parameter for each density tracer. I quickly (as will the reader) found that few parameters showed much if any change, and thus I choose to change the analysis to measure how many density tracers were consistent with change as each density tracer. As each density tracer is a semi-independent tracer of environment and thus offers an indication of which parameters of galaxies are affected most strongly by environment.

6.2 Methodology

For a given parameter we have used evenly spaced bins over the density range (e.g. $\log_{10}(\Sigma_5)$) for a given morphological type (early and late). Each coloured marker is then representative of the mean value in this bin. The error bar is the standard deviation in the bin divided by the square root of the number of galaxies in that bin. If a bin has less than 3 galaxies in it is discounted and neither plotted or fitted. For each morphological type, parameter vs density plot, we have first fitted a straight line (e.g. $y = mx + x$), using a χ^2 minimisation technique. We have repeated this method for each density tracers and morphological type. We test whether or not each fit is consistent with a change with density (i.e. $m = 0$?). We test if the change is greater than 3σ ie $\frac{m}{dm} \geq 3\sigma$.

For each parameter and morphological type we have calculated the number of density tracers that are consistent with a change with density ($m \neq 0$ with a significance greater than 3σ). If all 4 density tracers are consistent with a change with density then it is designated as having a 'Strong' change. If 2 or 3 density tracers are consistent with a change with density then it is designated as having a 'Moderate' change. If only 1 density tracer is consistent with a change with density then it is designated as having a 'Weak' change. Finally, if no

	late	early
Dust-to-Stars	Moderate (2)	No (0)
sSFR	Moderate (3)	Weak (1)
Gas-to-Stars	Strong (4)	-
Stellar Mass	Moderate (3)	Weak (1)
Average	Moderate (2.7)	Weak (0.7)

Table 6.1. Above shows a summary for all the parameters and density tracers for each morphologial type. For each morphological type and parameter we measuere how many density tracers are consistent with a change ($m \neq 0$) then; N=4, Strong; N=2 or 3, Moderate; N=1, Weak; and N=0, No. Above 'N' is shown in brackets. The bottom row contains the average for each measured correlation.

density tracers are consistent with a change with density then it is designated as having 'No' change. Figure 6.2 is a graphical representation of the above method. Table 6.1 lists each parameter and how strong (if at all) any change is with density. At the bottom of Table 6.1 we have calculated the mean number of density tracers that are consistent with change for each morphological type. Table C.2 includes all gradients and uncertainties for the lines fitted in Figure 6.2.

6.3 Morphology

Using the Galaxy Zoo weightings of probability of being a spiral ($p(S)$) or elliptical ($p(E)$). We have defined a new parameter (Φ), where $\Phi = p(S) - p(E)$. This is a non-integer way of describing a galaxy where values of $\Phi \simeq 1$ and -1 indicates the expected values for clear late and early-type morphologies. In Figure 6.1 we have calculated the change of Φ with all 4 environmental tracers. It is strongly affected by environment. This is a unique way of understanding the morphology density relation using a non-integer method. As we discussed in Chapter 1, the origin of the morphology density relation is still an open question. In the following sections we use the above described method to investigate some of the key parameters and how they change with environment in order to attempt to understand the role of environment on galaxies.

In Figure 6.2 and Table 6.1 we have measured the trends with density using a method that gives us the ability to test how/if it has changed with environmental density within the Coma and filament combined sample. As we have shown most properties are related to stellar mass and as such we have used stellar mass ratios rather than the parameter in isolation.

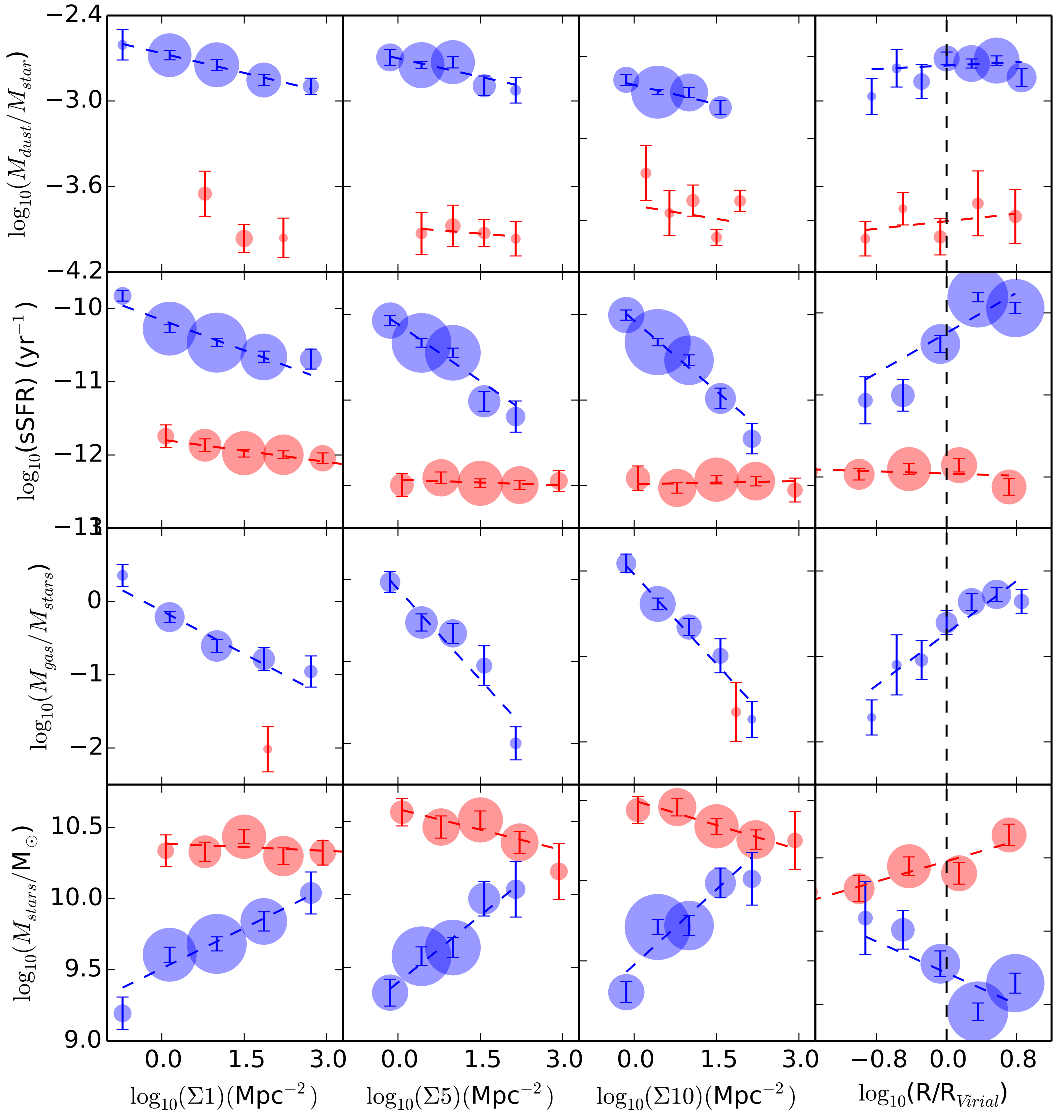

Figure 6.2. This plot shows how multiple parameters change with environmental density traced using Σ_1, Σ_5, Σ_{10}, and projected cluster radius (right to left). Σ_1, Σ_5, Σ_{10} are given in units of galaxies per Mpc^2, and projected cluster radius is given in units of the cluster's virial radius (3.01 Mpc). Red and blue markers and lines are for early and late-type galaxies, respectively. Each marker represents a given density bin's mean value, and its size represents the number of galaxies in each bin. Each line is fitted using a χ^2 minimisation technique (see text).

6.4 Dust-to-stars

For galaxies that do not qualify for dust mass and temperature to be found using an SED fitting method as previously described in Chapter 2 we estimate their dust mass using their 250 μm flux (if detected). We assume a fixed dust temperature of 20 K, which is approximately equal to the average found for galaxies we have fitted an SED in all samples in this thesis. This allows us to add a further 323 galaxies to our sample, yielding a total sample of 521 galaxies we have dust masses for in both the filament and cluster.

Table 6.1 shows the dust-to-stars ratio has a moderate change with density in late-type galaxies. Early-type galaxies show no change in their dust-to-stellar mass ratios with any density tracers. In Chapter 5 we used a KS test to show that there was no change between the cluster and the filament for late-type galaxies. The same is shown for cluster centric radius in this chapter. However, Σ_1 and Σ_{10} show a change in dust-to-stellar mass ratio with density. As here we find a moderate change it may suggest that the method shown in this chapter is more sensitive to any parameter changes with density.

6.5 sSFR

Late-type galaxies' sSFRs are moderately affected by environment, whereas early-type galaxies only show a weak change[1]. This would suggest that higher density environments lower star formation efficiency.

6.6 Gas-to-stars

Only 8 early-type galaxies have measured HI data and only 3 have both HI and FIR and thus we have not measured a trend for these galaxies. In late-type galaxies gas-to-stellar mass is strongly affected by environment.

6.7 Stellar mass

Stellar mass changes for late and early-type galaxies. Early-types are only weakly affected, late-types are affected. Late-types show an increase in stellar mass in higher density environments, whereas early-types shown the reverse.

[1] Brinchmann et al. (2004) state that for the non-emission line galaxies their SFR and sSFR caculations are far less reliable. As only 5 early-type galaxies are considered emission line galaxies we consider the change in sSFR in early-types could be unrelaible.

The stellar mass of a galaxy in the present day can be understood using the equation:

$$M_{star} = \int_{t_{start}}^{t_{present}} \psi(t)\mathrm{d}t \tag{6.1}$$

where M_{star} $\psi(t)$, $t_{present}$ and t_{start} are stellar mass, SFR, present time and start of SF. For late-type galaxies to have higher stellar masses and lower present day SFRs, ψ must have been significantly higher in the past or they must have started forming stars earlier ie t_{start} would be lower. Thus, this would suggest late-type galaxies' sSFRs and gas-to-stars ratios may be lower as are these galaxies are more evolved (Bower et al., 1998; Thomas et al., 2005; Shimakawa et al., 2014).

6.8 Discussion

This chapter has highlighted two key problems with many current methods of studying changes in galaxies' parameters and quantifying environment itself.

Firstly as discussed in the introduction to this chapter the field, group cluster paradigm is somewhat redundant as a description of environment as environment is far more nuanced. I have tried to understand environment using multiple density tracers eg Σ_N. However, the limitation of this method is that Σ_N is not the complete picture either. This parameter does not relate the density of hot ICM a galaxy resides in nor its velocity relative to it, both of which may have a far stronger impact on its evolution. The number of data points in this chapter is in some case $>10^3$, even so the intrinsic scatter is too large to measure change in many of the parameters. This is not only uncertainty in the measurement of the physical parameter but also the uncertainty of the density tracer.

Secondly single parameters (eg dust mass) are misleading if compared in isolation as stellar mass is not constant in different environments. Parameter ratios (eg dust-to-stellar mass) may be a better way of measuring change. Furthermore, this change in stellar mass shows that it is non-trivial to separate nature and nurture. Here nature would indicate galaxies form earlier and thus have lower gas-to-stars ratios and nurture where galaxies have had gas removed by the cluster environment.

Chapter 7
Mass Functions

"A voice had begun to sing. It was very far away and Digory found it hard to decide from what direction it was coming. Sometimes it seemed to come from all directions at once. Sometimes he almost thought it was coming out of the earth beneath them. Its lower notes were deep enough to be the voice of the earth herself. There were no words. There was hardly even a tune. But it was, beyond comparison, the most beautiful noise he had ever heard. It was so beautiful he could hardly bear it."

C S Lewis - The Magician's Nephew

In order to understand how the baryonic components of the galaxies change as a whole between the cluster and filament we have created mass functions. These are shown in Figure 7.1. We have estimated the volume of the cluster as a sphere with the cluster's virial radius (3.01 Mpc), yielding a cluster volume of 114.2 Mpc^3. Estimating the volume of the filament is not trivial as this is not a virialised region in the same sense as the cluster. Either way the normalisation is in some sense arbitrary because we are primarily interested in the shape of the mass functions which is independent of the assumed volumes. To make a crude comparison we have assumed that the filament is a sheet 6 Mpc ($2\times R_{Coma}$) with a cross sectional area of 23.4 $\times$21.7 Mpc as this is the survey's physical footprint at the distance of the Coma cluster. We then subtract the volume of the cluster from this region yielding a volume for the filament of 2872.8 Mpc^3.

All mass functions are prone to incompleteness at the lowest mass end. For our dust mass data it is straightforward to estimate the completeness. We take the 3σ 250 μm global noise (33.9 mJy / beam see Chapter 2) in the FIR map as a reasonable estimate for completeness. Assuming a fixed dust temperature of 20 K, this is a dust mass of $\log_{10}(M_{dust}/\mathrm{M}_{\odot}) = 6.4$,

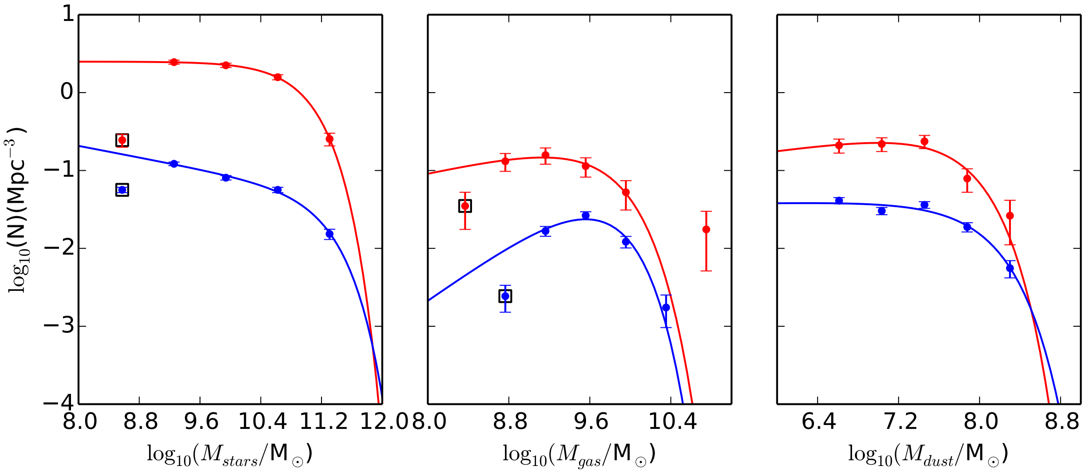

Figure 7.1. The three plots show mass functions for all the galaxies in the cluster and filament. Left-to-right the panels are stellar, gas (atomic) and dust mass. The red and blue markers and lines refer to the cluster and filament samples, respectivley. The lines are Schechter functions fit to the data (see text). The markers with black squares were excluded from the fitting process (see text).

Sample	$\phi \pm \sigma\phi$ (Mpc^{-3} dex^{-1})	$M^* \pm \sigma M^*$ (10^9 M$_\odot$)	$\alpha \pm \sigma\alpha$	ρ (10^9 M$_\odot$ Mpc^{-3})	Ref
Stellar Mass					
Coma	2.5±0.08	89±30	-1.0±0.01	220±10	(1)
Filament	0.05±0.01	175±48	-1.2±0.1	10.2±3.6	(1)
Virgo	0.3±0.1	192±117	-1.2±0.1	67±47	(2)
Field	0.0002±0.0001	100±20	-1.2±0.1	0.2±0.05	(4)
Gas Mass					
Coma	0.3±0.2	4.8±3.2	-0.7±0.4	1.3±1.2	(1)
Filament	0.06±0.01	3.9±1.5	-0.08±0.5	0.22±0.10	(1)
Virgo	0.6±0.3	4.5±1.6	-1.0±0.2	2.7±1.7	(2)
Field	0.009±0.001	5.0±0.1	-1.50±0.05	0.08±0.01	(5)
Dust Mass					
Coma	0.4±0.2	0.06±0.03	-0.8±0.2	0.02±0.02	(1)
Filament	0.04±0.02	0.1±0.04	-1.0±0.2	0.04±0.02	(1)
Virgo	0.7±0.1	0.06±0.01	-0.9±0.1	0.04±0.01	(2)
Field	0.006±0.001	0.040±0.004	-1.0±0.2	0.0002±0.0001	(3)

Table 7.1. The tabulated values of the Schechter function fits from Figure 7.1. The fits for stellar, gas (atomic) and dust mass are shown. We have calculated the mass density for each fit (see text) and listed it in the rightmost column. Refences are as follows: (1) This chapter, (2) Davies et al. (2014), (3) Dunne et al. (2011), (4) Panter et al. (2007), and (5) Davies et al. (2011).

and we take this to be the level of completeness in our dust masses. However, gas and stellar mass are more complex. Stellar masses are non-trivial to estimate completeness for as stellar mass is calculated using optical colour grid and quality of the SDSS spectrum. Atomic gas mass is again not trivial to calculate as discussed in Chapter 3. To overcome this problem we do not fit the lowest mass point for either stellar and gas mass functions.

We have fitted a Schechter function to each of the data points in Figure 7.1 created using the volumes as outlined above:

$$\phi(M)dM = \phi^* \left(\frac{M}{M^*}\right)^{\alpha} e^{-\frac{M}{M^*}} \frac{dM}{M^*} \tag{7.1}$$

We can then calculate the mass density (ρ) of each component using the Schechter best fit parameters shown in Table 7.1 using:

$$\rho = \phi M^* \Gamma(\alpha + 2) \tag{7.2}$$

7.1 Stellar mass function

The stellar mass shown in the leftmost panel of Figure 7.1 is the best constrained of all three mass functions as it represents the complete optical sample. Of the best fit Schechter parameters ϕ is set arbitrarily by one's choice in volume. However, M^* and α the so called 'characteristic mass' and 'faint end slope', respectively, are both independent of volume and thus interesting to compare. However, the values of M^* and α for the cluster and filament samples are consistent ($<3\sigma$) with each other. In Chapter 6 we showed that the mean stellar mass of galaxies increases inside the cluster, where late-type galaxies showed the largest increase. The implication of M^* and α being consistent between cluster and filament is that the increase in mass is consistent across the entire mass range of galaxies. If the increase in stellar mass was not consistent across the entire mass range, we would expect to see a change in M^* and α.

We can extend this analysis by including data from mass functions fitted in Davies et al. (2014) and Panter et al. (2007) for the Virgo cluster and field, respectively. Again, other than a change in ϕ there is no significant difference between any of the samples.

7.2 Atomic gas mass function

The atomic mass shown in the centre panel of Figure 7.1 is the worst constrained of all three mass functions as it represents a small fraction of the optical sample (58 and 172 galaxies

Sample	$\log_{10}(\rho_{gas}/\rho_{stars})$	$\log_{10}(\rho_{dust}/\rho_{stars})$
Coma	$-2.2^{+0.3}_{-1.3}$	$-4.0^{+0.2}_{-0.5}$
Filament	$-1.7^{+0.2}_{-0.4}$	$-3.4^{+0.2}_{-0.6}$
Virgo	$-1.4^{+0.3}_{-1.2}$	$-3.2^{+0.2}_{-0.6}$
Field	$-0.5^{+0.1}_{-0.1}$	$-3.0^{+0.1}_{-0.2}$

Table 7.2. Using the values of mass density in Table 7.1 this table displays the ratios of each component in galaxies inside each environment. We have normalised each ratio to stellar mass density.

in the cluster and filament, respectively). Again, the values of M^* and α for the cluster and filament samples are consistent ($<1\sigma$) with each other.

We can again extend this analysis by including data from mass functions fitted in Davies et al. (2014) and Davies et al. (2011) for the Virgo cluster and field, respectively. There is a slight change ($2\,\sigma$) between the Virgo cluster and the field, however, we lack the constraints in Coma cluster and filament samples to measure any difference between them and the field or Virgo cluster.

7.3 Dust mass function

The dust mass function is shown in the rightmost panel of Figure 7.1 and is well constrained, it represents the a significant fraction of the optical sample (88 and 379 galaxies in the cluster and filament, respectively). Again, the values of M^* and α for the cluster and filament samples are consistent ($<1\sigma$) with each other.

We can again extend this analysis by including data from mass functions fitted in Davies et al. (2014) and Dunne et al. (2011) for the Virgo cluster and field, respectively. Again, other than a change in ϕ there is no significant difference between any of the samples.

7.4 Density ratios

We can take the mass density (ρ) for each mass component and environment in Table 7.1 and create ratios of relative mass densities. We have created one for each of the four environments (Coma cluster, filament, Virgo cluster, and the field), normalising by stellar mass density. The advantage of this method is that each is given in a way that is volume independent. The above is shown in Table 7.2.

Table 7.2 shows that the ratios of the mass density of all the three main baryonic components. The Virgo, Coma and the filament are all statistically identical in terms of

Component	Mass ($M_\odot$)
Total Stellar Mass	2.1×10^{13}
Total Gas Mass	6.9×10^{10}
Total Dust Mass	2.3×10^{9}
Total Baryonic (Excluding X-ray gas)	2.1×10^{13}
Virial Mass	2.9×10^{15}

Table 7.3. Mass parameters for the Coma Cluster

$\log_{10}(\rho_{gas}/\rho_{stars})$ but all three show a significant difference to the field sample. However, all four environments are identical in terms of $\log_{10}(\rho_{dust}/\rho_{stars})$. These results would imply that gas is affected by higher density environments, whereas dust is less affected and only in the densest environments. Furthermore, they suggest that the filament is similar to the cluster samples in terms of its gas-to-stars ratio, and hence further suggesting physical processes at work well outside of the cluster environment.

7.5 Global cluster properties

Given that we have calculated the baryonic mass densities of the Coma cluster we can calculated the total masses given our estimate of volume (114.2 Mpc^3). Considering we have also accurately measured the velocity dispersion of the cluster, we can also measure the virial mass of the cluster using the equation:

$$M_{virial} = \frac{5R_{virial}\sigma^2}{G} \tag{7.3}$$

where M_{virial}, R_{virial}, σ, and G are the virial mass, virial radius, velocity dispersion and gravitational constant, respectively. By subtracting the total baryonic mass of the atomic gas, stars, and dust we can estimate the dark mass of the cluster in much the same way Zwicky (1937) did. The results are shown in Table 7.3. The overall mass to light ratio of the cluster is thus, $\frac{M}{L} = 140$.

Chapter 8
Summary & Conclusions

> *"Joy in looking and comprehending is nature's most beautiful gift."*
>
> Albert Einstein

In this Chapter I aim to summarise the entire thesis as well as focus on the key issues raised in my introduction. This is not an exhaustive discussion of the entire thesis as I have attempted to do this throughout the thesis where relevant.

8.1 Thesis Summary

The aim of this thesis was to use new data from the *Herschel Space Observatory* to investigate the effect of environment on the various components of the ISM in galaxies. I used the HeFoCS and H-ATLAS-NGP data to measure the FIR fluxes of galaxies in the nearby Fornax and Coma clusters as well as those in an associated 'filament'. In order to measure the FIR fluxes I used the optical shape and size of galaxies as a starting point. In the case of Fornax there was already a high quality optical catalogue, the FCC. However, in the case of the Coma cluster and filament I created my own using data from the SDSS spectroscopic survey, selecting galaxies based on position and velocity. In this way I created the Coma Cluster Catalogue (CCC) and Coma Filament Catalogue (CFC).

Using these optical catalogues as starting points I measured the FIR flux density of each galaxy in 5 *Herschel* bands. In the Fornax cluster I detected 30 of 237 (13 %) cluster galaxies in the SPIRE 250 μm band, a significantly lower detection rate than in the Virgo cluster (34 %; see Auld et al., 2013) which lies at a similar distance. Furthermore, I detected 99 of 744 (12 %) galaxies in the Coma cluster and 422 of 951 (44 %) galaxies in the filament.

Both of the above results at first glance would suggest that differing environments change the detection rate of galaxies in the FIR.

In order to better understand the global detection rates I separated galaxies into different morphological categories. In the case of Fornax and Virgo I sorted galaxies into 4 categories: dwarf (dE /dS0), early (E / S0), late (Sa / Sb/ Sc / Sd), and irregular (BCD / Sm / Im / dS). In the Coma cluster and filament I sorted galaxies into 3 categories using the Galaxy Zoo data: early, $p(E)>0.8$; late, $p(S)>0.8$ and uncertain where $p(E)<0.8$ and $p(S)<0.8$. I showed that between Fornax-Virgo and Coma cluster-filament the detection rates in each morphological category were identical, indicating that the differing global detection rates are a product of morphological make-up of each environment. Virgo and the filament have far more late-types, resulting in the highest detection rates when compared to Fornax and Coma.

For galaxies in the Coma cluster I compared the velocity dispersions of detected and undetected late and early-types. I found that all morphological types have velocity dispersions statistically identical to the cluster's overall velocity dispersion. This implies that all morphological types have been in the cluster longer than a crossing time and $\sim 25\times$ as long as the timescale for viscous stripping in the Coma cluster.

For galaxies detected in at least 3 and 5 *Herschel* bands for the HeFoCS and H-ATLAS-NGP galaxies, respectively, I fitted a modified blackbody with a fixed beta emissivity index of 2, that gave dust masses and temperatures for 22 and 198 HeFoCS and H-ATLAS-NGP galaxies, respectively. Early-type galaxies showed a lower mean dust mass and hotter temperature than was found for late-types.

When comparing early-type galaxies across all environments (Coma, Virgo and Fornax as well as the filament and a field sample), their FIR properties are found to be statistically identical. The same is true for the late-type galaxies. I only find a significant difference in dust-to-stellar mass for late-type galaxies between the filament and a field sample. This may suggest that the effect of the cluster and filament is more subtle than previously thought and that the evolution of the ISM components has mostly taken place well before the cluster was assembled.

I observed dust mass to be well correlated with stellar mass for late-type galaxies in the Fornax and Virgo samples. I suggest that this correlation has its origins in the mass-metallicity relation (Lequeux et al., 1979; Tremonti et al., 2004; Lara-López et al., 2010; Hughes et al., 2013), as the ratio between the mass of metals in the dust and the gas has been found to be $\sim$0.5 (Meyer et al., 1998; Davies et al., 2014). It therefore follows that any correlation with gas phase metallicity should also be observed between stellar and dust mass.

I found early-type galaxies to have a very large range of dust-to-stars ratios, $-1.3 \geq$

$\log_{10}(M_{star}/M_{dust}) \geq -6.2$. I argue that this supports a scenario where the dust in early-type galaxies is from an external origin, as has been previously suggested by other authors (Smith et al., 2012). As FIR properties are statistically identical between environments, therefore so must the balance between dust input/creation and removal/destruction. However, this conclusion is perplexing as mergers are thought to be far less common in clusters when compared to groups (Mihos, 2004), and dust destruction is largely regulated internally (Clemens et al., 2010), thus invariant with respect to environment.

In the Coma cluster and filament sample I have taken advantage of the large amount of auxiliary data (see Chapter 3). I Used recipes to estimate the total gas mass as well as the metallicity taking account of both metals in the gas and dust. Using these parameters I estimate the effective yield using a simple closed box model (Edmunds, 1990) and found galaxies in the cluster and filament again appeared statistically identical. I used a simple model to estimate the amount of dust per total mass, a galaxy could have for a given gas fraction (Edmunds & Eales, 1998). I found that almost all cluster and filament galaxies have less dust than expected. Furthermore, I found the ratio between the mass of metals in the dust and the gas to be 0.4 ± 0.1 which agrees with previous estimates of 0.5 (Meyer et al., 1998; Davies et al., 2014).

In Chapter 7 I use a method to compare multiple parameters for Coma cluster and filament galaxies (dust-to-stars, sSFR, morphology, and gas-to-stars) and how each is affected by environmental density (Σ_1, Σ_5, Σ_{10}, and projected cluster radius). Using the Galaxy Zoo weightings of probability of being a spiral ($p(S)$) or elliptical ($p(E)$) I have defined a new parameter (Φ), where $\Phi = p(S) - p(E)$. This is a non-integer way of describing a galaxy's morphology. I show that Φ is strongly affected by environment, which is another way of representing the morphology-density relation (Dressler, 1980). Using this method the measured parameters of early-types appear weakly or not affected by environmental density, whereas late types show a moderate change in most parameters with the exception of gas-to-stars, which is strongly affected by environmental density. I suggest that late-types' lower sSFRs and higher stellar masses in the cluster when compared to the filament indicate that the galaxies in the cluster formed earlier and are hence more evolved.

In order to understand how the baryonic components of the galaxies change as a whole between the cluster and filament I have created mass functions. Using Schechter function fits to stellar, gas and dust mass functions for the Coma cluster and filament I compare their parameters (ϕ, M^* and α) with values found for the Virgo cluster and a field sample. Other than ϕ which is dependent on the assumption of a volume (which is somewhat arbitrary) I found M^* and α to be identical between environments. I calculated the ratio of gas-to-stellar and dust-to-stellar mass densities for each environment finding that Virgo, Fornax, Coma and the filament were gas deficient when compared to the field, but all their dust mass functions appeared identical. Finally, I used our assumption for the volume of the

Coma cluster to calculate the total masses of each baryonic component. I found the ratio of total baryonic mass to virial mass (calculated from the velocity dispersion of the cluster) to be 140. This is much the same way as Zwicky (1937) did many years ago, where he found the ratio to be 137.

8.2 Conclusions

One of the key question I raised in the Introduction of this thesis was how does environment affect the ISM of galaxies. I have sampled galaxies in 3 key environments; Fornax and Coma, two nearby clusters and the filament associated with the Coma cluster. I have compared these data to the Virgo Cluster and various field samples.

The clusters offer examples of the densest structures in the local Universe. However, these are 3 very different environments in themselves. Coma has the hottest and most dense ICM, relative to Virgo and Fornax. This hot, dense ICM leads to Coma having a very short viscous stripping time ($\sim$40 Myr) for a typical 'L_*' galaxy. Coma's stripping timescale is 25$\times$ and 800$\times$ faster than that of the Virgo and Fornax clusters, respectively. In the case of Fornax this timescale is twice the Hubble time, thus making complete removal of a galaxy's ISM via any hydrodynamic stripping process impossible. The cluster environments are also very different dynamically, as Coma and Virgo have very high velocity dispersions $\sim$3$\times$ and 4$\times$ that of the Fornax cluster. Fornax's velocity dispersion is 300 m s^{-1} far closer to the typical rotational velocity of a typical 'L_*' galaxy, thus greatly increasing the destructive power of galaxy-galaxy interactions (Boselli & Gavazzi, 2006). Furthermore, Coma and Fornax are dynamically 'relaxed' both showing a smooth centrally concentrated distribution of galaxies, whereas Virgo is far more 'clumpy'. The dynamic relaxation would appear to have been key in determining the morphological make up of each of the clusters. As I have showed in Chapters 4 and 5 Coma and Fornax are dominated by early-types when compared to Virgo. Feeding clusters are the so called filaments, and the sample we define in Chapter 2 associated to the Coma cluster gives us a large filament sample to compare to the clusters.

So given these environments we have sampled, can we see any evidence for the origin of morphology segregation that has occurred within them? In Chapter 6 we show that sSFR is suppressed within the Coma cluster compared to the filament for late-type galaxies. We also show that the gas-to-stars ratio is also reduced. This possibly suggests that these galaxies have had a significant amount of their gas removed and thus a reduction in star formation efficiency has occurred as a result. I also show that the mean stellar masses of late-types have also increased, and make the argument that late-types can only have higher stellar masses and lower sSFRs if they formed earlier, and thus would have lower gas-to-stars ratios as they have had more time to convert gas into stars. Thus, it is non-trivial to separate nature vs nurture as potential theories explaining the properties of galaxies in different environments.

In Chapter 7 I use Schechter function fits to calculate the mass density ratios of different environments for gas-to-stars and dust-to-stars, and I show that dust-to-stellar density is invariant with environment. However, all 3 clusters and the filament sample have a lower gas-to-stellar mass density when compared to a field sample, but all appear identical to each other. This shows that the filament is gas deficient, suggesting that gas is affected well before entry into the cluster environment, and that overall amount of dust is difficult to affect.

In Chapters 4 and 5 I show that there is a difference in the FIR properties of late-type galaxies (using a KS test) between the filament and the field. A KS test cannot separate any of the clusters or the filament samples in their FIR properties. In Chapter 5 I show that the effective yield of the galaxies in the filament and Coma cluster are identical, further showing that the change associated with global environment is very subtle if there is any change at all.

In Chapter 5, I also show that velocity dispersion of the late-types is the same as that of the cluster as a whole. This implies that the late-types have been in the cluster environment for longer than a crossing time (1 Gyr), which is over 25$\times$ the viscous stripping timescale. This would suggest that viscous stripping is not capable, in the Coma cluster, of removing the dust. And as dust is co-located with the molecular gas (see Chapter 4), it is reasonable to presume that viscous stripping cannot remove molecular gas - the fuel for continued star formation.

Therefore, with regards to the morphology-density relation, I have found that any change in late-types' FIR properties has occurred well before entry into the cluster environment. However, there is a strong change in the fraction of late-to-early types between the cluster and the filament and at most a weak change in dust mass suggesting that stripping of the ISM only affects the atomic gas which is far more loosely bound than the dust. As we discuss in the introduction, if HI is removed by the cluster environment it could prove catastrophic for star formation. As Larson et al. (1980) proposed, a galaxy requires inflow of gas from an extended gas reservoir, because on a time scale of a few Gyrs star formation would exhaust the available gas and thus shut down star formation, producing 'red-and-dead' early-type galaxies via so called 'starvation'. The simple models of Edmunds & Eales (1998) show that for a large change in gas fraction, dust-to-stellar mass is constant. Thus, gas could be removed from the outskirts of a galaxy leading to it exhausting the available gas - suppressing star formation - without a significant change in its dust-to-stars ratio. Therefore, my findings in this thesis would be consistent with the theory of 'starvation' as a method of transforming the population of late-type galaxies without significantly altering the FIR properties of my samples.

8.3 Concluding Remarks

The *Herschel Space Observatory* has enabled astronomers to examine the coldest dusty phase of the ISM in Galaxies. I hope that my contribution - creating comprehensive catalogues of dust mass and flux density measurements in Fornax, Coma and the Filament - will be of great legacy value for many years to come.

Part IV

Supporting Information

Appendix A
Data Tables - Fornax

OBJECT	RA h:m:s (J2000)	Dec. d:m:s (J2000)	Type	Dust Temperature K	Duss Mass $\log(M_{Dust}/\mathrm{M}_{\odot})$	Stellar Mass $\log(M_{Stars}/\mathrm{M}_{\odot})$
FCC 48	03:26:42	-34:32:57	dE	8.78 (1.04)	6.48 (0.26)	7.93
FCC 67	03:28:48	-35:10:45	Sc	17.32 (0.56)	6.86 (0.05)	9.45
FCC 90	03:31:08	-36:17:27	E	20.32 (0.77)	5.6 (0.08)	8.98
FCC 113	03:33:06	-34:48:27	Scd	16.29 (1.43)	5.73 (0.14)	8.88
FCC 121	03:33:36	-36:08:17	Sbc	22.85 (0.44)	8.25 (0.03)	11.16
FCC 167	03:36:27	-34:58:31	S0	25.77 (0.88)	6.07 (0.04)	10.98
FCC 179	03:36:46	-35:59:58	Sa	23.67 (0.79)	6.78 (0.04)	10.5
FCC 184	03:36:57	-35:30:23	S0	24.52 (0.69)	6.56 (0.04)	10.77
FCC 215	03:38:37	-35:45:27	dE	15.64 (0.08)	5.23 (0.84)	6.87
FCC 235	03:40:09	-35:37:34	Im	15.78 (1.35)	6.62 (0.12)	9.78
FCC 261	03:41:21	-33:46:12	Irr	11.25 (0.73)	6.13 (0.15)	8.58
FCC 263	03:41:32	-34:53:22	SBcd	21.43 (0.8)	6.21 (0.06)	9.2
FCC 267	03:41:45	-33:47:29	Sm	15.42 (0.82)	5.49 (0.12)	8.48
FCC 282	03:42:45	-33:55:13	Im	18.04 (0.8)	5.83 (0.09)	9.0
FCC 285	03:43:02	-36:16:24	Sd	12.87 (0.94)	6.83 (0.14)	9.38
FCC 290	03:43:37	-35:51:14	Sc	19.08 (0.45)	7.01 (0.04)	10.1
FCC 306	03:45:45	-36:20:50	SBm	13.1 (1.31)	5.79 (0.25)	8.68
FCC 308	03:45:54	-36:21:31	Sd	17.22 (0.53)	6.76 (0.06)	9.39
FCC 312	03:46:18	-34:56:33	Scd	20.35 (0.55)	7.25 (0.04)	10.04
FCC 313	03:46:33	-34:41:12	dS0	8.76 (0.77)	6.52 (0.19)	7.78
FCC 332	03:49:49	-35:56:45	E	14.93 (1.62)	5.34 (0.24)	8.63
FCC 335	03:50:36	-35:54:36	E	18.55 (0.96)	5.54 (0.11)	9.21

Table A.1. 22 HeFoCS galaxies dust masses and temperetures given from fitting a modified blackbody ($\beta = 2$ emissivity) to 3 *Herschel* bands or more.

OBJECT	RA h:m:s (J2000)	Dec. d:m:s (J2000)	S_{500} (mJy)	E_{500} (mJy)	S_{350} (mJy)	E_{350} (mJy)	S_{250} (mJy)	E_{250} (mJy)	S_{160} (mJy)	E_{160} (mJy)	S_{100} (mJy)	E_{100} (mJy)
FCC 32	03:24:52	-35:26:08	0	24	42	11	93	15	-	-	-	-
FCC 34	03:25:02	-35:13:24	0	21	0	15	0	14	-	-	-	-
FCC 42	03:25:46	-35:30:29	0	22	0	19	0	16	-	-	-	-
FCC 44	03:26:07	-35:07:45	0	23	20	6	14	4	0	33	0	12
FCC 45	03:26:13	-34:33:15	0	31	0	22	0	15	-	-	-	-
FCC 47	03:26:32	-35:42:50	0	19	0	16	0	15	-	-	-	-
FCC 48	03:26:42	-34:32:57	26	8	30	7	27	5	-	-	-	-
FCC 50	03:26:53	-35:31:12	0	22	0	16	0	14	0	22	0	18
FCC 55	03:27:17	-34:31:37	0	22	0	23	0	15	-	-	-	-
FCC 56	03:27:21	-36:08:50	0	20	0	19	0	13	-	-	-	-
FCC 57	03:27:27	-35:55:26	0	20	0	18	0	12	-	-	-	-
FCC 65	03:28:06	-35:14:12	0	20	0	17	0	13	0	24	0	15
FCC 67	03:28:48	-35:10:45	414	40	921	74	1759	131	2220	317	1257	199
FCC 69	03:28:55	-36:26:13	0	26	0	23	0	16	-	-	-	-
FCC 71	03:29:26	-35:36:17	0	19	0	22	0	18	0	18	0	11
FCC 72	03:29:33	-35:52:03	0	26	0	15	0	12	0	19	0	10
FCC 73	03:29:34	-36:42:11	0	26	0	24	0	15	-	-	-	-
FCC 75	03:29:38	-35:24:02	0	22	0	20	0	12	0	18	0	13
FCC 77	03:29:41	-36:13:21	0	23	0	15	0	12	0	22	0	15
FCC 79	03:29:44	-36:03:18	0	25	0	21	0	17	0	18	0	10
FCC 78	03:29:45	-35:22:43	0	22	0	20	0	13	0	22	0	12
FCC 82	03:30:30	-34:15:35	0	18	0	21	0	16	0	24	0	13
FCC 83	03:30:34	-34:51:12	0	21	0	19	0	12	0	29	0	12
FCC 84	03:30:36	-35:02:30	0	24	0	41	0	61	0	27	0	8
FCC 85	03:30:46	-35:33:00	0	24	0	19	0	14	0	21	0	13
FCC 86	03:30:46	-35:21:17	0	23	0	17	0	16	0	40	0	12
FCC 90	03:31:08	-36:17:27	23	7	73	16	168	19	385	70	191	30
FCC 92	03:31:16	-34:57:43	0	18	0	17	0	14	0	30	0	16
FCC 93	03:31:19	-35:49:09	0	21	0	20	0	14	0	38	0	17
FCC 94	03:31:22	-34:58:13	0	17	0	19	0	9	0	19	0	14
FCC 95	03:31:24	-35:19:52	0	23	0	17	0	13	0	27	0	10
FCC 98	03:31:39	-36:16:39	0	22	0	17	0	15	0	19	0	11
FCC 99	03:31:44	-34:20:20	0	23	0	17	0	12	0	16	0	13
FCC 101	03:31:47	-35:40:34	0	21	0	20	0	15	0	18	0	12
FCC 100	03:31:47	-35:03:06	0	22	0	20	0	18	0	18	0	12
FCC 102	03:32:10	-36:13:13	0	20	0	17	0	14	0	20	0	12
FCC 103	03:32:27	-35:46:30	0	18	0	18	0	15	0	25	0	12
FCC 105	03:32:29	-36:05:16	0	22	0	20	0	14	0	22	0	11
FCC 104	03:32:30	-34:20:54	0	26	0	17	0	12	0	21	0	11
FCC 107	03:32:45	-37:50:11	0	20	0	18	0	17	-	-	-	-
FCC 109	03:32:47	-37:38:31	0	22	0	25	0	21	-	-	-	-
FCC 106	03:32:47	-34:14:20	0	24	0	17	0	16	0	24	0	10
FCC 108	03:32:48	-36:09:11	0	24	0	20	0	16	0	17	0	13
FCC 110	03:32:57	-35:44:16	0	22	0	18	0	14	0	21	0	13
FCC 112	03:33:03	-36:26:37	0	18	0	19	0	11	0	20	0	18
FCC 111	03:33:03	-33:43:30	0	25	0	21	0	14	0	34	0	45
FCC 117	03:33:06	-37:50:07	0	31	20	6	30	4	-	-	-	-
FCC 113	03:33:06	-34:48:27	22	6	58	14	117	21	116	29	0	12
FCC 114	03:33:08	-35:23:49	0	21	0	15	0	17	0	20	0	13
FCC 115	03:33:09	-35:43:06	0	23	0	22	0	15	0	25	0	13
FCC 116	03:33:12	-36:01:04	0	18	0	21	0	17	0	25	0	15
FCC 118	03:33:31	-34:27:21	0	22	0	17	0	18	0	17	0	16
FCC 119	03:33:33	-33:34:19	0	25	0	19	0	17	-	-	-	-
FCC 120	03:33:34	-36:36:21	0	24	0	18	0	11	0	18	0	13
FCC 121	03:33:36	-36:08:17	16468	464	45915	1274	107161	2785	205802	24769	207789	25002
FCC 123	03:33:43	-35:51:36	0	20	0	14	0	12	0	24	0	15
FCC 125	03:33:48	-35:50:09	0	19	0	15	0	14	0	18	0	16
FCC 124	03:33:49	-34:10:11	0	18	0	19	0	12	0	17	0	12
FCC 126	03:33:55	-34:20:48	0	22	0	18	0	17	0	15	0	14
FCC 127	03:34:06	-35:16:37	0	23	0	16	0	15	0	15	0	11
FCC 128	03:34:07	-36:27:58	0	24	0	18	0	12	0	16	0	13
FCC 129	03:34:07	-36:04:05	0	21	0	17	0	13	0	16	0	11
FCC 130	03:34:08	-35:31:54	0	20	0	16	0	14	0	17	0	13
FCC 131	03:34:12	-35:13:42	0	24	0	16	0	16	0	18	0	17
FCC 132	03:34:18	-35:47:41	0	15	0	15	0	13	0	17	0	10
FCC 133	03:34:20	-35:21:46	0	22	0	21	0	21	0	26	0	13
FCC 134	03:34:21	-34:35:34	0	20	0	15	0	13	0	18	0	13
FCC 136	03:34:29	-35:32:49	0	36	0	17	0	15	0	24	0	8
FCC 135	03:34:30	-34:17:51	0	25	0	19	0	12	0	22	0	17
FCC 137	03:34:44	-35:51:42	0	25	0	15	0	12	0	22	0	11
FCC 138	03:34:51	-36:19:22	0	27	0	15	0	11	0	24	0	11
FCC 140	03:34:56	-35:11:28	0	27	0	19	0	12	0	34	0	14
FCC 142	03:34:58	-35:02:35	0	20	0	18	0	11	0	17	0	15
FCC 143	03:34:59	-35:10:16	0	23	0	19	0	13	0	24	0	12
FCC 144	03:35:00	-35:19:20	0	20	0	21	0	12	0	24	0	9
FCC 145	03:35:05	-35:13:07	0	21	0	11	0	10	0	24	0	11
FCC 146	03:35:11	-35:19:23	0	20	0	17	0	13	0	24	0	11
FCC 147	03:35:16	-35:13:34	0	20	0	12	0	11	0	0	0	11
FCC 148	03:35:16	-35:15:59	0	21	0	19	0	12	0	30	0	16
FCC 149	03:35:23	-36:05:30	0	25	0	17	0	16	0	22	0	14
FCC 150	03:35:24	-36:21:51	0	25	0	23	0	16	0	20	0	31
FCC 151	03:35:25	-36:10:45	0	24	0	16	0	14	0	30	0	11
FCC 154	03:35:30	-35:15:07	0	18	0	19	0	12	0	36	0	10
FCC 153	03:35:30	-34:26:48	0	25	0	25	0	16	0	23	0	13
FCC 155	03:35:34	-34:48:17	0	15	0	15	0	12	0	14	0	13
FCC 157	03:35:42	-35:30:52	0	22	0	20	0	15	0	33	0	14
FCC 156	03:35:42	-35:20:19	0	16	0	14	0	14	0	18	0	12
FCC 158	03:35:46	-35:59:26	0	23	0	19	0	12	0	20	0	8
FCC 159	03:35:55	-34:49:40	0	18	0	14	0	12	0	21	0	12
FCC 161	03:36:03	-35:26:26	0	21	0	18	0	12	0	0	0	13
FCC 160	03:36:04	-35:23:20	0	25	0	16	0	11	0	18	0	10

Continued on next page

OBJECT	RA h:m:s (J2000)	Dec. d:m:s (J2000)	S_{500} (mJy)	E_{500} (mJy)	S_{350} (mJy)	E_{350} (mJy)	S_{250} (mJy)	E_{250} (mJy)	S_{160} (mJy)	E_{160} (mJy)	S_{100} (mJy)	E_{100} (mJy)
FCC 162	03:36:06	-35:25:54	0	22	0	16	0	15	0	14	0	16
FCC 163	03:36:06	-35:50:34	0	17	0	20	0	15	0	22	0	11
FCC 164	03:36:12	-36:10:00	0	28	0	21	0	14	0	19	0	15
FCC 165	03:36:23	-35:54:41	0	25	0	17	0	14	0	20	0	10
FCC 166	03:36:23	-37:09:51	0	34	0	23	0	14	0	21	0	13
FCC 167	03:36:27	-34:58:31	115	17	383	34	1077	83	2302	285	2600	317
FCC 168	03:36:27	-35:12:38	0	19	0	16	0	14	0	19	0	14
FCC 169	03:36:31	-34:48:02	0	19	0	14	0	15	0	23	0	14
FCC 170	03:36:31	-35:17:39	0	22	0	16	0	14	0	16	0	10
FCC 172	03:36:36	-37:21:54	0	35	0	16	0	15	0	21	0	10
FCC 171	03:36:41	-35:23:35	0	22	0	17	0	14	0	18	0	10
FCC 175	03:36:42	-35:26:02	0	23	0	18	0	13	0	14	0	12
FCC 173	03:36:43	-34:09:33	0	22	0	20	0	13	0	22	0	15
FCC 176	03:36:45	-36:15:19	0	24	0	18	0	14	0	19	0	18
FCC 179	03:36:46	-35:59:58	618	58	1609	120	4072	292	8208	1007	8593	1039
FCC 177	03:36:47	-34:44:22	0	19	21	5	32	8	0	23	0	12
FCC 178	03:36:48	-34:16:49	0	23	0	17	0	13	0	23	0	10
FCC 180	03:36:49	-36:13:48	0	25	0	17	0	12	0	19	0	10
FCC 183	03:36:52	-36:29:10	0	22	0	17	0	12	0	23	0	10
FCC 181	03:36:53	-34:56:19	0	23	0	14	0	12	0	18	0	13
FCC 182	03:36:53	-35:22:28	0	22	0	21	0	14	0	21	0	13
FCC 184	03:36:57	-35:30:23	348	31	1113	86	2870	204	6177	747	5916	716
FCC 185	03:37:02	-34:52:32	0	21	0	15	0	14	0	19	0	12
FCC 188	03:37:04	-35:35:25	0	22	0	13	0	17	0	14	0	10
FCC 187	03:37:04	-34:36:08	0	20	0	21	0	15	0	14	0	11
FCC 190	03:37:09	-35:11:43	0	26	0	23	0	18	0	24	0	15
FCC 191	03:37:10	-35:23:13	0	21	0	17	0	13	0	22	0	15
FCC 192	03:37:10	-35:53:18	0	23	0	16	0	14	0	23	0	15
FCC 193	03:37:11	-35:44:42	0	20	0	18	0	15	0	21	0	36
FCC 194	03:37:17	-35:41:57	0	20	0	16	0	13	0	18	0	11
FCC 195	03:37:23	-34:53:57	0	20	0	18	0	13	0	26	0	11
FCC 196	03:37:34	-35:49:46	0	21	0	14	0	12	0	36	0	13
FCC 197	03:37:41	-35:17:45	0	24	0	20	0	18	0	20	0	13
FCC 198	03:37:42	-37:12:31	36	6	0	19	20	4	0	18	0	13
FCC 199	03:37:43	-36:43:35	0	19	0	16	0	13	0	23	0	12
FCC 201	03:37:53	-37:16:48	0	17	0	17	0	15	0	19	0	15
FCC 200	03:37:54	-34:52:56	0	23	0	20	0	13	0	25	0	10
FCC 202	03:38:06	-35:26:25	0	26	0	20	0	16	0	26	0	6
FCC 203	03:38:09	-34:31:08	0	20	0	17	0	11	0	19	0	10
FCC 206	03:38:13	-37:17:24	0	17	23	6	24	5	0	19	0	14
FCC 204	03:38:13	-33:07:38	0	25	0	15	0	12	0	22	0	13
FCC 208	03:38:18	-35:31:51	0	19	0	20	0	18	0	12	0	10
FCC 207	03:38:19	-35:07:45	0	18	0	16	32	9	0	29	14	4
FCC 210	03:38:19	-36:03:57	0	26	0	20	0	15	0	19	0	14
FCC 212	03:38:21	-36:24:49	0	20	0	17	0	14	0	20	0	15
FCC 211	03:38:21	-35:15:35	0	22	0	16	0	13	0	19	0	12
FCC 209	03:38:22	-33:39:37	0	23	0	16	0	11	0	25	0	11
FCC 213	03:38:28	-35:26:58	0	105	0	149	0	141	0	25	0	12
FCC 214	03:38:36	-35:50:03	0	24	0	15	0	12	0	19	0	13
FCC 215	03:38:37	-35:45:27	22	7	26	5	22	5	0	24	14	4
FCC 216	03:38:39	-36:33:30	0	22	0	22	0	16	0	22	0	11
FCC 217	03:38:41	-36:43:38	0	25	0	17	0	17	0	20	0	14
FCC 218	03:38:45	-35:15:59	0	20	0	15	0	13	0	20	0	9
FCC 219	03:38:51	-35:35:36	0	18	0	18	0	16	0	20	0	18
FCC 220	03:38:55	-35:14:12	0	22	0	15	0	14	0	28	0	14
FCC 221	03:39:05	-36:05:57	0	23	0	19	0	15	0	21	0	11
FCC 222	03:39:13	-35:22:18	0	17	0	19	0	14	0	20	0	13
FCC 223	03:39:19	-35:43:29	0	20	0	15	0	11	0	27	0	11
FCC 225	03:39:37	-36:33:13	0	17	0	18	0	13	0	45	0	12
FCC 226	03:39:50	-35:01:15	0	18	0	17	0	12	0	19	0	11
FCC 227	03:39:50	-35:31:21	0	26	0	17	0	14	0	28	0	13
FCC 228	03:39:51	-35:19:20	0	17	0	17	0	14	0	22	0	12
FCC 229	03:39:55	-35:39:44	0	21	0	20	0	13	0	21	0	11
FCC 230	03:40:01	-34:45:30	0	19	0	17	0	16	0	25	0	11
FCC 231	03:40:04	-34:10:04	0	17	0	17	0	18	0	18	0	13
FCC 235	03:40:09	-35:37:34	207	28	406	45	695	66	1080	199	14	3
FCC 236	03:40:09	-35:50:10	0	18	0	18	0	10	0	18	0	15
FCC 234	03:40:09	-34:26:49	0	20	0	14	0	13	0	22	0	11
FCC 238	03:40:17	-36:32:05	0	19	0	16	0	9	0	19	0	13
FCC 239	03:40:18	-37:29:58	0	16	0	16	0	16	0	22	0	11
FCC 237	03:40:18	-33:25:17	0	25	0	15	0	16	0	22	0	8
FCC 241	03:40:23	-35:16:36	0	21	0	17	0	16	0	28	0	8
FCC 243	03:40:27	-36:29:57	0	21	0	19	0	16	0	22	0	15
FCC 244	03:40:30	-35:52:40	0	18	0	18	0	13	0	20	0	11
FCC 245	03:40:33	-35:01:23	0	20	0	17	0	15	0	18	0	12
FCC 246	03:40:37	-36:07:16	0	23	0	18	0	12	0	20	0	11
FCC 249	03:40:42	-37:30:39	0	53	0	19	0	20	0	16	0	11
FCC 247	03:40:42	-35:39:40	0	21	0	18	0	13	0	19	0	12
FCC 248	03:40:43	-35:51:40	0	16	0	17	0	14	0	17	0	12
FCC 250	03:40:44	-37:24:31	0	17	0	19	0	16	0	15	0	12
FCC 251	03:40:49	-35:01:25	0	20	0	18	0	13	0	20	0	10
FCC 252	03:40:50	-35:44:55	0	21	0	43	0	15	0	19	0	12
FCC 254	03:41:00	-35:44:34	0	18	0	18	0	12	0	20	0	9
FCC 255	03:41:03	-33:46:43	0	19	0	20	0	14	0	16	0	10
FCC 256	03:41:03	-34:57:16	0	17	0	16	0	12	0	21	0	15
FCC 258	03:41:07	-35:41:25	0	22	0	19	0	14	0	24	0	13
FCC 259	03:41:07	-35:30:52	0	22	0	19	0	18	0	19	0	16
FCC 260	03:41:13	-35:09:30	0	20	0	13	0	14	0	32	0	15
FCC 261	03:41:21	-33:46:12	20	6	43	11	63	12	22	7	0	9
FCC 262	03:41:21	-35:56:56	0	17	0	19	0	13	0	32	0	11
FCC 264	03:41:31	-35:35:23	0	23	0	21	0	12	0	19	0	11

Continued on next page

OBJECT	RA h:m:s (J2000)	Dec. d:m:s (J2000)	S_{500} (mJy)	E_{500} (mJy)	S_{350} (mJy)	E_{350} (mJy)	S_{250} (mJy)	E_{250} (mJy)	S_{160} (mJy)	E_{160} (mJy)	S_{100} (mJy)	E_{100} (mJy)
FCC 263	03:41:32	-34:53:22	139	19	359	37	787	62	1408	184	1262	169
FCC 266	03:41:41	-35:10:13	0	18	0	14	0	16	0	21	0	11
FCC 265	03:41:42	-33:29:04	0	22	0	18	0	17	0	17	0	9
FCC 267	03:41:45	-33:47:29	0	17	28	5	50	11	0	25	17	4
FCC 268	03:41:49	-36:37:51	0	15	0	15	0	12	0	20	0	13
FCC 269	03:41:57	-35:17:32	0	27	0	22	0	11	0	33	0	12
FCC 271	03:42:06	-34:50:58	0	24	0	17	0	14	0	15	0	12
FCC 272	03:42:10	-35:26:32	0	21	0	19	0	12	0	20	0	15
FCC 273	03:42:15	-34:27:20	0	23	0	18	0	12	0	20	0	14
FCC 274	03:42:17	-35:32:27	0	17	0	15	0	11	0	17	0	13
FCC 275	03:42:19	-35:33:38	0	18	0	14	0	13	0	17	0	17
FCC 276	03:42:19	-35:23:37	0	27	0	19	0	14	-	-	-	-
FCC 277	03:42:22	-35:09:12	0	23	0	22	0	14	0	29	0	11
FCC 279	03:42:26	-36:41:14	0	19	0	16	0	13	0	18	0	20
FCC 278	03:42:27	-33:52:15	0	19	0	15	0	14	0	22	0	12
FCC 280	03:42:36	-35:57:21	0	22	0	19	0	14	0	21	0	14
FCC 281	03:42:38	-35:52:04	0	23	0	16	0	11	0	23	0	15
FCC 282	03:42:45	-33:55:13	40	13	97	16	192	21	258	53	147	27
FCC 284	03:42:55	-35:20:36	0	27	0	16	0	15	0	26	0	12
FCC 285	03:43:02	-36:16:24	200	34	348	52	465	55	460	96	19	3
FCC 286	03:43:12	-34:38:35	0	24	0	17	0	12	0	30	0	14
FCC 288	03:43:22	-33:56:20	0	21	0	15	0	14	0	17	0	15
FCC 289	03:43:23	-34:41:43	0	24	0	20	0	17	0	21	0	11
FCC 290	03:43:37	-35:51:14	610	54	1706	129	3899	281	5616	749	3008	421
FCC 291	03:43:39	-35:12:58	0	25	0	21	0	14	0	16	0	12
FCC 293	03:44:25	-35:51:25	0	20	0	16	0	10	0	20	0	11
FCC 294	03:44:27	-35:39:52	0	23	0	15	0	14	0	21	0	13
FCC 295	03:44:30	-35:10:42	0	30	0	24	0	14	0	23	0	15
FCC 296	03:44:32	-35:11:46	0	27	0	22	0	17	0	20	0	11
FCC 297	03:44:39	-35:58:57	0	20	0	22	0	12	0	15	0	13
FCC 298	03:44:44	-35:41:02	0	22	0	19	0	19	0	15	0	20
FCC 299	03:44:58	-36:53:43	0	24	0	20	0	16	0	21	0	10
FCC 300	03:44:59	-36:19:11	0	24	0	19	0	13	0	23	0	15
FCC 301	03:45:03	-35:58:23	0	20	0	17	0	19	0	14	0	10
FCC 302	03:45:12	-35:34:14	0	25	0	15	0	14	0	26	0	21
FCC 304	03:45:30	-34:30:18	0	21	0	21	0	13	0	20	0	13
FCC 306	03:45:45	-36:20:50	26	7	35	6	68	14	20	6	19	3
FCC 307	03:45:47	-35:03:38	0	21	0	19	0	15	0	22	0	10
FCC 308	03:45:54	-36:21:31	341	38	740	69	1408	111	1624	212	983	133
FCC 310	03:46:13	-36:41:47	0	24	0	18	0	13	0	22	0	7
FCC 312	03:46:18	-34:56:33	1338	107	3448	250	7650	545	12081	1466	9806	1202
FCC 313	03:46:33	-34:41:12	26	7	37	5	29	4	0	20	0	12
FCC 316	03:47:01	-36:26:17	0	25	25	6	26	3	0	31	0	9
FCC 318	03:47:08	-36:19:39	0	23	0	23	0	14	0	20	0	12
FCC 321	03:47:33	-35:57:09	0	23	0	18	0	13	0	28	0	11
FCC 323	03:47:37	-36:21:49	0	19	0	21	0	13	0	20	0	14
FCC 324	03:47:52	-36:28:17	0	18	0	15	0	15	0	20	0	34
FCC 325	03:48:02	-35:01:36	0	18	0	17	0	15	0	18	0	14
FCC 328	03:48:22	-36:06:25	0	18	0	17	0	12	0	21	0	17
FCC 329	03:48:55	-35:57:11	0	15	0	13	0	12	0	19	0	16
FCC 330	03:49:13	-35:55:37	0	17	0	15	0	13	0	13	0	15
FCC 332	03:49:49	-35:56:45	0	14	18	6	47	11	22	6	14	4
FCC 333	03:49:58	-36:05:18	0	21	0	19	0	18	0	21	0	12
FCC 334	03:50:23	-35:14:53	0	20	0	16	0	19	0	22	0	14
FCC 335	03:50:36	-35:54:36	26	6	46	12	108	18	171	38	93	19

Table A.2. 5 band FIR fluxes, uncertainties and upperlimits for FCC galaxies. If flux density is equal to zero, then E_{band} represents an upper-limit for the galaxy in question, the upper-limit is calculated from the 3σ noise in the PSF convolved map. Some PACS fluxes are not measured and denoted by a (-) symbol.

Appendix B

Data Tables - Coma

OBJECT	RA h:m:s (J2000)	Dec. d:m:s (J2000)	S_{500} (mJy)	E_{500} (mJy)	S_{350} (mJy)	E_{350} (mJy)	S_{250} (mJy)	E_{250} (mJy)	S_{160} (mJy)	E_{160} (mJy)	S_{100} (mJy)	E_{100} (mJy)
CCC001	12:51:40	+28:03:11	0	20	0	19	0	17	0	27	0	23
CCC002	12:51:43	+27:57:46	0	21	32	7	54	8	0	28	0	18
CCC003	12:51:53	+27:58:40	23	7	24	6	32	7	0	27	0	17
CCC004	12:52:05	+27:35:46	0	26	0	21	0	23	0	29	0	20
CCC005	12:52:37	+27:19:30	0	32	0	29	0	19	0	30	0	18
CCC006	12:52:46	+27:54:24	0	26	0	23	0	19	0	25	0	22
CCC007	12:52:48	+27:24:06	37	9	99	12	289	33	535	80	474	64
CCC008	12:52:50	+27:44:45	0	23	0	24	0	20	0	27	0	20
CCC009	12:52:53	+28:22:16	446	47	1238	124	3015	289	5620	680	4940	597
CCC010	12:52:56	+28:48:43	0	32	0	22	0	16	0	28	0	18
CCC011	12:53:04	+27:27:52	0	19	0	18	0	20	0	25	0	18
CCC012	12:53:07	+27:02:17	0	24	0	14	0	17	0	24	0	22
CCC013	12:53:11	+27:50:16	0	22	0	19	0	17	0	33	0	17
CCC014	12:53:12	+27:19:23	0	17	0	24	0	14	0	30	0	22
CCC015	12:53:12	+28:00:14	0	22	0	19	0	19	0	28	0	18
CCC016	12:53:16	+27:05:39	0	23	0	21	0	24	0	29	0	118
CCC017	12:53:18	+28:12:41	0	20	0	21	0	18	0	30	0	19
CCC018	12:53:23	+27:02:00	0	24	26	7	39	6	0	23	0	20
CCC019	12:53:23	+27:30:47	0	23	0	19	0	20	0	24	0	18
CCC020	12:53:30	+27:40:30	0	22	0	17	0	19	0	27	0	25
CCC021	12:53:31	+27:27:48	0	26	0	20	0	18	0	26	0	26
CCC022	12:53:35	+27:45:31	0	27	0	21	0	20	0	30	0	19
CCC023	12:53:37	+27:47:03	0	31	0	20	0	18	0	29	0	16
CCC024	12:53:44	+27:46:51	0	28	0	25	0	19	0	27	0	16
CCC025	12:53:45	+27:14:58	0	21	0	25	0	19	0	30	0	24
CCC026	12:53:46	+27:23:08	0	24	54	9	110	11	0	13	0	8
CCC027	12:53:49	+28:56:33	0	26	0	21	0	20	0	36	0	19
CCC028	12:53:51	+28:58:45	58	10	158	17	430	45	691	92	483	67
CCC029	12:53:53	+28:11:11	29	8	93	11	254	31	239	40	194	35
CCC030	12:53:54	+26:57:59	0	23	0	20	0	20	0	27	0	20
CCC031	12:53:55	+28:23:37	0	24	0	16	0	19	0	25	0	21
CCC032	12:54:05	+27:04:07	0	26	0	22	0	16	0	29	0	21
CCC033	12:54:05	+27:01:08	0	21	0	18	0	18	0	25	0	19
CCC034	12:54:06	+29:14:33	0	27	0	22	0	19	0	25	0	19
CCC035	12:54:07	+27:12:59	0	24	0	22	0	20	0	24	0	18
CCC036	12:54:09	+28:05:33	0	22	0	23	0	17	0	23	0	19
CCC037	12:54:16	+27:18:13	0	27	0	24	0	16	0	31	0	23
CCC038	12:54:16	+28:04:35	0	21	0	23	0	18	0	26	0	20
CCC039	12:54:19	+28:05:28	0	22	0	23	0	16	0	24	0	21
CCC040	12:54:22	+27:05:03	0	26	0	22	0	20	0	27	0	16
CCC041	12:54:22	+27:44:40	0	29	0	21	0	17	0	33	0	16
CCC042	12:54:22	+26:47:58	0	23	0	21	0	14	0	30	0	21
CCC043	12:54:24	+27:21:50	0	25	0	22	0	19	0	28	0	24
CCC044	12:54:32	+28:22:36	0	20	0	20	0	16	0	26	0	23
CCC045	12:54:33	+27:37:57	80	10	253	24	651	65	910	116	642	86
CCC046	12:54:35	+26:45:05	0	19	0	16	0	16	0	30	0	20
CCC047	12:54:36	+26:56:05	0	22	0	18	0	18	0	23	0	21
CCC048	12:54:37	+27:19:03	0	25	0	22	0	20	0	32	0	23
CCC049	12:54:37	+27:41:31	0	26	0	23	0	19	0	25	0	20
CCC050	12:54:41	+27:02:29	0	26	0	23	0	21	0	22	0	19
CCC051	12:54:41	+28:02:45	0	21	0	20	0	15	0	30	0	21
CCC052	12:54:42	+27:38:20	0	26	0	19	0	16	0	27	0	19
CCC053	12:54:43	+27:27:19	0	25	0	23	0	19	0	30	0	18
CCC054	12:54:44	+27:24:39	0	25	0	24	0	19	0	43	0	18
CCC055	12:54:51	+27:29:40	0	25	0	20	0	21	0	24	0	27
CCC056	12:54:52	+26:34:33	0	15	0	24	0	14	0	24	0	22
CCC057	12:54:53	+28:25:01	59	9	155	26	281	33	536	77	376	57

Continued on next page

OBJECT	RA h:m:s (J2000)	Dec. d:m:s (J2000)	S_{500} (mJy)	E_{500} (mJy)	S_{350} (mJy)	E_{350} (mJy)	S_{250} (mJy)	E_{250} (mJy)	S_{160} (mJy)	E_{160} (mJy)	S_{100} (mJy)	E_{100} (mJy)
CCC058	12:54:55	+27:24:45	41	8	135	14	364	39	686	93	454	64
CCC059	12:54:55	+29:00:44	0	20	0	19	0	19	0	23	0	19
CCC060	12:54:55	+28:04:00	0	21	0	14	0	19	0	24	0	19
CCC061	12:54:56	+28:07:34	0	19	0	21	0	21	0	23	0	22
CCC062	12:54:57	+28:18:30	0	17	0	18	0	19	0	24	0	22
CCC063	12:55:00	+27:11:37	0	24	0	21	0	15	0	26	0	22
CCC064	12:55:00	+27:29:00	0	27	0	20	48	7	0	8	0	34
CCC065	12:55:04	+28:03:45	0	23	0	17	0	15	0	27	0	20
CCC066	12:55:05	+26:43:27	0	22	40	7	83	9	0	9	0	8
CCC067	12:55:13	+27:42:32	0	26	0	18	0	22	0	27	0	20
CCC068	12:55:15	+28:15:07	0	23	0	21	0	17	0	33	0	24
CCC069	12:55:19	+27:55:30	0	26	0	18	0	15	0	28	0	24
CCC070	12:55:20	+27:52:00	0	32	0	25	0	14	0	23	0	21
CCC071	12:55:20	+26:47:59	0	23	0	22	23	5	0	37	0	7
CCC072	12:55:20	+27:08:58	0	26	0	14	0	19	0	34	0	22
CCC073	12:55:20	+27:40:08	0	24	0	21	0	18	0	27	0	22
CCC074	12:55:22	+28:28:04	0	25	0	27	0	16	0	30	0	22
CCC075	12:55:24	+27:16:49	0	25	0	21	0	18	0	31	0	18
CCC076	12:55:24	+28:34:16	0	24	0	26	0	13	0	16	0	12
CCC077	12:55:25	+27:47:52	0	22	22	6	48	7	0	11	0	24
CCC078	12:55:26	+27:36:14	0	24	0	22	0	17	0	27	0	28
CCC079	12:55:26	+27:25:21	0	27	0	23	0	26	0	27	0	18
CCC080	12:55:27	+27:39:22	0	28	0	20	0	19	0	29	0	22
CCC081	12:55:28	+27:56:58	0	27	0	24	0	18	0	29	0	24
CCC082	12:55:29	+27:31:17	0	22	0	19	0	19	0	24	0	21
CCC083	12:55:30	+27:32:39	0	23	0	18	0	16	0	29	0	22
CCC084	12:55:34	+27:50:30	0	26	0	22	0	21	0	26	0	23
CCC085	12:55:35	+27:46:01	0	19	0	21	0	23	0	23	0	20
CCC086	12:55:36	+26:33:51	0	24	0	17	0	20	0	29	0	21
CCC087	12:55:36	+26:54:41	0	26	0	24	0	19	0	28	0	22
CCC088	12:55:37	+26:38:31	0	20	0	19	0	19	0	29	0	18
CCC089	12:55:41	+27:15:02	0	26	0	21	0	18	0	33	0	21
CCC090	12:55:44	+27:42:59	0	20	0	20	0	23	0	26	0	20
CCC091	12:55:45	+27:47:46	0	15	0	24	0	17	0	28	0	19
CCC092	12:55:47	+28:15:22	32	9	116	13	269	26	577	79	337	52
CCC093	12:55:49	+27:54:21	0	23	0	21	0	17	0	23	0	19
CCC094	12:55:49	+27:45:06	0	18	0	23	0	19	0	23	0	22
CCC095	12:55:49	+27:05:19	0	26	0	23	0	18	0	27	0	18
CCC096	12:55:56	+27:36:35	0	23	0	18	0	17	0	22	0	17
CCC097	12:55:57	+27:54:17	0	25	0	28	0	22	0	24	0	19
CCC098	12:55:58	+28:24:26	0	28	0	26	0	14	0	25	0	20
CCC099	12:55:59	+27:57:18	0	25	0	19	0	23	0	25	0	20
CCC100	12:55:59	+28:11:13	0	29	0	26	0	23	0	19	0	17
CCC101	12:56:01	+28:02:18	0	29	0	21	0	18	0	29	0	19
CCC102	12:56:01	+26:45:23	0	27	0	23	0	19	0	28	0	23
CCC103	12:56:01	+27:39:52	0	19	0	19	0	18	0	27	0	21
CCC104	12:56:01	+26:55:14	0	28	0	21	0	20	0	25	0	20
CCC105	12:56:02	+28:02:52	0	31	0	20	0	19	0	28	0	19
CCC106	12:56:03	+28:26:05	0	24	0	29	0	14	0	27	0	20
CCC107	12:56:03	+27:09:01	0	28	0	23	0	19	0	30	0	22
CCC108	12:56:04	+27:17:07	0	24	0	21	0	20	0	31	0	18
CCC109	12:56:06	+27:40:41	54	8	121	13	297	28	771	105	893	112
CCC110	12:56:06	+27:38:52	0	21	0	19	0	13	0	22	0	21
CCC111	12:56:09	+28:18:39	0	29	0	22	0	16	0	27	0	19
CCC112	12:56:09	+27:50:39	0	23	0	23	0	19	0	40	0	24
CCC113	12:56:10	+28:09:47	41	9	126	13	325	31	730	97	654	85
CCC114	12:56:11	+29:23:53	0	28	39	7	39	8	0	33	0	19
CCC115	12:56:14	+27:48:56	0	23	0	26	0	19	0	31	0	23
CCC116	12:56:14	+27:30:22	0	24	0	19	0	14	0	24	0	17
CCC117	12:56:16	+27:26:45	0	29	0	17	0	16	0	33	0	21
CCC118	12:56:18	+26:21:32	0	23	35	7	73	9	240	42	224	38
CCC119	12:56:19	+27:45:03	0	22	0	19	0	23	0	28	0	17
CCC120	12:56:20	+29:18:00	0	32	0	22	0	18	0	25	0	23
CCC121	12:56:20	+28:03:02	0	29	0	22	0	17	0	26	0	17
CCC122	12:56:20	+26:42:14	0	21	0	21	0	18	0	26	0	18
CCC123	12:56:21	+28:29:12	0	20	0	20	0	17	0	32	0	18
CCC124	12:56:23	+27:32:38	0	21	0	16	0	18	0	33	0	17
CCC125	12:56:23	+27:14:02	0	24	0	21	0	18	0	32	0	17
CCC126	12:56:26	+27:43:38	0	20	0	18	0	18	0	22	0	20
CCC127	12:56:26	+27:49:50	0	24	0	29	0	18	0	25	0	19
CCC128	12:56:27	+26:59:14	81	12	266	33	629	65	1156	149	693	92
CCC129	12:56:28	+28:04:57	0	33	0	19	0	19	0	25	0	23
CCC130	12:56:28	+27:17:28	67	9	248	37	470	56	510	72	414	61
CCC131	12:56:28	+29:08:13	0	23	25	7	42	7	0	10	0	23
CCC132	12:56:28	+26:32:36	0	18	0	20	0	18	0	25	0	22
CCC133	12:56:29	+26:57:25	0	29	0	16	0	20	0	27	0	21
CCC134	12:56:29	+27:56:24	0	23	0	27	0	19	0	27	0	18
CCC135	12:56:32	+27:03:20	0	24	0	18	0	19	0	27	0	21
CCC136	12:56:34	+27:41:14	0	19	0	17	0	17	0	23	0	22
CCC137	12:56:34	+27:32:20	0	17	0	20	0	17	0	28	0	18
CCC138	12:56:34	+27:13:39	19	6	54	8	118	12	0	11	0	8
CCC139	12:56:35	+28:16:31	0	25	0	21	0	17	0	29	0	21
CCC140	12:56:35	+27:43:07	0	21	0	16	0	17	0	24	0	22
CCC141	12:56:36	+26:54:17	0	25	0	24	0	15	0	26	0	17
CCC142	12:56:36	+27:53:05	0	23	0	25	0	15	0	27	0	17
CCC143	12:56:38	+28:06:22	0	31	0	21	0	22	0	24	0	20
CCC144	12:56:38	+27:34:15	0	17	0	24	0	17	0	25	0	19
CCC145	12:56:38	+28:04:52	0	22	0	18	0	20	0	26	0	21
CCC146	12:56:40	+28:13:03	0	26	0	25	0	21	0	30	0	18
CCC147	12:56:40	+27:26:51	0	24	0	25	0	16	0	23	0	23
CCC148	12:56:42	+27:32:53	0	19	0	24	0	17	0	26	0	17

Continued on next page

OBJECT	RA h:m:s (J2000)	Dec. d:m:s (J2000)	S_{500} (mJy)	E_{500} (mJy)	S_{350} (mJy)	E_{350} (mJy)	S_{250} (mJy)	E_{250} (mJy)	S_{160} (mJy)	E_{160} (mJy)	S_{100} (mJy)	E_{100} (mJy)
CCC149	12:56:42	+28:01:13	0	20	0	21	0	19	0	26	0	17
CCC150	12:56:43	+26:44:31	0	22	0	19	0	18	0	27	0	21
CCC151	12:56:43	+27:02:05	0	23	0	25	0	22	0	26	0	24
CCC152	12:56:43	+27:10:43	0	26	0	23	0	18	0	24	0	17
CCC153	12:56:45	+28:03:05	0	24	0	17	0	17	0	35	0	18
CCC154	12:56:47	+27:03:24	0	23	0	22	0	21	0	24	0	24
CCC155	12:56:47	+27:17:32	0	22	0	26	0	17	0	26	0	19
CCC156	12:56:47	+27:25:15	0	20	0	25	0	17	0	26	0	23
CCC157	12:56:47	+28:11:31	0	26	0	22	0	18	0	22	0	17
CCC158	12:56:49	+27:05:38	31	8	80	10	147	15	210	39	0	8
CCC159	12:56:50	+28:55:47	0	31	0	20	0	20	0	24	0	20
CCC160	12:56:50	+27:37:40	0	22	0	14	0	18	0	21	0	17
CCC161	12:56:51	+26:53:56	49	9	167	17	480	53	913	119	607	79
CCC162	12:56:51	+29:22:41	0	23	0	20	0	18	0	27	0	23
CCC163	12:56:52	+26:29:15	154	27	357	42	803	83	1090	141	720	97
CCC164	12:56:52	+28:11:17	0	27	0	21	0	20	0	22	0	17
CCC165	12:56:53	+27:55:46	0	24	0	23	0	15	0	30	0	17
CCC166	12:56:55	+27:27:44	0	25	0	21	0	18	0	24	0	21
CCC167	12:56:56	+28:37:24	0	31	0	18	0	16	0	22	0	13
CCC168	12:57:01	+29:03:45	0	26	0	22	0	20	0	28	0	18
CCC169	12:57:01	+27:22:19	0	18	0	24	0	18	0	26	0	19
CCC170	12:57:02	+27:39:24	0	19	0	17	0	16	0	22	0	18
CCC171	12:57:04	+27:43:48	0	26	0	20	20	5	0	29	0	20
CCC172	12:57:04	+27:31:33	0	22	0	21	0	16	0	28	0	21
CCC173	12:57:04	+27:46:22	0	26	0	73	0	112	0	139	0	115
CCC174	12:57:04	+26:18:09	0	25	0	27	0	29	0	25	0	20
CCC175	12:57:04	+27:40:38	0	22	0	18	0	15	0	24	0	20
CCC176	12:57:06	+28:57:30	0	23	0	19	0	17	0	30	0	19
CCC177	12:57:07	+27:20:26	0	24	0	25	0	16	0	22	0	21
CCC178	12:57:09	+27:27:59	0	22	0	22	0	17	0	27	0	21
CCC179	12:57:10	+27:24:17	0	20	0	25	0	51	0	28	0	20
CCC180	12:57:11	+29:02:42	0	26	0	19	0	20	0	31	0	26
CCC181	12:57:11	+27:06:12	0	23	0	20	0	17	0	25	0	18
CCC182	12:57:14	+27:15:13	0	20	0	21	0	16	0	35	0	23
CCC183	12:57:15	+26:27:58	0	25	0	21	0	17	0	25	0	20
CCC184	12:57:15	+27:43:47	0	26	0	22	0	17	0	26	0	18
CCC185	12:57:16	+27:37:06	0	18	0	23	0	17	0	26	0	19
CCC186	12:57:17	+28:26:19	0	23	0	19	0	19	0	22	0	19
CCC187	12:57:17	+27:48:39	0	26	0	22	0	17	0	26	0	19
CCC188	12:57:18	+27:44:50	0	28	0	21	0	20	0	35	0	19
CCC189	12:57:18	+26:58:46	0	25	0	26	0	18	0	24	0	21
CCC190	12:57:18	+26:56:15	0	20	0	23	0	16	0	30	0	20
CCC191	12:57:19	+27:36:49	0	18	0	21	0	17	0	26	0	20
CCC192	12:57:19	+26:25:56	0	25	0	17	0	17	0	29	0	19
CCC193	12:57:21	+27:01:22	0	23	0	24	0	16	0	28	0	23
CCC194	12:57:21	+27:28:29	0	22	0	20	0	17	0	30	0	21
CCC195	12:57:21	+27:52:49	0	22	0	20	0	16	0	24	0	17
CCC196	12:57:22	+26:59:15	0	26	0	16	0	16	0	29	0	28
CCC197	12:57:22	+27:29:34	0	21	0	19	0	17	0	30	0	22
CCC198	12:57:23	+27:45:58	0	30	0	23	0	17	0	33	0	18
CCC199	12:57:23	+27:32:59	0	19	0	20	0	19	0	28	0	21
CCC200	12:57:24	+27:29:52	0	17	0	19	0	16	0	31	0	21
CCC201	12:57:25	+28:29:45	0	24	0	21	0	14	0	27	0	18
CCC202	12:57:25	+27:32:46	0	19	0	20	0	17	0	28	0	21
CCC203	12:57:26	+27:39:33	0	25	0	20	0	19	0	29	0	17
CCC204	12:57:26	+26:41:38	0	25	0	25	0	15	0	25	0	21
CCC205	12:57:27	+28:26:22	0	25	0	19	0	18	0	25	0	19
CCC206	12:57:27	+27:38:10	0	24	0	19	0	17	0	37	0	17
CCC207	12:57:28	+27:42:02	0	26	0	21	0	17	0	29	0	18
CCC208	12:57:28	+28:10:35	0	28	0	25	0	23	0	25	0	28
CCC209	12:57:29	+28:11:17	0	28	0	20	0	20	0	23	0	22
CCC210	12:57:30	+27:32:34	0	19	0	20	0	16	0	28	0	18
CCC211	12:57:31	+26:30:43	98	12	387	42	953	94	1715	213	1429	177
CCC212	12:57:31	+28:01:06	0	25	0	23	0	15	0	24	0	14
CCC213	12:57:31	+28:28:37	0	25	0	19	0	17	0	21	0	19
CCC214	12:57:32	+27:36:37	0	26	0	22	0	17	0	30	0	22
CCC215	12:57:33	+28:28:56	0	25	0	21	37	6	0	20	0	16
CCC216	12:57:34	+27:18:37	0	25	0	27	0	18	0	25	0	21
CCC217	12:57:35	+27:29:35	0	22	0	18	0	16	0	30	0	19
CCC218	12:57:36	+27:29:05	0	20	0	18	0	15	0	30	0	20
CCC219	12:57:36	+28:14:00	0	27	0	22	0	19	0	22	0	18
CCC220	12:57:36	+28:04:37	0	25	0	22	0	18	0	29	0	18
CCC221	12:57:36	+27:01:52	0	24	0	22	0	17	0	28	0	19
CCC222	12:57:37	+28:02:25	0	27	0	21	0	17	0	25	0	16
CCC223	12:57:43	+26:51:08	0	29	0	21	0	14	0	38	0	20
CCC224	12:57:43	+27:34:39	0	25	0	23	0	19	0	29	0	20
CCC225	12:57:44	+29:01:13	0	22	0	22	0	18	0	28	0	18
CCC226	12:57:45	+27:54:21	0	26	0	21	0	17	0	24	0	14
CCC227	12:57:45	+29:07:48	0	24	0	28	0	17	0	29	0	19
CCC228	12:57:45	+27:25:45	0	23	0	19	0	18	0	26	0	24
CCC229	12:57:46	+27:45:25	0	28	0	23	0	18	0	30	0	24
CCC230	12:57:46	+28:08:26	0	26	0	21	0	20	0	26	0	22
CCC231	12:57:47	+29:08:58	0	24	0	23	0	14	0	31	0	21
CCC232	12:57:47	+27:49:59	0	26	0	22	0	17	0	28	0	17
CCC233	12:57:47	+27:46:10	0	28	0	25	0	15	0	30	0	21
CCC234	12:57:48	+27:52:59	0	27	0	21	0	19	0	29	0	16
CCC235	12:57:48	+28:10:49	0	29	0	20	0	15	0	23	0	15
CCC236	12:57:49	+28:37:27	0	19	0	17	0	16	0	21	0	13
CCC237	12:57:50	+27:38:37	0	22	0	23	0	18	0	25	0	20
CCC238	12:57:50	+27:52:46	0	28	0	21	0	16	0	30	0	15
CCC239	12:57:50	+27:29:27	0	22	0	21	0	17	0	28	0	15

Continued on next page

OBJECT	RA h:m:s (J2000)	Dec. d:m:s (J2000)	S_{500} (mJy)	E_{500} (mJy)	S_{350} (mJy)	E_{350} (mJy)	S_{250} (mJy)	E_{250} (mJy)	S_{160} (mJy)	E_{160} (mJy)	S_{100} (mJy)	E_{100} (mJy)
CCC240	12:57:52	+27:44:22	0	25	0	19	0	18	0	27	0	19
CCC241	12:57:53	+27:42:26	0	23	0	20	0	17	0	27	0	19
CCC242	12:57:53	+28:29:59	0	22	0	17	0	17	0	26	0	17
CCC243	12:57:54	+27:29:26	29	7	26	6	30	6	0	25	0	6
CCC244	12:57:55	+27:13:55	0	25	0	26	0	18	0	33	0	18
CCC245	12:57:56	+27:22:56	0	23	0	23	0	18	0	22	0	17
CCC246	12:57:56	+27:02:15	25	8	61	8	115	12	0	14	173	30
CCC247	12:57:56	+27:26:33	0	25	0	26	0	67	0	28	0	21
CCC248	12:57:57	+28:03:42	42	10	102	12	294	33	511	71	547	74
CCC249	12:58:00	+27:27:14	0	23	0	24	0	18	0	22	0	20
CCC250	12:58:01	+27:29:22	0	24	0	23	0	16	0	26	0	18
CCC251	12:58:01	+27:51:12	0	21	0	20	0	17	0	31	0	19
CCC252	12:58:02	+26:51:34	0	27	0	20	0	13	0	30	0	17
CCC253	12:58:02	+27:58:42	0	29	0	25	0	19	0	25	0	24
CCC254	12:58:03	+26:54:57	0	24	0	19	0	22	0	28	0	26
CCC255	12:58:03	+27:48:53	0	25	0	18	0	16	0	26	0	18
CCC256	12:58:03	+27:40:56	0	22	0	21	0	18	0	31	0	16
CCC257	12:58:04	+26:22:14	0	28	0	25	0	17	0	34	0	20
CCC258	12:58:05	+28:14:33	158	24	527	56	1279	127	2511	306	2541	310
CCC259	12:58:05	+29:01:02	0	22	0	25	0	15	0	24	0	22
CCC260	12:58:05	+28:22:15	0	31	0	24	0	17	0	31	0	18
CCC261	12:58:06	+27:25:08	0	23	0	23	0	20	0	20	0	18
CCC262	12:58:06	+27:34:36	0	19	0	22	0	18	0	25	0	22
CCC263	12:58:06	+29:02:04	0	20	0	23	0	15	0	19	0	22
CCC264	12:58:07	+26:47:13	0	26	0	19	47	7	0	8	0	8
CCC265	12:58:07	+26:19:36	0	25	0	22	0	21	0	28	0	21
CCC266	12:58:09	+28:42:30	105	11	382	42	879	90	1469	184	935	116
CCC267	12:58:09	+26:39:50	0	22	0	26	0	25	0	31	0	23
CCC268	12:58:09	+27:32:57	0	25	0	21	0	16	0	27	0	19
CCC269	12:58:11	+27:51:36	0	23	0	16	0	16	0	27	0	16
CCC270	12:58:11	+27:56:23	0	29	0	21	0	19	0	27	0	21
CCC271	12:58:11	+27:53:37	0	26	0	23	0	19	0	26	0	21
CCC272	12:58:11	+27:32:32	0	25	0	22	0	17	0	27	0	19
CCC273	12:58:12	+26:23:48	0	24	0	29	0	18	0	31	0	21
CCC274	12:58:13	+28:56:53	0	23	0	27	0	12	0	26	0	15
CCC275	12:58:13	+28:10:57	0	26	0	19	0	16	0	23	0	19
CCC276	12:58:15	+28:31:18	0	21	0	24	0	20	0	25	0	18
CCC277	12:58:15	+27:05:14	0	29	0	20	0	17	0	28	0	22
CCC278	12:58:16	+27:48:09	0	26	0	17	0	13	0	25	0	16
CCC279	12:58:17	+28:02:24	0	22	0	19	0	16	0	26	0	22
CCC280	12:58:18	+27:50:54	0	19	0	26	0	17	0	28	0	17
CCC281	12:58:18	+29:07:43	0	29	0	51	0	145	0	305	0	183
CCC282	12:58:18	+27:18:38	89	22	127	15	309	35	635	87	650	87
CCC283	12:58:19	+27:45:43	0	23	0	18	0	13	0	26	0	18
CCC284	12:58:19	+28:41:54	0	21	0	16	26	4	0	11	0	5
CCC285	12:58:20	+26:55:14	0	25	0	26	0	18	0	26	0	22
CCC286	12:58:20	+27:25:45	0	28	0	21	0	20	0	26	0	21
CCC287	12:58:21	+28:08:55	0	22	0	18	0	12	0	24	0	17
CCC288	12:58:21	+27:58:04	0	26	35	7	84	10	0	10	72	10
CCC289	12:58:21	+27:53:32	0	27	0	19	0	18	0	26	0	21
CCC290	12:58:22	+28:09:07	0	22	0	19	0	14	0	21	0	18
CCC291	12:58:22	+27:53:05	0	27	0	20	0	17	0	26	0	20
CCC292	12:58:23	+28:19:44	0	31	0	21	0	16	0	28	0	18
CCC293	12:58:25	+27:12:00	0	24	0	28	0	15	0	27	0	17
CCC294	12:58:26	+29:36:44	0	22	0	23	0	18	0	35	0	19
CCC295	12:58:27	+27:42:23	0	23	0	21	0	14	0	23	0	18
CCC296	12:58:27	+28:58:26	0	23	0	23	0	14	0	21	0	18
CCC297	12:58:28	+27:33:33	0	26	0	18	0	16	0	37	0	19
CCC298	12:58:29	+28:18:04	0	33	0	18	0	17	0	26	0	16
CCC299	12:58:30	+28:00:53	0	24	0	20	0	18	0	23	0	22
CCC300	12:58:30	+28:51:31	0	16	0	18	0	15	0	18	0	12
CCC301	12:58:30	+28:14:01	0	29	0	17	0	17	0	26	0	18
CCC302	12:58:31	+27:40:24	0	23	0	18	0	17	0	27	0	20
CCC303	12:58:31	+28:02:58	0	25	0	20	0	16	0	27	0	22
CCC304	12:58:32	+27:27:22	0	31	0	22	0	20	0	23	0	24
CCC305	12:58:32	+28:22:40	0	31	0	17	0	16	0	25	0	19
CCC306	12:58:33	+27:21:51	0	25	0	18	0	15	0	28	0	20
CCC307	12:58:33	+27:50:12	0	19	0	26	0	17	0	20	0	22
CCC308	12:58:35	+27:35:47	63	10	227	22	616	58	1636	209	1648	204
CCC309	12:58:36	+28:06:49	0	26	0	19	0	17	0	40	0	15
CCC310	12:58:36	+27:06:14	0	26	0	24	0	21	0	25	0	17
CCC311	12:58:36	+27:50:58	0	21	0	23	0	16	0	24	0	19
CCC312	12:58:37	+27:27:50	0	30	49	8	112	12	291	49	177	33
CCC313	12:58:38	+27:32:38	0	29	0	18	0	14	0	24	0	16
CCC314	12:58:38	+27:00:47	0	24	0	20	44	7	0	41	0	7
CCC315	12:58:38	+27:57:13	0	20	0	19	0	19	0	20	0	21
CCC316	12:58:40	+27:49:36	0	19	0	0	0	16	0	25	0	17
CCC317	12:58:41	+28:11:07	0	28	0	21	0	19	0	25	0	20
CCC318	12:58:43	+28:54:36	0	19	39	7	86	9	0	8	0	6
CCC319	12:58:43	+28:16:57	0	28	0	21	0	16	0	26	0	18
CCC320	12:58:44	+28:02:56	0	26	0	17	0	15	0	24	0	19
CCC321	12:58:45	+27:52:47	0	27	0	19	0	19	0	22	0	17
CCC322	12:58:45	+27:45:14	0	22	0	20	0	15	0	25	0	18
CCC323	12:58:46	+27:51:39	0	19	0	24	0	18	0	21	0	19
CCC324	12:58:47	+27:40:29	0	23	0	17	0	16	0	25	0	19
CCC325	12:58:48	+28:01:07	0	29	0	19	0	14	0	31	0	17
CCC326	12:58:48	+27:48:37	0	19	0	15	0	16	0	28	0	19
CCC327	12:58:48	+28:32:24	0	20	0	20	0	14	0	27	0	15
CCC328	12:58:50	+27:59:43	0	35	0	18	0	15	0	29	0	20
CCC329	12:58:50	+28:05:02	0	25	0	17	0	15	0	23	0	19
CCC330	12:58:50	+28:00:25	0	37	0	15	0	18	0	28	0	17

Continued on next page

OBJECT	RA h:m:s (J2000)	Dec. d:m:s (J2000)	S_{500} (mJy)	E_{500} (mJy)	S_{350} (mJy)	E_{350} (mJy)	S_{250} (mJy)	E_{250} (mJy)	S_{160} (mJy)	E_{160} (mJy)	S_{100} (mJy)	E_{100} (mJy)
CCC331	12:58:52	+27:47:06	0	24	0	19	0	16	0	30	0	17
CCC332	12:58:52	+28:14:01	0	22	0	19	0	19	0	25	0	20
CCC333	12:58:53	+27:48:48	0	21	0	19	0	15	0	32	0	19
CCC334	12:58:53	+28:07:33	0	35	0	21	0	17	0	23	0	17
CCC335	12:58:54	+28:13:22	0	24	0	20	0	19	0	24	0	20
CCC336	12:58:54	+27:47:44	0	25	0	19	0	15	0	30	0	17
CCC337	12:58:55	+27:57:52	0	35	0	18	0	14	0	23	0	19
CCC338	12:58:55	+27:50:00	81	10	277	35	645	79	893	115	726	95
CCC339	12:58:56	+28:27:49	0	21	0	21	0	57	0	32	0	22
CCC340	12:58:56	+27:49:19	0	27	0	29	0	21	0	28	0	21
CCC341	12:58:57	+27:47:07	0	23	0	19	0	18	0	27	0	17
CCC342	12:58:58	+27:35:41	0	28	0	20	0	14	0	21	0	22
CCC343	12:58:59	+27:56:04	0	31	0	16	0	14	0	28	0	19
CCC344	12:59:00	+27:58:02	0	25	0	19	0	22	0	29	0	19
CCC345	12:59:01	+28:13:31	0	24	40	8	106	11	209	37	229	36
CCC346	12:59:01	+26:48:56	32	7	42	7	95	10	0	13	200	34
CCC347	12:59:03	+28:07:25	0	28	0	24	0	20	0	27	0	21
CCC348	12:59:04	+27:57:32	0	27	0	20	0	17	0	27	0	19
CCC349	12:59:04	+26:57:29	0	28	0	19	0	20	0	29	0	19
CCC350	12:59:04	+27:54:39	0	26	0	19	0	19	0	30	0	20
CCC351	12:59:04	+28:03:01	0	28	0	21	0	15	0	38	0	19
CCC352	12:59:06	+27:59:48	0	40	0	19	0	18	0	32	0	18
CCC353	12:59:06	+27:29:37	0	33	0	24	0	20	0	24	0	23
CCC354	12:59:06	+27:46:20	0	25	0	16	0	18	0	23	0	20
CCC355	12:59:07	+27:46:04	0	24	0	14	0	17	0	24	0	17
CCC356	12:59:07	+27:51:17	0	26	0	23	44	7	0	11	0	7
CCC357	12:59:08	+27:47:02	0	30	0	18	0	18	0	23	0	18
CCC358	12:59:08	+28:43:41	0	22	0	17	0	11	0	19	0	12
CCC359	12:59:09	+27:53:51	0	24	0	20	0	18	0	30	0	20
CCC360	12:59:09	+28:02:27	0	26	0	18	0	14	0	44	0	19
CCC361	12:59:09	+27:52:02	0	26	0	22	0	21	0	32	0	18
CCC362	12:59:09	+28:09:52	0	22	0	24	0	20	0	26	0	21
CCC363	12:59:10	+27:37:11	0	29	0	22	0	15	0	29	0	18
CCC364	12:59:11	+28:00:33	0	35	0	20	0	18	0	38	0	17
CCC365	12:59:13	+27:46:28	0	26	0	18	0	18	0	24	0	19
CCC366	12:59:13	+27:24:09	0	31	0	24	0	23	0	29	0	17
CCC367	12:59:13	+28:04:34	0	24	0	20	0	19	0	37	0	18
CCC368	12:59:14	+27:53:44	0	23	0	22	0	17	0	31	0	18
CCC369	12:59:14	+28:15:03	0	26	0	27	0	17	0	27	0	19
CCC370	12:59:15	+27:58:14	0	29	0	18	0	28	0	27	0	28
CCC371	12:59:16	+27:09:29	0	17	0	19	0	16	0	34	0	18
CCC372	12:59:16	+27:06:22	49	9	113	12	343	43	590	79	574	77
CCC373	12:59:18	+26:53:23	0	23	0	21	0	17	0	25	0	21
CCC374	12:59:18	+27:42:56	0	24	0	17	0	12	0	32	0	17
CCC375	12:59:18	+27:30:48	0	28	0	18	0	14	0	22	0	23
CCC376	12:59:18	+27:35:37	0	27	0	20	0	17	0	33	0	23
CCC377	12:59:19	+27:58:24	0	29	0	17	0	21	0	28	0	20
CCC378	12:59:19	+28:05:03	0	30	63	9	158	16	389	58	392	58
CCC379	12:59:20	+27:53:09	0	28	0	21	0	20	0	31	0	18
CCC380	12:59:20	+28:04:27	0	23	0	25	0	17	0	25	0	23
CCC381	12:59:20	+28:11:52	0	21	0	21	0	14	0	28	0	19
CCC382	12:59:20	+27:26:06	0	27	0	19	0	20	0	31	0	23
CCC383	12:59:21	+28:26:29	0	22	0	19	0	16	0	38	0	18
CCC384	12:59:21	+27:58:24	0	1	0	19	0	21	0	26	0	20
CCC385	12:59:22	+26:47:49	0	25	0	21	0	18	0	42	0	19
CCC386	12:59:22	+27:53:48	0	23	0	22	0	18	0	28	0	19
CCC387	12:59:23	+28:29:19	0	19	38	6	89	9	0	12	0	6
CCC388	12:59:23	+27:55:10	0	26	0	22	0	15	0	31	0	22
CCC389	12:59:24	+27:31:02	0	25	0	20	0	14	0	25	0	21
CCC390	12:59:24	+27:44:19	0	26	0	19	0	21	0	29	0	23
CCC391	12:59:25	+27:59:48	0	38	0	18	0	20	0	25	0	18
CCC392	12:59:25	+27:58:04	0	28	0	15	0	22	0	25	0	20
CCC393	12:59:25	+27:56:04	0	6	0	24	0	24	0	27	0	20
CCC394	12:59:25	+27:58:23	0	27	0	16	0	22	0	26	0	21
CCC395	12:59:25	+28:11:13	0	22	0	24	0	15	0	32	0	20
CCC396	12:59:26	+28:17:15	0	23	0	25	0	22	0	33	0	19
CCC397	12:59:26	+27:59:54	0	41	0	19	0	22	0	25	0	15
CCC398	12:59:27	+27:47:06	0	29	0	14	0	18	0	27	0	21
CCC399	12:59:28	+28:02:25	0	26	0	22	0	15	0	26	0	19
CCC400	12:59:29	+27:51:00	0	26	21	6	52	7	181	38	0	7
CCC401	12:59:29	+27:57:23	0	6	0	23	0	22	0	30	0	21
CCC402	12:59:30	+28:42:00	0	19	0	16	0	15	0	18	0	15
CCC403	12:59:30	+26:26:07	0	23	0	18	0	13	0	22	0	17
CCC404	12:59:30	+27:47:29	0	26	0	16	0	18	0	26	0	23
CCC405	12:59:30	+27:53:03	0	24	0	24	24	6	0	10	0	6
CCC406	12:59:31	+27:57:17	0	44	0	18	0	19	0	30	0	20
CCC407	12:59:31	+28:02:47	0	27	0	21	0	15	0	23	0	21
CCC408	12:59:31	+28:06:02	0	24	0	20	0	15	0	25	0	22
CCC409	12:59:31	+27:51:40	0	26	0	23	0	19	0	28	0	21
CCC410	12:59:32	+27:43:13	0	25	0	20	0	14	0	31	0	19
CCC411	12:59:32	+27:59:00	0	32	0	22	0	17	0	27	0	18
CCC412	12:59:34	+27:56:48	0	37	0	17	32	6	0	27	0	8
CCC413	12:59:35	+27:51:49	0	29	0	25	0	18	0	27	0	18
CCC414	12:59:35	+28:33:04	0	17	0	15	0	15	0	27	0	20
CCC415	12:59:35	+27:57:33	0	34	0	23	0	17	0	27	0	20
CCC416	12:59:36	+27:49:32	0	28	0	20	0	17	0	30	0	18
CCC417	12:59:37	+27:20:09	0	24	0	19	0	15	0	27	0	16
CCC418	12:59:37	+28:09:58	0	33	0	26	0	22	0	35	0	22
CCC419	12:59:37	+27:46:36	0	29	0	10	0	15	0	29	0	26
CCC420	12:59:37	+27:54:26	0	25	0	23	0	17	0	25	0	18
CCC421	12:59:37	+28:00:03	0	34	0	21	0	19	0	34	0	18

Continued on next page

OBJECT	RA h:m:s (J2000)	Dec. d:m:s (J2000)	S_{500} (mJy)	E_{500} (mJy)	S_{350} (mJy)	E_{350} (mJy)	S_{250} (mJy)	E_{250} (mJy)	S_{160} (mJy)	E_{160} (mJy)	S_{100} (mJy)	E_{100} (mJy)
CCC422	12:59:38	+27:59:13	0	36	0	19	0	24	0	32	0	19
CCC423	12:59:39	+28:53:43	26	8	100	11	255	24	439	59	371	49
CCC424	12:59:39	+27:51:16	0	28	0	23	0	18	0	26	0	19
CCC425	12:59:39	+27:57:14	0	41	0	21	0	17	0	29	0	20
CCC426	12:59:39	+28:55:35	0	23	0	19	0	20	0	19	0	13
CCC427	12:59:39	+27:34:35	0	25	36	7	78	8	0	10	0	8
CCC428	12:59:40	+28:37:50	26	7	68	8	150	21	0	11	162	29
CCC429	12:59:40	+27:58:05	0	30	0	21	0	20	0	26	0	18
CCC430	12:59:40	+28:08:40	0	34	0	25	0	20	0	27	0	22
CCC431	12:59:41	+28:30:25	0	20	0	16	0	14	0	25	0	19
CCC432	12:59:41	+27:39:35	0	26	0	16	0	14	0	27	0	15
CCC433	12:59:42	+27:55:29	0	49	0	16	0	15	0	25	0	16
CCC434	12:59:43	+27:59:40	0	27	0	19	0	17	0	28	0	18
CCC435	12:59:44	+28:10:34	0	26	0	23	0	25	0	31	0	19
CCC436	12:59:44	+27:57:30	0	35	0	23	0	18	0	31	0	18
CCC437	12:59:44	+27:52:03	0	26	0	21	0	16	0	26	0	25
CCC438	12:59:44	+27:54:44	0	25	0	20	0	17	0	23	0	17
CCC439	12:59:44	+28:15:23	0	23	0	30	0	22	0	27	0	19
CCC440	12:59:44	+27:53:23	0	25	0	21	0	18	0	25	0	21
CCC441	12:59:46	+27:51:26	0	26	0	21	0	15	0	25	0	26
CCC442	12:59:46	+27:58:25	0	35	0	22	0	19	0	28	0	18
CCC443	12:59:46	+27:59:30	0	33	0	18	0	18	0	31	0	19
CCC444	12:59:47	+27:42:37	0	27	0	17	0	17	0	25	0	19
CCC445	12:59:47	+28:05:52	0	27	0	23	0	25	0	32	0	18
CCC446	12:59:49	+26:58:27	0	25	29	7	43	9	0	25	0	20
CCC447	12:59:50	+27:54:45	0	20	0	19	0	19	0	25	0	22
CCC448	12:59:50	+28:08:39	0	38	0	25	0	21	0	27	0	21
CCC449	12:59:51	+27:49:58	0	27	0	24	0	17	0	26	0	24
CCC450	12:59:51	+28:04:24	0	26	0	16	0	20	0	27	0	19
CCC451	12:59:51	+28:05:54	0	25	0	24	0	23	0	27	0	19
CCC452	12:59:54	+26:49:11	0	20	0	20	0	21	0	26	0	20
CCC453	12:59:54	+27:47:45	0	29	0	18	0	11	0	24	0	21
CCC454	12:59:55	+28:07:42	0	28	0	20	0	21	0	27	0	18
CCC455	12:59:56	+28:02:05	0	29	0	20	0	23	0	31	0	24
CCC456	12:59:56	+27:44:46	0	27	0	17	0	16	0	25	0	21
CCC457	12:59:56	+27:55:48	0	19	0	16	0	15	0	30	0	18
CCC458	12:59:57	+28:03:54	0	24	0	17	0	22	0	31	0	18
CCC459	12:59:57	+28:14:48	0	21	0	22	0	16	0	29	0	19
CCC460	12:59:59	+27:56:26	0	23	0	20	0	13	0	30	0	17
CCC461	13:00:00	+27:56:43	0	23	0	22	0	12	0	30	0	19
CCC462	13:00:01	+26:57:22	0	25	0	25	0	25	0	20	0	17
CCC463	13:00:01	+27:43:52	0	26	0	18	0	19	0	32	0	21
CCC464	13:00:01	+28:26:05	0	18	0	18	0	17	0	25	0	19
CCC465	13:00:03	+28:14:25	0	18	0	20	0	17	0	29	0	21
CCC466	13:00:03	+26:53:53	0	22	0	24	0	22	0	23	0	19
CCC467	13:00:03	+27:57:52	0	21	0	20	0	14	0	29	0	17
CCC468	13:00:04	+28:09:18	0	27	0	23	0	20	0	24	0	19
CCC469	13:00:04	+28:36:12	0	23	0	18	0	18	0	32	0	18
CCC470	13:00:04	+27:59:15	0	21	0	21	0	15	0	29	0	16
CCC471	13:00:04	+27:01:56	0	22	0	20	0	19	0	26	0	19
CCC472	13:00:05	+28:01:28	0	23	0	15	0	18	0	30	0	24
CCC473	13:00:05	+27:48:27	0	31	0	26	19	5	0	24	0	21
CCC474	13:00:05	+27:55:35	0	23	0	22	0	12	0	30	0	21
CCC475	13:00:06	+27:58:41	0	24	0	23	0	14	0	31	0	17
CCC476	13:00:06	+27:41:07	0	23	0	18	0	20	0	29	0	16
CCC477	13:00:06	+27:18:02	0	25	0	18	0	20	0	28	0	21
CCC478	13:00:06	+27:46:32	0	27	0	19	0	18	0	31	0	23
CCC479	13:00:06	+28:00:14	0	25	0	20	0	15	0	30	0	23
CCC480	13:00:06	+29:27:45	0	25	0	23	0	15	0	23	0	18
CCC481	13:00:07	+27:57:29	0	25	0	21	0	14	0	31	0	19
CCC482	13:00:07	+28:04:42	0	27	0	24	0	23	0	24	0	20
CCC483	13:00:08	+27:46:23	0	30	0	24	0	18	0	26	0	22
CCC484	13:00:08	+27:58:37	0	24	0	23	0	15	0	35	0	18
CCC485	13:00:08	+28:09:35	0	25	0	28	0	20	0	29	0	22
CCC486	13:00:09	+28:10:13	0	24	0	27	0	19	0	28	0	22
CCC487	13:00:09	+27:51:59	0	28	0	24	73	8	0	10	456	68
CCC488	13:00:10	+27:57:32	0	25	0	22	0	15	0	29	0	17
CCC489	13:00:10	+27:35:42	0	23	0	16	0	19	0	24	0	21
CCC490	13:00:10	+26:27:40	0	27	0	15	0	17	0	27	0	21
CCC491	13:00:10	+29:27:59	0	26	0	23	0	16	0	26	0	17
CCC492	13:00:11	+28:03:54	0	23	0	21	0	19	0	26	0	20
CCC493	13:00:11	+27:27:36	0	22	0	21	0	17	0	28	0	18
CCC494	13:00:12	+27:46:54	0	25	0	22	0	18	0	28	0	17
CCC495	13:00:12	+28:04:31	0	22	0	20	0	17	0	23	0	19
CCC496	13:00:13	+28:03:11	0	24	0	19	0	19	0	26	0	19
CCC497	13:00:13	+27:52:01	0	28	0	22	0	13	0	21	0	19
CCC498	13:00:14	+28:49:41	0	21	0	15	0	15	0	20	0	12
CCC499	13:00:14	+28:27:29	0	24	0	20	0	14	0	30	0	19
CCC500	13:00:14	+28:02:28	0	25	0	18	0	20	0	26	0	21
CCC501	13:00:15	+27:15:24	0	25	0	20	0	18	0	26	0	24
CCC502	13:00:16	+27:58:03	0	25	0	22	0	12	0	40	0	17
CCC503	13:00:17	+28:03:50	0	26	0	20	0	17	0	22	0	20
CCC504	13:00:17	+27:47:03	0	29	0	24	0	17	0	25	0	18
CCC505	13:00:17	+28:12:08	40	8	91	12	229	22	464	66	305	44
CCC506	13:00:18	+27:57:23	0	26	0	25	0	36	0	141	0	27
CCC507	13:00:18	+28:05:49	0	27	0	22	0	17	0	25	0	23
CCC508	13:00:18	+27:48:55	0	33	0	23	0	17	0	23	0	17
CCC509	13:00:18	+27:56:13	0	25	0	22	0	13	0	27	0	18
CCC510	13:00:18	+28:00:33	0	26	0	19	0	11	0	34	0	19
CCC511	13:00:19	+27:33:13	0	20	0	25	0	19	0	22	0	25
CCC512	13:00:19	+28:26:21	0	25	0	19	0	17	0	31	0	19

Continued on next page

OBJECT	RA h:m:s (J2000)	Dec. d:m:s (J2000)	S_{500} (mJy)	E_{500} (mJy)	S_{350} (mJy)	E_{350} (mJy)	S_{250} (mJy)	E_{250} (mJy)	S_{160} (mJy)	E_{160} (mJy)	S_{100} (mJy)	E_{100} (mJy)
CCC513	13:00:20	+27:50:36	0	25	0	22	0	13	0	25	0	18
CCC514	13:00:21	+27:53:54	0	24	0	27	0	15	0	25	0	18
CCC515	13:00:22	+28:02:49	0	27	0	19	0	20	0	24	0	20
CCC516	13:00:22	+28:14:49	0	22	0	24	0	17	0	23	0	18
CCC517	13:00:22	+27:37:24	0	23	0	21	0	18	0	28	0	16
CCC518	13:00:22	+28:34:28	0	24	0	24	0	18	0	20	0	21
CCC519	13:00:23	+27:17:12	0	26	0	19	0	21	0	25	0	23
CCC520	13:00:24	+27:55:35	0	25	0	22	0	14	0	27	0	18
CCC521	13:00:25	+27:33:08	0	20	0	19	0	19	0	25	0	22
CCC522	13:00:25	+28:52:04	0	25	0	18	0	18	0	18	0	14
CCC523	13:00:26	+27:30:56	0	19	0	16	0	18	0	23	0	23
CCC524	13:00:27	+27:37:30	0	24	0	19	0	19	0	22	0	16
CCC525	13:00:27	+27:16:18	0	26	0	20	0	19	0	20	0	18
CCC526	13:00:27	+27:57:21	0	26	0	22	0	17	0	30	0	18
CCC527	13:00:28	+27:58:20	0	20	0	16	0	12	0	28	0	17
CCC528	13:00:29	+26:40:31	0	21	0	23	0	20	0	30	0	21
CCC529	13:00:29	+28:27:20	0	28	0	20	0	18	0	32	0	19
CCC530	13:00:29	+27:46:12	0	30	0	23	0	19	0	44	0	20
CCC531	13:00:30	+28:09:36	0	25	0	28	0	20	0	24	0	21
CCC532	13:00:30	+28:20:46	0	24	0	19	0	16	0	24	0	17
CCC533	13:00:30	+28:06:30	0	24	0	22	0	14	0	24	0	20
CCC534	13:00:31	+28:57:01	0	26	37	6	53	8	0	7	0	4
CCC535	13:00:32	+28:15:21	0	21	0	21	0	17	0	27	0	17
CCC536	13:00:32	+27:45:58	0	29	0	24	0	18	0	37	0	22
CCC537	13:00:33	+27:49:27	0	32	0	25	0	18	0	22	0	19
CCC538	13:00:34	+27:56:04	0	26	0	25	0	14	0	30	0	15
CCC539	13:00:35	+27:56:33	0	27	0	21	0	15	0	26	0	19
CCC540	13:00:35	+28:08:46	0	24	0	24	0	16	0	22	0	20
CCC541	13:00:35	+27:34:27	44	8	128	13	363	35	710	94	568	74
CCC542	13:00:37	+28:39:50	0	25	0	20	0	16	0	22	0	19
CCC543	13:00:37	+28:03:29	110	13	375	36	956	91	2291	281	2280	278
CCC544	13:00:38	+28:00:52	0	21	0	19	0	22	0	25	0	19
CCC545	13:00:39	+29:01:09	161	25	465	51	1014	101	1463	186	717	100
CCC546	13:00:39	+27:55:26	0	23	0	22	0	18	0	22	0	20
CCC547	13:00:40	+27:59:47	0	29	0	21	0	16	0	24	0	18
CCC548	13:00:41	+28:02:42	0	24	0	18	0	22	0	26	0	21
CCC549	13:00:42	+27:58:16	0	26	43	8	106	11	342	63	191	34
CCC550	13:00:42	+27:57:47	0	26	0	22	0	17	0	26	0	18
CCC551	13:00:43	+28:24:58	0	20	0	20	0	15	0	26	0	15
CCC552	13:00:44	+28:20:14	0	23	0	21	0	17	0	21	0	20
CCC553	13:00:44	+28:06:02	0	23	0	23	0	18	0	24	0	18
CCC554	13:00:45	+27:44:49	0	27	0	27	0	18	0	25	0	19
CCC555	13:00:45	+27:50:07	0	29	0	26	0	17	0	28	0	18
CCC556	13:00:47	+27:55:19	0	24	0	27	0	22	0	19	0	18
CCC557	13:00:47	+29:04:02	0	25	0	21	0	18	0	30	0	20
CCC558	13:00:47	+29:12:02	0	22	0	18	0	19	0	30	0	20
CCC559	13:00:48	+28:05:26	0	23	25	7	38	7	0	26	0	6
CCC560	13:00:48	+28:09:30	65	9	210	30	467	51	534	82	181	37
CCC561	13:00:49	+27:24:20	0	25	0	19	0	17	0	24	0	18
CCC562	13:00:51	+27:44:34	0	29	0	18	0	21	0	25	0	16
CCC563	13:00:51	+28:02:49	0	27	0	24	0	35	0	37	0	20
CCC564	13:00:52	+28:21:58	0	23	0	24	0	17	0	23	0	16
CCC565	13:00:52	+27:48:17	0	33	0	21	0	16	0	25	0	25
CCC566	13:00:54	+27:47:01	0	125	0	271	0	590	0	27	0	23
CCC567	13:00:54	+28:00:27	0	26	0	21	0	19	0	27	0	17
CCC568	13:00:54	+27:50:31	0	29	0	24	0	14	0	19	0	20
CCC569	13:00:55	+27:07:17	0	22	0	19	0	19	0	29	0	18
CCC570	13:00:55	+27:53:54	0	26	0	25	0	16	0	24	0	18
CCC571	13:00:56	+27:47:27	320	40	839	88	2034	201	3380	410	2415	296
CCC572	13:00:58	+27:39:07	0	21	0	18	0	15	0	26	0	20
CCC573	13:01:00	+28:47:31	0	24	0	22	0	13	0	18	0	14
CCC574	13:01:04	+27:53:30	0	26	0	26	0	19	0	27	0	19
CCC575	13:01:05	+28:03:43	0	23	0	17	0	20	0	28	0	21
CCC576	13:01:05	+27:42:32	0	21	0	17	0	17	0	21	0	17
CCC577	13:01:06	+27:23:52	0	26	0	20	0	17	0	24	0	18
CCC578	13:01:06	+26:48:34	0	29	0	20	0	19	0	25	0	22
CCC579	13:01:09	+28:21:35	0	29	0	22	0	18	0	34	0	21
CCC580	13:01:09	+27:49:05	0	22	0	23	0	17	0	22	0	22
CCC581	13:01:09	+28:01:59	0	30	0	18	0	20	0	30	0	18
CCC582	13:01:10	+27:48:10	0	22	0	22	0	17	0	25	0	20
CCC583	13:01:10	+27:14:47	0	24	0	19	0	18	0	34	0	18
CCC584	13:01:11	+27:44:33	0	19	0	18	0	21	0	28	0	18
CCC585	13:01:11	+29:39:50	0	25	0	22	0	18	0	24	0	21
CCC586	13:01:12	+27:36:16	0	24	0	18	0	18	0	25	0	21
CCC587	13:01:13	+27:54:51	0	24	0	24	0	19	0	31	0	20
CCC588	13:01:13	+28:04:59	0	31	0	24	0	19	0	23	0	21
CCC589	13:01:14	+28:31:18	0	23	0	23	0	19	0	23	0	22
CCC590	13:01:15	+27:40:09	0	20	0	17	0	14	0	30	0	21
CCC591	13:01:15	+28:52:19	0	24	0	25	0	18	0	20	0	10
CCC592	13:01:17	+27:48:32	0	23	0	21	0	22	0	26	0	22
CCC593	13:01:17	+28:05:49	0	29	0	19	0	20	0	22	0	20
CCC594	13:01:19	+28:07:41	0	27	0	26	0	17	0	23	0	21
CCC595	13:01:19	+27:51:37	0	20	0	21	0	19	0	33	0	19
CCC596	13:01:19	+27:57:39	0	21	0	20	0	19	0	28	0	22
CCC597	13:01:20	+26:53:12	0	29	0	20	0	19	0	27	0	19
CCC598	13:01:21	+26:47:47	0	29	0	20	0	21	0	30	0	23
CCC599	13:01:22	+28:11:45	0	22	0	23	0	16	0	22	0	20
CCC600	13:01:25	+28:40:38	72	10	254	32	595	62	1053	135	637	82
CCC601	13:01:26	+27:53:09	0	92	0	170	0	326	0	496	0	21
CCC602	13:01:26	+28:26:09	0	27	0	17	0	17	0	26	0	18
CCC603	13:01:27	+27:59:57	0	22	0	21	0	22	0	28	0	17

Continued on next page

OBJECT	RA h:m:s (J2000)	Dec. d:m:s (J2000)	S_{500} (mJy)	E_{500} (mJy)	S_{350} (mJy)	E_{350} (mJy)	S_{250} (mJy)	E_{250} (mJy)	S_{160} (mJy)	E_{160} (mJy)	S_{100} (mJy)	E_{100} (mJy)
CCC604	13:01:28	+27:55:35	0	24	0	20	0	16	0	37	0	18
CCC605	13:01:31	+27:50:51	0	23	0	20	0	17	0	32	0	16
CCC606	13:01:33	+29:07:50	58	10	164	18	426	41	860	111	648	85
CCC607	13:01:33	+27:54:40	0	20	0	23	0	15	0	30	0	16
CCC608	13:01:35	+28:08:49	0	27	0	19	0	20	0	26	0	19
CCC609	13:01:36	+27:42:28	0	23	0	16	0	14	0	27	0	23
CCC610	13:01:37	+28:00:56	0	22	0	20	0	18	0	22	0	22
CCC611	13:01:39	+28:14:45	0	26	0	23	0	21	0	28	0	17
CCC612	13:01:40	+27:32:56	0	24	0	22	0	18	0	24	0	16
CCC613	13:01:43	+28:17:52	0	27	0	28	0	20	0	25	0	16
CCC614	13:01:43	+29:10:42	0	23	0	22	0	17	0	25	0	14
CCC615	13:01:43	+29:02:40	233	36	505	58	982	99	1638	207	909	115
CCC616	13:01:43	+28:59:58	0	28	0	62	0	20	0	17	0	12
CCC617	13:01:44	+28:12:51	0	28	0	24	0	20	0	37	0	20
CCC618	13:01:47	+28:05:42	0	26	0	21	0	19	0	24	0	20
CCC619	13:01:47	+29:04:36	0	23	0	31	0	20	0	24	0	16
CCC620	13:01:47	+27:37:18	0	26	0	20	0	17	0	29	0	20
CCC621	13:01:47	+28:39:36	0	15	0	17	0	14	0	27	0	18
CCC622	13:01:47	+27:21:17	0	23	0	17	0	18	0	35	0	19
CCC623	13:01:48	+27:43:42	0	27	0	23	0	13	0	25	0	28
CCC624	13:01:48	+27:36:14	0	28	0	23	0	17	0	28	0	19
CCC625	13:01:48	+28:10:19	0	23	0	25	0	19	0	47	0	16
CCC626	13:01:50	+27:53:36	0	20	0	17	0	19	0	26	0	22
CCC627	13:01:53	+27:37:28	0	30	0	22	0	16	0	34	0	22
CCC628	13:01:55	+29:19:22	0	27	0	23	0	15	0	24	0	16
CCC629	13:01:57	+28:00:21	28	7	77	10	171	17	385	55	278	43
CCC630	13:01:59	+28:42:34	0	21	0	16	0	14	0	18	0	15
CCC631	13:02:01	+27:39:10	0	27	0	23	0	14	0	26	0	17
CCC632	13:02:03	+29:09:01	0	24	0	24	0	17	0	18	0	13
CCC633	13:02:04	+29:15:12	29	8	62	7	122	13	378	60	285	48
CCC634	13:02:04	+27:41:58	0	23	0	21	0	14	0	24	0	18
CCC635	13:02:04	+28:53:40	0	25	0	16	0	15	0	19	0	10
CCC636	13:02:05	+27:17:50	0	22	0	21	0	16	0	25	0	19
CCC637	13:02:06	+27:45:54	0	28	0	21	0	18	0	30	0	21
CCC638	13:02:07	+27:38:53	60	11	177	18	548	57	944	121	969	121
CCC639	13:02:08	+28:09:03	0	27	0	21	0	18	0	23	0	18
CCC640	13:02:09	+27:35:21	0	28	0	23	0	16	0	28	0	21
CCC641	13:02:10	+28:11:30	0	25	0	21	24	5	0	21	0	19
CCC642	13:02:11	+28:27:23	0	28	0	21	0	24	0	19	0	21
CCC643	13:02:14	+28:21:09	0	29	0	23	0	16	0	19	0	14
CCC644	13:02:14	+28:06:05	0	25	0	25	0	19	0	23	0	16
CCC645	13:02:21	+28:13:50	0	30	0	19	0	16	0	21	0	17
CCC646	13:02:21	+28:15:21	0	30	0	20	21	5	0	8	0	19
CCC647	13:02:24	+29:27:05	0	28	0	25	0	17	0	21	0	18
CCC648	13:02:25	+27:58:20	0	25	0	19	0	22	0	21	0	14
CCC649	13:02:27	+29:29:15	0	28	0	22	0	17	0	25	0	18
CCC650	13:02:31	+27:56:08	0	30	0	17	0	20	0	15	0	14
CCC651	13:02:31	+28:26:21	0	34	0	20	0	22	0	24	0	17
CCC652	13:02:32	+27:23:36	0	25	0	26	0	17	0	25	0	20
CCC653	13:02:32	+27:17:44	0	28	0	19	0	16	0	26	0	18
CCC654	13:02:34	+27:56:56	0	29	0	20	0	19	0	17	0	14
CCC655	13:02:35	+27:26:22	0	28	0	21	0	15	0	24	0	18
CCC656	13:02:35	+28:44:42	0	16	0	18	0	15	0	15	0	13
CCC657	13:02:35	+26:39:44	0	26	0	22	0	19	0	38	0	21
CCC658	13:02:37	+27:10:34	0	26	0	16	0	17	0	25	0	24
CCC659	13:02:38	+28:30:06	0	29	0	18	0	14	0	31	0	15
CCC660	13:02:38	+28:06:52	0	28	0	26	0	20	0	26	0	14
CCC661	13:02:40	+28:22:16	0	39	59	9	119	13	234	37	171	27
CCC662	13:02:44	+28:02:43	0	24	0	23	0	20	0	27	0	14
CCC663	13:02:51	+28:28:56	0	26	0	23	0	16	0	24	0	14
CCC664	13:02:52	+27:51:59	0	21	0	23	0	16	0	23	0	13
CCC665	13:02:56	+28:04:13	0	27	0	27	0	19	0	21	0	12
CCC666	13:02:57	+28:22:32	0	28	0	23	0	15	0	21	0	17
CCC667	13:02:59	+28:16:31	0	31	0	21	0	15	0	18	0	15
CCC668	13:03:00	+28:01:56	0	25	0	25	0	16	0	22	0	16
CCC669	13:03:05	+27:47:02	0	30	0	22	0	15	0	18	0	15
CCC670	13:03:05	+26:31:52	39	8	57	9	198	29	195	38	190	34
CCC671	13:03:09	+28:35:00	0	21	0	17	0	14	0	21	0	15
CCC672	13:03:09	+28:29:22	0	24	0	19	0	15	0	22	0	14
CCC673	13:03:12	+28:10:21	0	30	0	16	0	24	0	25	0	17
CCC674	13:03:13	+27:22:08	0	24	0	18	0	15	0	22	0	16
CCC675	13:03:16	+28:01:49	74	9	216	34	370	44	604	81	450	60
CCC676	13:03:19	+28:37:02	0	20	0	17	0	14	0	21	0	21
CCC677	13:03:21	+28:18:32	0	32	0	25	0	20	0	25	0	17
CCC678	13:03:22	+28:47:47	0	18	0	17	0	14	0	14	0	12
CCC679	13:03:22	+27:56:09	0	26	0	19	0	21	0	24	0	13
CCC680	13:03:23	+28:51:51	0	20	0	15	0	14	0	15	0	12
CCC681	13:03:23	+27:18:25	0	20	0	19	0	16	0	22	0	19
CCC682	13:03:25	+28:00:50	0	19	0	21	0	17	0	22	0	18
CCC683	13:03:27	+28:33:51	0	17	0	18	26	5	0	26	0	21
CCC684	13:03:29	+26:33:01	170	24	479	58	1106	121	1288	163	799	105
CCC685	13:03:30	+28:16:28	0	29	0	23	0	15	0	25	0	22
CCC686	13:03:31	+28:05:32	0	19	0	20	0	10	0	28	0	20
CCC687	13:03:33	+29:03:37	0	15	0	23	0	18	0	20	0	14
CCC688	13:03:33	+28:14:21	0	25	0	19	0	16	0	21	0	23
CCC689	13:03:35	+28:10:01	0	25	0	14	0	14	0	33	0	19
CCC690	13:03:36	+28:05:52	0	20	0	19	0	13	0	35	0	22
CCC691	13:03:42	+28:54:19	0	15	0	18	0	17	0	19	0	13
CCC692	13:03:44	+28:32:45	0	21	0	15	0	13	0	28	0	16
CCC693	13:03:44	+28:05:03	27	7	55	8	102	10	255	42	205	33
CCC694	13:03:46	+27:59:12	0	23	0	15	0	14	0	23	0	21

Continued on next page

OBJECT	RA h:m:s (J2000)	Dec. d:m:s (J2000)	S_{500} (mJy)	E_{500} (mJy)	S_{350} (mJy)	E_{350} (mJy)	S_{250} (mJy)	E_{250} (mJy)	S_{160} (mJy)	E_{160} (mJy)	S_{100} (mJy)	E_{100} (mJy)
CCC695	13:03:49	+28:11:08	0	20	0	13	0	14	0	27	0	19
CCC696	13:03:50	+28:10:43	0	19	0	14	0	12	0	35	0	20
CCC697	13:03:50	+28:03:15	0	16	0	12	0	13	0	27	0	18
CCC698	13:03:50	+27:59:18	0	22	0	16	0	15	0	26	0	23
CCC699	13:03:53	+27:49:19	0	24	0	19	0	15	0	28	0	16
CCC700	13:03:54	+28:18:37	0	28	0	25	0	18	0	26	0	19
CCC701	13:03:54	+28:11:15	0	23	0	16	0	13	0	26	0	21
CCC702	13:04:04	+27:51:01	0	22	0	21	0	12	0	28	0	18
CCC703	13:04:07	+27:57:53	0	19	0	20	0	17	0	33	0	15
CCC704	13:04:10	+28:14:52	0	19	0	19	25	4	0	28	0	6
CCC705	13:04:10	+29:00:55	0	21	0	19	0	15	0	19	0	14
CCC706	13:04:11	+27:29:25	0	24	45	8	115	12	0	15	0	10
CCC707	13:04:13	+27:33:36	0	21	0	18	0	15	0	24	0	17
CCC708	13:04:15	+28:32:43	0	18	0	19	0	14	0	24	0	25
CCC709	13:04:16	+27:30:23	0	22	0	20	0	12	0	25	0	20
CCC710	13:04:16	+26:28:31	0	18	25	6	27	4	0	26	0	20
CCC711	13:04:17	+29:01:46	0	25	0	20	0	17	0	18	0	13
CCC712	13:04:18	+28:28:05	0	18	0	22	0	20	0	21	0	22
CCC713	13:04:22	+28:48:38	46	8	127	21	291	35	611	88	549	74
CCC714	13:04:26	+27:18:15	45	9	113	20	241	30	574	90	364	59
CCC715	13:04:29	+28:59:15	0	22	0	24	0	17	0	24	0	13
CCC716	13:04:35	+28:37:39	31	7	77	22	90	9	0	13	193	33
CCC717	13:04:36	+28:15:01	0	19	0	20	0	15	0	26	0	21
CCC718	13:04:37	+29:08:48	0	19	0	24	0	17	0	18	0	17
CCC719	13:04:38	+28:58:21	0	24	0	19	0	16	0	22	0	16
CCC720	13:04:38	+29:13:29	0	19	33	8	55	7	0	10	0	6
CCC721	13:04:41	+28:13:39	0	20	0	17	0	16	0	22	0	20
CCC722	13:04:43	+28:15:05	0	20	0	17	0	16	0	21	0	20
CCC723	13:04:49	+28:39:40	0	24	0	15	0	16	0	28	0	21
CCC724	13:04:49	+28:16:10	0	22	0	19	0	17	0	24	0	19
CCC725	13:04:52	+26:55:08	0	24	0	21	0	17	0	23	0	19
CCC726	13:04:58	+29:11:40	0	18	0	20	0	16	0	24	0	17
CCC727	13:04:58	+29:07:20	0	22	0	21	69	14	0	8	0	6
CCC728	13:05:02	+28:44:20	0	23	0	19	0	14	0	21	0	15
CCC729	13:05:03	+27:32:13	0	21	0	20	0	21	0	23	0	19
CCC730	13:05:06	+28:38:28	0	21	0	21	0	18	0	30	0	18
CCC731	13:05:08	+27:30:46	0	21	0	21	0	22	0	24	0	20
CCC732	13:05:12	+27:34:11	0	23	0	21	0	23	0	23	0	17
CCC733	13:05:12	+28:09:08	0	26	0	20	0	15	0	30	0	18
CCC734	13:05:15	+28:37:35	0	22	0	23	0	17	0	30	0	19
CCC735	13:05:17	+28:34:57	0	26	0	20	0	15	0	29	0	18
CCC736	13:05:19	+29:11:50	0	17	0	17	0	16	0	22	0	19
CCC737	13:05:23	+27:06:05	0	25	0	20	0	20	0	28	0	21
CCC738	13:05:25	+29:17:47	0	22	0	23	0	19	0	28	0	17
CCC739	13:05:32	+29:00:41	39	8	122	23	214	27	221	35	105	20
CCC740	13:05:45	+27:18:55	0	27	0	24	0	20	0	24	0	21
CCC741	13:05:45	+28:52:16	0	21	31	8	73	8	0	10	162	29
CCC742	13:05:48	+28:06:23	0	24	0	24	0	20	0	34	0	16
CCC743	13:05:53	+27:47:44	0	29	0	26	0	16	0	27	0	20
CCC744	13:05:53	+28:06:44	55	9	128	22	315	41	535	87	423	61
CCC745	13:06:05	+28:47:14	0	20	0	20	0	16	0	17	0	14
CCC746	13:06:05	+28:35:34	0	25	0	21	0	17	0	24	0	19
CCC747	13:06:06	+28:42:06	0	19	0	21	0	18	0	27	0	20
CCC748	13:06:09	+28:03:52	0	23	0	28	0	18	0	29	0	19
CCC749	13:06:11	+27:42:00	0	29	0	25	0	21	0	28	0	14
CCC750	13:06:14	+29:03:52	0	128	0	89	0	91	0	979	0	67
CCC751	13:06:15	+28:42:44	0	28	0	23	0	18	0	29	0	17
CCC752	13:06:17	+29:03:47	285	37	789	90	1569	157	2379	292	1943	238
CCC753	13:06:18	+27:15:18	0	28	0	21	0	17	0	26	0	20
CCC754	13:06:19	+28:03:09	0	25	0	25	0	18	0	28	0	18
CCC755	13:06:35	+27:10:07	0	27	0	21	0	16	0	34	0	22
CCC756	13:06:36	+27:52:22	83	11	261	25	658	62	1677	210	1492	183
CCC757	13:06:37	+28:14:05	0	31	0	22	0	18	0	26	0	22
CCC758	13:06:37	+28:20:15	0	24	0	19	0	18	0	26	0	15
CCC759	13:06:38	+28:50:54	0	30	0	96	0	142	0	283	0	134
CCC760	13:06:38	+27:32:40	0	28	0	24	0	18	0	31	0	26
CCC761	13:06:39	+28:31:03	0	27	0	22	37	6	0	29	0	8
CCC762	13:06:40	+28:55:48	0	20	0	11	0	13	0	22	0	12
CCC763	13:06:41	+27:53:02	0	23	0	21	0	20	0	33	0	17
CCC764	13:06:41	+28:54:24	0	19	0	17	0	13	0	19	0	12
CCC765	13:06:54	+28:32:52	0	29	0	24	0	24	0	29	0	20
CCC766	13:07:13	+28:02:49	74	12	222	32	416	46	615	84	416	62
CCC767	13:07:14	+28:15:29	0	28	0	22	0	15	0	25	0	21
CCC768	13:07:14	+28:20:35	0	29	0	23	0	24	0	31	0	21
CCC769	13:07:16	+28:17:02	0	22	0	21	0	16	0	31	0	20
CCC770	13:07:23	+27:51:55	0	21	0	25	0	14	0	22	0	16
CCC771	13:07:37	+27:29:56	0	25	30	9	87	10	171	32	183	32
CCC772	13:07:37	+28:19:32	0	26	0	26	41	6	0	11	0	20
CCC773	13:07:43	+27:30:34	0	28	0	32	0	20	0	32	0	17
CCC774	13:08:00	+28:04:52	0	30	0	32	0	17	0	25	0	19

Table B.1. The Coma Cluster Catalogue galaxies and their FIR properties. This table includes the Herchel fluxes from all detected galaxies, and stricked upper limits placed on undetected galaxies. If a galaxy was rejected by-eye then flux from the PSF-convolved map was used as an upper limit and the flux asterisked.

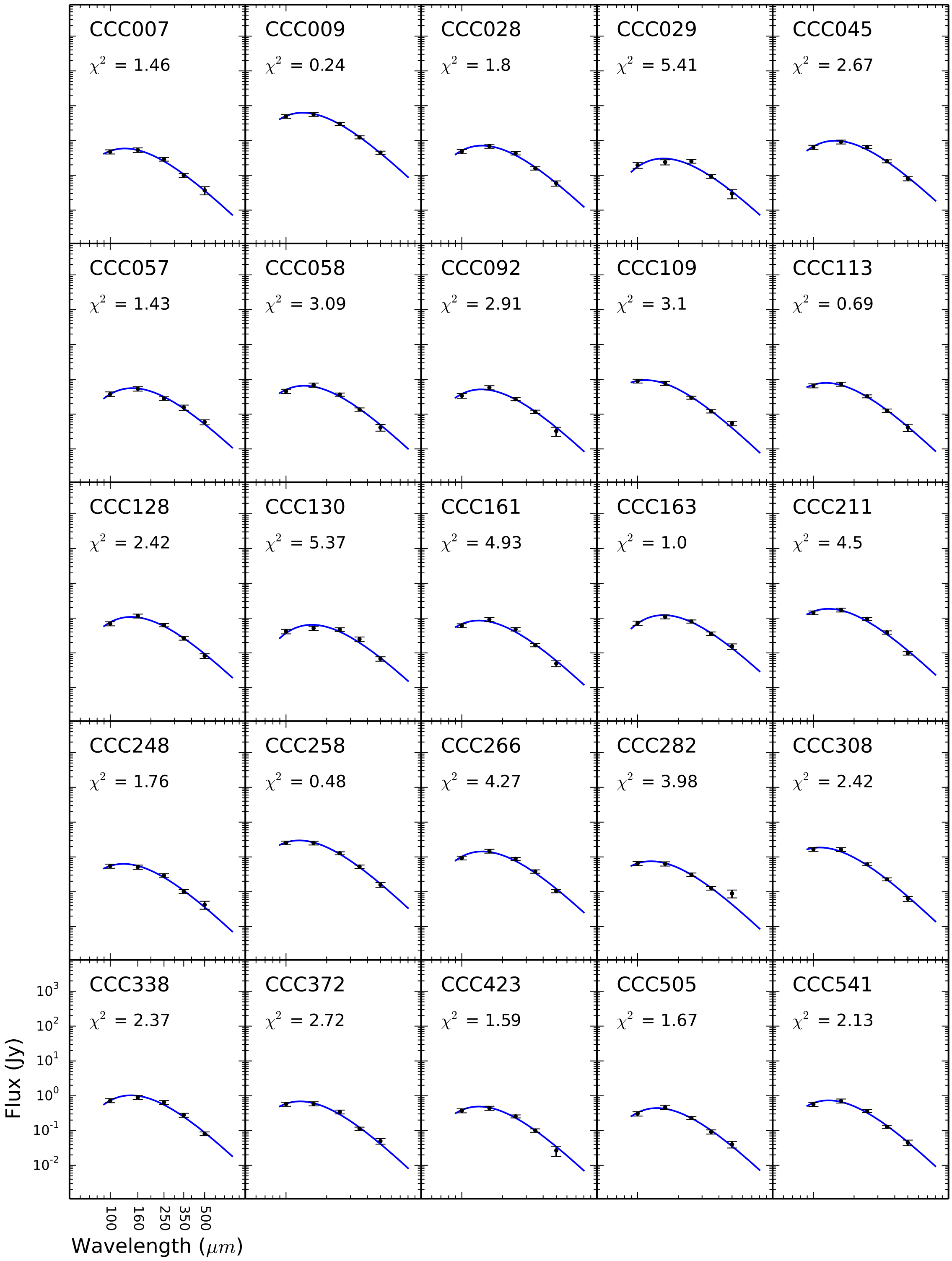

Figure B.1. 198 CCC and CFC galaxies dust masses and temperetures given from fitting a modified blackbody ($\beta = 2$ emissivity) to 5 *Herschel* bands.

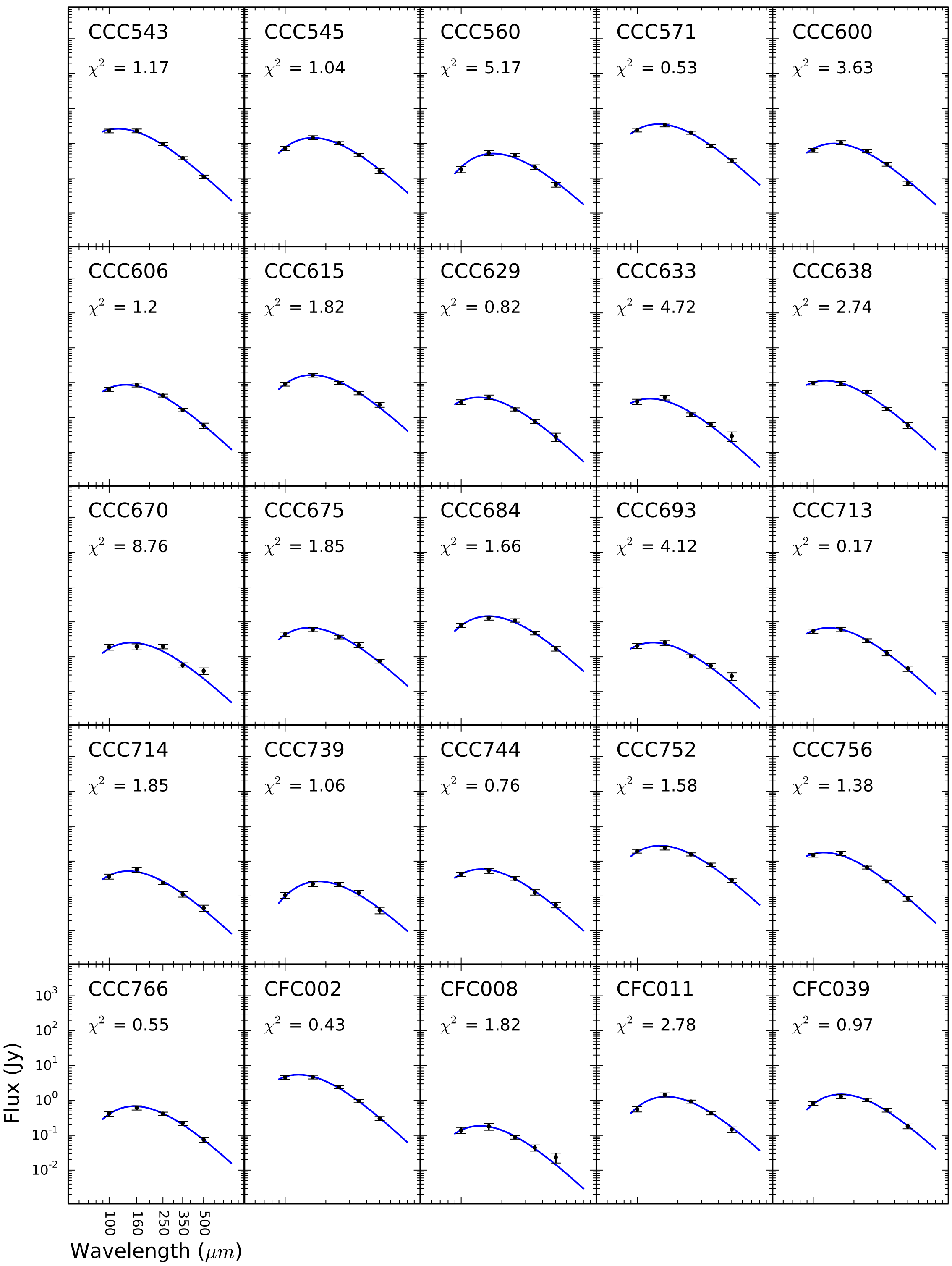
CCC543
χ^2 = 1.17
CCC545
χ^2 = 1.04
CCC560
χ^2 = 5.17
CCC571
χ^2 = 0.53
CCC600
χ^2 = 3.63
CCC606
χ^2 = 1.2
CCC615
χ^2 = 1.82
CCC629
χ^2 = 0.82
CCC633
χ^2 = 4.72
CCC638
χ^2 = 2.74
CCC670
χ^2 = 8.76
CCC675
χ^2 = 1.85
CCC684
χ^2 = 1.66
CCC693
χ^2 = 4.12
CCC713
χ^2 = 0.17
CCC714
χ^2 = 1.85
CCC739
χ^2 = 1.06
CCC744
χ^2 = 0.76
CCC752
χ^2 = 1.58
CCC756
χ^2 = 1.38
CCC766
χ^2 = 0.55
CFC002
χ^2 = 0.43
CFC008
χ^2 = 1.82
CFC011
χ^2 = 2.78
CFC039
χ^2 = 0.97
Flux (Jy)
10^3
10^2
10^1
10^0
10^{-1}
10^{-2}
100
160
250
350
500
Wavelength (μm)

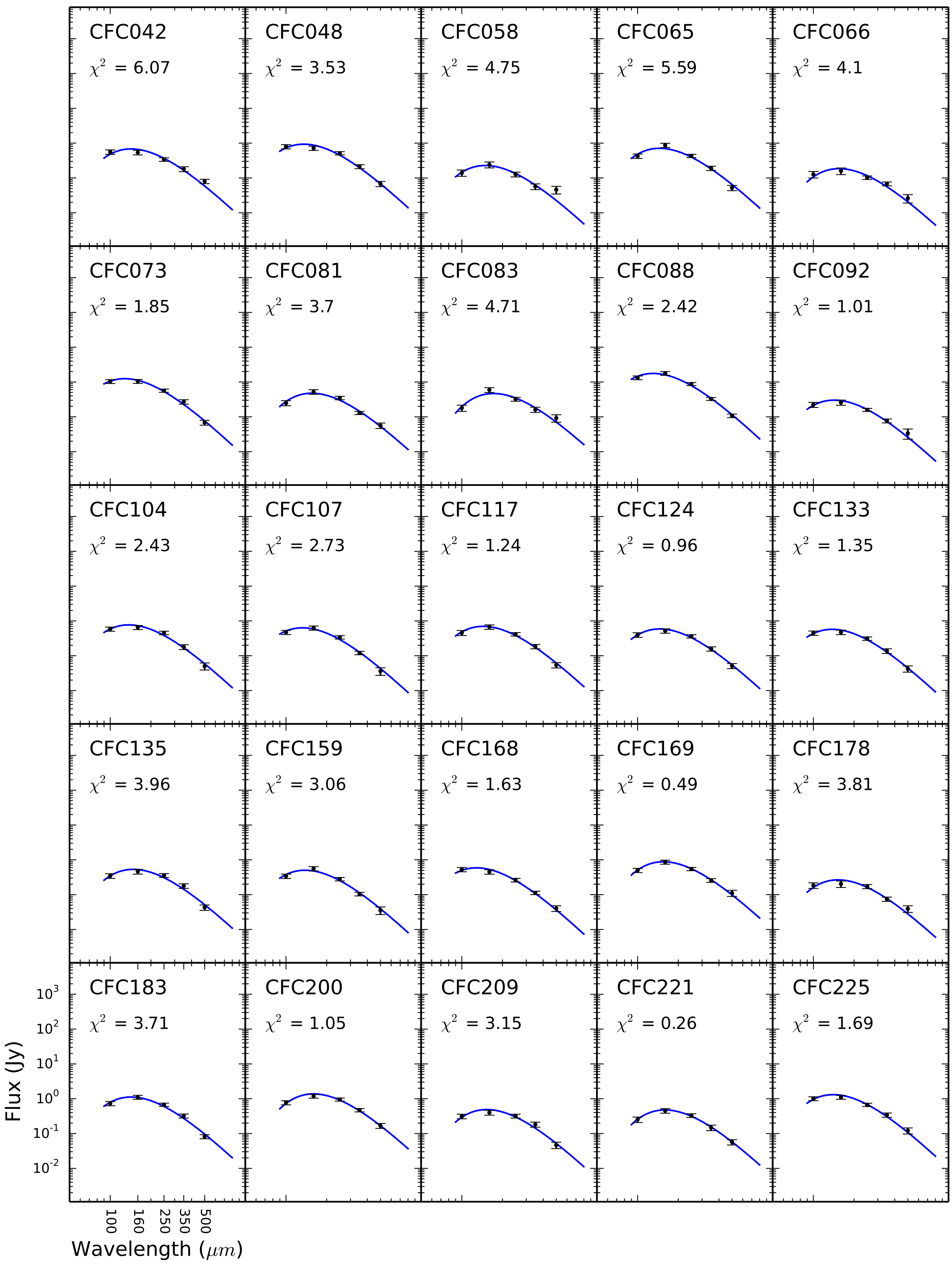
CFC042
χ^2 = 6.07
CFC048
χ^2 = 3.53
CFC058
χ^2 = 4.75
CFC065
χ^2 = 5.59
CFC066
χ^2 = 4.1
CFC073
χ^2 = 1.85
CFC081
χ^2 = 3.7
CFC083
χ^2 = 4.71
CFC088
χ^2 = 2.42
CFC092
χ^2 = 1.01
CFC104
χ^2 = 2.43
CFC107
χ^2 = 2.73
CFC117
χ^2 = 1.24
CFC124
χ^2 = 0.96
CFC133
χ^2 = 1.35
CFC135
χ^2 = 3.96
CFC159
χ^2 = 3.06
CFC168
χ^2 = 1.63
CFC169
χ^2 = 0.49
CFC178
χ^2 = 3.81
CFC183
χ^2 = 3.71
CFC200
χ^2 = 1.05
CFC209
χ^2 = 3.15
CFC221
χ^2 = 0.26
CFC225
χ^2 = 1.69
Flux (Jy)
10^3
10^2
10^1
10^0
10^{-1}
10^{-2}
100
160
250
350
500
Wavelength (μm)

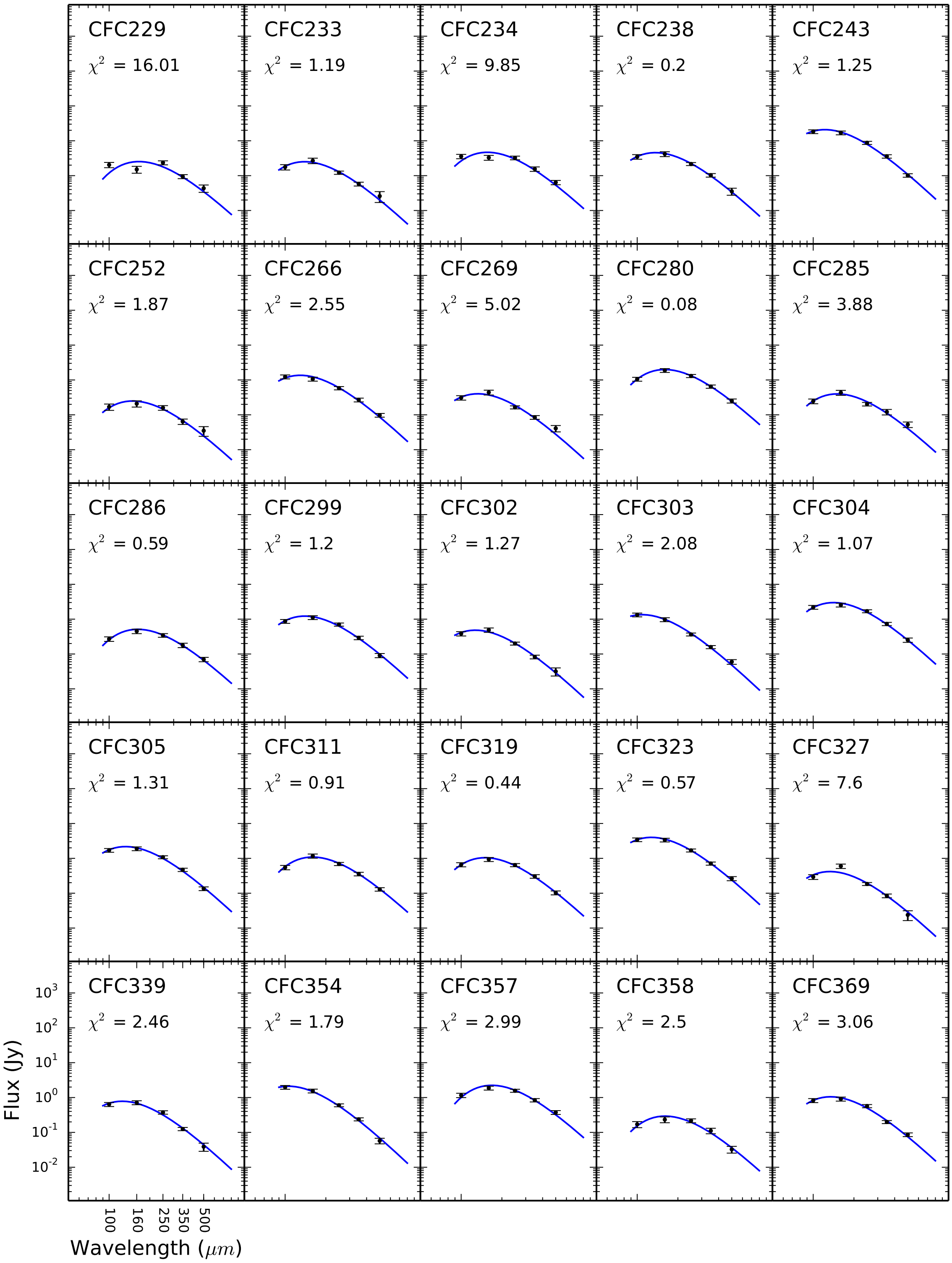
CFC229
χ^2 = 16.01
CFC233
χ^2 = 1.19
CFC234
χ^2 = 9.85
CFC238
χ^2 = 0.2
CFC243
χ^2 = 1.25
CFC252
χ^2 = 1.87
CFC266
χ^2 = 2.55
CFC269
χ^2 = 5.02
CFC280
χ^2 = 0.08
CFC285
χ^2 = 3.88
CFC286
χ^2 = 0.59
CFC299
χ^2 = 1.2
CFC302
χ^2 = 1.27
CFC303
χ^2 = 2.08
CFC304
χ^2 = 1.07
CFC305
χ^2 = 1.31
CFC311
χ^2 = 0.91
CFC319
χ^2 = 0.44
CFC323
χ^2 = 0.57
CFC327
χ^2 = 7.6
CFC339
χ^2 = 2.46
CFC354
χ^2 = 1.79
CFC357
χ^2 = 2.99
CFC358
χ^2 = 2.5
CFC369
χ^2 = 3.06
Flux (Jy)
10^3
10^2
10^1
10^0
10^{-1}
10^{-2}
100
160
250
350
500
Wavelength (μm)

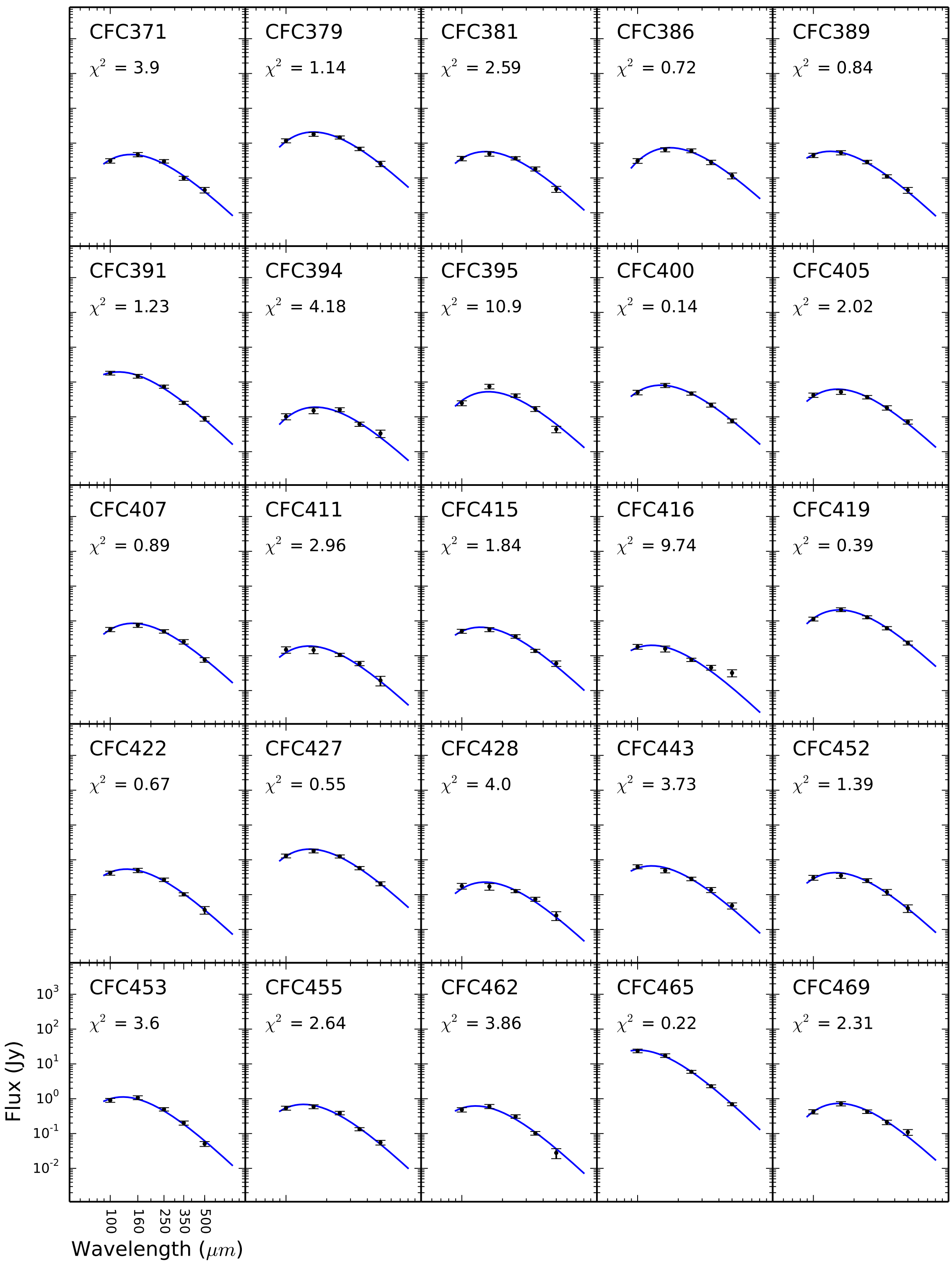
CFC371
χ^2 = 3.9
CFC379
χ^2 = 1.14
CFC381
χ^2 = 2.59
CFC386
χ^2 = 0.72
CFC389
χ^2 = 0.84
CFC391
χ^2 = 1.23
CFC394
χ^2 = 4.18
CFC395
χ^2 = 10.9
CFC400
χ^2 = 0.14
CFC405
χ^2 = 2.02
CFC407
χ^2 = 0.89
CFC411
χ^2 = 2.96
CFC415
χ^2 = 1.84
CFC416
χ^2 = 9.74
CFC419
χ^2 = 0.39
CFC422
χ^2 = 0.67
CFC427
χ^2 = 0.55
CFC428
χ^2 = 4.0
CFC443
χ^2 = 3.73
CFC452
χ^2 = 1.39
CFC453
χ^2 = 3.6
CFC455
χ^2 = 2.64
CFC462
χ^2 = 3.86
CFC465
χ^2 = 0.22
CFC469
χ^2 = 2.31
Flux (Jy)
10^3
10^2
10^1
10^0
10^{-1}
10^{-2}
100
160
250
350
500
Wavelength (μm)

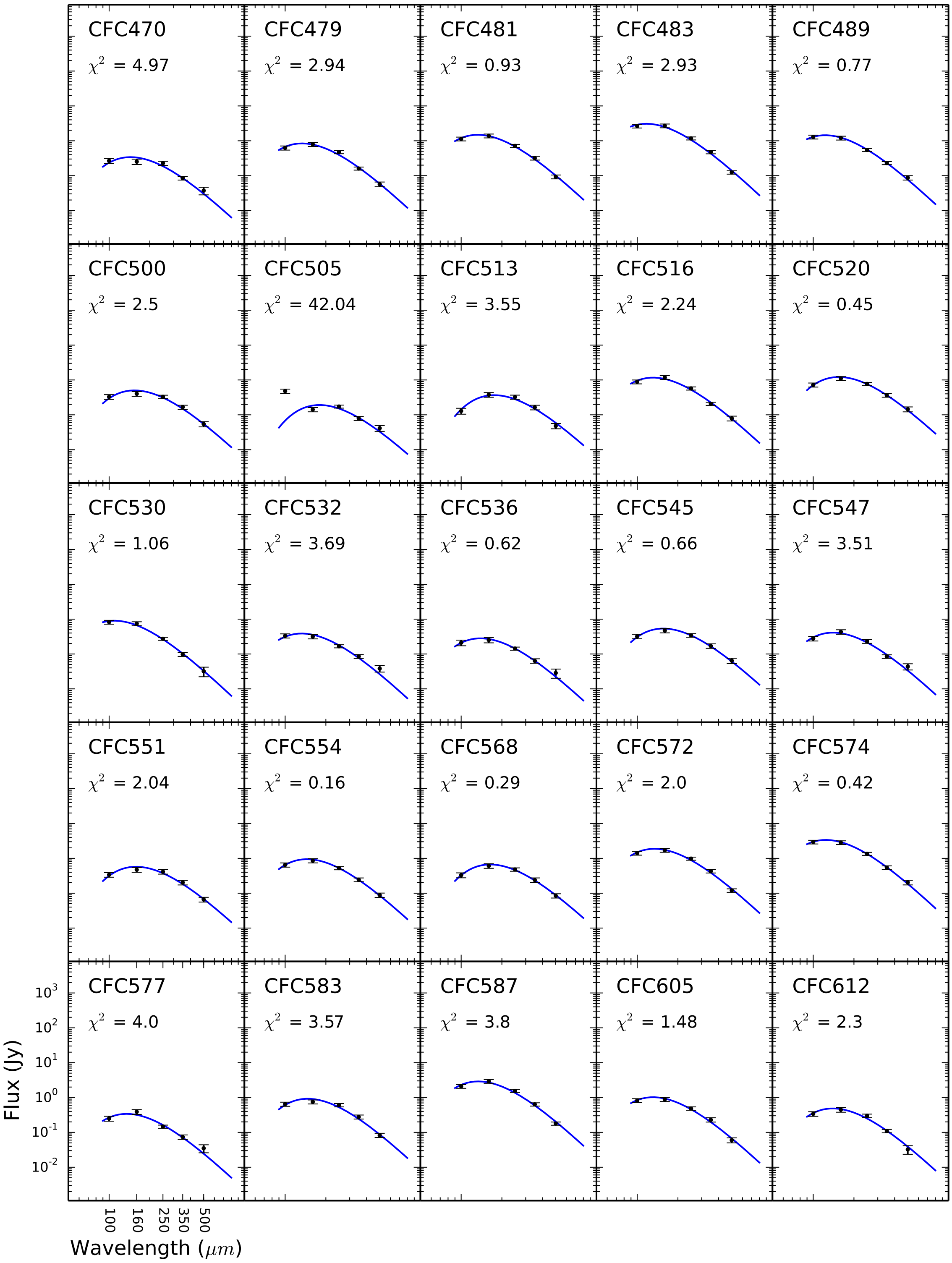
CFC470
χ^2 = 4.97
CFC479
χ^2 = 2.94
CFC481
χ^2 = 0.93
CFC483
χ^2 = 2.93
CFC489
χ^2 = 0.77
CFC500
χ^2 = 2.5
CFC505
χ^2 = 42.04
CFC513
χ^2 = 3.55
CFC516
χ^2 = 2.24
CFC520
χ^2 = 0.45
CFC530
χ^2 = 1.06
CFC532
χ^2 = 3.69
CFC536
χ^2 = 0.62
CFC545
χ^2 = 0.66
CFC547
χ^2 = 3.51
CFC551
χ^2 = 2.04
CFC554
χ^2 = 0.16
CFC568
χ^2 = 0.29
CFC572
χ^2 = 2.0
CFC574
χ^2 = 0.42
CFC577
χ^2 = 4.0
CFC583
χ^2 = 3.57
CFC587
χ^2 = 3.8
CFC605
χ^2 = 1.48
CFC612
χ^2 = 2.3
Flux (Jy)
10^3
10^2
10^1
10^0
10^{-1}
10^{-2}
100
160
250
350
500
Wavelength (μm)

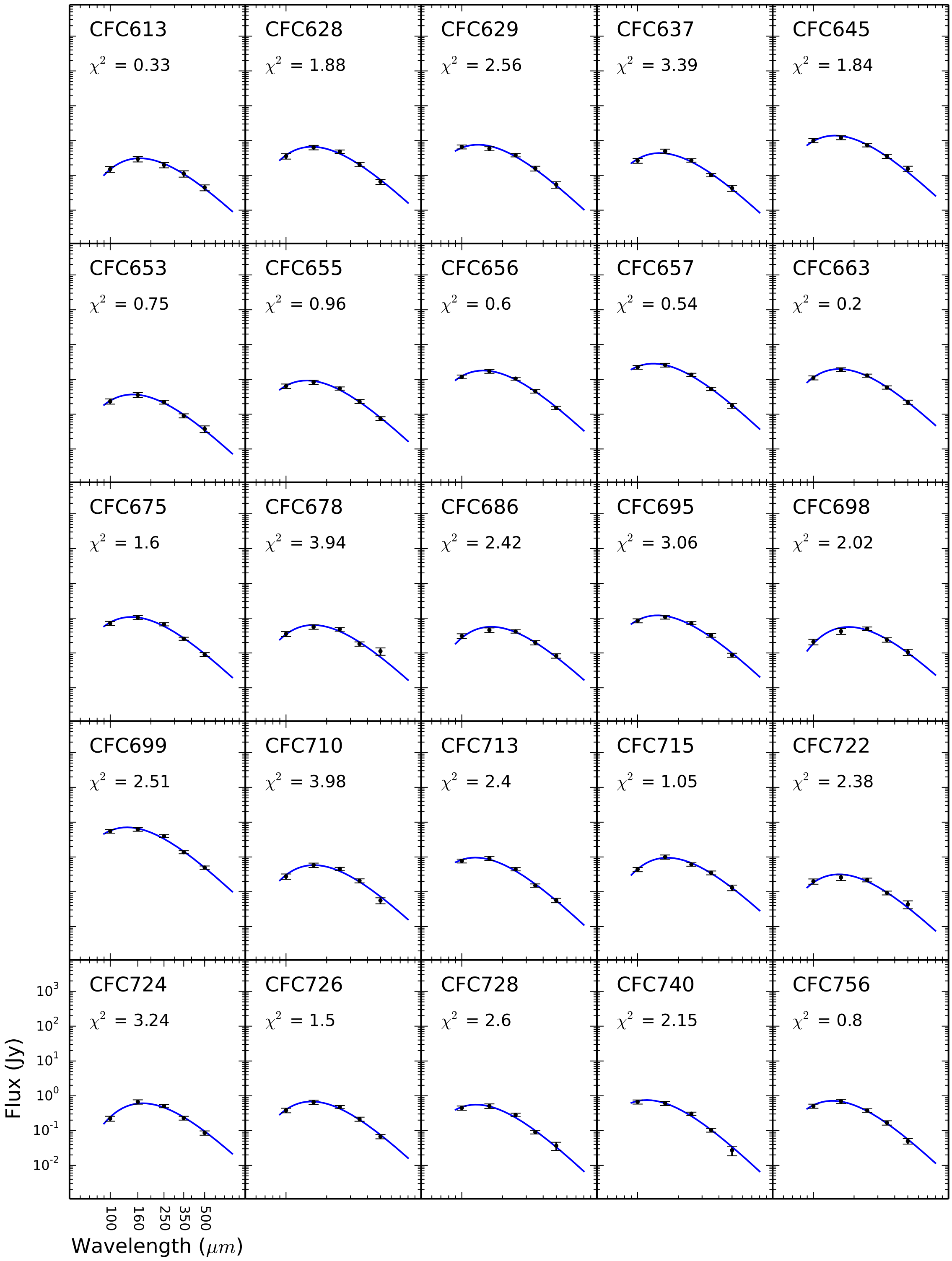

CFC613
χ^2 = 0.33
CFC628
χ^2 = 1.88
CFC629
χ^2 = 2.56
CFC637
χ^2 = 3.39
CFC645
χ^2 = 1.84
CFC653
χ^2 = 0.75
CFC655
χ^2 = 0.96
CFC656
χ^2 = 0.6
CFC657
χ^2 = 0.54
CFC663
χ^2 = 0.2
CFC675
χ^2 = 1.6
CFC678
χ^2 = 3.94
CFC686
χ^2 = 2.42
CFC695
χ^2 = 3.06
CFC698
χ^2 = 2.02
CFC699
χ^2 = 2.51
CFC710
χ^2 = 3.98
CFC713
χ^2 = 2.4
CFC715
χ^2 = 1.05
CFC722
χ^2 = 2.38
CFC724
χ^2 = 3.24
CFC726
χ^2 = 1.5
CFC728
χ^2 = 2.6
CFC740
χ^2 = 2.15
CFC756
χ^2 = 0.8
Flux (Jy)
10^3
10^2
10^1
10^0
10^{-1}
10^{-2}
100
160
250
350
500
Wavelength (μm)

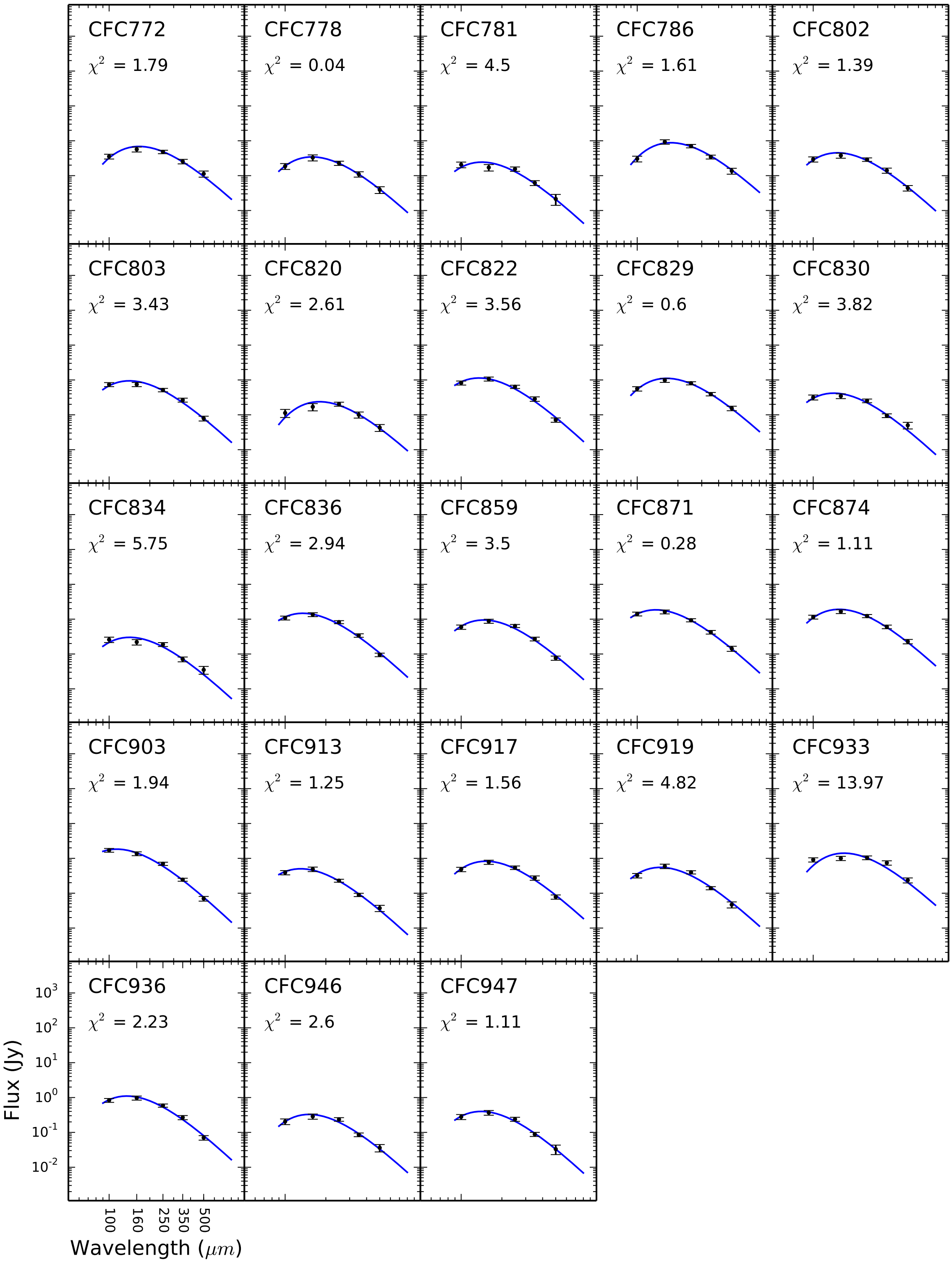
CFC772
χ^2 = 1.79
CFC778
χ^2 = 0.04
CFC781
χ^2 = 4.5
CFC786
χ^2 = 1.61
CFC802
χ^2 = 1.39
CFC803
χ^2 = 3.43
CFC820
χ^2 = 2.61
CFC822
χ^2 = 3.56
CFC829
χ^2 = 0.6
CFC830
χ^2 = 3.82
CFC834
χ^2 = 5.75
CFC836
χ^2 = 2.94
CFC859
χ^2 = 3.5
CFC871
χ^2 = 0.28
CFC874
χ^2 = 1.11
CFC903
χ^2 = 1.94
CFC913
χ^2 = 1.25
CFC917
χ^2 = 1.56
CFC919
χ^2 = 4.82
CFC933
χ^2 = 13.97
CFC936
χ^2 = 2.23
CFC946
χ^2 = 2.6
CFC947
χ^2 = 1.11
Flux (Jy)
10^3
10^2
10^1
10^0
10^{-1}
10^{-2}
100
160
250
350
500
Wavelength (μm)

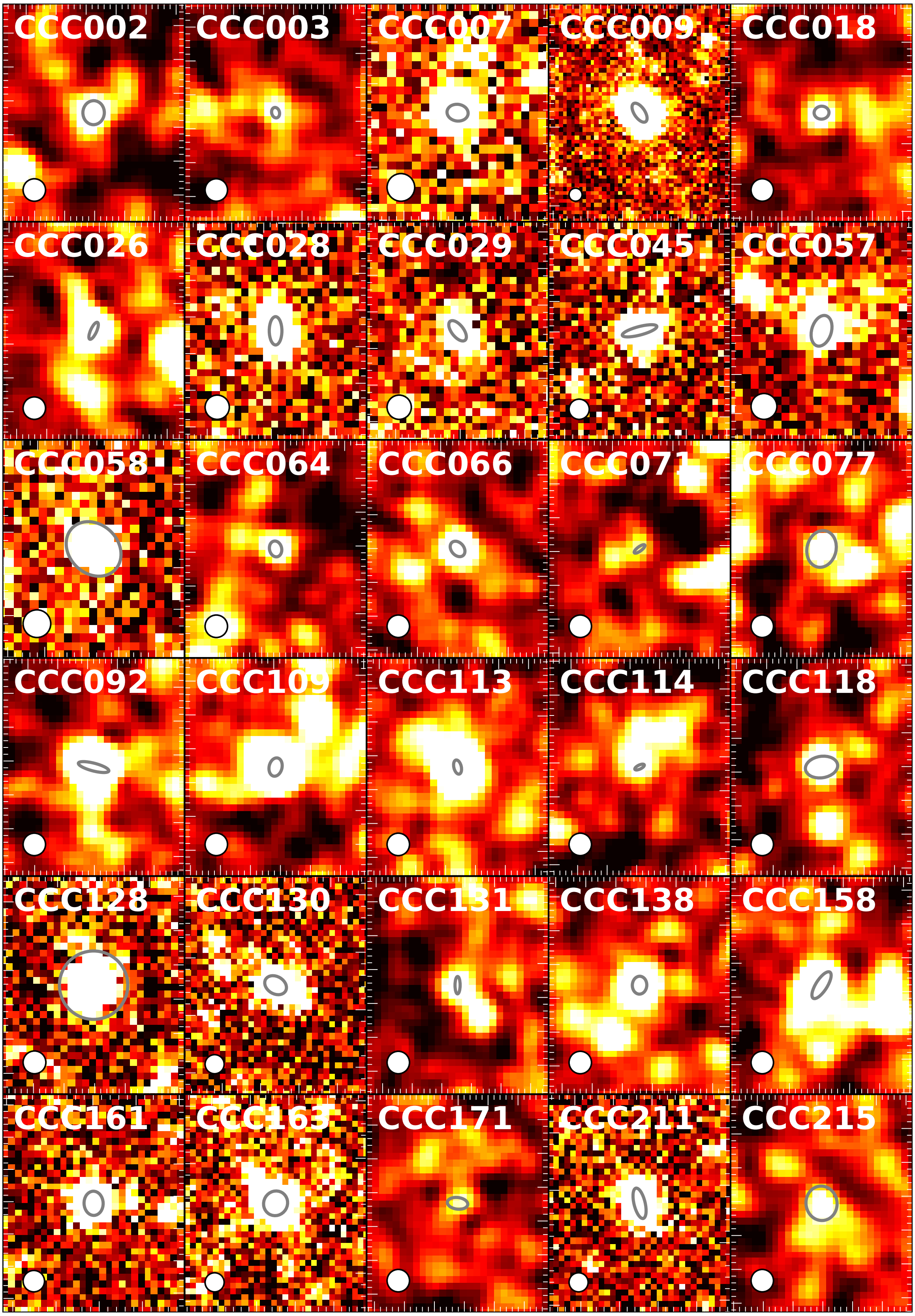

Figure B.-5. The CCC and CFC galaxies detected at 250 μm. The beam size is shown in the lower left hand corner. The grey ellipses indicate the optical extent (D_{25}) of each galaxy.

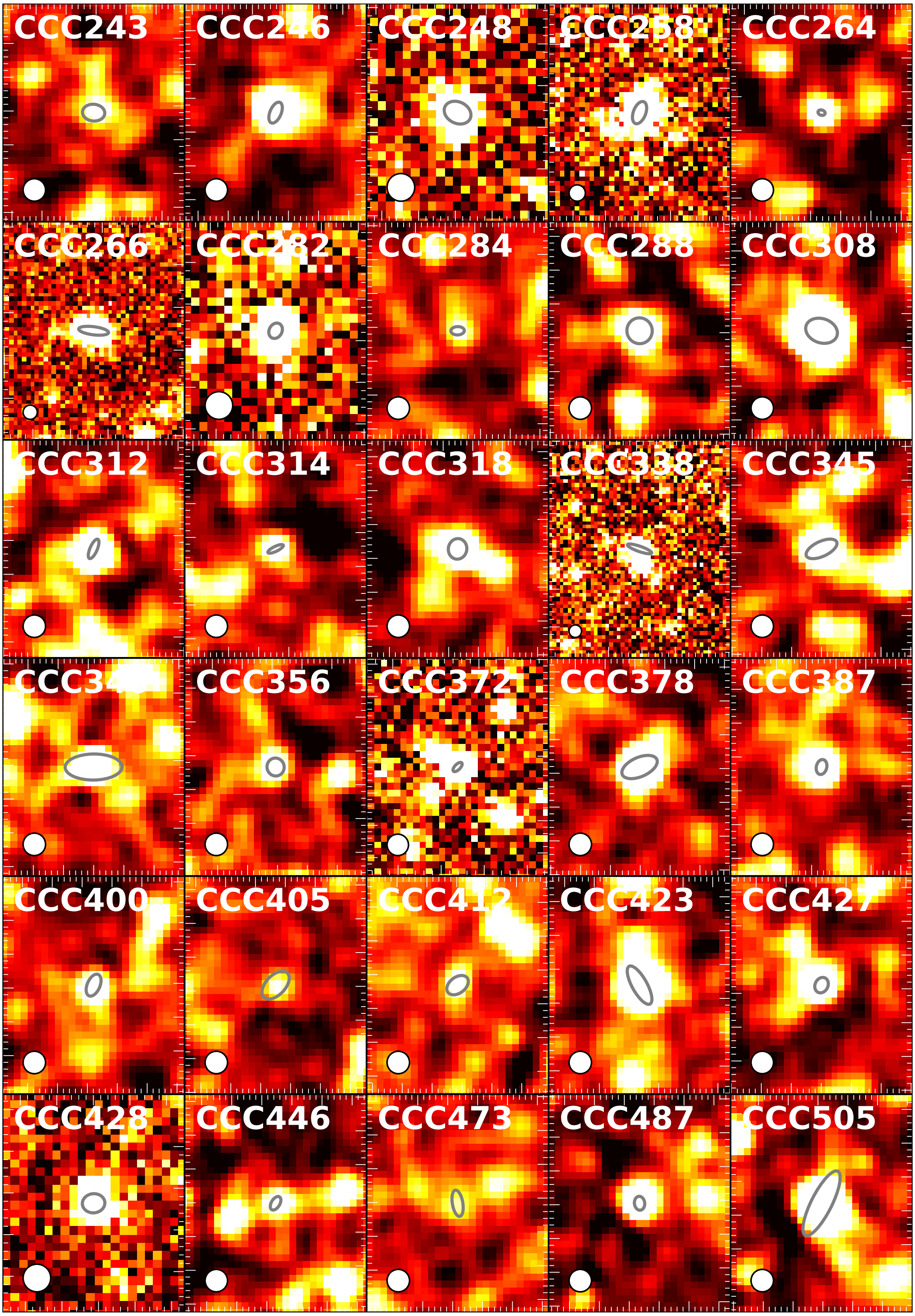
CCC243
CCC246
CCC248
CCC258
CCC264
CCC266
CCC282
CCC284
CCC288
CCC308
CCC312
CCC314
CCC318
CCC338
CCC345
CCC356
CCC372
CCC378
CCC387
CCC400
CCC405
CCC412
CCC423
CCC427
CCC428
CCC446
CCC473
CCC487
CCC505

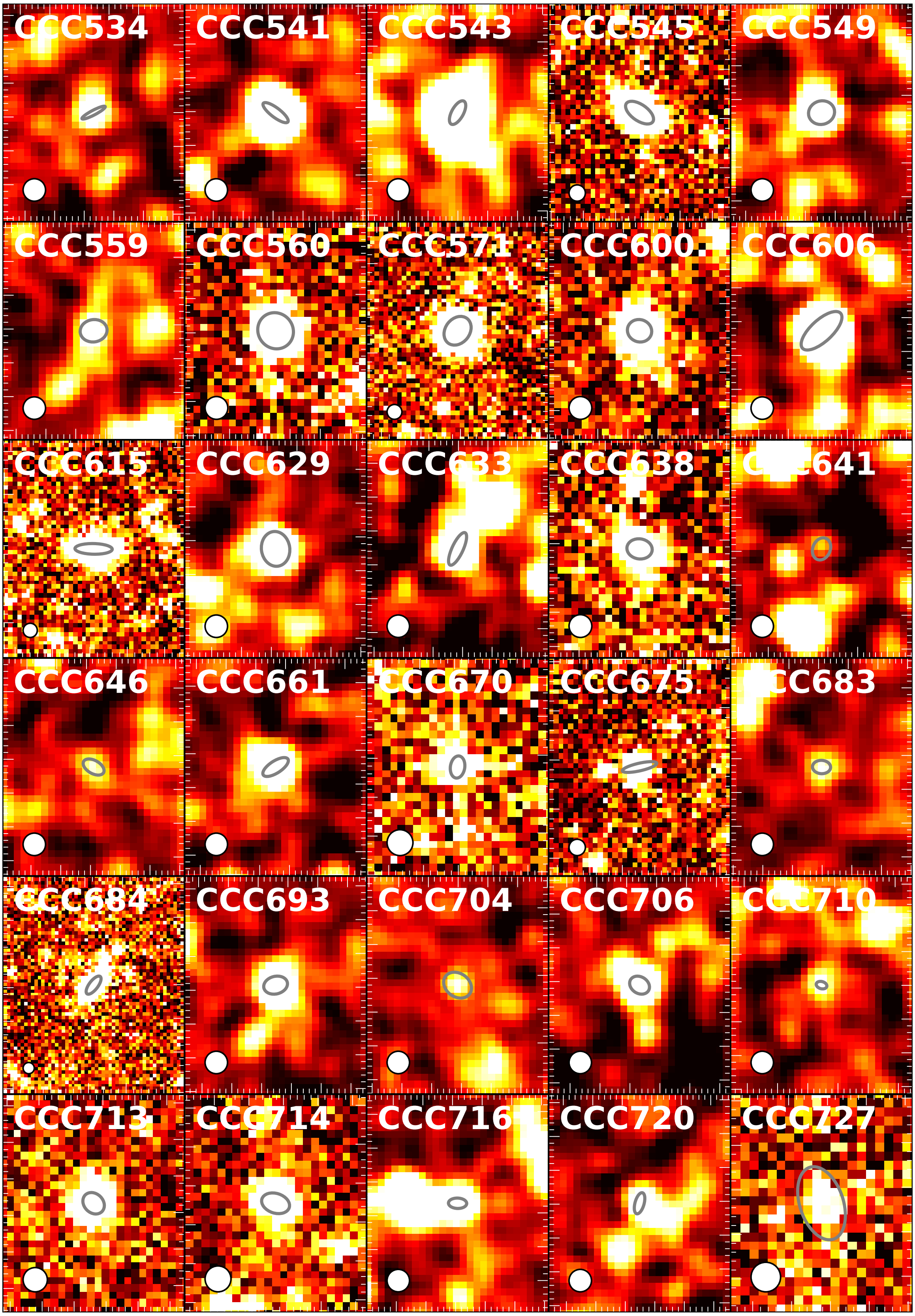
CCC534
CCC541
CCC543
CCC545
CCC549
CCC559
CCC560
CCC571
CCC600
CCC606
CCC615
CCC629
CCC633
CCC638
CCC641
CCC646
CCC661
CCC670
CCC675
CCC683
CCC684
CCC693
CCC704
CCC706
CCC710
CCC713
CCC714
CCC716
CCC720
CCC727

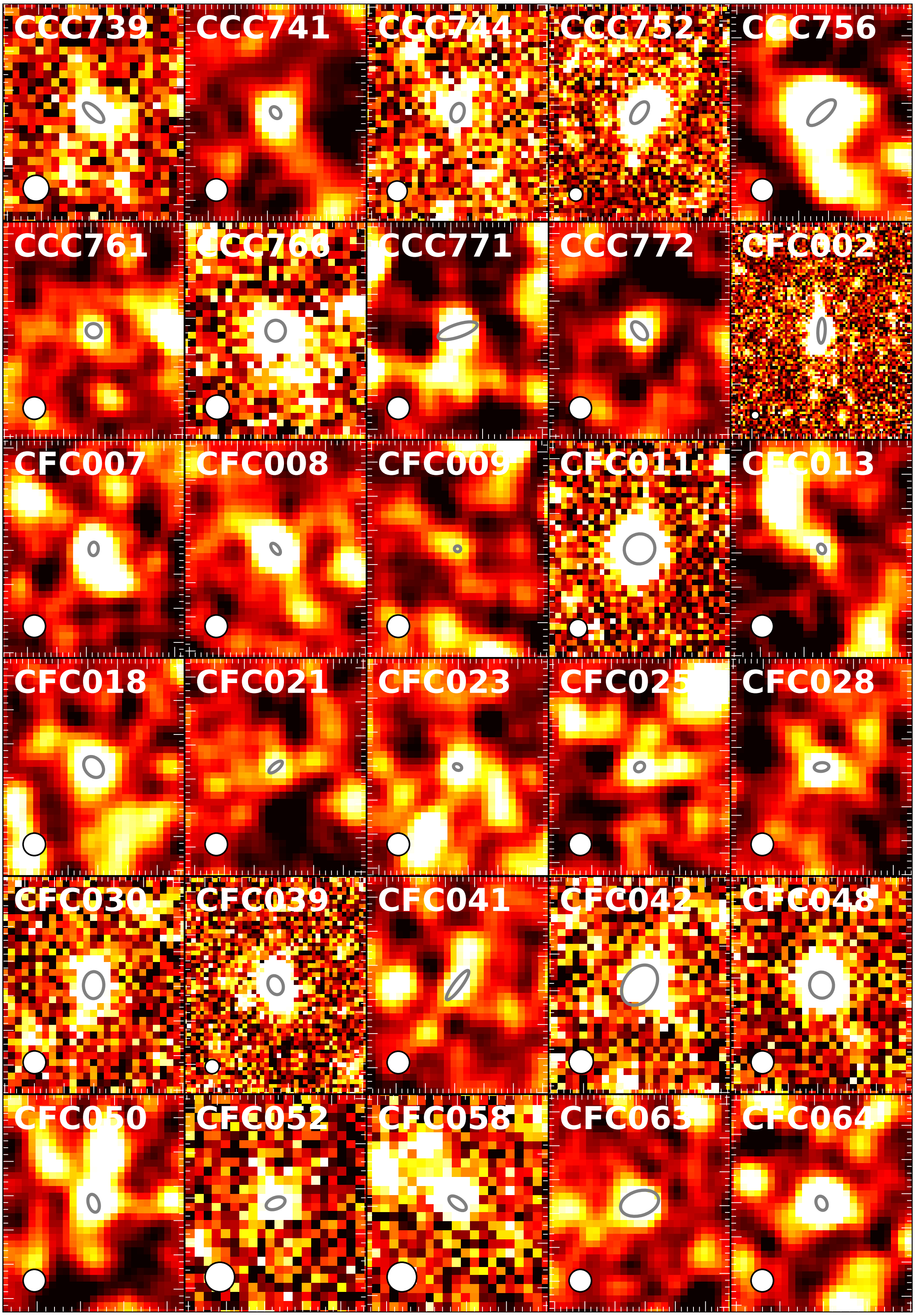
CCC739
CCC741
CCC744
CCC752
CCC756
CCC761
CCC766
CCC771
CCC772
CFC002
CFC007
CFC008
CFC009
CFC011
CFC013
CFC018
CFC021
CFC023
CFC025
CFC028
CFC030
CFC039
CFC041
CFC042
CFC048
CFC050
CFC052
CFC058
CFC063
CFC064

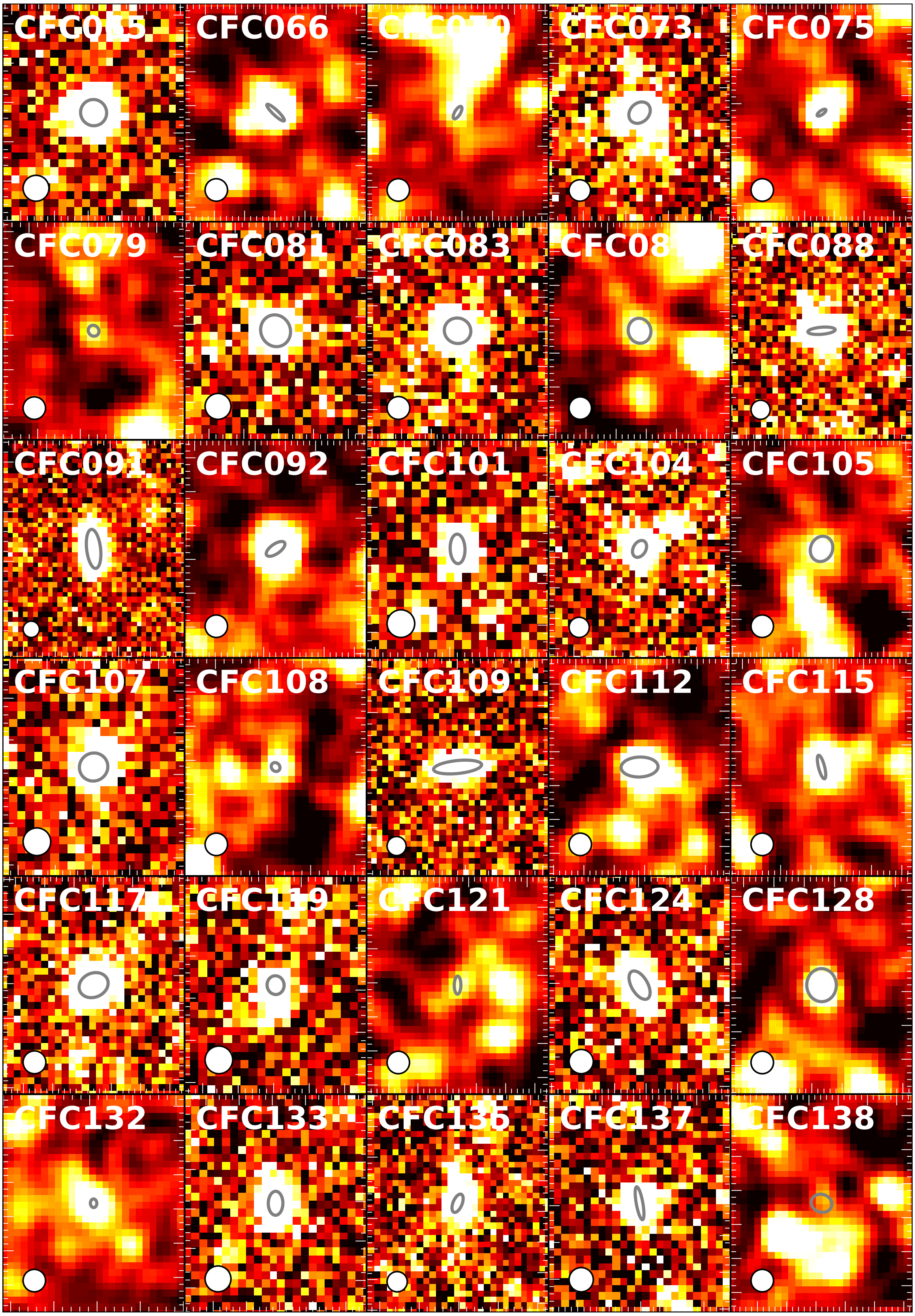
CFC066
CFC073
CFC075
CFC079
CFC081
CFC083
CFC088
CFC091
CFC092
CFC101
CFC104
CFC105
CFC107
CFC108
CFC109
CFC112
CFC115
CFC124
CFC128
CFC133
CFC137

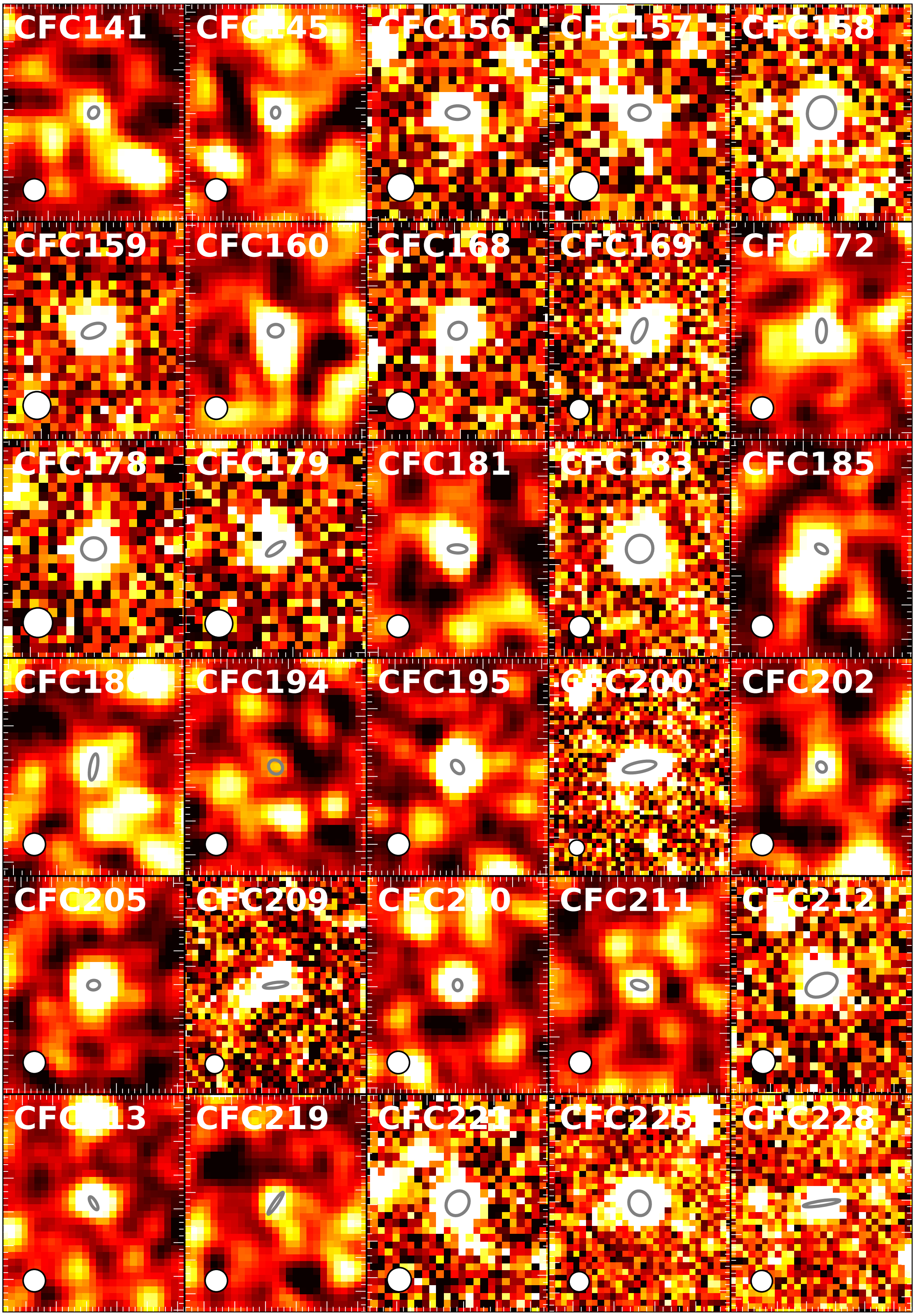
CFC141
CFC156
CFC157
CFC158
CFC159
CFC160
CFC168
CFC169
CFC178
CFC179
CFC181
CFC183
CFC185
CFC194
CFC195
CFC202
CFC205
CFC209
CFC211
CFC212
CFC219
CFC221
CFC225
CFC228

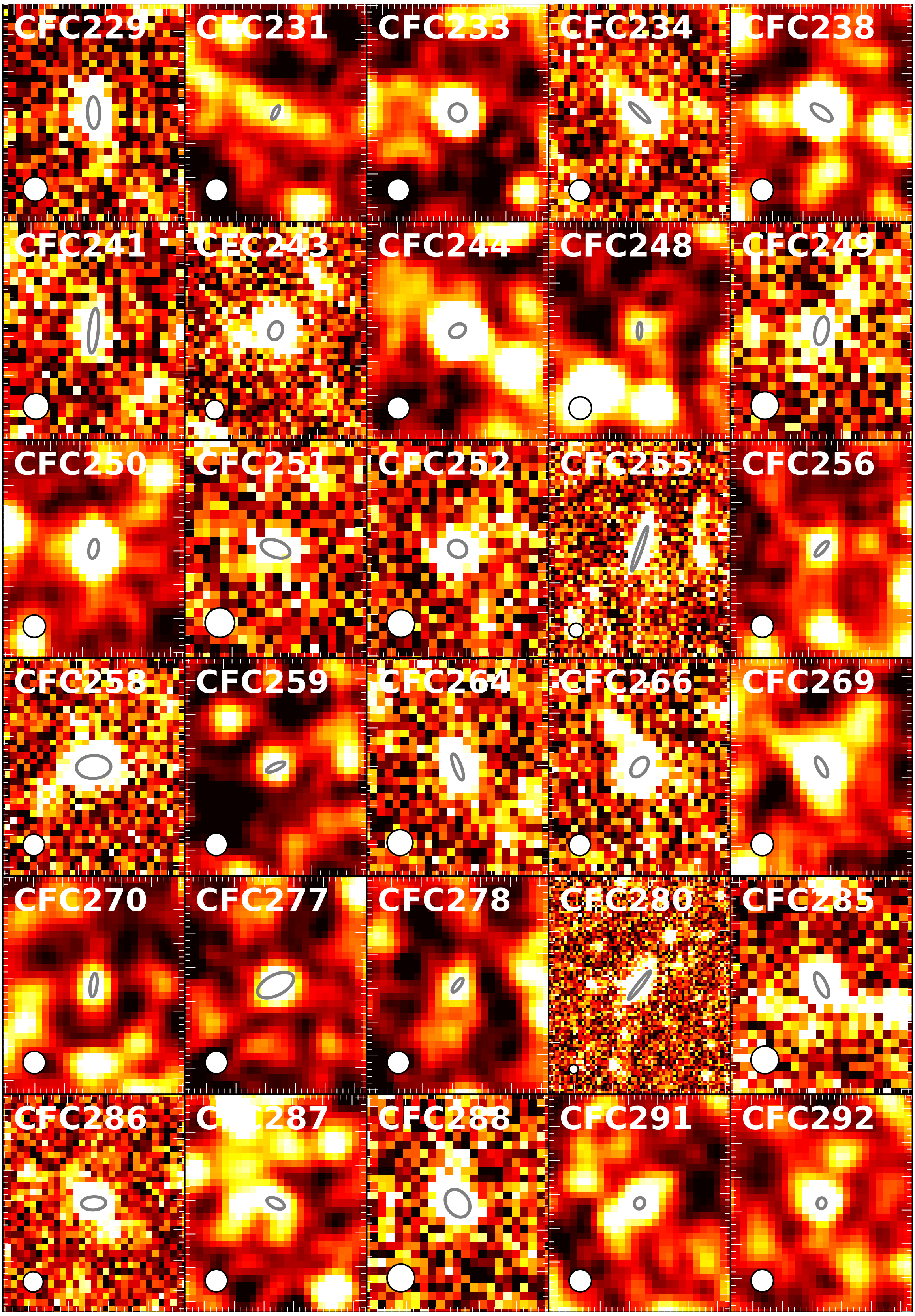
CFC229
CFC231
CFC233
CFC234
CFC238
CFC241
CFC243
CFC244
CFC248
CFC249
CFC250
CFC251
CFC252
CFC255
CFC256
CFC258
CFC259
CFC264
CFC266
CFC269
CFC270
CFC277
CFC278
CFC280
CFC285
CFC286
CFC287
CFC288
CFC291
CFC292

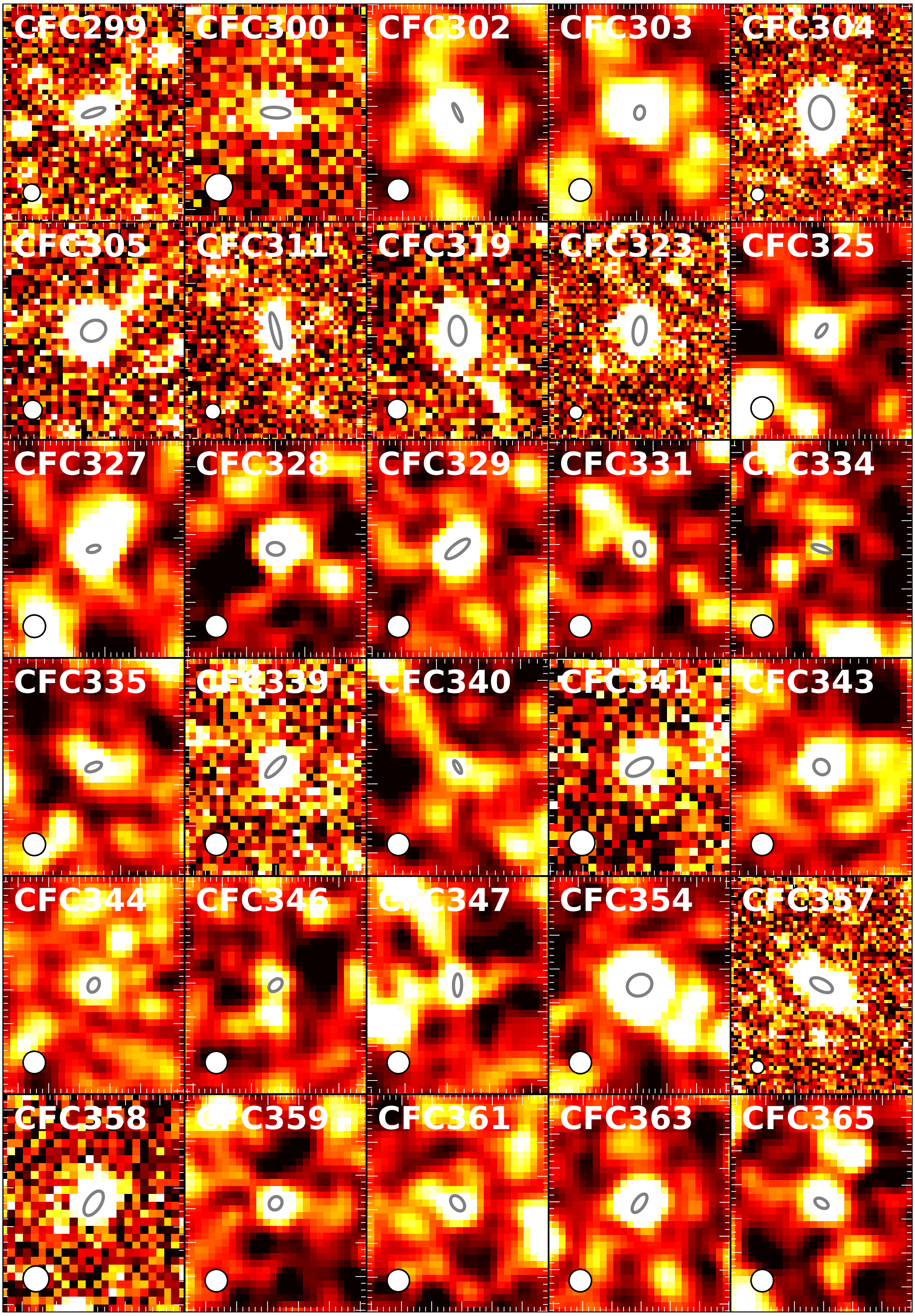
CFC299
CFC300
CFC302
CFC303
CFC304
CFC305
CFC311
CFC319
CFC323
CFC325
CFC327
CFC328
CFC329
CFC331
CFC334
CFC335
CFC339
CFC340
CFC341
CFC343
CFC344
CFC346
CFC347
CFC354
CFC357
CFC358
CFC359
CFC361
CFC363
CFC365

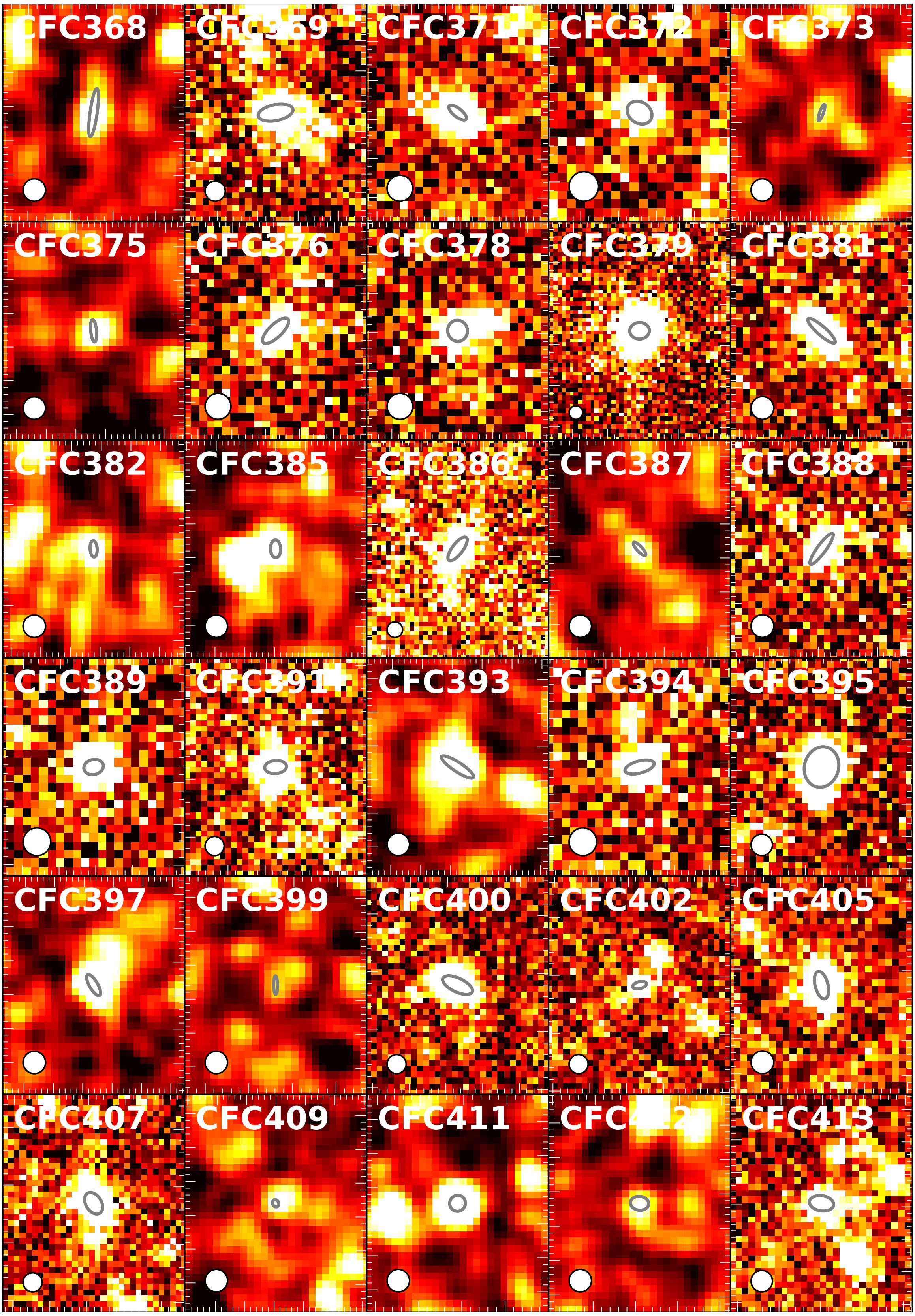
CFC368
CFC371
CFC375
CFC376
CFC378
CFC379
CFC381
CFC382
CFC385
CFC386
CFC387
CFC388
CFC389
CFC391
CFC393
CFC394
CFC395
CFC397
CFC399
CFC400
CFC402
CFC405
CFC407
CFC409
CFC411
CFC413

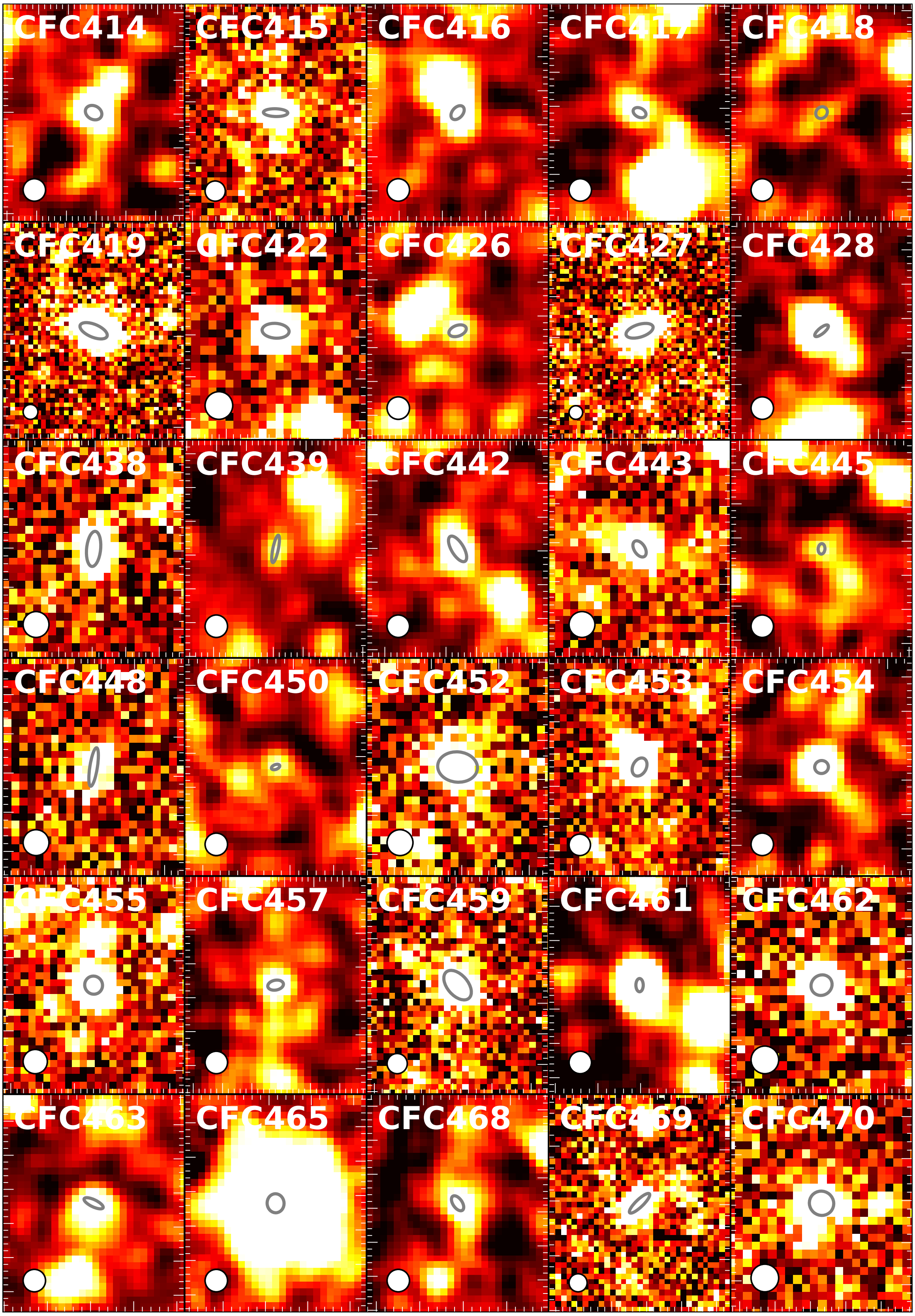
CFC414
CFC415
CFC416
CFC417
CFC418
CFC419
CFC422
CFC426
CFC427
CFC428
CFC438
CFC439
CFC442
CFC443
CFC445
CFC448
CFC450
CFC452
CFC453
CFC454
CFC455
CFC457
CFC459
CFC461
CFC462
CFC463
CFC465
CFC468
CFC469
CFC470

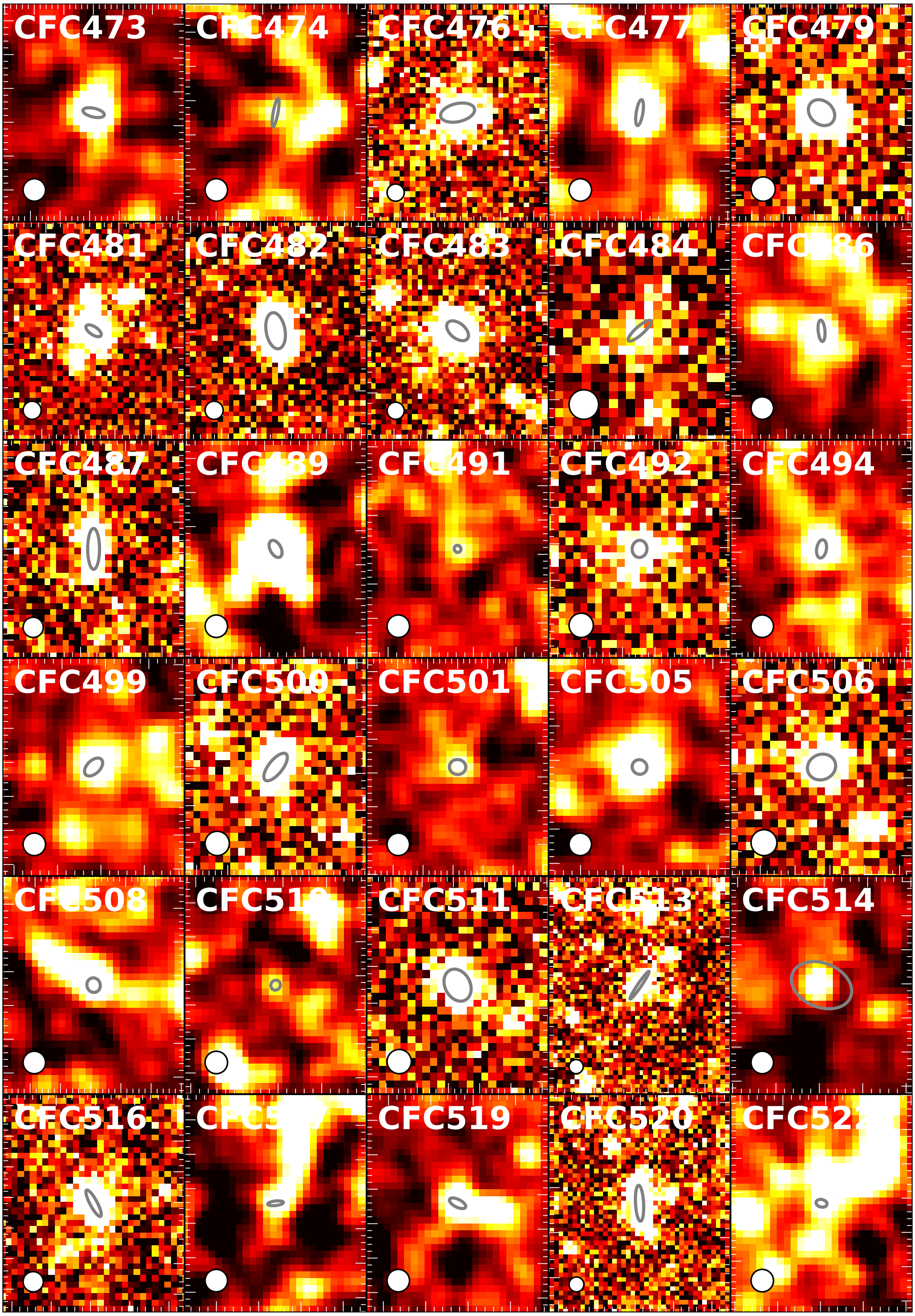
CFC473
CFC474
CFC476
CFC477
CFC479
CFC481
CFC482
CFC483
CFC484
CFC487
CFC492
CFC494
CFC499
CFC500
CFC501
CFC505
CFC506
CFC508
CFC511
CFC513
CFC514
CFC516
CFC519
CFC520

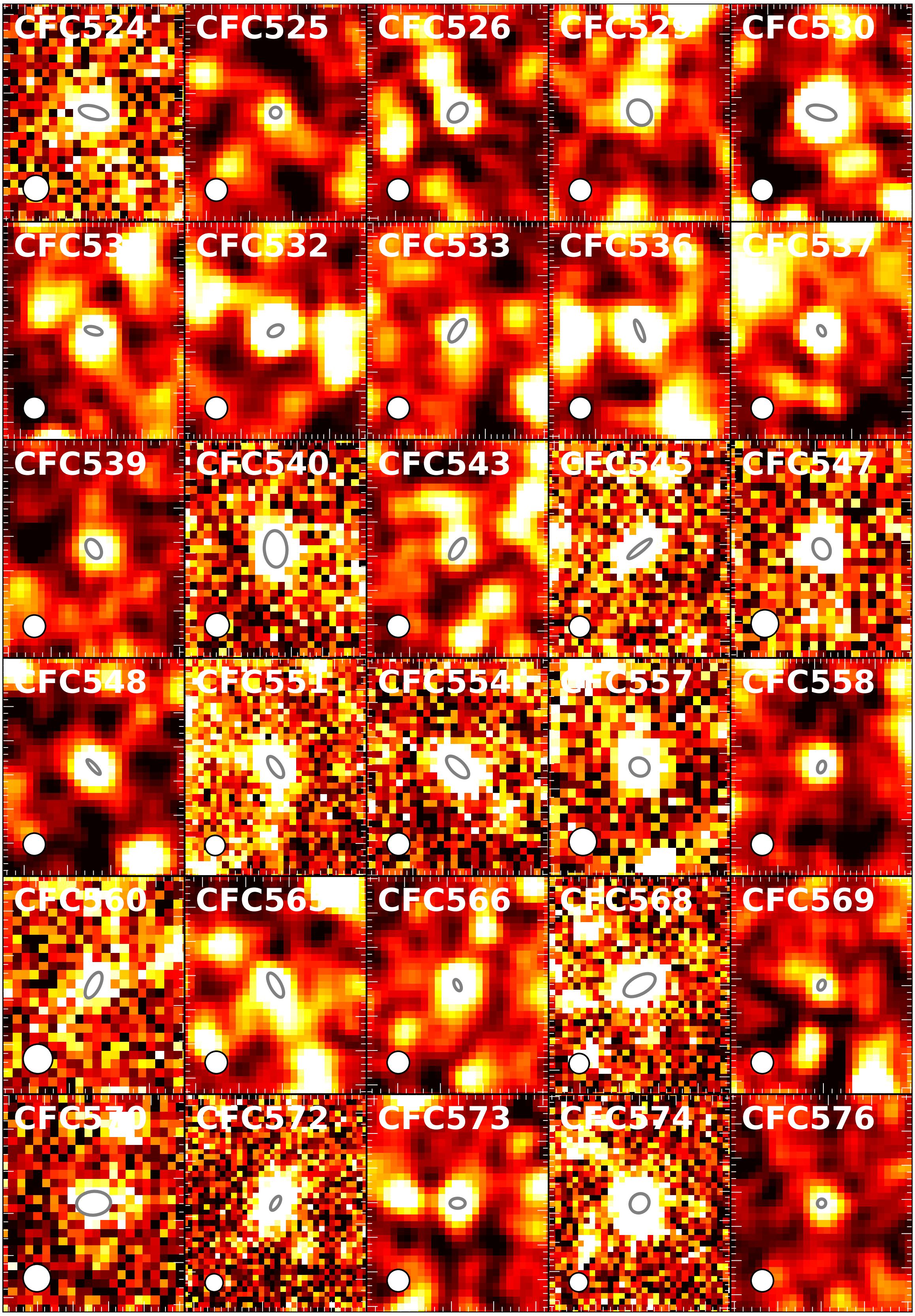
CFC524
CFC525
CFC526
CFC530
CFC532
CFC533
CFC536
CFC539
CFC540
CFC543
CFC545
CFC547
CFC548
CFC554
CFC557
CFC558
CFC566
CFC568
CFC569
CFC572
CFC573
CFC574
CFC576

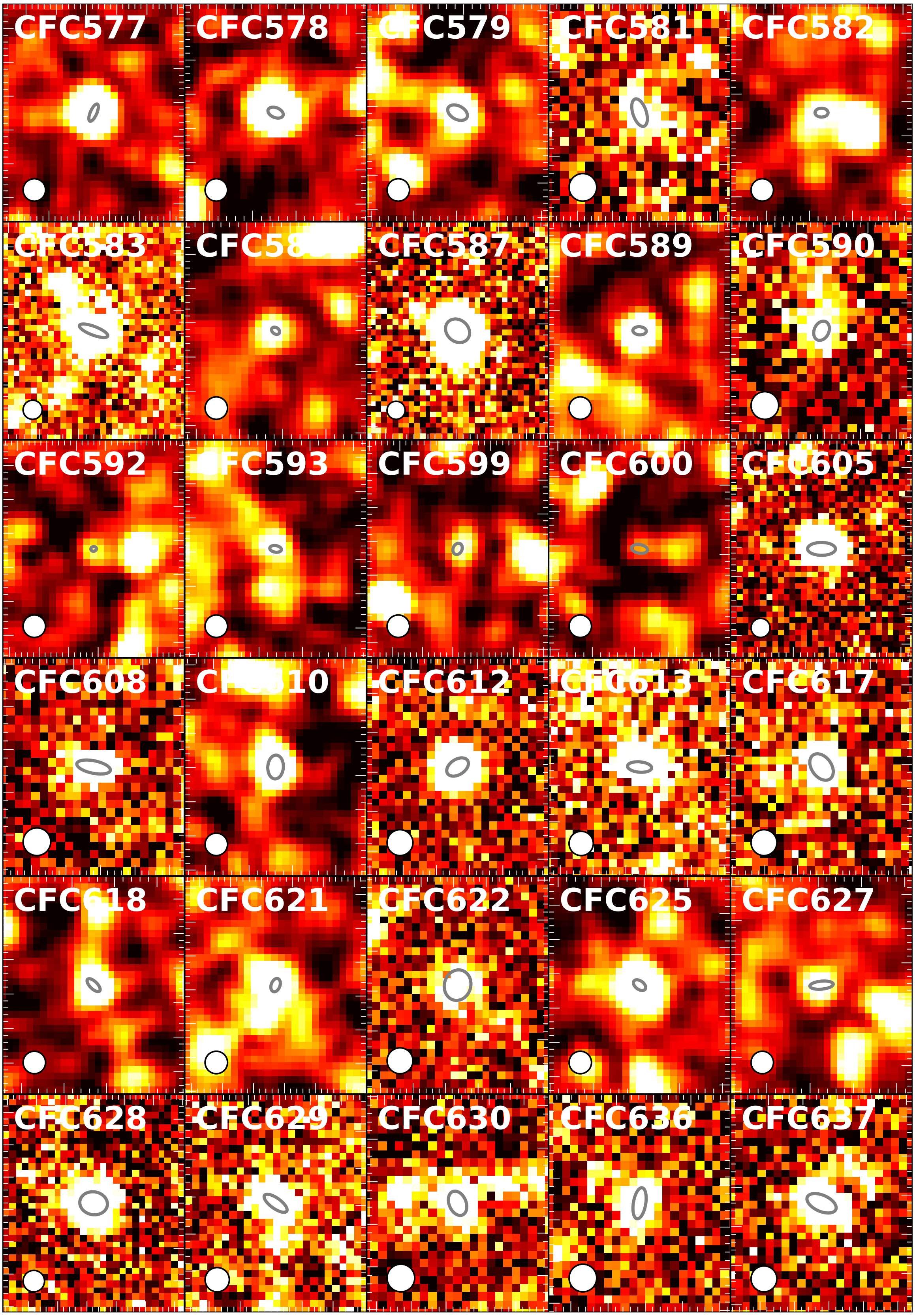
CFC577
CFC578
CFC579
CFC581
CFC582
CFC583
CFC587
CFC589
CFC590
CFC592
CFC593
CFC599
CFC600
CFC605
CFC608
CFC612
CFC613
CFC617
CFC618
CFC621
CFC622
CFC625
CFC627
CFC628
CFC629
CFC630
CFC636
CFC637

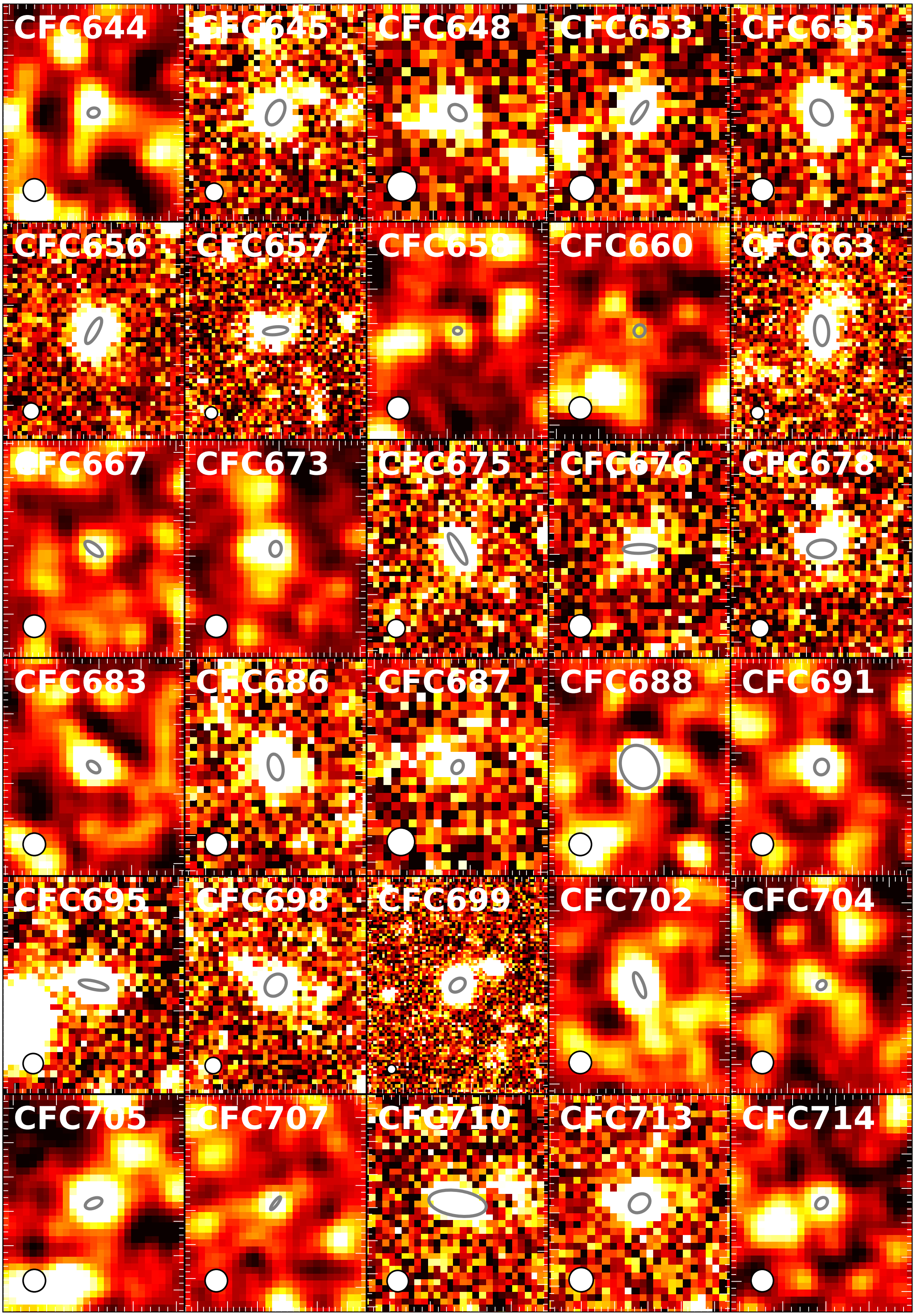
CFC644
CFC645
CFC648
CFC653
CFC655
CFC656
CFC657
CFC658
CFC660
CFC663
CFC667
CFC673
CFC675
CFC676
CFC678
CFC683
CFC686
CFC687
CFC688
CFC691
CFC695
CFC698
CFC699
CFC702
CFC704
CFC705
CFC707
CFC710
CFC713
CFC714

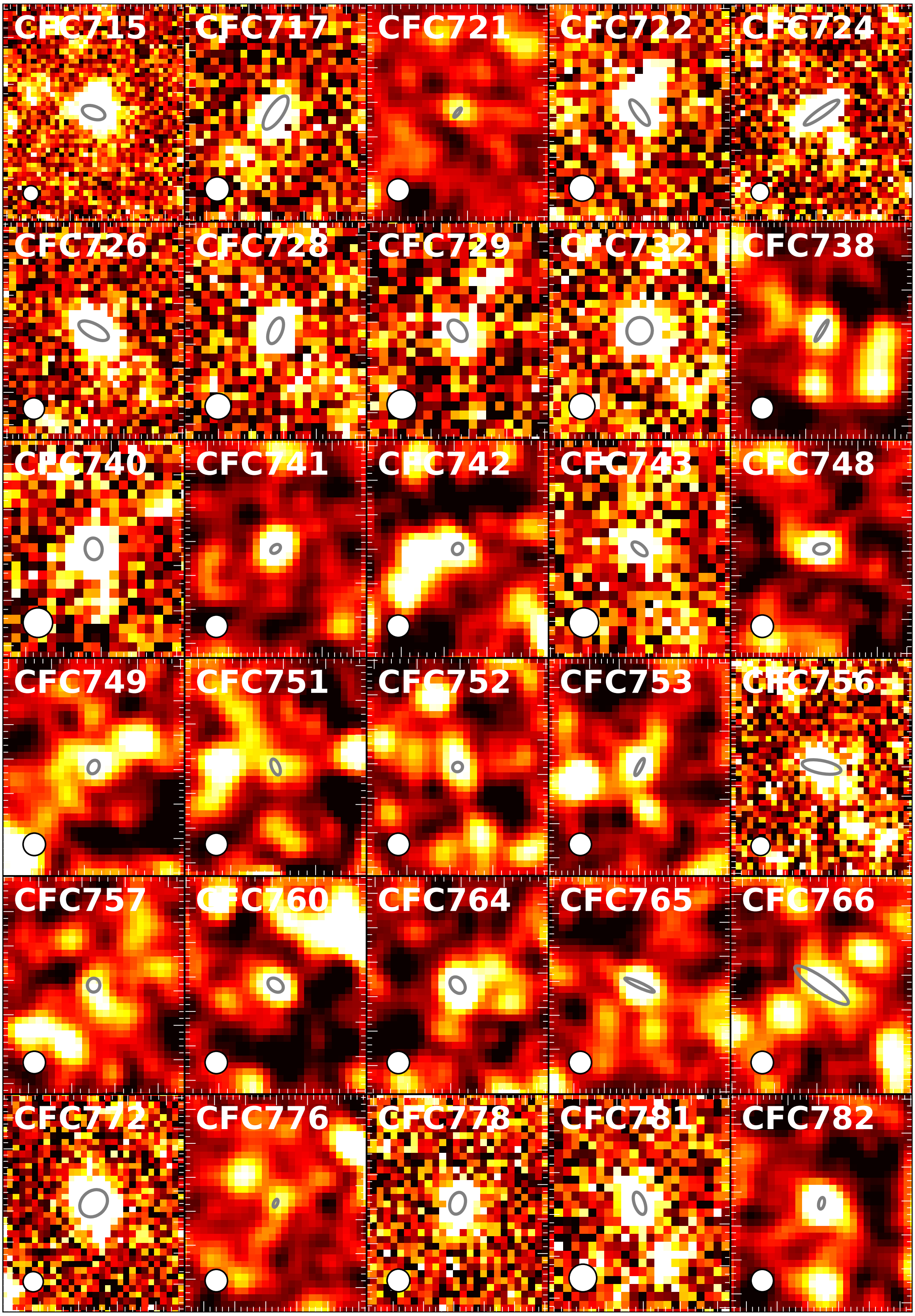
CFC715
CFC717
CFC721
CFC722
CFC724
CFC726
CFC728
CFC729
CFC732
CFC738
CFC740
CFC741
CFC742
CFC743
CFC748
CFC749
CFC751
CFC752
CFC753
CFC756
CFC757
CFC760
CFC764
CFC765
CFC766
CFC772
CFC776
CFC778
CFC781
CFC782

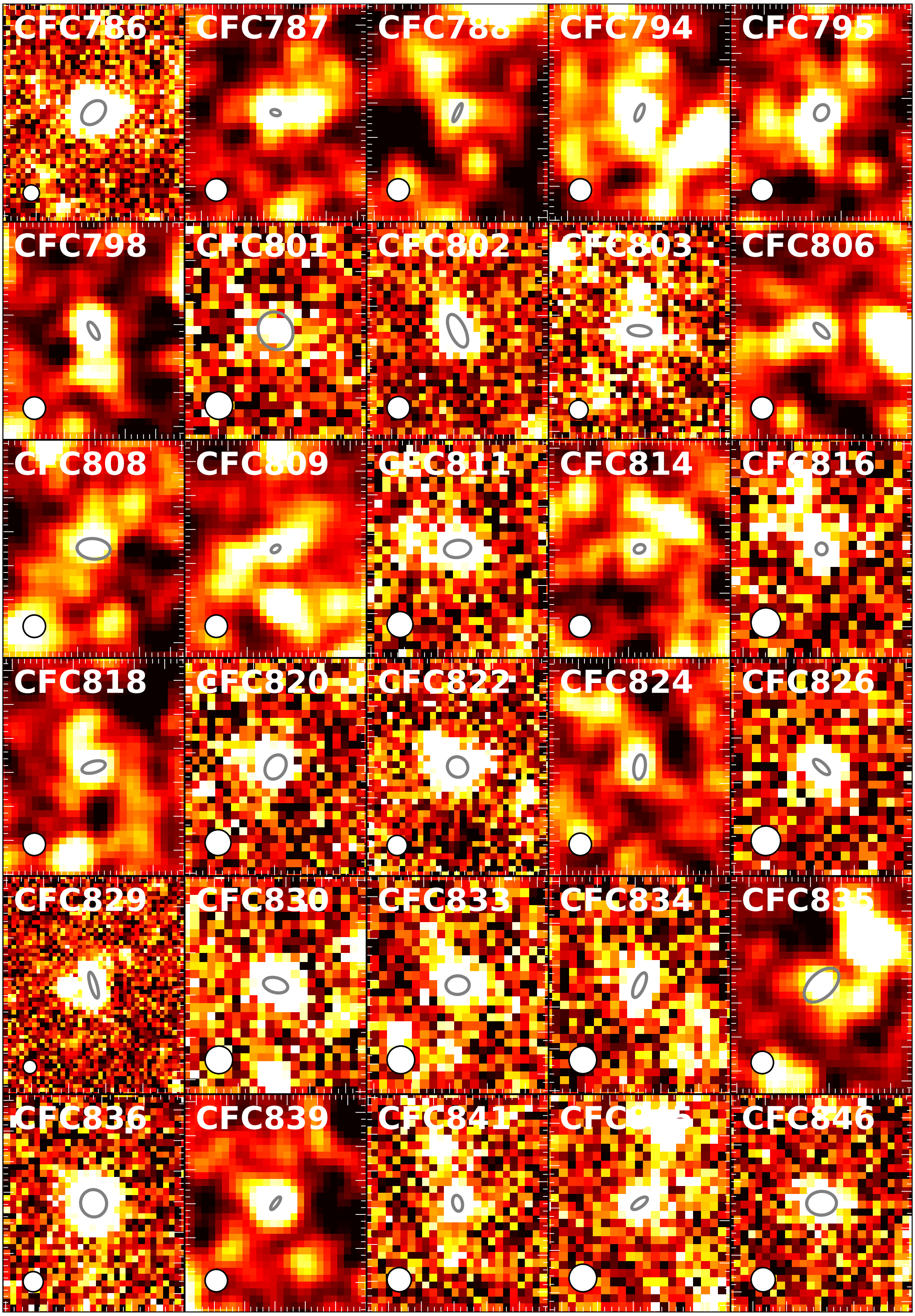
CFC786
CFC787
CFC794
CFC795
CFC798
CFC801
CFC802
CFC803
CFC806
CFC808
CFC814
CFC818
CFC820
CFC822
CFC824
CFC826
CFC829
CFC830
CFC833
CFC834
CFC836
CFC839
CFC841
CFC846

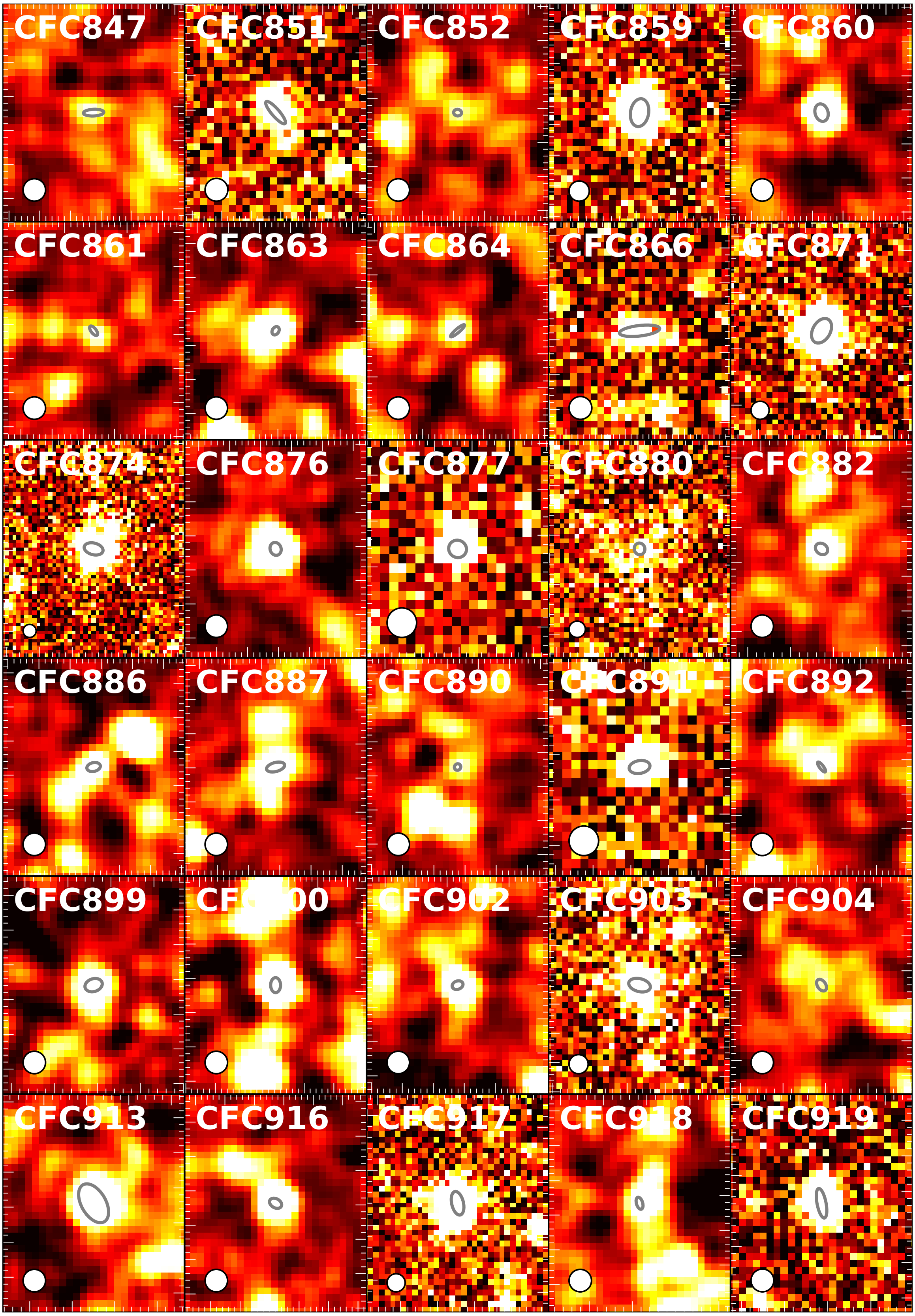
CFC847
CFC851
CFC852
CFC859
CFC860
CFC861
CFC863
CFC864
CFC866
CFC871
CFC874
CFC876
CFC877
CFC880
CFC882
CFC886
CFC887
CFC890
CFC891
CFC892
CFC899
CFC902
CFC903
CFC904
CFC913
CFC916
CFC917
CFC919

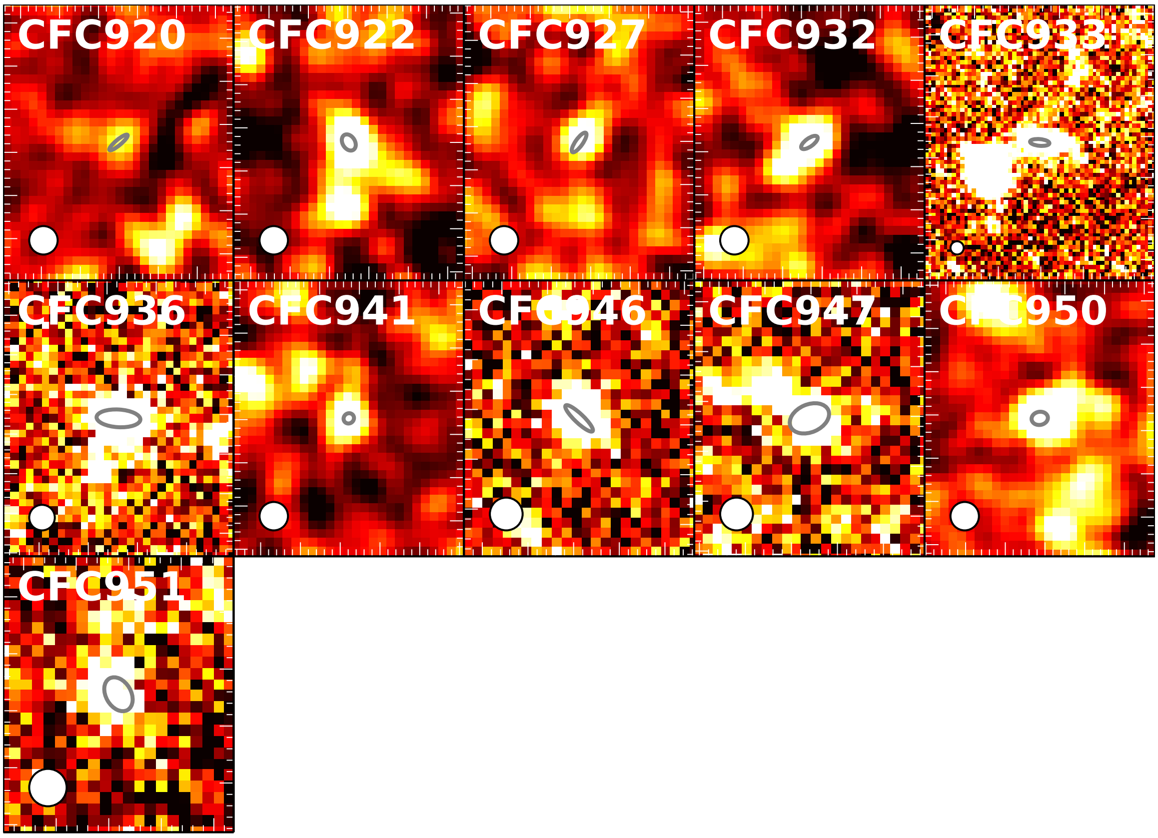
CFC920
CFC922
CFC927
CFC932
CFC933
CFC936
CFC941
CFC946
CFC947
CFC950
CFC951

OBJECT	RA h:m:s (J2000)	Dec. d:m:s (J2000)	S_{500} (mJy)	E_{500} (mJy)	S_{350} (mJy)	E_{350} (mJy)	S_{250} (mJy)	E_{250} (mJy)	S_{160} (mJy)	E_{160} (mJy)	S_{100} (mJy)	E_{100} (mJy)
CFC001	12:45:45	+31:52:34	0	26	0	32	0	20	0	40	0	22
CFC002	12:46:10	+30:43:54	305	38	957	97	2416	236	4710	577	4626	563
CFC003	12:46:15	+30:38:05	0	26	0	27	0	26	0	28	0	22
CFC004	12:46:18	+32:11:15	0	28	0	28	0	21	0	29	0	20
CFC005	12:46:19	+31:05:04	0	35	0	24	0	23	0	23	0	14
CFC006	12:46:25	+32:10:54	0	26	0	29	0	22	0	28	0	21
CFC007	12:46:27	+30:30:56	25	8	48	8	86	9	0	9	0	7
CFC008	12:46:29	+30:50:55	23	7	44	8	87	10	180	40	140	28
CFC009	12:47:00	+30:43:39	0	27	0	22	22	5	0	26	0	18
CFC010	12:47:02	+32:52:16	0	25	0	24	0	22	0	25	0	22
CFC011	12:47:26	+29:47:16	147	26	435	49	930	94	1451	193	563	96
CFC012	12:47:34	+30:37:11	0	31	0	19	0	19	0	25	0	16
CFC013	12:47:37	+31:43:29	0	25	28	8	31	6	0	24	0	22
CFC014	12:47:39	+33:40:17	0	20	0	21	0	19	0	28	0	19
CFC015	12:47:39	+30:36:36	0	35	0	23	0	19	0	26	0	19
CFC016	12:47:54	+30:22:25	0	29	0	26	0	16	0	26	0	18
CFC017	12:47:58	+28:10:26	0	27	0	13	0	14	0	22	0	19
CFC018	12:48:05	+29:26:35	34	9	37	7	66	8	0	23	0	27
CFC019	12:48:24	+28:18:24	0	27	0	21	0	18	0	22	0	16
CFC020	12:48:24	+30:42:37	0	23	0	20	0	15	0	27	0	24
CFC021	12:48:30	+29:15:36	0	26	0	24	28	6	0	27	0	18
CFC022	12:48:36	+27:21:59	0	23	0	15	0	18	0	29	0	16
CFC023	12:48:38	+29:11:25	0	26	28	7	42	6	0	12	0	6
CFC024	12:48:42	+29:14:21	0	23	0	21	0	20	0	31	0	23
CFC025	12:48:46	+30:53:19	0	22	24	7	36	5	0	8	0	16
CFC026	12:48:46	+30:58:55	0	25	0	25	0	15	0	22	0	16
CFC027	12:48:49	+29:25:27	0	24	0	21	0	19	0	31	0	19
CFC028	12:48:58	+27:50:08	0	19	27	7	55	8	0	11	0	21
CFC029	12:49:02	+26:53:35	0	26	0	21	0	18	0	30	0	16
CFC030	12:49:03	+30:55:35	88	20	171	31	234	32	0	8	0	6
CFC031	12:49:07	+27:47:50	0	24	0	17	0	21	0	27	0	20
CFC032	12:49:08	+27:22:07	0	25	0	22	0	17	0	23	0	16
CFC033	12:49:11	+27:23:06	0	25	0	22	0	16	0	26	0	17
CFC034	12:49:15	+28:29:51	0	25	0	18	0	22	0	22	0	14
CFC035	12:49:22	+26:44:38	0	27	0	18	0	19	0	28	0	19
CFC036	12:49:23	+29:19:16	0	21	0	25	0	20	0	23	0	23
CFC037	12:49:27	+27:16:03	0	21	0	26	0	17	0	31	0	19
CFC038	12:49:35	+27:11:51	0	25	0	28	0	19	0	22	0	20
CFC039	12:49:36	+30:50:43	182	28	528	64	1047	110	1306	170	826	113
CFC040	12:49:41	+28:50:41	0	20	0	20	0	22	0	28	0	24
CFC041	12:49:41	+30:45:08	21	6	0	28	37	6	0	8	0	15
CFC042	12:49:42	+26:53:31	79	11	180	29	339	39	541	81	558	80
CFC043	12:49:42	+34:05:57	0	23	0	22	0	33	0	23	0	19
CFC044	12:49:44	+27:40:10	0	25	0	25	0	26	0	25	0	16
CFC045	12:49:44	+27:35:30	0	25	0	22	0	19	0	28	0	20
CFC046	12:49:45	+27:22:08	0	23	0	21	0	20	0	31	0	18
CFC047	12:49:46	+27:38:26	0	24	0	23	0	23	0	26	0	18
CFC048	12:49:47	+32:04:49	67	11	212	27	514	55	715	99	792	110
CFC049	12:49:57	+27:49:20	0	21	0	22	0	24	0	29	0	19
CFC050	12:49:58	+32:23:19	40	9	44	9	65	9	0	25	0	21
CFC051	12:49:59	+27:09:09	0	25	0	26	0	21	0	30	0	18
CFC052	12:50:09	+32:00:23	27	7	43	7	87	16	0	12	0	7
CFC053	12:50:11	+27:22:11	0	20	0	19	0	17	0	26	0	28
CFC054	12:50:13	+26:46:33	0	29	0	25	0	18	0	24	0	17
CFC055	12:50:15	+27:03:37	0	23	0	21	0	17	0	19	0	18
CFC056	12:50:16	+27:22:48	0	23	0	22	0	17	0	26	0	24
CFC057	12:50:19	+27:19:26	0	20	0	21	0	18	0	25	0	20
CFC058	12:50:20	+26:44:59	45	11	56	10	126	19	241	46	140	28
CFC059	12:50:20	+27:56:13	0	24	0	16	0	18	0	22	0	20
CFC060	12:50:22	+27:10:31	0	21	0	18	0	18	0	29	0	21
CFC061	12:50:26	+26:42:32	0	29	0	25	0	15	0	28	0	19
CFC062	12:50:26	+26:44:07	0	32	0	29	0	17	0	26	0	27
CFC063	12:50:28	+27:26:05	0	24	24	7	69	8	0	11	150	29
CFC064	12:50:29	+31:36:25	0	24	66	8	157	16	373	56	350	52
CFC065	12:50:31	+30:50:48	52	8	189	26	430	46	867	122	424	60
CFC066	12:50:31	+27:18:50	26	7	68	8	102	11	158	34	126	26
CFC067	12:50:37	+27:28:58	0	22	0	21	0	17	0	24	0	19
CFC068	12:50:45	+34:03:57	0	26	0	19	0	19	0	25	0	17
CFC069	12:50:51	+31:02:24	0	26	0	20	0	27	0	23	0	22
CFC070	12:50:51	+25:15:32	25	8	38	6	32	6	0	24	0	24
CFC071	12:50:52	+34:09:24	0	24	0	20	0	18	0	25	0	18
CFC072	12:50:54	+27:50:30	0	24	0	20	0	16	0	25	0	19
CFC073	12:51:01	+28:55:40	68	10	271	39	567	60	1046	134	1039	134
CFC074	12:51:03	+26:26:44	0	24	0	20	0	16	0	26	0	20
CFC075	12:51:06	+29:11:48	0	24	33	8	58	7	0	27	109	27
CFC076	12:51:07	+27:19:13	0	24	0	22	0	18	0	24	0	18
CFC077	12:51:08	+28:47:17	0	104	0	222	0	392	0	529	0	320
CFC078	12:51:09	+27:24:24	0	25	0	19	0	16	0	29	0	23
CFC079	12:51:10	+34:03:29	0	23	0	17	22	6	0	22	0	21
CFC080	12:51:15	+27:33:44	0	23	0	25	0	18	0	26	0	19
CFC081	12:51:17	+27:06:22	56	10	129	13	348	39	523	79	249	41
CFC082	12:51:18	+33:10:01	0	27	0	27	0	17	0	21	0	20
CFC083	12:51:19	+31:03:34	92	22	161	27	322	41	595	95	179	36
CFC084	12:51:20	+34:06:08	0	26	0	20	0	19	0	25	0	19
CFC085	12:51:25	+28:43:13	0	23	0	25	0	16	0	31	0	17
CFC086	12:51:25	+28:07:14	0	23	0	25	0	23	0	24	0	18
CFC087	12:51:26	+27:25:16	0	25	0	20	32	7	0	9	0	18
CFC088	12:51:29	+31:48:52	107	12	326	31	878	87	1776	223	1328	165
CFC089	12:51:35	+26:37:44	0	24	0	28	0	16	0	21	0	21
CFC090	12:51:37	+27:18:38	0	22	0	24	0	13	0	29	0	20

Continued on next page

OBJECT	RA h:m:s (J2000)	Dec. d:m:s (J2000)	S_{500} (mJy)	E_{500} (mJy)	S_{350} (mJy)	E_{350} (mJy)	S_{250} (mJy)	E_{250} (mJy)	S_{160} (mJy)	E_{160} (mJy)	S_{100} (mJy)	E_{100} (mJy)
CFC091	12:51:37	+31:21:09	105	20	235	31	471	53	550	90	0	5
CFC092	12:51:44	+27:01:06	33	10	76	9	159	16	258	44	222	37
CFC093	12:51:50	+27:21:38	0	21	0	16	0	17	0	27	0	22
CFC094	12:51:51	+27:07:06	0	25	0	17	0	17	0	29	0	21
CFC095	12:51:51	+27:15:20	0	22	0	19	0	14	0	33	0	20
CFC096	12:51:55	+26:33:29	0	31	0	26	0	17	0	24	0	20
CFC097	12:51:55	+26:46:58	0	26	0	23	0	21	0	26	0	19
CFC098	12:51:56	+27:05:18	0	31	0	21	0	18	0	27	0	18
CFC099	12:52:00	+26:09:33	0	21	0	21	0	21	0	29	0	26
CFC100	12:52:03	+34:11:12	0	22	0	20	0	21	0	28	0	18
CFC101	12:52:03	+27:09:57	40	9	71	10	183	23	226	46	0	7
CFC102	12:52:05	+29:17:17	0	34	0	21	0	18	0	23	0	20
CFC103	12:52:05	+26:11:54	0	24	0	19	0	17	0	26	0	26
CFC104	12:52:06	+27:01:34	50	11	178	27	453	53	650	87	585	79
CFC105	12:52:11	+26:52:29	0	25	0	30	35	7	0	25	0	6
CFC106	12:52:17	+27:09:29	0	21	0	20	0	18	0	32	0	25
CFC107	12:52:17	+27:05:07	36	8	120	13	338	37	627	86	470	64
CFC108	12:52:23	+31:41:50	0	20	0	21	43	7	0	11	0	7
CFC109	12:52:36	+26:44:59	46	8	144	24	271	33	0	10	0	18
CFC110	12:52:36	+30:25:00	0	23	0	19	0	22	0	27	0	23
CFC111	12:52:41	+26:21:57	0	21	0	17	0	17	0	23	0	16
CFC112	12:52:44	+26:28:13	0	21	46	7	109	12	193	37	199	33
CFC113	12:52:56	+26:35:40	0	24	0	23	0	15	0	29	0	20
CFC114	12:52:58	+32:24:44	0	24	0	25	0	69	0	26	0	22
CFC115	12:52:59	+26:43:13	0	23	60	9	85	10	0	11	0	7
CFC116	12:52:59	+32:08:12	0	25	0	22	0	20	0	30	0	26
CFC117	12:53:02	+32:06:25	53	9	184	26	414	47	672	97	455	75
CFC118	12:53:03	+26:28:35	0	21	0	21	0	19	0	25	0	20
CFC119	12:53:03	+32:19:36	0	23	43	8	121	22	0	24	0	8
CFC120	12:53:21	+26:21:41	0	22	0	17	0	21	0	24	0	18
CFC121	12:53:31	+30:43:24	0	24	29	7	22	6	0	34	0	7
CFC122	12:53:43	+31:56:29	0	21	0	19	0	17	0	29	0	21
CFC123	12:53:44	+32:42:15	0	24	0	18	0	17	0	19	0	21
CFC124	12:53:52	+31:06:25	51	8	157	22	362	40	517	75	396	60
CFC125	12:53:52	+32:14:30	0	23	0	20	0	17	0	24	0	23
CFC126	12:53:53	+26:41:02	0	26	0	22	0	17	0	26	0	20
CFC127	12:53:55	+31:13:12	0	24	0	24	0	21	0	24	0	15
CFC128	12:53:59	+26:26:38	0	23	31	7	69	8	0	10	0	9
CFC129	12:53:59	+32:39:18	0	26	0	21	0	20	0	25	0	19
CFC130	12:54:02	+29:36:13	0	87	0	161	0	304	0	633	0	206
CFC131	12:54:02	+25:45:38	0	25	0	25	0	20	0	29	0	14
CFC132	12:54:17	+32:22:08	0	26	23	6	49	7	0	9	0	7
CFC133	12:54:40	+32:22:01	42	8	137	21	311	35	472	69	448	64
CFC134	12:54:43	+31:36:43	0	22	0	19	0	16	0	31	0	23
CFC135	12:54:47	+30:32:41	42	7	178	26	355	43	459	70	345	52
CFC136	12:54:50	+26:19:29	0	20	0	19	0	16	0	24	0	18
CFC137	12:54:57	+30:42:29	28	7	82	10	225	27	369	60	0	7
CFC138	12:55:07	+30:30:45	41	9	25	7	18	5	0	24	0	6
CFC139	12:55:10	+29:34:41	0	32	0	20	0	20	0	26	0	20
CFC140	12:55:14	+26:15:00	0	24	0	17	0	16	0	25	0	22
CFC141	12:55:16	+25:57:24	0	26	26	8	34	6	0	21	0	18
CFC142	12:55:21	+31:58:41	0	23	0	23	0	21	0	23	0	20
CFC143	12:55:26	+29:31:57	0	28	0	21	0	18	0	32	0	16
CFC144	12:55:34	+32:12:21	0	22	0	21	0	22	0	29	0	33
CFC145	12:55:52	+25:10:58	0	26	0	27	49	7	0	14	0	9
CFC146	12:55:54	+23:48:09	0	27	0	21	0	18	0	32	0	18
CFC147	12:56:14	+30:12:00	0	22	0	21	0	16	0	32	0	22
CFC148	12:56:18	+29:48:28	0	24	0	78	0	95	0	29	0	19
CFC149	12:56:19	+32:39:17	0	18	0	21	0	19	0	27	0	24
CFC150	12:56:24	+29:48:17	0	23	0	20	0	18	0	32	0	21
CFC151	12:56:35	+30:46:08	0	20	0	19	0	19	0	24	0	19
CFC152	12:56:35	+29:44:50	0	25	0	22	0	17	0	29	0	24
CFC153	12:56:44	+30:43:09	0	19	0	23	0	15	0	22	0	17
CFC154	12:56:46	+24:59:50	0	23	0	20	0	20	0	26	0	20
CFC155	12:56:49	+31:29:55	0	17	0	17	0	15	0	23	0	14
CFC156	12:56:52	+31:17:42	0	26	67	10	202	25	323	53	0	7
CFC157	12:56:54	+30:40:35	27	8	65	12	144	21	264	48	0	7
CFC158	12:56:57	+30:42:57	50	8	143	28	284	37	210	44	0	7
CFC159	12:57:02	+31:37:31	35	8	103	12	279	31	558	79	339	48
CFC160	12:57:05	+30:39:54	26	7	52	11	62	8	0	30	0	6
CFC161	12:57:23	+33:27:21	0	23	0	29	0	55	0	27	0	23
CFC162	12:57:40	+26:12:19	0	23	0	21	0	19	0	25	0	22
CFC163	12:57:41	+31:16:31	0	30	0	18	0	20	0	29	0	18
CFC164	12:57:49	+31:16:31	0	28	0	19	0	18	0	27	0	17
CFC165	12:57:54	+23:30:57	0	27	0	25	0	21	0	37	0	26
CFC166	12:57:55	+32:43:42	0	27	0	20	0	18	0	26	0	19
CFC167	12:57:56	+32:28:54	0	52	0	28	0	22	0	30	0	22
CFC168	12:58:09	+24:20:56	40	7	112	12	261	31	453	66	527	73
CFC169	12:58:10	+32:00:59	110	22	257	31	545	58	861	114	498	68
CFC170	12:58:13	+33:10:51	0	23	0	23	0	21	0	28	0	17
CFC171	12:58:14	+32:40:22	0	28	0	28	0	64	0	31	0	21
CFC172	12:58:16	+31:09:32	28	7	47	9	77	9	0	11	266	40
CFC173	12:58:18	+30:32:16	0	23	0	30	0	52	0	26	0	21
CFC174	12:58:19	+34:06:06	0	29	0	25	0	21	0	22	0	17
CFC175	12:58:23	+30:08:34	0	27	0	24	0	17	0	25	0	20
CFC176	12:58:45	+24:14:02	0	28	0	27	0	26	0	29	0	17
CFC177	12:59:12	+25:00:14	0	25	0	21	0	19	0	25	0	18
CFC178	12:59:22	+26:01:34	39	8	74	10	171	23	203	42	184	33
CFC179	12:59:22	+29:53:16	0	26	67	11	182	24	247	46	206	34
CFC180	12:59:29	+31:20:08	0	23	0	19	0	18	0	33	0	17
CFC181	12:59:33	+32:17:28	0	35	44	8	72	9	0	8	0	14

Continued on next page

OBJECT	RA h:m:s (J2000)	Dec. d:m:s (J2000)	S_{500} (mJy)	E_{500} (mJy)	S_{350} (mJy)	E_{350} (mJy)	S_{250} (mJy)	E_{250} (mJy)	S_{160} (mJy)	E_{160} (mJy)	S_{100} (mJy)	E_{100} (mJy)
CFC182	12:59:40	+30:14:49	0	20	0	18	0	19	0	31	0	22
CFC183	12:59:45	+32:02:42	81	10	320	42	673	70	1103	146	728	101
CFC184	12:59:45	+29:53:46	0	29	0	26	0	18	0	30	0	21
CFC185	12:59:52	+33:17:51	27	7	37	7	59	7	0	9	0	6
CFC186	12:59:57	+31:30:21	29	7	28	7	46	7	0	8	0	5
CFC187	13:00:01	+29:54:14	0	27	0	27	0	25	0	24	0	18
CFC188	13:00:05	+33:59:38	0	26	0	20	0	18	0	31	0	18
CFC189	13:00:28	+34:22:46	0	25	0	20	0	18	0	33	0	22
CFC190	13:00:29	+32:22:02	0	23	0	19	0	18	0	24	0	16
CFC191	13:00:53	+23:09:51	0	29	0	22	0	17	0	27	0	19
CFC192	13:01:22	+23:47:41	0	30	0	15	0	18	0	27	0	21
CFC193	13:01:29	+23:46:05	0	29	0	18	0	20	0	26	0	21
CFC194	13:01:30	+24:37:46	0	21	0	18	16	4	0	31	0	19
CFC195	13:01:43	+29:55:36	0	25	64	8	162	16	349	52	371	50
CFC196	13:01:45	+33:25:58	0	28	0	22	0	18	0	26	0	23
CFC197	13:02:08	+32:42:59	0	23	0	24	0	20	0	27	0	22
CFC198	13:02:16	+33:19:00	0	28	0	22	0	20	0	27	0	21
CFC199	13:02:17	+26:08:33	0	25	0	22	0	20	0	27	0	18
CFC200	13:02:18	+32:53:26	167	27	470	52	950	97	1189	152	771	104
CFC201	13:02:21	+33:12:54	0	24	0	17	0	19	0	30	0	17
CFC202	13:02:25	+33:41:32	0	25	0	24	35	7	0	8	0	6
CFC203	13:02:26	+32:45:46	0	28	0	24	0	13	0	23	0	20
CFC204	13:02:29	+34:44:01	0	35	0	45	0	167	0	310	0	197
CFC205	13:02:39	+25:23:00	0	25	35	8	95	10	0	10	256	42
CFC206	13:02:44	+32:05:06	0	23	0	14	0	13	0	27	0	25
CFC207	13:02:44	+31:28:41	0	27	0	30	0	25	0	34	0	22
CFC208	13:02:54	+23:39:25	0	22	0	25	0	15	0	32	0	23
CFC209	13:03:01	+32:12:38	46	9	182	30	318	40	400	63	311	46
CFC210	13:03:05	+25:28:30	0	28	30	7	80	9	231	44	0	7
CFC211	13:03:13	+31:19:14	0	29	0	25	34	6	0	30	0	20
CFC212	13:03:16	+32:43:17	50	7	127	24	202	29	0	8	0	6
CFC213	13:03:17	+26:03:36	0	32	0	23	57	8	0	7	0	5
CFC214	13:03:25	+31:19:03	0	29	0	24	0	17	0	28	0	21
CFC215	13:03:41	+29:49:05	0	22	0	23	0	20	0	27	0	17
CFC216	13:03:57	+31:36:47	0	27	0	24	0	18	0	24	0	18
CFC217	13:04:07	+25:43:30	0	20	0	19	0	16	0	23	0	18
CFC218	13:04:14	+26:06:58	0	26	0	27	0	25	0	24	0	15
CFC219	13:04:21	+24:25:49	25	8	24	7	30	6	0	25	0	6
CFC220	13:04:25	+32:32:53	0	23	0	19	0	20	0	30	0	19
CFC221	13:04:28	+23:34:30	56	9	147	26	329	40	451	68	251	45
CFC222	13:04:47	+29:36:53	0	26	0	21	0	16	0	33	0	17
CFC223	13:04:51	+25:50:21	0	19	0	20	0	13	0	23	0	15
CFC224	13:05:08	+29:52:51	0	22	0	21	0	19	0	34	0	18
CFC225	13:05:16	+25:57:27	120	23	341	47	667	71	1104	140	1007	128
CFC226	13:05:16	+29:35:15	0	23	0	19	0	19	0	28	0	18
CFC227	13:05:23	+29:30:37	0	27	0	19	0	16	0	29	0	20
CFC228	13:05:26	+25:11:28	34	7	84	10	197	28	182	41	0	7
CFC229	13:05:28	+33:50:55	43	10	94	12	234	30	150	33	204	35
CFC230	13:05:34	+29:39:11	0	76	0	22	0	21	0	26	0	19
CFC231	13:05:36	+30:47:26	0	27	20	6	28	5	0	26	0	17
CFC232	13:05:38	+29:21:00	0	28	0	21	0	19	0	24	0	23
CFC233	13:05:39	+26:06:23	25	8	57	7	121	13	268	48	175	30
CFC234	13:05:44	+25:23:06	63	9	155	22	324	39	328	52	356	51
CFC235	13:05:49	+26:25:51	0	27	0	25	0	19	0	16	0	21
CFC236	13:05:51	+29:48:36	0	31	0	18	0	18	0	26	0	22
CFC237	13:05:57	+32:50:20	0	33	0	60	0	84	0	26	0	21
CFC238	13:05:58	+25:27:56	35	8	102	11	215	21	418	67	348	52
CFC239	13:05:59	+29:16:43	0	21	0	15	0	17	0	27	0	17
CFC240	13:06:03	+29:42:34	0	33	0	65	0	21	0	26	0	21
CFC241	13:06:08	+30:12:33	28	8	42	10	102	17	0	10	0	7
CFC242	13:06:15	+29:21:58	0	24	0	19	0	16	0	21	0	18
CFC243	13:06:15	+25:27:38	101	11	357	40	874	89	1691	209	1831	225
CFC244	13:06:19	+32:58:25	0	29	102	12	310	30	929	121	930	116
CFC245	13:06:21	+29:10:12	0	26	0	22	0	16	0	19	0	15
CFC246	13:06:22	+29:39:27	0	30	0	34	0	92	0	150	0	25
CFC247	13:06:24	+31:08:11	0	26	0	21	0	18	0	26	0	19
CFC248	13:06:25	+25:14:16	0	24	0	20	26	5	0	27	0	19
CFC249	13:06:33	+29:21:56	23	8	56	9	107	18	0	26	0	7
CFC250	13:06:33	+29:11:02	0	27	80	9	190	18	371	53	224	36
CFC251	13:06:33	+24:57:46	24	8	36	8	86	16	0	29	0	18
CFC252	13:06:36	+25:25:46	35	10	64	11	159	24	209	42	168	34
CFC253	13:06:45	+29:22:17	0	25	0	25	0	13	0	27	0	19
CFC254	13:06:46	+29:07:50	0	25	0	14	0	16	0	18	0	14
CFC255	13:07:24	+32:51:45	112	24	238	35	408	47	274	47	0	7
CFC256	13:07:31	+25:30:17	0	20	0	21	43	6	0	26	0	7
CFC257	13:07:37	+29:55:36	0	26	0	19	0	19	0	26	0	19
CFC258	13:07:37	+32:46:31	56	10	162	26	319	41	219	45	0	8
CFC259	13:07:38	+31:29:13	0	23	0	20	39	7	0	30	0	7
CFC260	13:07:39	+32:14:13	0	24	0	24	0	19	0	27	0	21
CFC261	13:07:39	+28:49:43	0	22	0	17	0	13	0	25	0	15
CFC262	13:07:42	+24:48:38	0	63	0	119	0	191	0	395	0	22
CFC263	13:07:47	+29:09:10	0	28	0	19	0	16	0	18	0	14
CFC264	13:07:53	+28:22:59	0	30	70	9	192	24	224	42	0	8
CFC265	13:07:54	+32:18:23	0	26	0	22	0	17	0	23	0	16
CFC266	13:07:55	+34:55:10	97	11	267	33	583	63	1062	137	1232	159
CFC267	13:07:57	+28:42:38	0	15	0	19	0	12	0	30	0	23
CFC268	13:08:02	+28:15:05	0	24	0	19	0	15	0	32	0	19
CFC269	13:08:02	+27:18:40	40	8	84	10	164	16	439	69	309	45
CFC270	13:08:03	+28:59:53	0	23	0	21	37	5	0	23	0	17
CFC271	13:08:09	+27:49:35	0	23	0	22	0	20	0	31	0	16
CFC272	13:08:14	+27:30:57	0	19	0	19	0	18	0	29	0	18

Continued on next page

OBJECT	RA h:m:s (J2000)	Dec. d:m:s (J2000)	S_{500} (mJy)	E_{500} (mJy)	S_{350} (mJy)	E_{350} (mJy)	S_{250} (mJy)	E_{250} (mJy)	S_{160} (mJy)	E_{160} (mJy)	S_{100} (mJy)	E_{100} (mJy)
CFC273	13:08:15	+29:01:22	0	23	0	19	0	18	0	22	0	13
CFC274	13:08:21	+29:13:42	0	26	0	23	0	19	0	21	0	19
CFC275	13:08:26	+29:45:16	0	25	0	24	0	21	0	27	0	20
CFC276	13:08:26	+28:08:07	0	29	0	17	0	20	0	32	0	18
CFC277	13:08:27	+28:19:13	0	21	35	9	63	9	0	11	0	8
CFC278	13:08:27	+28:21:02	0	22	0	20	34	6	0	33	0	20
CFC279	13:08:30	+27:52:45	0	26	0	21	0	17	0	28	0	17
CFC280	13:08:31	+24:42:02	251	33	647	69	1304	133	1879	235	1056	135
CFC281	13:08:32	+30:44:53	0	24	0	24	0	56	0	102	0	21
CFC282	13:08:40	+24:04:37	0	32	0	26	0	21	0	23	0	21
CFC283	13:08:49	+32:17:37	0	26	0	24	0	74	0	27	0	20
CFC284	13:08:50	+33:01:22	0	27	0	23	0	26	0	36	0	21
CFC285	13:08:51	+28:37:45	52	9	120	21	203	23	433	70	245	38
CFC286	13:08:55	+29:02:26	70	10	177	25	343	41	450	66	270	40
CFC287	13:08:55	+28:01:26	35	11	33	7	41	7	0	10	0	6
CFC288	13:08:57	+28:16:49	46	8	80	10	166	24	0	29	0	7
CFC289	13:08:58	+27:36:50	0	28	0	23	0	23	0	25	0	20
CFC290	13:09:05	+28:29:27	0	20	0	19	0	16	0	27	0	23
CFC291	13:09:07	+29:49:51	0	24	0	27	67	7	0	11	0	6
CFC292	13:09:07	+28:40:06	0	21	39	6	65	9	0	15	0	6
CFC293	13:09:08	+28:53:33	0	16	0	15	0	13	0	23	0	19
CFC294	13:09:12	+28:28:03	0	22	0	18	0	21	0	25	0	19
CFC295	13:09:18	+28:12:45	0	21	0	20	0	14	0	28	0	18
CFC296	13:09:21	+28:18:41	0	23	0	21	0	16	0	26	0	17
CFC297	13:09:22	+28:19:16	0	29	0	20	0	15	0	23	0	18
CFC298	13:09:23	+28:16:53	0	23	0	17	0	18	0	26	0	18
CFC299	13:09:26	+28:24:57	90	12	290	33	701	72	1112	140	868	109
CFC300	13:09:30	+28:59:09	0	18	50	7	118	18	183	30	160	26
CFC301	13:09:37	+26:09:32	0	26	0	17	0	19	0	17	0	16
CFC302	13:09:38	+30:29:54	31	8	82	10	199	19	488	69	383	54
CFC303	13:09:45	+28:37:16	59	9	158	16	364	35	972	127	1328	164
CFC304	13:09:47	+28:54:25	251	35	729	78	1692	168	2545	316	2197	277
CFC305	13:09:49	+24:34:39	134	16	469	51	1077	107	1893	236	1700	209
CFC306	13:09:51	+28:54:01	0	27	0	20	0	20	0	35	0	20
CFC307	13:09:52	+28:22:56	0	30	0	62	0	85	0	87	0	19
CFC308	13:09:52	+24:33:37	0	31	0	20	0	17	0	24	0	19
CFC309	13:09:59	+28:48:54	0	22	0	18	0	15	0	27	0	19
CFC310	13:10:08	+28:17:23	0	25	0	19	0	19	0	26	0	22
CFC311	13:10:20	+32:28:59	129	14	355	41	691	71	1170	159	547	78
CFC312	13:10:21	+31:22:41	0	24	0	26	0	19	0	24	0	22
CFC313	13:10:23	+33:20:09	0	30	0	32	0	71	0	30	0	18
CFC314	13:10:27	+30:44:24	0	27	0	22	0	21	0	31	0	21
CFC315	13:10:40	+32:17:44	0	27	0	19	0	19	0	26	0	21
CFC316	13:10:46	+28:38:31	0	24	0	18	0	22	0	30	0	20
CFC317	13:10:46	+25:04:44	0	21	0	20	0	18	0	22	0	20
CFC318	13:10:47	+28:59:42	0	18	0	24	0	22	0	16	0	13
CFC319	13:10:47	+29:42:35	102	13	304	36	640	66	933	124	659	89
CFC320	13:10:52	+24:51:55	0	93	0	97	0	123	0	28	0	21
CFC321	13:10:58	+28:31:08	0	20	0	21	0	17	0	22	0	25
CFC322	13:11:01	+29:38:12	0	29	0	24	0	23	0	22	0	20
CFC323	13:11:01	+29:34:42	263	35	709	73	1687	166	3360	409	3425	415
CFC324	13:11:02	+31:24:14	0	25	0	22	0	19	0	26	0	17
CFC325	13:11:04	+30:28:58	0	23	57	10	75	10	0	11	0	7
CFC326	13:11:05	+23:58:48	0	29	0	21	0	18	0	24	0	22
CFC327	13:11:12	+26:48:50	23	7	84	10	184	18	597	86	293	45
CFC328	13:11:18	+30:29:17	26	7	55	9	91	11	0	9	0	6
CFC329	13:11:18	+29:47:38	0	22	67	8	130	14	249	44	283	45
CFC330	13:11:18	+27:58:00	0	17	0	20	0	11	0	31	0	22
CFC331	13:11:24	+30:35:56	0	21	0	19	52	7	0	9	0	6
CFC332	13:11:25	+24:51:34	0	25	0	21	0	16	0	21	0	19
CFC333	13:11:25	+30:37:10	0	18	0	19	0	16	0	24	0	21
CFC334	13:11:30	+32:31:35	0	27	0	21	25	7	0	43	0	24
CFC335	13:11:31	+34:19:45	0	25	27	7	52	7	0	9	0	20
CFC336	13:11:35	+29:03:46	0	24	0	20	0	16	0	17	0	13
CFC337	13:11:36	+31:30:29	0	24	0	25	0	19	0	25	0	19
CFC338	13:11:42	+34:33:40	0	25	0	21	0	20	0	31	0	24
CFC339	13:11:48	+30:58:21	38	10	125	13	374	42	714	94	634	84
CFC340	13:11:49	+34:35:44	0	30	0	20	30	7	0	30	0	20
CFC341	13:11:52	+34:02:00	36	9	65	9	158	23	166	35	0	7
CFC342	13:11:53	+27:35:37	0	27	0	25	0	17	0	23	0	21
CFC343	13:11:55	+33:18:25	0	27	42	8	117	12	0	14	326	49
CFC344	13:11:57	+24:42:04	0	24	36	8	50	7	0	30	0	7
CFC345	13:11:57	+34:21:54	0	27	0	25	0	23	0	30	0	22
CFC346	13:12:00	+30:23:58	0	19	0	17	28	7	0	25	0	19
CFC347	13:12:05	+34:15:23	0	26	37	12	56	7	0	30	0	32
CFC348	13:12:07	+27:19:21	0	21	0	19	0	18	0	30	0	18
CFC349	13:12:07	+34:16:13	0	27	0	25	0	17	0	37	0	25
CFC350	13:12:07	+27:19:49	0	23	0	19	0	17	0	27	0	16
CFC351	13:12:19	+34:02:01	0	23	0	21	0	18	0	31	0	22
CFC352	13:12:19	+27:07:37	0	22	0	23	0	17	0	27	0	20
CFC353	13:12:21	+30:20:46	0	22	0	25	0	18	0	27	0	18
CFC354	13:12:25	+28:32:15	57	10	237	23	599	57	1547	192	1970	241
CFC355	13:12:26	+33:13:15	0	19	0	22	0	20	0	30	0	17
CFC356	13:12:38	+26:47:54	0	27	0	20	0	15	0	30	0	19
CFC357	13:12:44	+31:48:33	374	46	839	93	1568	158	1872	237	1158	165
CFC358	13:12:51	+27:52:48	32	7	111	20	216	27	232	43	170	33
CFC359	13:12:53	+23:38:04	0	20	23	6	59	8	170	40	0	6
CFC360	13:12:53	+29:57:41	0	26	0	18	0	20	0	26	0	20
CFC361	13:12:54	+26:32:05	0	21	0	20	47	7	0	24	0	6
CFC362	13:12:58	+31:15:31	0	33	0	107	0	120	0	223	0	21
CFC363	13:13:10	+30:11:29	0	25	59	9	143	15	269	42	269	41

Continued on next page

OBJECT	RA h:m:s (J2000)	Dec. d:m:s (J2000)	S_{500} (mJy)	E_{500} (mJy)	S_{350} (mJy)	E_{350} (mJy)	S_{250} (mJy)	E_{250} (mJy)	S_{160} (mJy)	E_{160} (mJy)	S_{100} (mJy)	E_{100} (mJy)
CFC364	13:13:10	+29:58:49	0	25	0	22	0	18	0	28	0	17
CFC365	13:13:12	+30:21:43	0	31	36	8	64	7	0	28	0	9
CFC366	13:13:20	+30:33:35	0	30	0	73	0	106	0	33	0	22
CFC367	13:13:21	+30:19:11	0	32	0	30	0	72	0	114	0	19
CFC368	13:13:25	+33:17:24	0	21	27	8	46	6	0	8	0	18
CFC369	13:13:25	+27:45:48	85	10	198	20	568	60	908	120	822	109
CFC370	13:13:26	+27:48:08	0	113	0	184	0	381	0	605	0	400
CFC371	13:13:35	+29:07:35	45	8	98	12	302	34	470	66	311	45
CFC372	13:13:48	+31:44:46	0	21	39	8	103	18	0	10	0	19
CFC373	13:13:49	+27:28:09	0	26	0	13	21	5	0	30	0	20
CFC374	13:13:53	+28:04:14	0	26	0	17	0	22	0	24	0	22
CFC375	13:13:54	+28:17:44	0	28	24	6	39	6	0	23	0	21
CFC376	13:14:01	+29:24:25	27	8	76	9	182	23	185	35	0	5
CFC377	13:14:02	+30:37:56	0	23	0	19	0	18	0	36	0	19
CFC378	13:14:26	+30:15:01	41	9	68	9	167	26	219	45	0	7
CFC379	13:14:32	+30:42:20	256	44	686	78	1458	148	1797	229	1173	154
CFC380	13:14:37	+29:19:04	0	24	0	20	0	16	0	24	0	14
CFC381	13:14:40	+29:59:50	47	9	182	24	368	40	495	73	363	53
CFC382	13:14:42	+28:28:20	0	24	23	7	41	7	0	10	0	7
CFC383	13:14:42	+30:45:11	0	24	0	19	0	17	0	29	0	17
CFC384	13:14:46	+24:30:45	0	26	0	24	0	50	0	29	0	18
CFC385	13:14:49	+28:01:08	49	9	53	8	42	7	0	9	0	21
CFC386	13:14:53	+27:00:29	116	22	281	40	605	77	650	89	310	48
CFC387	13:14:58	+30:56:37	0	27	0	21	31	6	0	9	0	19
CFC388	13:14:59	+30:54:17	46	9	126	21	198	25	157	33	0	8
CFC389	13:15:02	+28:02:10	44	8	111	12	288	32	533	74	447	62
CFC390	13:15:04	+24:56:19	0	23	0	22	0	18	0	32	0	24
CFC391	13:15:08	+30:24:13	88	13	253	25	738	77	1476	184	1810	224
CFC392	13:15:08	+30:42:25	0	22	0	19	0	13	0	33	0	20
CFC393	13:15:25	+27:18:11	45	7	95	23	81	10	0	24	0	25
CFC394	13:15:26	+33:09:26	33	8	61	8	161	21	151	28	102	20
CFC395	13:15:34	+29:40:33	44	9	169	27	408	47	748	112	248	40
CFC396	13:15:37	+29:39:30	0	24	0	18	0	20	0	32	0	18
CFC397	13:15:39	+29:36:39	22	7	37	7	85	10	0	10	0	6
CFC398	13:15:42	+34:32:25	0	21	0	16	0	12	0	24	0	21
CFC399	13:15:43	+30:45:13	25	8	24	7	19	4	0	29	0	20
CFC400	13:15:47	+31:50:47	76	9	219	28	468	50	802	110	503	75
CFC401	13:15:52	+31:39:08	0	20	0	22	0	42	0	29	0	16
CFC402	13:15:59	+31:31:50	22	6	42	7	168	33	0	9	0	22
CFC403	13:16:03	+31:08:18	0	28	0	21	0	16	0	29	0	19
CFC404	13:16:04	+33:55:19	0	21	0	15	0	18	0	25	0	23
CFC405	13:16:12	+34:03:46	71	10	182	26	368	42	517	76	422	59
CFC406	13:16:17	+31:10:34	0	22	0	20	0	13	0	47	0	21
CFC407	13:16:20	+30:40:42	76	11	253	37	502	57	756	105	570	79
CFC408	13:16:27	+31:01:53	0	22	0	20	0	19	0	25	0	18
CFC409	13:16:27	+29:25:11	0	21	0	21	33	6	0	5	0	14
CFC410	13:16:32	+30:46:02	0	21	0	24	0	18	0	30	0	18
CFC411	13:16:33	+31:32:47	19	6	60	8	106	11	146	31	149	31
CFC412	13:16:35	+34:07:50	0	21	0	19	29	6	0	27	0	16
CFC413	13:16:41	+31:22:02	36	9	97	20	178	30	162	32	0	5
CFC414	13:16:44	+28:12:00	0	23	38	6	94	11	0	14	337	55
CFC415	13:16:50	+31:37:50	60	10	138	14	360	42	566	75	507	67
CFC416	13:16:53	+31:42:39	32	7	45	7	76	8	158	30	182	28
CFC417	13:16:53	+31:35:55	27	7	23	5	36	6	0	20	0	14
CFC418	13:16:59	+33:42:00	0	23	0	21	17	5	0	22	0	17
CFC419	13:17:00	+34:06:06	233	30	620	68	1276	127	2114	267	1138	145
CFC420	13:17:02	+23:17:32	0	27	0	21	0	23	0	30	0	20
CFC421	13:17:19	+25:12:53	0	21	0	18	0	17	0	28	0	20
CFC422	13:17:21	+31:03:33	36	8	102	10	268	31	499	70	417	56
CFC423	13:17:24	+27:45:00	0	19	0	16	0	19	0	32	0	20
CFC424	13:17:30	+31:00:20	0	27	0	19	0	22	0	17	0	14
CFC425	13:17:37	+33:51:15	0	19	0	19	0	18	0	24	0	24
CFC426	13:17:44	+29:38:45	28	9	27	8	27	8	0	22	0	14
CFC427	13:17:45	+27:34:11	206	26	579	62	1253	126	1800	222	1298	163
CFC428	13:18:04	+33:51:18	25	7	74	9	126	13	170	36	177	32
CFC429	13:18:04	+31:05:46	0	20	0	20	0	19	0	30	0	20
CFC430	13:18:05	+30:08:27	0	28	0	22	0	17	0	19	0	12
CFC431	13:18:09	+34:11:59	0	23	0	26	0	23	0	24	0	20
CFC432	13:18:11	+31:46:53	0	23	0	23	0	15	0	25	0	21
CFC433	13:18:28	+25:13:12	0	25	0	71	0	87	0	107	0	81
CFC434	13:18:47	+30:53:00	0	26	0	18	0	15	0	26	0	16
CFC435	13:18:53	+30:48:13	0	24	0	22	0	14	0	31	0	19
CFC436	13:18:58	+27:48:43	0	26	0	19	0	17	0	32	0	17
CFC437	13:18:59	+30:46:51	0	20	0	21	0	13	0	27	0	18
CFC438	13:19:00	+30:49:00	42	9	85	11	185	24	228	44	0	6
CFC439	13:19:05	+27:49:06	0	29	0	20	23	5	0	22	0	23
CFC440	13:19:08	+28:30:24	0	115	0	258	0	450	0	674	0	19
CFC441	13:19:19	+31:03:06	0	25	0	30	0	33	0	34	0	18
CFC442	13:19:19	+24:59:00	27	7	51	7	52	7	0	24	0	4
CFC443	13:19:28	+27:44:56	48	9	137	23	283	33	490	69	636	84
CFC444	13:19:35	+25:24:39	0	23	0	24	0	21	0	19	0	13
CFC445	13:19:45	+31:52:21	0	30	25	6	24	5	0	24	0	24
CFC446	13:19:46	+29:41:33	0	22	0	17	0	17	0	28	0	18
CFC447	13:19:48	+31:27:41	0	25	0	23	0	18	0	25	0	14
CFC448	13:19:54	+31:14:05	27	9	54	7	110	19	0	28	0	6
CFC449	13:19:54	+34:33:35	0	25	0	21	0	18	0	32	0	21
CFC450	13:19:55	+30:50:19	0	30	0	22	24	6	0	28	0	18
CFC451	13:19:56	+29:26:53	0	22	0	24	0	13	0	17	0	14
CFC452	13:19:56	+30:07:08	40	10	118	22	254	32	350	57	308	49
CFC453	13:19:58	+28:14:49	50	8	201	27	497	55	1074	138	903	116
CFC454	13:19:58	+34:02:09	30	9	56	8	115	13	0	11	0	8

Continued on next page

OBJECT	RA h:m:s (J2000)	Dec. d:m:s (J2000)	S_{500} (mJy)	E_{500} (mJy)	S_{350} (mJy)	E_{350} (mJy)	S_{250} (mJy)	E_{250} (mJy)	S_{160} (mJy)	E_{160} (mJy)	S_{100} (mJy)	E_{100} (mJy)
CFC455	13:19:58	+29:25:38	55	8	133	14	389	45	591	76	538	70
CFC456	13:20:01	+31:54:33	0	24	0	18	0	13	0	36	0	21
CFC457	13:20:08	+29:56:42	0	26	0	23	41	6	0	30	0	15
CFC458	13:20:08	+30:03:20	0	26	0	19	0	16	0	25	0	18
CFC459	13:20:14	+30:59:16	40	9	184	32	321	42	320	56	0	7
CFC460	13:20:15	+30:54:02	0	44	0	144	0	297	0	667	0	644
CFC461	13:20:18	+33:19:52	0	30	100	12	236	23	551	87	346	50
CFC462	13:20:25	+30:36:10	27	8	102	12	309	35	601	81	482	68
CFC463	13:20:29	+31:57:19	28	6	42	7	55	7	0	29	0	21
CFC464	13:20:30	+32:00:14	0	21	0	21	0	17	0	25	0	20
CFC465	13:20:35	+34:08:21	696	66	2287	217	5940	564	17419	2093	23700	2845
CFC466	13:20:37	+30:10:18	0	26	0	19	0	21	0	24	0	19
CFC467	13:20:39	+34:09:07	0	25	0	26	0	19	0	50	0	21
CFC468	13:20:42	+31:11:06	0	24	0	23	37	7	0	35	0	19
CFC469	13:20:51	+31:21:59	109	20	210	31	426	50	723	102	424	59
CFC470	13:20:53	+32:11:26	37	9	85	10	226	31	252	44	266	42
CFC471	13:20:55	+30:11:13	0	22	0	17	0	16	0	30	0	17
CFC472	13:20:56	+34:19:10	0	22	0	28	0	21	0	31	0	18
CFC473	13:20:59	+28:58:10	0	20	34	7	81	9	0	28	0	21
CFC474	13:21:01	+33:03:51	28	8	29	8	26	6	0	27	0	22
CFC475	13:21:09	+31:56:46	0	18	0	20	0	19	0	25	0	17
CFC476	13:21:13	+31:13:18	118	22	231	37	407	51	395	73	0	7
CFC477	13:21:15	+31:55:49	24	6	61	9	111	12	0	9	0	7
CFC478	13:21:18	+31:23:17	0	27	0	21	0	17	0	26	0	18
CFC479	13:21:19	+31:33:08	56	8	160	16	475	49	794	107	624	84
CFC480	13:21:34	+33:29:23	0	26	0	26	0	21	0	25	0	21
CFC481	13:21:34	+26:18:16	92	11	319	39	712	76	1384	174	1133	141
CFC482	13:21:40	+31:21:03	110	20	259	36	562	61	406	65	0	8
CFC483	13:21:45	+31:14:14	123	13	477	54	1172	116	2693	332	2647	324
CFC484	13:21:49	+31:33:47	25	7	36	9	63	14	0	34	0	22
CFC485	13:21:56	+24:43:44	0	20	0	23	0	19	0	29	0	28
CFC486	13:21:57	+32:05:59	34	7	39	6	54	6	0	6	0	7
CFC487	13:21:59	+26:44:01	39	9	125	22	250	33	0	9	0	20
CFC488	13:22:00	+26:31:11	0	19	0	20	0	22	0	19	0	17
CFC489	13:22:02	+31:16:42	87	12	229	22	546	52	1201	151	1287	165
CFC490	13:22:09	+25:24:29	0	20	0	20	0	23	0	27	0	16
CFC491	13:22:22	+33:23:32	0	20	28	7	25	7	0	9	0	17
CFC492	13:22:23	+27:10:57	36	9	64	8	162	30	0	7	0	6
CFC493	13:22:23	+27:34:53	0	18	0	17	0	20	0	27	0	19
CFC494	13:22:25	+29:56:34	0	21	42	7	65	8	0	12	0	6
CFC495	13:22:27	+31:50:12	0	19	0	21	0	18	0	36	0	22
CFC496	13:22:36	+30:19:01	0	26	0	16	0	18	0	28	0	20
CFC497	13:22:40	+29:20:31	0	21	0	24	0	17	0	22	0	14
CFC498	13:22:45	+30:53:14	0	26	0	21	0	14	0	25	0	18
CFC499	13:22:48	+31:19:27	0	26	37	8	47	6	0	25	0	6
CFC500	13:22:51	+31:49:33	54	9	165	22	327	37	402	62	328	51
CFC501	13:22:51	+27:23:37	0	19	20	5	28	5	0	32	0	20
CFC502	13:23:02	+33:03:35	0	24	0	21	0	19	0	35	0	24
CFC503	13:23:05	+26:51:16	0	25	0	23	0	23	0	23	0	19
CFC504	13:23:20	+32:03:48	0	28	0	35	0	82	0	112	0	22
CFC505	13:23:23	+33:43:26	41	7	79	10	172	17	141	19	479	67
CFC506	13:23:24	+26:32:36	0	39	72	9	187	27	147	35	0	20
CFC507	13:23:25	+32:06:11	0	19	0	25	0	15	0	24	0	19
CFC508	13:23:31	+26:32:49	0	26	41	8	74	8	0	7	0	6
CFC509	13:23:33	+26:30:14	0	30	0	28	0	24	0	24	0	15
CFC510	13:23:39	+30:56:19	0	27	0	26	18	4	0	7	0	17
CFC511	13:23:41	+31:38:46	37	7	73	10	225	34	341	63	0	6
CFC512	13:23:42	+31:30:55	0	21	0	30	0	18	0	22	0	17
CFC513	13:23:43	+30:33:49	48	8	163	24	323	43	376	57	129	24
CFC514	13:23:45	+31:33:56	0	19	0	23	40	8	0	25	0	7
CFC515	13:23:56	+30:59:17	0	26	0	26	0	29	0	83	0	26
CFC516	13:23:59	+30:55:56	79	12	207	21	572	59	1178	151	884	112
CFC517	13:24:04	+34:20:49	0	26	31	7	41	7	0	28	0	18
CFC518	13:24:06	+31:45:44	0	28	0	22	0	66	0	32	0	21
CFC519	13:24:09	+34:09:20	0	21	35	6	54	8	0	24	0	6
CFC520	13:24:15	+31:20:42	145	23	361	41	769	79	1102	143	721	95
CFC521	13:24:18	+31:35:17	0	20	0	28	0	21	0	24	0	17
CFC522	13:24:27	+33:06:23	34	7	36	7	37	7	0	8	0	7
CFC523	13:24:33	+31:40:17	0	25	0	33	0	19	0	26	0	20
CFC524	13:24:33	+31:32:47	27	8	73	9	159	23	0	10	169	31
CFC525	13:24:34	+32:11:45	0	21	0	21	36	5	0	9	0	17
CFC526	13:24:40	+31:01:35	0	23	35	7	95	10	0	12	74	10
CFC527	13:24:45	+32:31:00	0	27	0	24	0	21	0	32	0	19
CFC528	13:24:46	+25:48:16	0	19	0	26	0	21	0	24	0	22
CFC529	13:24:46	+26:44:18	0	27	27	8	49	6	0	29	0	7
CFC530	13:24:56	+26:27:48	32	9	97	12	273	26	744	96	821	103
CFC531	13:25:07	+25:50:53	38	8	49	7	60	8	0	9	0	23
CFC532	13:25:13	+29:24:51	38	7	85	10	167	16	316	45	332	45
CFC533	13:25:20	+29:29:38	23	7	28	7	44	8	0	20	0	14
CFC534	13:25:20	+33:06:45	0	86	0	26	0	19	0	24	0	17
CFC535	13:25:26	+23:45:22	0	25	0	20	0	19	0	29	0	22
CFC536	13:25:33	+26:00:05	28	8	63	9	143	14	252	43	211	38
CFC537	13:25:38	+31:59:38	0	27	39	8	88	10	262	49	0	6
CFC538	13:25:40	+30:44:22	0	23	0	27	0	21	0	26	0	19
CFC539	13:25:42	+33:08:21	0	21	24	6	39	6	0	8	0	19
CFC540	13:25:57	+31:37:05	0	28	111	20	236	32	391	68	0	8
CFC541	13:26:24	+32:25:04	0	31	0	19	0	16	0	23	0	22
CFC542	13:26:31	+33:10:59	0	25	0	26	0	21	0	26	0	18
CFC543	13:26:35	+32:45:39	0	23	34	6	41	6	0	28	0	15
CFC544	13:26:37	+31:40:00	0	26	0	18	0	19	0	23	0	20
CFC545	13:26:38	+27:02:23	64	11	170	25	343	40	470	66	321	47

Continued on next page

OBJECT	RA h:m:s (J2000)	Dec. d:m:s (J2000)	S_{500} (mJy)	E_{500} (mJy)	S_{350} (mJy)	E_{350} (mJy)	S_{250} (mJy)	E_{250} (mJy)	S_{160} (mJy)	E_{160} (mJy)	S_{100} (mJy)	E_{100} (mJy)
CFC546	13:26:41	+32:55:27	0	27	0	25	0	24	0	28	0	18
CFC547	13:26:43	+30:30:24	43	8	84	9	230	28	432	64	278	42
CFC548	13:26:46	+31:56:39	0	21	39	9	67	8	0	8	0	6
CFC549	13:26:47	+30:58:32	0	30	0	20	0	17	0	41	0	19
CFC550	13:26:51	+26:35:27	0	29	0	83	0	107	0	173	0	239
CFC551	13:26:58	+32:32:11	65	10	202	30	412	60	471	73	338	50
CFC552	13:26:59	+26:08:46	0	26	0	20	0	19	0	27	0	19
CFC553	13:26:59	+32:42:22	0	21	0	32	0	18	0	26	0	19
CFC554	13:27:03	+30:58:36	88	12	243	29	524	54	857	117	648	89
CFC555	13:27:13	+32:05:18	0	20	0	23	0	14	0	26	0	27
CFC556	13:27:16	+32:01:50	0	121	0	209	0	316	0	27	0	21
CFC557	13:27:19	+31:47:17	37	10	78	10	202	29	0	12	162	34
CFC558	13:27:31	+26:37:14	0	25	0	20	47	8	0	8	0	7
CFC559	13:27:37	+26:57:56	0	18	0	24	0	19	0	24	0	23
CFC560	13:27:40	+26:03:41	49	9	56	8	99	17	0	9	0	28
CFC561	13:27:40	+25:27:02	0	25	0	20	0	16	0	30	0	19
CFC562	13:27:46	+32:03:36	0	26	0	21	0	15	0	24	0	16
CFC563	13:27:47	+25:26:58	0	21	0	19	0	15	0	21	0	22
CFC564	13:28:04	+33:35:35	0	30	0	25	0	60	0	30	0	109
CFC565	13:28:06	+31:55:54	30	9	41	8	57	10	0	28	0	21
CFC566	13:28:08	+33:32:00	30	9	36	7	66	8	0	11	0	8
CFC567	13:28:13	+26:27:23	0	25	0	71	0	78	0	100	0	20
CFC568	13:28:25	+30:48:56	84	11	239	34	479	52	608	90	329	53
CFC569	13:28:30	+31:12:57	0	25	0	23	27	7	0	26	0	18
CFC570	13:28:33	+32:04:09	0	22	40	8	114	20	0	15	210	38
CFC571	13:28:34	+31:07:52	0	22	0	21	0	20	0	27	0	20
CFC572	13:28:38	+33:36:18	119	13	427	47	982	99	1704	213	1408	174
CFC573	13:28:53	+34:44:32	0	20	21	6	59	8	0	29	0	7
CFC574	13:28:56	+32:52:44	203	31	544	64	1349	133	2832	345	2940	356
CFC575	13:28:56	+34:57:59	0	25	0	19	0	16	0	31	0	22
CFC576	13:29:03	+31:52:23	0	23	0	21	32	6	0	24	0	21
CFC577	13:29:17	+26:47:18	35	9	73	10	146	15	388	60	249	40
CFC578	13:29:19	+32:00:17	0	23	70	10	179	18	670	96	788	101
CFC579	13:29:21	+33:49:28	0	27	54	7	69	9	0	25	0	6
CFC580	13:29:22	+32:05:11	0	19	0	22	0	18	0	24	0	17
CFC581	13:29:28	+33:50:04	0	29	50	7	119	20	0	30	0	18
CFC582	13:29:32	+32:34:17	44	8	101	26	34	6	0	34	0	6
CFC583	13:29:35	+26:24:35	82	11	278	36	605	67	752	99	647	87
CFC584	13:29:36	+32:24:02	0	28	0	95	0	147	0	221	0	20
CFC585	13:29:36	+32:12:56	0	22	34	7	38	6	0	26	0	23
CFC586	13:29:37	+26:25:21	0	26	0	20	0	65	0	31	0	86
CFC587	13:29:48	+31:07:48	179	18	636	69	1551	152	2922	362	2094	255
CFC588	13:29:49	+33:01:35	0	24	0	22	0	19	0	28	0	19
CFC589	13:29:50	+31:25:15	0	26	27	7	65	8	0	8	0	17
CFC590	13:29:50	+31:18:07	29	7	59	8	127	23	200	42	0	19
CFC591	13:29:54	+26:24:40	0	21	0	20	0	23	0	21	0	16
CFC592	13:29:56	+29:46:19	0	26	0	21	19	6	0	26	0	19
CFC593	13:30:02	+31:46:36	0	24	0	17	35	6	0	27	0	18
CFC594	13:30:02	+31:00:41	0	31	0	56	0	180	0	452	0	336
CFC595	13:30:02	+25:46:58	0	27	0	22	0	18	0	29	0	21
CFC596	13:30:06	+31:23:17	0	25	0	17	0	16	0	26	0	22
CFC597	13:30:11	+34:51:31	0	22	0	22	0	16	0	16	0	15
CFC598	13:30:13	+26:20:21	0	30	0	22	0	20	0	25	0	18
CFC599	13:30:13	+26:39:56	0	27	0	19	26	7	0	21	0	17
CFC600	13:30:17	+34:54:01	0	21	0	16	15	4	0	22	0	5
CFC601	13:30:25	+31:37:14	0	119	0	255	0	482	0	772	0	479
CFC602	13:30:26	+35:02:26	0	27	0	28	0	24	0	20	0	14
CFC603	13:30:30	+34:17:35	0	22	0	16	0	17	0	26	0	16
CFC604	13:30:30	+31:21:29	0	23	0	17	0	18	0	33	0	15
CFC605	13:30:36	+34:55:02	59	9	229	32	484	53	884	116	820	105
CFC606	13:30:37	+28:54:37	0	24	0	24	0	20	0	30	0	23
CFC607	13:30:38	+34:56:13	0	27	0	25	0	17	0	26	0	19
CFC608	13:30:38	+35:20:20	28	9	53	9	113	19	143	32	0	19
CFC609	13:30:42	+34:49:50	0	23	0	24	0	13	0	24	0	19
CFC610	13:30:43	+31:55:03	31	8	42	7	76	9	0	30	0	23
CFC611	13:30:44	+32:45:38	0	31	0	19	0	66	0	25	0	16
CFC612	13:30:44	+32:17:37	32	8	109	12	299	34	447	68	340	51
CFC613	13:30:45	+26:31:17	44	8	112	23	198	34	296	53	151	28
CFC614	13:30:45	+27:18:34	0	27	0	23	0	16	0	25	0	17
CFC615	13:30:47	+31:31:02	0	24	0	25	0	22	0	26	0	18
CFC616	13:30:47	+34:48:43	0	22	0	21	0	14	0	18	0	15
CFC617	13:30:48	+34:38:25	0	24	79	17	167	23	0	7	0	16
CFC618	13:31:01	+34:09:11	0	25	29	8	69	8	0	7	0	5
CFC619	13:31:01	+30:39:24	0	23	0	18	0	17	0	26	0	20
CFC620	13:31:04	+34:26:08	0	22	0	19	0	52	0	23	0	17
CFC621	13:31:04	+24:24:06	0	25	51	9	74	9	0	11	0	20
CFC622	13:31:05	+34:41:07	23	7	49	7	127	22	0	21	0	5
CFC623	13:31:06	+32:18:53	0	20	0	19	0	13	0	24	0	24
CFC624	13:31:07	+33:53:45	0	22	0	20	0	15	0	28	0	18
CFC625	13:31:09	+32:46:53	0	28	75	9	162	16	339	51	371	53
CFC626	13:31:09	+27:18:51	0	22	0	19	0	15	0	25	0	19
CFC627	13:31:17	+32:10:06	0	24	0	23	39	7	0	25	0	17
CFC628	13:31:21	+25:37:08	65	10	206	29	482	53	634	93	356	63
CFC629	13:31:29	+32:52:58	54	11	157	24	381	42	585	78	660	86
CFC630	13:31:33	+34:15:47	28	6	58	7	143	21	0	33	161	29
CFC631	13:31:37	+33:44:24	0	22	0	19	0	17	0	25	0	18
CFC632	13:31:41	+34:48:56	0	18	0	15	0	13	0	24	0	22
CFC633	13:31:55	+33:44:46	0	24	0	24	0	21	0	30	0	18
CFC634	13:31:56	+31:01:58	0	36	0	22	0	51	0	24	0	20
CFC635	13:31:57	+34:32:49	0	23	0	14	0	16	0	30	0	21
CFC636	13:31:58	+27:01:14	52	9	70	9	158	21	267	53	0	6

Continued on next page

OBJECT	RA h:m:s (J2000)	Dec. d:m:s (J2000)	S_{500} (mJy)	E_{500} (mJy)	S_{350} (mJy)	E_{350} (mJy)	S_{250} (mJy)	E_{250} (mJy)	S_{160} (mJy)	E_{160} (mJy)	S_{100} (mJy)	E_{100} (mJy)
CFC637	13:32:10	+28:23:20	43	8	101	10	270	30	494	72	264	42
CFC638	13:32:18	+25:58:35	0	23	0	20	0	19	0	26	0	20
CFC639	13:32:19	+28:19:02	0	23	0	17	0	19	0	24	0	15
CFC640	13:32:20	+35:19:49	0	24	0	15	0	16	0	33	0	18
CFC641	13:32:21	+34:43:08	0	19	0	19	0	16	0	27	0	21
CFC642	13:32:26	+33:30:44	0	20	0	19	0	14	0	29	0	20
CFC643	13:32:33	+33:44:18	0	25	0	29	0	18	0	31	0	19
CFC644	13:32:38	+35:21:44	0	22	0	19	47	6	0	9	0	23
CFC645	13:32:38	+25:26:28	155	27	355	48	733	77	1216	157	1001	129
CFC646	13:32:44	+32:55:58	0	21	0	23	0	52	0	25	0	18
CFC647	13:32:44	+27:52:52	0	21	0	22	0	21	0	22	0	15
CFC648	13:32:52	+32:58:18	0	20	45	9	131	19	212	43	0	8
CFC649	13:32:53	+34:09:18	0	25	0	34	0	67	0	230	0	202
CFC650	13:32:57	+27:43:04	0	17	0	19	0	17	0	17	0	14
CFC651	13:32:58	+27:41:10	0	22	0	27	0	53	0	81	0	19
CFC652	13:33:01	+32:17:35	0	20	0	18	0	42	0	25	0	20
CFC653	13:33:03	+34:33:01	37	8	90	12	222	28	356	58	234	39
CFC654	13:33:03	+33:31:30	0	24	0	23	0	17	0	24	0	19
CFC655	13:33:06	+33:09:03	75	9	233	30	548	57	829	113	641	93
CFC656	13:33:13	+33:06:35	151	16	454	50	1051	104	1707	212	1183	148
CFC657	13:33:16	+34:32:13	175	27	534	59	1358	139	2575	318	2229	272
CFC658	13:33:17	+33:29:27	0	22	0	21	21	6	0	25	0	8
CFC659	13:33:18	+33:07:11	0	24	0	21	0	13	0	29	0	22
CFC660	13:33:21	+34:50:55	0	25	0	18	19	5	0	27	0	19
CFC661	13:33:23	+33:31:30	0	26	0	18	0	17	0	34	0	20
CFC662	13:33:24	+33:12:48	0	20	0	17	0	15	0	30	0	17
CFC663	13:33:29	+33:02:32	219	33	586	63	1286	130	1906	243	1110	145
CFC664	13:33:30	+33:52:31	0	24	0	27	0	21	0	26	0	21
CFC665	13:33:32	+34:25:13	0	20	0	25	0	19	0	26	0	22
CFC666	13:33:33	+34:24:00	0	19	0	25	0	18	0	25	0	20
CFC667	13:33:41	+31:14:01	0	20	0	22	29	6	0	26	0	16
CFC668	13:33:54	+34:57:45	0	28	0	23	0	18	0	36	0	20
CFC669	13:33:58	+34:49:41	0	25	0	23	0	18	0	27	0	18
CFC670	13:33:59	+34:32:42	0	17	0	22	0	18	0	26	0	20
CFC671	13:34:01	+34:44:05	0	28	0	24	0	16	0	24	0	22
CFC672	13:34:02	+26:05:39	0	28	0	18	0	17	0	23	0	21
CFC673	13:34:05	+27:33:40	40	8	31	8	45	7	0	21	0	5
CFC674	13:34:09	+28:54:07	0	17	0	18	0	14	0	27	0	20
CFC675	13:34:09	+34:45:54	90	11	257	25	669	68	1048	138	712	95
CFC676	13:34:14	+34:11:38	0	26	72	9	168	24	0	11	0	8
CFC677	13:34:14	+31:25:30	0	23	0	25	0	75	0	27	0	20
CFC678	13:34:17	+34:55:45	112	26	182	25	479	55	561	81	353	57
CFC679	13:34:18	+34:51:47	0	31	0	57	0	76	0	28	0	20
CFC680	13:34:19	+34:58:58	0	27	0	21	0	20	0	25	0	21
CFC681	13:34:21	+34:46:22	0	26	0	24	0	13	0	28	0	31
CFC682	13:34:25	+34:38:19	0	20	0	21	0	14	0	26	0	17
CFC683	13:34:30	+35:27:18	0	30	31	7	67	9	0	9	0	21
CFC684	13:34:30	+34:39:33	0	23	0	26	0	23	0	24	0	22
CFC685	13:34:30	+33:41:24	0	23	0	16	0	14	0	33	0	20
CFC686	13:34:31	+35:14:32	82	11	198	28	417	46	455	68	307	48
CFC687	13:34:34	+33:37:40	0	28	47	7	125	23	0	10	0	10
CFC688	13:34:35	+34:46:40	0	25	72	10	179	18	443	70	382	55
CFC689	13:34:36	+34:36:44	0	21	0	21	0	19	0	27	0	19
CFC690	13:34:40	+32:57:04	0	26	0	28	0	17	0	22	0	18
CFC691	13:34:42	+27:34:21	0	28	37	8	76	8	0	10	0	6
CFC692	13:34:45	+25:02:15	0	23	0	22	0	18	0	24	0	19
CFC693	13:34:45	+25:26:59	0	19	0	19	0	19	0	23	0	20
CFC694	13:34:46	+34:34:45	0	17	0	23	0	19	0	30	0	20
CFC695	13:34:51	+34:03:19	86	11	321	38	721	72	1077	137	845	111
CFC696	13:34:51	+34:28:22	0	19	0	26	0	61	0	25	0	15
CFC697	13:34:54	+26:12:22	0	24	0	16	0	15	0	21	0	35
CFC698	13:34:55	+31:23:36	106	21	238	34	499	58	422	81	208	37
CFC699	13:34:57	+34:02:38	495	54	1373	135	3979	394	6242	754	5502	666
CFC700	13:34:57	+34:48:14	0	27	0	22	0	15	0	28	0	20
CFC701	13:35:03	+33:47:38	0	25	0	22	0	15	0	30	0	21
CFC702	13:35:05	+34:28:30	33	7	67	9	109	12	136	32	0	7
CFC703	13:35:07	+34:17:43	0	23	0	25	0	15	0	26	0	17
CFC704	13:35:08	+25:29:43	29	7	30	5	25	5	0	27	0	19
CFC705	13:35:09	+32:39:41	0	16	54	7	90	10	221	48	138	29
CFC706	13:35:11	+25:56:49	0	17	0	15	0	15	0	27	0	19
CFC707	13:35:11	+28:32:10	0	21	17	5	34	6	0	24	0	6
CFC708	13:35:11	+34:38:48	0	25	0	21	0	24	0	24	0	19
CFC709	13:35:11	+32:48:33	0	25	0	23	0	19	0	28	0	18
CFC710	13:35:13	+34:40:38	56	11	207	27	453	49	583	83	276	48
CFC711	13:35:13	+34:26:00	0	18	0	23	0	17	0	27	0	22
CFC712	13:35:13	+27:37:48	0	23	0	20	0	19	0	32	0	18
CFC713	13:35:14	+25:02:41	56	8	151	16	447	48	916	122	770	98
CFC714	13:35:15	+32:57:12	0	18	0	20	33	7	0	9	0	18
CFC715	13:35:19	+26:25:29	131	24	350	44	612	68	1000	139	438	61
CFC716	13:35:22	+33:47:52	0	22	0	23	0	16	0	26	0	20
CFC717	13:35:24	+27:54:42	29	7	66	9	162	23	301	52	0	6
CFC718	13:35:25	+33:26:41	0	24	0	22	0	18	0	31	0	19
CFC719	13:35:26	+33:43:30	0	24	0	22	0	54	0	28	0	16
CFC720	13:35:27	+35:26:11	0	24	0	21	0	19	0	35	0	18
CFC721	13:35:31	+34:13:55	0	33	0	23	25	6	0	28	0	22
CFC722	13:35:31	+34:09:07	43	11	92	11	219	27	256	46	199	34
CFC723	13:35:34	+33:18:59	0	23	0	23	0	21	0	23	0	20
CFC724	13:35:35	+33:28:46	85	12	228	28	506	53	669	94	221	35
CFC725	13:35:36	+33:23:12	0	30	0	26	0	21	0	27	0	19
CFC726	13:35:38	+25:52:30	67	9	214	28	474	49	653	93	381	57
CFC727	13:35:38	+33:40:07	0	26	0	25	0	18	0	26	0	23

Continued on next page

OBJECT	RA h:m:s (J2000)	Dec. d:m:s (J2000)	S_{500} (mJy)	E_{500} (mJy)	S_{350} (mJy)	E_{350} (mJy)	S_{250} (mJy)	E_{250} (mJy)	S_{160} (mJy)	E_{160} (mJy)	S_{100} (mJy)	E_{100} (mJy)
CFC728	13:35:40	+34:47:44	36	9	90	10	282	33	509	74	445	62
CFC729	13:35:40	+32:54:57	0	19	42	8	101	17	0	27	0	24
CFC730	13:35:42	+35:05:18	0	21	0	21	0	16	0	27	0	22
CFC731	13:35:43	+33:33:39	0	24	0	20	0	20	0	24	0	25
CFC732	13:35:43	+27:24:33	25	8	76	9	247	31	196	43	0	7
CFC733	13:35:45	+34:41:32	0	24	0	23	0	22	0	28	0	19
CFC734	13:35:45	+35:07:40	0	20	0	22	0	18	0	45	0	22
CFC735	13:35:48	+34:59:50	0	113	0	225	0	492	0	868	0	19
CFC736	13:35:49	+34:34:33	0	24	0	27	0	26	0	29	0	25
CFC737	13:35:49	+25:25:30	0	22	0	18	0	48	0	30	0	23
CFC738	13:35:51	+29:12:50	0	25	18	4	42	6	0	25	0	7
CFC739	13:35:51	+27:52:00	0	25	0	21	0	17	0	27	0	21
CFC740	13:35:52	+33:19:37	27	8	102	12	305	33	608	82	667	89
CFC741	13:35:53	+23:45:26	0	21	33	8	60	9	0	12	0	32
CFC742	13:35:53	+33:38:04	0	25	42	8	46	7	0	26	0	22
CFC743	13:35:53	+33:13:21	30	8	53	8	104	18	0	10	0	9
CFC744	13:35:56	+34:41:13	0	23	0	20	0	14	0	28	0	18
CFC745	13:35:57	+33:25:48	0	26	0	69	0	96	0	28	0	22
CFC746	13:35:58	+33:28:26	0	25	0	22	0	20	0	22	0	16
CFC747	13:36:00	+34:49:04	0	27	0	19	0	17	0	23	0	14
CFC748	13:36:04	+30:08:27	0	22	0	16	52	7	0	12	282	44
CFC749	13:36:05	+33:16:57	0	27	28	8	42	7	0	27	0	7
CFC750	13:36:05	+33:41:32	0	26	0	26	0	17	0	28	0	21
CFC751	13:36:06	+34:51:57	0	28	0	19	21	7	0	26	0	21
CFC752	13:36:08	+33:26:31	0	23	0	25	33	6	0	30	0	19
CFC753	13:36:10	+30:02:54	0	26	19	6	40	6	0	11	0	6
CFC754	13:36:11	+35:20:52	0	19	0	17	0	19	0	28	0	18
CFC755	13:36:18	+33:43:14	0	27	0	24	0	22	0	26	0	17
CFC756	13:36:19	+33:25:24	49	8	167	23	379	42	694	97	506	68
CFC757	13:36:19	+32:52:30	0	22	0	19	26	7	0	31	0	19
CFC758	13:36:20	+28:47:52	0	26	0	23	0	26	0	26	0	19
CFC759	13:36:23	+30:01:15	0	19	0	18	0	15	0	25	0	18
CFC760	13:36:23	+33:12:57	0	26	0	17	47	7	0	27	0	19
CFC761	13:36:28	+29:30:45	0	27	0	20	0	16	0	18	0	12
CFC762	13:36:28	+33:16:28	0	24	0	23	0	17	0	35	0	21
CFC763	13:36:35	+34:28:36	0	26	0	20	0	18	0	23	0	19
CFC764	13:36:41	+33:17:44	0	24	35	6	64	8	0	8	0	19
CFC765	13:36:42	+26:39:00	0	18	21	6	52	8	0	22	0	17
CFC766	13:36:42	+34:44:46	0	24	0	18	36	6	0	27	0	26
CFC767	13:36:46	+24:24:28	0	21	0	27	0	16	0	31	0	20
CFC768	13:36:48	+33:29:20	0	24	0	23	0	21	0	21	0	19
CFC769	13:36:53	+34:36:44	0	24	0	22	0	16	0	29	0	18
CFC770	13:36:55	+29:48:03	0	22	0	18	0	13	0	24	0	17
CFC771	13:36:57	+26:58:45	0	27	0	17	0	17	0	29	0	18
CFC772	13:36:59	+33:34:12	113	22	255	37	480	54	568	91	355	55
CFC773	13:37:03	+27:14:19	0	23	0	21	0	16	0	25	0	15
CFC774	13:37:06	+33:19:38	0	27	0	20	0	19	0	23	0	18
CFC775	13:37:07	+25:59:29	0	23	0	21	0	20	0	23	0	20
CFC776	13:37:23	+24:37:10	0	21	0	17	17	5	0	32	0	20
CFC777	13:37:34	+33:16:42	0	25	0	21	0	15	0	26	0	22
CFC778	13:37:38	+28:48:09	39	8	109	19	228	31	328	64	186	35
CFC779	13:37:39	+24:06:08	0	24	0	25	0	73	0	28	0	22
CFC780	13:37:44	+32:27:39	0	22	0	22	0	19	0	28	0	22
CFC781	13:37:44	+27:47:11	21	7	61	9	155	22	171	35	206	38
CFC782	13:37:51	+25:39:54	0	33	29	8	81	9	0	11	190	33
CFC783	13:38:02	+26:53:27	0	21	0	15	0	15	0	24	0	21
CFC784	13:38:08	+26:51:46	0	17	0	19	0	19	0	24	0	18
CFC785	13:38:10	+26:44:35	0	21	0	19	0	17	0	24	0	15
CFC786	13:38:13	+32:49:22	136	26	343	43	706	80	931	135	304	56
CFC787	13:38:13	+23:58:09	34	8	40	7	52	7	0	9	0	8
CFC788	13:38:15	+32:47:26	0	30	25	7	34	6	0	29	0	22
CFC789	13:38:20	+26:45:35	0	21	0	19	0	23	0	26	0	18
CFC790	13:38:23	+23:58:19	0	26	0	22	0	17	0	27	0	22
CFC791	13:38:24	+26:46:45	0	20	0	18	0	21	0	22	0	19
CFC792	13:38:25	+26:44:32	0	19	0	22	0	19	0	24	0	12
CFC793	13:38:26	+24:27:51	0	24	0	18	0	17	0	33	0	21
CFC794	13:38:29	+26:04:39	33	9	70	9	117	12	0	12	0	6
CFC795	13:38:29	+30:59:12	24	6	45	8	85	9	0	9	0	9
CFC796	13:38:31	+33:30:11	0	21	0	24	0	18	0	34	0	17
CFC797	13:38:31	+26:06:19	0	25	0	20	0	21	0	29	0	24
CFC798	13:38:40	+26:43:50	0	22	38	7	78	10	0	7	0	5
CFC799	13:38:42	+31:14:57	0	25	0	21	0	16	0	23	0	18
CFC800	13:38:43	+24:41:14	0	24	0	20	0	15	0	29	0	24
CFC801	13:38:43	+31:16:13	0	24	21	6	92	21	0	24	0	6
CFC802	13:38:44	+26:19:42	44	7	140	23	289	33	378	62	295	49
CFC803	13:38:45	+30:28:49	78	12	266	34	515	58	745	102	741	98
CFC804	13:38:45	+26:47:48	0	22	0	16	0	18	0	22	0	21
CFC805	13:38:46	+26:29:55	0	19	0	21	0	20	0	28	0	16
CFC806	13:38:50	+32:22:12	0	21	33	9	42	7	0	25	0	23
CFC807	13:38:50	+34:20:58	0	26	0	21	0	20	0	41	0	22
CFC808	13:38:57	+24:58:48	0	32	0	25	40	7	0	30	0	18
CFC809	13:38:58	+26:29:47	26	7	31	6	44	6	0	9	0	6
CFC810	13:38:59	+31:21:54	0	21	0	23	0	20	0	23	0	18
CFC811	13:39:03	+32:09:23	51	10	103	20	192	27	210	40	0	6
CFC812	13:39:04	+27:24:25	0	24	0	19	0	22	0	26	0	18
CFC813	13:39:12	+26:28:47	0	23	0	23	0	17	0	23	0	22
CFC814	13:39:13	+24:53:35	37	11	0	20	35	7	0	28	0	6
CFC815	13:39:14	+25:47:37	0	28	0	18	0	20	0	26	0	20
CFC816	13:39:20	+34:41:16	0	26	41	6	133	20	229	44	306	49
CFC817	13:39:29	+31:17:59	0	61	0	24	0	20	0	34	0	18
CFC818	13:39:32	+26:46:39	0	24	26	6	46	7	0	21	0	5

Continued on next page

OBJECT	RA h:m:s (J2000)	Dec. d:m:s (J2000)	S_{500} (mJy)	E_{500} (mJy)	S_{350} (mJy)	E_{350} (mJy)	S_{250} (mJy)	E_{250} (mJy)	S_{160} (mJy)	E_{160} (mJy)	S_{100} (mJy)	E_{100} (mJy)
CFC819	13:39:33	+25:33:22	0	19	0	18	0	16	0	31	0	21
CFC820	13:39:40	+35:01:24	43	9	100	19	203	26	169	39	113	29
CFC821	13:39:41	+30:17:02	0	23	0	22	0	15	0	28	0	19
CFC822	13:39:44	+27:46:35	71	10	285	41	637	69	1071	140	823	109
CFC823	13:39:47	+26:41:11	0	23	0	17	0	17	0	23	0	15
CFC824	13:39:51	+28:02:39	0	24	34	9	44	7	0	29	0	20
CFC825	13:39:55	+28:23:44	0	208	0	522	0	1249	0	3108	0	2698
CFC826	13:40:01	+26:58:43	0	21	64	9	181	22	238	41	276	41
CFC827	13:40:05	+28:22:47	0	29	0	20	0	19	0	32	0	19
CFC828	13:40:10	+26:50:27	0	23	0	18	0	18	0	29	0	22
CFC829	13:40:17	+26:20:58	153	22	393	44	806	83	980	129	560	80
CFC830	13:40:18	+32:09:11	50	10	94	11	253	30	344	53	318	51
CFC831	13:40:35	+32:01:11	0	29	0	23	0	19	0	24	0	16
CFC832	13:40:42	+26:00:31	0	20	0	19	0	14	0	30	0	21
CFC833	13:40:43	+25:54:30	38	9	67	9	189	25	269	54	0	7
CFC834	13:40:45	+25:57:19	35	8	70	11	188	24	219	39	258	45
CFC835	13:40:46	+25:53:50	0	27	0	28	46	7	0	9	0	7
CFC836	13:40:51	+24:28:23	94	11	340	38	822	83	1353	172	1083	139
CFC837	13:40:57	+31:25:08	0	19	0	25	0	19	0	29	0	19
CFC838	13:40:58	+25:12:52	0	27	0	22	0	18	0	25	0	19
CFC839	13:40:58	+27:43:35	0	26	34	8	85	10	0	10	175	31
CFC840	13:41:02	+25:49:53	0	25	0	21	0	21	0	32	0	19
CFC841	13:41:04	+27:41:38	32	10	64	10	175	29	0	11	0	9
CFC842	13:41:06	+32:29:31	0	30	0	83	0	98	0	26	0	21
CFC843	13:41:10	+26:08:11	0	19	0	20	0	17	0	33	0	22
CFC844	13:41:17	+25:42:48	0	22	0	22	0	20	0	36	0	28
CFC845	13:41:17	+32:31:37	33	8	82	21	124	22	152	37	0	8
CFC846	13:41:18	+24:29:46	32	8	93	19	181	26	0	10	132	31
CFC847	13:41:18	+26:06:20	0	22	0	21	25	5	0	25	0	20
CFC848	13:41:21	+28:56:33	0	26	0	21	0	21	0	26	0	20
CFC849	13:41:27	+29:57:23	0	24	0	24	0	16	0	31	0	21
CFC850	13:41:28	+34:49:31	0	25	0	24	0	23	0	27	0	22
CFC851	13:41:28	+32:11:33	43	9	99	19	169	27	162	36	0	6
CFC852	13:41:30	+24:28:52	0	21	0	21	22	7	0	26	0	18
CFC853	13:41:30	+24:20:34	0	23	0	18	0	19	0	23	0	19
CFC854	13:41:32	+33:41:44	0	34	0	23	0	30	0	35	0	22
CFC855	13:41:33	+32:25:57	0	27	0	23	0	13	0	28	0	24
CFC856	13:41:38	+24:40:38	0	19	0	20	0	21	0	28	0	21
CFC857	13:41:39	+24:49:20	0	28	0	21	0	22	0	32	0	17
CFC858	13:41:44	+26:07:29	0	26	0	20	0	17	0	20	0	18
CFC859	13:41:45	+27:00:17	76	10	270	33	638	65	877	115	593	83
CFC860	13:41:45	+27:06:22	0	30	40	6	84	10	0	10	0	9
CFC861	13:41:49	+24:20:58	0	22	0	14	31	6	0	26	0	18
CFC862	13:41:50	+30:33:57	0	24	0	22	0	21	0	28	0	21
CFC863	13:41:50	+24:40:47	0	23	30	8	61	8	0	7	0	8
CFC864	13:41:54	+27:03:45	0	23	0	19	36	7	0	26	0	7
CFC865	13:42:01	+31:54:10	0	27	0	20	0	24	0	27	0	19
CFC866	13:42:05	+32:01:43	42	10	70	10	167	24	216	41	0	8
CFC867	13:42:09	+27:34:13	0	21	0	25	0	13	0	31	0	20
CFC868	13:42:10	+26:50:12	0	25	0	18	0	18	0	20	0	23
CFC869	13:42:11	+29:53:44	0	25	0	24	0	20	0	26	0	16
CFC870	13:42:16	+35:06:43	0	19	0	19	0	20	0	32	0	17
CFC871	13:42:22	+35:37:26	142	23	423	50	932	95	1620	204	1412	176
CFC872	13:42:32	+26:13:57	0	22	0	20	0	23	0	30	0	21
CFC873	13:42:34	+31:31:51	0	27	0	24	0	15	0	27	0	20
CFC874	13:42:34	+35:01:13	228	33	602	71	1231	128	1650	206	1151	146
CFC875	13:42:38	+24:27:54	0	25	0	17	0	20	0	30	0	20
CFC876	13:42:40	+25:33:53	0	26	63	9	127	12	260	49	130	30
CFC877	13:42:44	+35:03:46	0	22	55	7	160	21	332	53	305	45
CFC878	13:42:45	+24:35:24	0	32	0	19	0	19	0	32	0	18
CFC879	13:42:49	+25:50:27	0	24	0	17	0	17	0	23	0	19
CFC880	13:42:50	+24:31:49	138	38	186	50	272	58	0	30	0	17
CFC881	13:42:51	+34:02:55	0	24	0	27	0	65	0	27	0	23
CFC882	13:42:58	+34:16:17	0	18	29	8	58	8	0	10	0	23
CFC883	13:43:06	+33:41:12	0	22	0	20	0	17	0	30	0	23
CFC884	13:43:08	+35:07:00	0	19	0	25	0	69	0	34	0	26
CFC885	13:43:10	+24:27:36	0	28	0	20	0	22	0	31	0	19
CFC886	13:43:18	+24:37:41	0	26	0	29	46	7	0	9	0	22
CFC887	13:43:20	+24:25:05	0	25	32	7	47	7	0	11	0	21
CFC888	13:43:23	+33:49:59	0	19	0	23	0	19	0	38	0	21
CFC889	13:43:32	+25:31:57	0	24	0	23	0	21	0	28	0	20
CFC890	13:43:36	+24:47:12	0	23	0	23	25	6	0	24	0	20
CFC891	13:43:37	+33:56:56	37	8	70	10	152	21	0	10	0	7
CFC892	13:43:38	+30:56:18	0	23	30	7	42	6	0	25	0	20
CFC893	13:43:44	+25:23:31	0	25	0	21	0	17	0	24	0	20
CFC894	13:43:48	+35:10:44	0	19	0	19	0	17	0	29	0	22
CFC895	13:43:49	+31:02:46	0	20	0	19	0	19	0	33	0	19
CFC896	13:44:03	+32:51:38	0	19	0	19	0	16	0	27	0	19
CFC897	13:44:05	+33:54:46	0	29	0	25	0	23	0	29	0	20
CFC898	13:44:20	+26:05:03	0	19	0	20	0	20	0	22	0	18
CFC899	13:44:24	+34:07:48	0	29	38	8	63	8	0	33	0	26
CFC900	13:44:30	+30:42:29	0	18	37	8	118	12	279	50	314	48
CFC901	13:44:34	+23:47:47	0	26	0	24	0	19	0	29	0	20
CFC902	13:44:42	+25:31:24	0	23	32	6	69	8	0	13	0	11
CFC903	13:44:47	+31:36:56	69	10	244	24	698	74	1363	171	1707	211
CFC904	13:44:48	+35:29:41	32	9	29	8	22	6	0	27	0	16
CFC905	13:44:51	+32:31:33	0	25	0	24	0	14	0	30	0	17
CFC906	13:45:03	+34:52:41	0	25	0	15	0	16	0	32	0	19
CFC907	13:45:03	+35:20:54	0	23	0	21	0	19	0	26	0	17
CFC908	13:45:06	+31:00:22	0	22	0	20	0	17	0	22	0	22
CFC909	13:45:09	+23:47:48	0	25	0	19	0	21	0	23	0	26

Continued on next page

OBJECT	RA h:m:s (J2000)	Dec. d:m:s (J2000)	S_{500} (mJy)	E_{500} (mJy)	S_{350} (mJy)	E_{350} (mJy)	S_{250} (mJy)	E_{250} (mJy)	S_{160} (mJy)	E_{160} (mJy)	S_{100} (mJy)	E_{100} (mJy)
CFC910	13:45:20	+35:28:25	0	25	0	20	0	20	0	22	0	18
CFC911	13:45:27	+31:05:18	0	21	0	18	0	14	0	25	0	19
CFC912	13:45:33	+35:43:13	0	21	0	14	0	16	0	35	0	19
CFC913	13:45:34	+35:36:40	37	7	89	9	228	22	489	72	390	54
CFC914	13:45:43	+23:53:32	0	22	0	24	0	14	0	26	0	25
CFC915	13:45:46	+35:42:10	0	24	0	22	0	20	0	32	0	24
CFC916	13:45:48	+31:20:55	0	18	40	6	95	10	295	57	0	6
CFC917	13:45:52	+26:46:30	78	10	273	39	540	62	776	106	483	69
CFC918	13:46:03	+33:50:16	0	33	25	7	54	8	0	11	172	35
CFC919	13:46:03	+35:31:13	46	9	139	14	398	42	594	86	320	47
CFC920	13:46:04	+26:25:42	0	24	0	15	18	5	0	37	0	23
CFC921	13:46:07	+34:28:36	0	29	0	27	0	70	0	26	0	19
CFC922	13:46:09	+25:12:54	0	24	31	7	62	8	0	11	0	6
CFC923	13:46:20	+33:53:00	0	26	0	29	0	18	0	29	0	20
CFC924	13:46:26	+32:09:48	0	28	0	26	0	54	0	28	0	18
CFC925	13:46:35	+34:08:46	0	16	0	21	0	18	0	29	0	20
CFC926	13:46:37	+25:00:27	0	30	0	25	0	22	0	51	0	18
CFC927	13:46:37	+25:02:24	0	29	22	7	44	8	0	42	0	21
CFC928	13:46:39	+34:13:28	0	29	0	21	0	20	0	32	0	25
CFC929	13:46:47	+28:40:13	0	25	0	19	0	20	0	28	0	20
CFC930	13:46:52	+25:27:14	0	25	0	23	0	21	0	29	0	20
CFC931	13:46:56	+29:39:29	0	22	0	23	0	23	0	21	0	15
CFC932	13:47:01	+25:04:41	29	8	34	7	58	7	0	9	0	21
CFC933	13:47:01	+33:53:36	235	38	743	106	1041	129	1002	139	909	125
CFC934	13:47:04	+28:33:31	0	25	0	26	0	20	0	29	0	19
CFC935	13:47:04	+24:59:47	0	26	0	84	0	122	0	245	0	165
CFC936	13:47:10	+34:05:19	70	10	267	36	589	62	971	128	831	106
CFC937	13:47:36	+32:00:04	0	21	0	23	0	20	0	25	0	17
CFC938	13:47:37	+26:29:10	0	17	0	15	0	17	0	29	0	20
CFC939	13:47:42	+32:06:53	0	26	0	25	0	17	0	29	0	30
CFC940	13:47:53	+25:33:23	0	26	0	23	0	16	0	31	0	19
CFC941	13:47:54	+24:18:06	0	21	0	20	45	7	0	9	0	21
CFC942	13:48:14	+24:46:39	0	21	0	24	0	96	0	21	0	21
CFC943	13:48:17	+25:07:26	0	26	0	18	0	23	0	27	0	20
CFC944	13:48:18	+23:57:26	0	32	0	24	0	18	0	30	0	22
CFC945	13:48:22	+25:31:24	0	22	0	20	0	20	0	28	0	17
CFC946	13:48:34	+24:53:29	36	8	85	10	236	28	286	48	205	38
CFC947	13:48:35	+24:00:54	33	10	88	11	239	31	367	56	278	46
CFC948	13:48:49	+24:00:02	0	25	0	27	0	20	0	27	0	22
CFC949	13:49:09	+24:31:11	0	22	0	24	0	20	0	38	0	20
CFC950	13:49:14	+24:46:03	25	7	44	7	68	8	0	10	0	22
CFC951	13:49:18	+24:05:42	24	7	46	8	116	20	160	40	0	8

Table B.2. The Coma Filament Catalogue galaxies and their FIR properties. This table includes the Herchel fluxes from all detected galaxies, and stricked upper limits placed on undetected galaxies. If a galaxy was rejected by-eye then flux from the PSF-convolved map was used as an upper limit and the flux asterisked.

OBJECT	RA h:m:s (J2000)	Dec. d:m:s (J2000)	Dust Temperature K	Duss Mass $\log(M_{Dust}/\mathrm{M}_{\odot})$	Stellar Mass $\log(M_{Stars}/\mathrm{M}_{\odot})$
CFC002	12:46:10.11	+30:43:54.9	23.1 (0.79)	8.1 (0.06)	11.04
CFC008	12:46:29.76	+30:50:55.1	21.05 (1.19)	6.83 (0.1)	9.65
CFC011	12:47:26.16	+29:47:16.0	17.71 (0.49)	8.04 (0.06)	10.76
CFC039	12:49:36.87	+30:50:43.8	18.06 (0.61)	8.07 (0.07)	10.53
CFC042	12:49:42.29	+26:53:31.3	20.35 (1.01)	7.46 (0.1)	11.05
CFC048	12:49:47.42	+32:04:49.8	21.45 (1.06)	7.49 (0.09)	10.44
CFC058	12:50:20.22	+26:44:59.5	19.44 (0.99)	7.09 (0.1)	9.51
CFC065	12:50:31.41	+30:50:48.9	19.96 (0.58)	7.52 (0.06)	10.34
CFC066	12:50:31.65	+27:18:50.3	18.73 (1.21)	7.08 (0.1)	9.61
CFC073	12:51:01.73	+28:55:40.7	22.65 (0.83)	7.49 (0.07)	10.34
CFC081	12:51:17.93	+27:06:22.2	18.7 (0.54)	7.49 (0.06)	10.5
CFC083	12:51:19.93	+31:03:34.7	16.9 (0.62)	7.7 (0.08)	10.78
CFC088	12:51:29.55	+31:48:52.4	22.22 (0.64)	7.69 (0.05)	10.69
CFC092	12:51:44.93	+27:01:06.1	20.36 (1.0)	7.11 (0.09)	9.59
CFC104	12:52:06.87	+27:01:34.8	21.15 (0.88)	7.43 (0.08)	10.16
CFC107	12:52:17.72	+27:05:07.9	21.93 (0.77)	7.27 (0.06)	10.41
CFC117	12:53:02.94	+32:06:25.2	20.17 (0.78)	7.49 (0.07)	10.69
CFC124	12:53:52.17	+31:06:25.5	19.9 (0.76)	7.45 (0.07)	10.03
CFC133	12:54:40.02	+32:22:01.5	21.07 (0.85)	7.31 (0.08)	10.1
CFC135	12:54:47.82	+30:32:41.4	19.62 (0.69)	7.44 (0.08)	9.86
CFC159	12:57:02.89	+31:37:31.9	20.98 (0.7)	7.26 (0.07)	10.1
CFC168	12:58:09.99	+24:20:56.1	22.57 (1.1)	7.18 (0.08)	9.73
CFC169	12:58:10.06	+32:00:59.5	18.7 (0.62)	7.76 (0.07)	10.62
CFC178	12:59:22.70	+26:01:34.4	19.05 (1.01)	7.2 (0.1)	9.69
CFC183	12:59:45.33	+32:02:42.1	20.35 (0.62)	7.68 (0.06)	10.3
CFC200	13:02:18.29	+32:53:26.2	18.16 (0.63)	8.02 (0.07)	11.19
CFC209	13:03:01.71	+32:12:38.6	18.99 (0.77)	7.47 (0.08)	10.06
CFC221	13:04:28.27	+23:34:30.1	18.22 (0.69)	7.55 (0.08)	10.39
CFC225	13:05:16.02	+25:57:27.5	20.67 (0.9)	7.71 (0.08)	10.33
CFC229	13:05:28.88	+33:50:55.6	17.46 (1.14)	7.37 (0.12)	9.64
CFC233	13:05:39.11	+26:06:23.6	20.84 (0.94)	6.98 (0.08)	9.42
CFC234	13:05:44.61	+25:23:06.0	18.57 (1.04)	7.5 (0.1)	9.89
CFC238	13:05:58.70	+25:27:56.5	21.31 (0.91)	7.19 (0.07)	10.08

Continued on next page

OBJECT	RA h:m:s (J2000)	Dec. d:m:s (J2000)	Dust Temperature K	Duss Mass $\log(M_{Dust}/M_{\odot})$	Stellar Mass $\log(M_{Stars}/M_{\odot})$
CFC243	13:06:15.12	+25:27:38.0	23.82 (0.85)	7.61 (0.06)	10.27
CFC252	13:06:36.40	+25:25:46.7	19.45 (1.09)	7.12 (0.1)	9.69
CFC266	13:07:55.34	+34:55:10.0	22.42 (1.04)	7.55 (0.08)	9.99
CFC269	13:08:02.57	+27:18:40.1	21.82 (0.93)	7.08 (0.08)	9.27
CFC280	13:08:31.58	+24:42:02.8	18.14 (0.49)	8.18 (0.06)	11.17
CFC285	13:08:51.55	+28:37:45.4	19.29 (0.76)	7.35 (0.08)	9.69
CFC286	13:08:55.07	+29:02:26.8	17.81 (0.61)	7.63 (0.07)	10.42
CFC299	13:09:26.35	+28:24:57.1	20.77 (0.67)	7.67 (0.06)	10.48
CFC302	13:09:38.20	+30:29:54.1	22.81 (0.86)	7.07 (0.07)	9.98
CFC303	13:09:45.77	+28:37:16.4	26.62 (1.16)	7.18 (0.07)	9.85
CFC304	13:09:47.48	+28:54:25.0	20.52 (0.68)	8.09 (0.06)	10.85
CFC305	13:09:49.99	+24:34:39.3	21.95 (0.72)	7.8 (0.06)	10.51
CFC311	13:10:20.14	+32:28:59.5	18.17 (0.53)	7.91 (0.06)	10.04
CFC319	13:10:47.64	+29:42:35.6	19.32 (0.64)	7.76 (0.06)	10.35
CFC323	13:11:01.71	+29:34:42.1	22.8 (0.86)	7.99 (0.06)	11.11
CFC327	13:11:12.74	+26:48:50.4	21.82 (0.77)	7.1 (0.07)	9.92
CFC339	13:11:48.03	+30:58:21.3	23.22 (0.83)	7.24 (0.06)	10.52
CFC354	13:12:25.85	+28:32:15.7	27.4 (1.14)	7.31 (0.06)	10.59
CFC357	13:12:44.75	+31:48:33.8	17.22 (0.59)	8.34 (0.07)	10.97
CFC358	13:12:51.85	+27:52:48.2	18.07 (0.86)	7.36 (0.09)	9.94
CFC369	13:13:25.70	+27:45:48.4	21.6 (0.76)	7.52 (0.06)	10.58
CFC371	13:13:35.28	+29:07:35.5	20.37 (0.7)	7.3 (0.06)	10.0
CFC379	13:14:32.45	+30:42:20.8	18.22 (0.6)	8.19 (0.07)	10.98
CFC381	13:14:40.51	+29:59:50.1	19.39 (0.7)	7.49 (0.06)	10.03
CFC386	13:14:53.43	+27:00:29.2	16.73 (0.57)	7.92 (0.08)	10.18
CFC389	13:15:02.15	+28:02:10.9	21.78 (0.8)	7.25 (0.06)	9.86
CFC391	13:15:08.21	+30:24:13.6	25.15 (0.97)	7.46 (0.06)	10.5
CFC394	13:15:26.04	+33:09:26.0	17.57 (0.79)	7.23 (0.09)	9.38
CFC395	13:15:34.89	+29:40:33.9	18.43 (0.54)	7.57 (0.06)	11.08
CFC400	13:15:47.11	+31:50:47.1	19.59 (0.66)	7.62 (0.06)	9.77
CFC405	13:16:12.07	+34:03:46.9	19.22 (0.8)	7.55 (0.08)	10.8
CFC407	13:16:20.53	+30:40:42.0	19.75 (0.7)	7.63 (0.07)	10.31
CFC411	13:16:33.36	+31:32:47.1	19.59 (1.26)	6.99 (0.1)	9.61
CFC415	13:16:50.67	+31:37:50.4	21.15 (0.83)	7.36 (0.07)	9.95
CFC416	13:16:53.02	+31:42:39.8	22.78 (1.39)	6.68 (0.11)	9.47
CFC419	13:17:00.03	+34:06:06.0	18.64 (0.52)	8.14 (0.06)	11.03
CFC422	13:17:21.30	+31:03:33.8	21.99 (0.82)	7.19 (0.07)	9.64
CFC427	13:17:45.18	+27:34:11.5	19.32 (0.6)	8.05 (0.06)	10.84
CFC428	13:18:04.11	+33:51:18.2	19.55 (1.21)	7.08 (0.1)	9.69
CFC443	13:19:28.01	+27:44:56.3	22.86 (1.22)	7.2 (0.09)	10.06
CFC452	13:19:56.35	+30:07:08.3	19.89 (1.02)	7.31 (0.09)	10.67
CFC453	13:19:58.32	+28:14:49.3	23.43 (0.85)	7.37 (0.06)	10.3
CFC455	13:19:58.90	+29:25:38.8	21.57 (0.79)	7.34 (0.06)	10.43
CFC462	13:20:25.62	+30:36:10.8	22.95 (0.92)	7.16 (0.07)	10.26
CFC465	13:20:35.41	+34:08:21.6	28.65 (1.19)	8.28 (0.06)	10.44
CFC469	13:20:51.77	+31:21:59.5	18.75 (0.66)	7.67 (0.08)	9.85
CFC470	13:20:53.48	+32:11:26.8	20.15 (1.03)	7.18 (0.09)	10.37
CFC479	13:21:19.67	+31:33:08.9	21.75 (0.72)	7.41 (0.06)	10.0
CFC481	13:21:34.92	+26:18:16.8	21.91 (0.68)	7.64 (0.06)	10.06
CFC483	13:21:45.45	+31:14:14.1	24.82 (0.87)	7.69 (0.06)	10.49
CFC489	13:22:02.10	+31:16:42.2	23.68 (0.93)	7.46 (0.06)	10.46
CFC500	13:22:51.08	+31:49:33.3	18.85 (0.78)	7.5 (0.08)	9.56
CFC505	13:23:23.01	+33:43:26.4	16.16 (1.21)	7.41 (0.15)	10.1
CFC513	13:23:43.36	+30:33:49.3	16.54 (0.52)	7.64 (0.06)	10.21
CFC516	13:23:59.95	+30:55:56.7	22.14 (0.71)	7.51 (0.06)	10.61
CFC520	13:24:15.82	+31:20:42.5	18.76 (0.62)	7.89 (0.06)	10.36
CFC530	13:24:56.27	+26:27:48.7	26.53 (1.13)	7.01 (0.07)	10.74
CFC532	13:25:13.85	+29:24:51.1	21.91 (1.08)	7.06 (0.08)	10.01
CFC536	13:25:33.29	+26:00:05.8	20.88 (0.98)	7.02 (0.08)	10.56
CFC545	13:26:38.85	+27:02:23.5	18.61 (0.7)	7.55 (0.07)	9.88
CFC547	13:26:43.48	+30:30:24.1	20.7 (0.81)	7.21 (0.07)	10.03
CFC551	13:26:58.33	+32:32:11.3	18.35 (0.65)	7.61 (0.07)	10.57
CFC554	13:27:03.19	+30:58:36.6	20.02 (0.66)	7.64 (0.06)	10.12
CFC568	13:28:25.72	+30:48:56.6	17.69 (0.58)	7.76 (0.07)	10.16
CFC572	13:28:38.17	+33:36:18.4	21.65 (0.72)	7.77 (0.06)	10.58
CFC574	13:28:56.70	+32:52:44.0	23.42 (0.94)	7.85 (0.07)	10.62
CFC577	13:29:17.29	+26:47:18.2	21.52 (0.98)	7.04 (0.08)	9.84
CFC583	13:29:35.11	+26:24:35.8	19.75 (0.74)	7.66 (0.07)	10.57
CFC587	13:29:48.19	+31:07:48.5	21.7 (0.64)	7.95 (0.05)	10.91
CFC605	13:30:36.96	+34:55:02.6	22.15 (0.76)	7.45 (0.07)	10.69
CFC612	13:30:44.96	+32:17:37.0	20.79 (0.78)	7.27 (0.07)	9.97
CFC613	13:30:45.40	+26:31:17.7	17.57 (0.8)	7.44 (0.09)	9.53
CFC628	13:31:21.82	+25:37:08.8	18.65 (0.63)	7.64 (0.07)	10.23
CFC629	13:31:29.97	+32:52:58.4	22.01 (0.99)	7.34 (0.08)	10.09
CFC637	13:32:10.68	+28:23:20.8	19.91 (0.61)	7.32 (0.06)	10.61
CFC645	13:32:38.96	+25:26:28.2	20.16 (0.79)	7.79 (0.08)	10.82
CFC653	13:33:03.10	+34:33:01.4	19.76 (0.74)	7.26 (0.07)	9.78
CFC655	13:33:06.57	+33:09:03.8	20.37 (0.69)	7.59 (0.06)	10.11
CFC656	13:33:13.27	+33:06:35.1	20.15 (0.6)	7.91 (0.05)	10.59
CFC657	13:33:16.29	+34:32:13.2	22.22 (0.73)	7.89 (0.06)	11.07
CFC663	13:33:29.02	+33:02:32.5	18.69 (0.53)	8.11 (0.06)	11.16
CFC675	13:34:09.99	+34:45:54.6	20.25 (0.59)	7.68 (0.05)	10.78
CFC678	13:34:17.08	+34:55:45.6	18.26 (0.77)	7.67 (0.08)	11.25
CFC686	13:34:31.42	+35:14:32.8	17.56 (0.7)	7.7 (0.08)	10.16
CFC695	13:34:51.23	+34:03:19.9	20.63 (0.64)	7.68 (0.06)	10.52
CFC698	13:34:55.35	+31:23:36.6	15.89 (0.59)	7.91 (0.08)	9.59
CFC699	13:34:57.27	+34:02:38.7	21.77 (0.7)	8.34 (0.06)	10.71
CFC710	13:35:13.34	+34:40:38.8	18.03 (0.58)	7.66 (0.07)	11.4
CFC713	13:35:14.80	+25:02:41.1	23.04 (0.75)	7.34 (0.05)	10.54
CFC715	13:35:19.25	+26:25:29.1	17.49 (0.53)	7.94 (0.06)	10.7
CFC722	13:35:31.23	+34:09:07.7	18.75 (0.81)	7.31 (0.08)	10.18

Continued on next page

OBJECT	RA h:m:s (J2000)	Dec. d:m:s (J2000)	Dust Temperature K	Duss Mass $\log(M_{Dust}/M_{\odot})$	Stellar Mass $\log(M_{Stars}/M_{\odot})$
CFC724	13:35:35.95	+33:28:46.5	16.69 (0.47)	7.84 (0.06)	10.52
CFC726	13:35:38.41	+25:52:30.9	18.79 (0.61)	7.64 (0.06)	10.56
CFC728	13:35:40.80	+34:47:44.1	22.75 (0.94)	7.13 (0.07)	10.41
CFC740	13:35:52.67	+33:19:37.5	24.82 (1.06)	7.08 (0.07)	9.79
CFC756	13:36:19.64	+33:25:24.4	20.96 (0.72)	7.42 (0.06)	10.86
CFC772	13:36:59.25	+33:34:12.8	17.42 (0.71)	7.81 (0.08)	10.12
CFC778	13:37:38.11	+28:48:09.4	18.36 (0.78)	7.39 (0.09)	9.67
CFC781	13:37:44.49	+27:47:11.4	20.41 (1.23)	7.01 (0.11)	9.72
CFC786	13:38:13.05	+32:49:22.4	16.38 (0.51)	8.05 (0.07)	10.67
CFC802	13:38:44.12	+26:19:42.7	19.21 (0.89)	7.41 (0.09)	10.76
CFC803	13:38:45.88	+30:28:49.5	20.55 (0.81)	7.58 (0.07)	10.53
CFC820	13:39:40.29	+35:01:24.2	16.15 (0.94)	7.51 (0.12)	10.35
CFC822	13:39:44.15	+27:46:35.3	21.36 (0.69)	7.58 (0.06)	10.38
CFC829	13:40:17.96	+26:20:58.5	17.58 (0.56)	7.99 (0.07)	10.76
CFC830	13:40:18.25	+32:09:11.3	20.45 (1.0)	7.24 (0.08)	9.95
CFC834	13:40:45.45	+25:57:19.3	20.45 (1.28)	7.1 (0.11)	10.25
CFC836	13:40:51.16	+24:28:23.9	21.48 (0.66)	7.68 (0.06)	10.91
CFC859	13:41:45.21	+27:00:17.0	19.77 (0.66)	7.67 (0.06)	10.77
CFC871	13:42:22.01	+35:37:26.8	21.15 (0.76)	7.81 (0.07)	10.02
CFC874	13:42:34.19	+35:01:13.2	18.65 (0.59)	8.1 (0.06)	10.74
CFC903	13:44:47.61	+31:36:56.5	25.49 (1.03)	7.41 (0.06)	10.54
CFC913	13:45:34.99	+35:36:40.1	22.25 (0.82)	7.14 (0.07)	11.09
CFC917	13:45:52.96	+26:46:30.6	19.02 (0.64)	7.69 (0.07)	10.57
CFC919	13:46:03.93	+35:31:13.2	19.55 (0.57)	7.46 (0.06)	10.61
CFC933	13:47:01.23	+33:53:36.9	17.16 (0.96)	8.15 (0.12)	9.93
CFC936	13:47:10.73	+34:05:19.5	21.45 (0.75)	7.56 (0.07)	10.62
CFC946	13:48:34.19	+24:53:29.3	19.27 (0.76)	7.26 (0.07)	10.23
CFC947	13:48:35.64	+24:00:54.3	20.63 (0.87)	7.2 (0.08)	11.13

Table B.4. 143 CFC galaxies dust masses and temperetures given from fitting a modified blackbody ($\beta = 2$ emissivity) to 5 *Herschel* bands or more.

OBJECT	RA h:m:s (J2000)	Dec. d:m:s (J2000)	Dust Temperature K	Duss Mass $\log(M_{Dust}/\mathrm{M}_{\odot})$	Stellar Mass $\log(M_{Stars}/\mathrm{M}_{\odot})$
CCC007	12:52:48.89	+27:24:06.6	22.63 (0.82)	7.17 (0.07)	9.7
CCC009	12:52:53.58	+28:22:16.5	21.83 (0.72)	8.28 (0.06)	11.04
CCC028	12:53:51.50	+28:58:45.8	20.55 (0.7)	7.46 (0.07)	10.32
CCC029	12:53:53.93	+28:11:11.7	18.69 (0.82)	7.3 (0.08)	10.01
CCC045	12:54:33.18	+27:37:57.9	20.05 (0.57)	7.66 (0.06)	10.72
CCC057	12:54:53.68	+28:25:01.1	19.88 (0.82)	7.43 (0.08)	10.54
CCC058	12:54:55.17	+27:24:45.7	21.27 (0.7)	7.35 (0.06)	11.42
CCC092	12:55:47.82	+28:15:22.0	20.8 (0.75)	7.29 (0.07)	10.55
CCC109	12:56:06.10	+27:40:41.2	25.34 (1.04)	7.13 (0.06)	9.27
CCC113	12:56:10.98	+28:09:47.4	23.42 (0.94)	7.22 (0.07)	10.38
CCC128	12:56:27.86	+26:59:14.7	20.3 (0.6)	7.67 (0.06)	11.16
CCC130	12:56:28.57	+27:17:28.6	18.67 (0.77)	7.63 (0.08)	10.07
CCC161	12:56:51.17	+26:53:56.0	21.71 (0.68)	7.42 (0.06)	10.26
CCC163	12:56:52.28	+26:29:15.8	18.68 (0.63)	7.9 (0.06)	10.62
CCC211	12:57:31.21	+26:30:43.8	22.45 (0.69)	7.68 (0.06)	10.51
CCC248	12:57:57.72	+28:03:42.4	23.15 (0.96)	7.15 (0.07)	10.03
CCC258	12:58:05.59	+28:14:33.3	23.2 (0.86)	7.82 (0.06)	10.86
CCC266	12:58:09.23	+28:42:30.9	20.45 (0.55)	7.78 (0.05)	10.48
CCC282	12:58:18.63	+27:18:38.9	23.09 (0.99)	7.23 (0.08)	9.71
CCC308	12:58:35.19	+27:35:47.0	26.02 (1.02)	7.37 (0.06)	10.97
CCC338	12:58:55.96	+27:50:00.2	20.4 (0.67)	7.64 (0.06)	10.69
CCC372	12:59:16.67	+27:06:22.1	22.82 (0.92)	7.22 (0.07)	10.2
CCC423	12:59:39.11	+28:53:43.8	21.67 (0.81)	7.18 (0.07)	10.88
CCC505	13:00:17.93	+28:12:08.6	20.83 (0.74)	7.22 (0.07)	11.36
CCC541	13:00:35.67	+27:34:27.2	22.41 (0.78)	7.29 (0.06)	10.04
CCC543	13:00:37.86	+28:03:29.1	24.82 (0.85)	7.62 (0.05)	10.15
CCC545	13:00:39.55	+29:01:09.9	18.11 (0.49)	8.04 (0.06)	10.78
CCC560	13:00:48.80	+28:09:30.0	16.78 (0.48)	7.76 (0.06)	10.91
CCC571	13:00:56.06	+27:47:27.1	20.25 (0.6)	8.19 (0.06)	11.33
CCC600	13:01:25.08	+28:40:38.0	20.36 (0.57)	7.63 (0.06)	10.38
CCC606	13:01:33.60	+29:07:50.1	21.82 (0.72)	7.42 (0.06)	11.23
CCC615	13:01:43.37	+29:02:40.8	18.44 (0.58)	8.06 (0.07)	11.0
CCC629	13:01:57.57	+28:00:21.0	21.62 (0.92)	7.07 (0.07)	11.23
CCC633	13:02:04.20	+29:15:12.4	23.33 (1.21)	6.87 (0.08)	10.98
CCC638	13:02:07.88	+27:38:53.9	23.49 (0.87)	7.37 (0.06)	10.3
CCC670	13:03:05.94	+26:31:52.1	19.9 (1.11)	7.09 (0.1)	10.07
CCC675	13:03:16.24	+28:01:49.5	19.3 (0.7)	7.58 (0.07)	10.56
CCC684	13:03:29.08	+26:33:01.8	18.2 (0.53)	8.04 (0.06)	10.72
CCC693	13:03:44.95	+28:05:03.2	22.12 (1.12)	6.86 (0.09)	10.51
CCC713	13:04:22.68	+28:48:38.8	22.32 (0.94)	7.26 (0.08)	9.76
CCC714	13:04:26.55	+27:18:15.5	20.95 (0.87)	7.28 (0.08)	9.14
CCC739	13:05:32.85	+29:00:41.8	16.38 (0.7)	7.52 (0.09)	9.76
CCC744	13:05:53.49	+28:06:44.8	20.58 (0.86)	7.38 (0.08)	10.44
CCC752	13:06:17.29	+29:03:47.5	19.69 (0.69)	8.15 (0.06)	11.05
CCC756	13:06:36.39	+27:52:22.6	24.2 (0.87)	7.5 (0.06)	10.16
CCC766	13:07:13.20	+28:02:49.0	18.86 (0.71)	7.63 (0.07)	10.07

Table B.3. 45 CCC galaxies dust masses and temperetures given from fitting a modified blackbody ($\beta = 2$ emissivity) to 5 *Herschel* bands or more.

Appendix C
Coma - Trends with Density

C.1 Stellar Mass (continued)

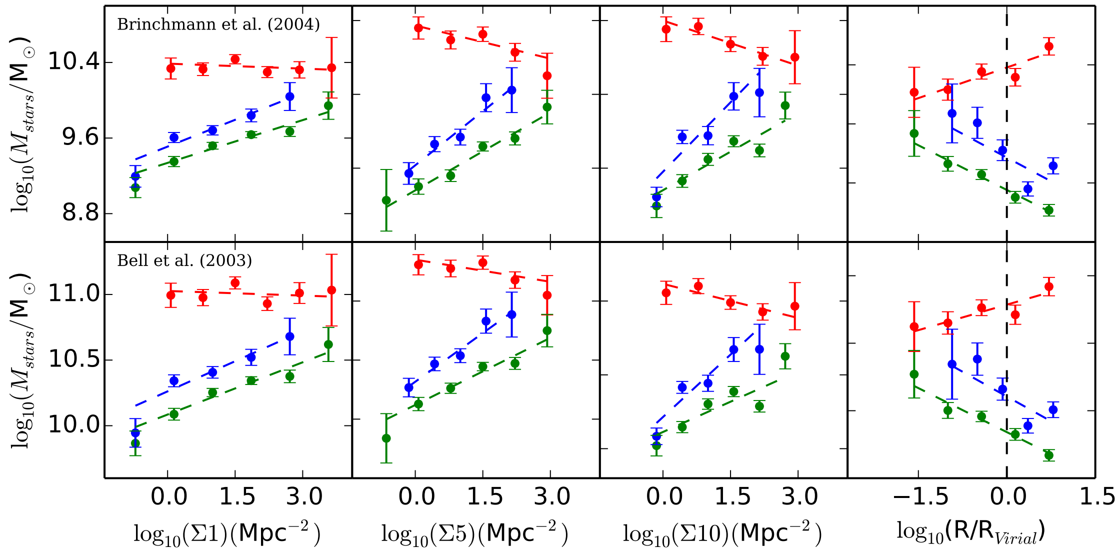

Figure C.1. The above figure has been created and lines have been fitted as decribed in Section 5. The upper and lower panels are stellar mass from Brinchmann et al. (2004) and Bell et al. (2003), respectively. The three morphological types have markers and lines coloured red, blue and green for early, uncertain and late-type galaxies, respectively.

	Gradient of straight line fit (m)			
Sample type	Σ_1	Σ_5	Σ_{10}	Radius
Brinchmann et al. (2004)				
late	0.19±0.04	0.24±0.05	0.31±0.1	-0.21±0.15
uncertain	0.15±0.03	0.18±0.02	0.17±0.04	-0.2±0.02
early	-0.02±0.04	-0.07±0.03	-0.1±0.02	0.14±0.05
Bell et al. (2003)				
late	0.15±0.04	0.22±0.04	0.28±0.08	-0.2±0.12
uncertain	0.13±0.02	0.15±0.02	0.14±0.05	-0.17±0.02
early	-0.01±0.04	-0.05±0.03	-0.08±0.03	0.1±0.04

Table C.1. Above shows the gradients for the straight line fit parameters from Figure C.1.

Morphological type	Σ_1 m±dm	Σ_1 $m = 0\,?\ (\frac{m}{dm})$	Σ_5 m±dm	Σ_5 $m = 0\,?\ (\frac{m}{dm})$	Σ_{10} m±dm	Σ_{10} $m = 0\,?\ (\frac{m}{dm})$	Radius m±dm	Radius $m = 0\,?\ (\frac{m}{dm})$
Dust-to-Stars								
late	-0.11±0.02	No(7σ)	-0.1±0.06	Yes(2σ)	-0.12±0.04	No(3σ)	0.11±0.08	Yes(1σ)
early	-	-	0.1±0.08	Yes(1σ)	-0.0±0.1	Yes(0σ)	-0.09±0.06	Yes(1σ)
sSFR								
late	-0.28±0.05	No(5σ)	-0.44±0.09	No(5σ)	-0.55±0.06	No(9σ)	0.49±0.25	Yes(2σ)
early	-0.1±0.03	No(4σ)	-0.02±0.02	Yes(1σ)	0.01±0.04	Yes(0σ)	-0.03±0.06	Yes(0σ)
Gas-to-Stars								
late	-0.39±0.07	No(6σ)	-0.59±0.11	No(5σ)	-0.7±0.08	No(9σ)	0.76±0.16	No(5σ)
Stellar Mass								
late	0.19±0.04	No(4σ)	0.24±0.05	No(5σ)	0.31±0.1	No(3σ)	-0.21±0.15	Yes(1σ)
early	-0.02±0.04	Yes(0σ)	-0.07±0.03	Yes(2σ)	-0.1±0.02	No(4σ)	0.14±0.05	Yes(3σ)
Φ								
all	-0.24±0.01	No(17σ)	-0.31±0.04	No(9σ)	-0.32±0.02	No(14σ)	0.39±0.05	No(8σ)

Table C.2. Above shows the gradients for the straight line fit parameters from Figure 6.2. For each pannel in Figure 6.2 here we tabulate the gradient, as well as whether it is consistent with a gradient of zero, ie no change in each respevitly parameter with density for a given morphological type and density tracer.

Bibliography

Aaronson M., Olszewski E. W., 1984, Nature, 309, 414

Abell G. O., 1965, ARA&A, 3, 1

Asplund M., García Pérez A. E., 2001, A&A, 372, 601

Auld R. et al., 2013, MNRAS, 428, 1880

Baes M. et al., 2010, A&A, 518, L53

Barnes D. G. et al., 2001, MNRAS, 322, 486

Beichman C. A., 1987, ARA&A, 25, 521

Bell E. F., McIntosh D. H., Katz N., Weinberg M. D., 2003, ApJS, 149, 289

Bendo G. J. et al., 2003, AJ, 125, 2361

Bianchi S., 2013, A&A, 552, A89

Bicay M. D., Giovanelli R., 1987, ApJ, 321, 645

Binggeli B., Sandage A., Tammann G. A., 1985, AJ, 90, 1681

Boquien M. et al., 2012, A&A, 539, A145

Boselli A. et al., 2010, PASP, 122, 261

Boselli A., Gavazzi G., 2006, PASP, 118, 517

Bower R. G., Kodama T., Terlevich A., 1998, MNRAS, 299, 1193

Brinchmann J., Charlot S., White S. D. M., Tremonti C., Kauffmann G., Heckman T., Brinkmann J., 2004, MNRAS, 351, 1151

Castander F. J. et al., 2001, AJ, 121, 2331

Chabrier G., 2003, PASP, 115, 763

Chapin E. L. et al., 2011, MNRAS, 411, 505

Chen Y., Reiprich T. H., Böhringer H., Ikebe Y., Zhang Y.-Y., 2007, A&A, 466, 805

Ciesla L. et al., 2012, A&A, 543, A161

Clemens M. S. et al., 2010, A&A, 518, L50

Colless M., Dunn A., 1995, PASP, 12, 122

Colless M., Dunn A. M., 1996, ApJ, 458, 435

Combes F., Dupraz C., Casoli F., Pagani L., 1988, A&A, 203, L9

Conrow T. P. et al., 1993, in Bulletin of the American Astronomical Society, Vol. 25, American Astronomical Society Meeting Abstracts, p. 1291

Contursi A., Boselli A., Gavazzi G., Bertagna E., Tuffs R., Lequeux J., 2001, A&A, 365, 11

Corbelli E. et al., 2012, A&A, 542, A32

Cortese L., 2012, A&A, 543, A132

Cortese L. et al., 2010a, A&A, 518, L63

Cortese L. et al., 2012a, A&A, 544, A101

Cortese L. et al., 2012b, A&A, 540, A52

Cortese L. et al., 2010b, A&A, 518, L49

Cortese L. et al., 2014, MNRAS, 440, 942

Cowie L. L., McKee C. F., 1977, ApJ, 211, 135

Cox P., Mezger P. G., 1987, in NASA Conference Publication, Vol. 2466, NASA Conference Publication, Lonsdale Persson C. J., ed., pp. 23–35

Davies J. I. et al., 2011, MNRAS, 415, 1883

Davies J. I. et al., 2010, A&A, 518, L48

Davies J. I. et al., 2014, MNRAS

Davies J. I. et al., 2012a, MNRAS, 57

Davies J. I. et al., 2012b, MNRAS, 419, 3505

Davis T. A. et al., 2013, MNRAS, 429, 534

Davis T. A. et al., 2011, MNRAS, 417, 882

de Graauw T. et al., 2010, A&A, 518, L6

de Jong T., Clegg P. E., Rowan-Robinson M., Soifer B. T., Habing H. J., Houck J. R., Aumann H. H., Raimond E., 1984, ApJ, 278, L67

De Looze I. et al., 2013, MNRAS

De Looze I. et al., 2010, A&A, 518, L54

De Vaucouleurs G., De Vaucouleurs A., Corwin, Jr. H. G., Buta R. J., Paturel G., Fouqué P., 1991, Third Reference Catalogue of Bright Galaxies. Volume I: Explanations and references. Volume II: Data for galaxies between 0^h and 12^h. Volume III: Data for galaxies between 12^h and 24^h.

Di Serego Alighieri S. et al., 2013, A&A, 552, A8

di Serego Alighieri S. et al., 2007, A&A, 474, 851

Doyon R., Joseph R. D., 1989, Ap&SS, 157, 211

Draine B. T., 2003, ARA&A, 41, 241

Draine B. T., Li A., 2007, ApJ, 657, 810

Dressler A., 1980, ApJ, 236, 351

Dressler A. et al., 1997, ApJ, 490, 577

Drinkwater M. J., Gregg M. D., Colless M., 2001, ApJ, 548, L139

Driver S. P., Popescu C. C., Tuffs R. J., Graham A. W., Liske J., Baldry I., 2008, ApJ, 678, L101

Dunne L. et al., 2011, MNRAS, 417, 1510

Eales S. et al., 2010, PASP, 122, 499

Eales S. et al., 2012, ApJ, 761, 168

Eckert D., Molendi S., Paltani S., 2011, A&A, 526, A79

Edmunds M. G., 1990, MNRAS, 246, 678

Edmunds M. G., Eales S. A., 1998, MNRAS, 299, L29

Edwards L. O. V., Fadda D., 2011, AJ, 142, 148

Ferguson H. C., 1989, AJ, 98, 367

Ferrière K. M., 2001, Reviews of Modern Physics, 73, 1031

Fuller C. et al., 2014, MNRAS

Gavazzi G., Boselli A., 1996, A UBVJHK photometric catalogue of 1022 galaxies in 8 nearby clusters

Gavazzi G., O'Neil K., Boselli A., van Driel W., 2006, A&A, 449, 929

Geller M. J., Diaferio A., Kurtz M. J., 1999, ApJ, 517, L23

Godwin J. G., Peach J. V., 1977, MNRAS, 181, 323

Griffin M. J. et al., 2010, A&A, 518, L3

Grossi M. et al., 2009, A&A, 498, 407

Grossi M., Giovanardi C., Corbelli E., Giovanelli R., Haynes M. P., Martin A. M., Saintonge A., Dowell J. D., 2008, A&A, 487, 161

Grossi M. et al., 2010, A&A, 518, L52

Gunn J. E., Gott, III J. R., 1972, ApJ, 176, 1

Gupta A., Mathur S., Krongold Y., Nicastro F., Galeazzi M., 2012, ApJ, 756, L8

Hambly N. C. et al., 2001, MNRAS, 326, 1279

Haynes M. P., Giovanelli R., 1984, AJ, 89, 758

Haynes M. P., Giovanelli R., Chincarini G. L., 1984, ARA&A, 22, 445

Haynes M. P. et al., 2011, AJ, 142, 170

Helfer T. T., Thornley M. D., Regan M. W., Wong T., Sheth K., Vogel S. N., Blitz L., Bock D. C.-J., 2003, ApJS, 145, 259

Helou G., Walker D. W., eds., 1988, Infrared astronomical satellite (IRAS) catalogs and atlases. Volume 7: The small scale structure catalog, Vol. 7

Hickinbottom S. et al., 2014, MNRAS, 442, 1286

Hollenbach D., Salpeter E. E., 1971, ApJ, 163, 155

Hubble E., Humason M. L., 1931, ApJ, 74, 43

Hubble E. P., 1925, Popular Astronomy, 33, 252

Hughes J. P., 1989, ApJ, 337, 21

Hughes T. M., Cortese L., Boselli A., Gavazzi G., Davies J. I., 2013, A&A, 550, A115

Ibar E. et al., 2010, MNRAS, 409, 38

Jones A. P., Nuth J. A., 2011, A&A, 530, A44

Kauffmann G. et al., 2003, MNRAS, 341, 33

Kenney J. D. P., Rubin V. C., Planesas P., Young J. S., 1995, ApJ, 438, 135

Kenney J. D. P., Young J. S., 1989, ApJ, 344, 171

Kennicutt, Jr. R. C., 1998, ApJ, 498, 541

Kent S. M., Gunn J. E., 1982, AJ, 87, 945

Kessler M. F. et al., 1996, A&A, 315, L27

Krajnović D. et al., 2011, MNRAS, 414, 2923

Kroupa P., 2002, Science, 295, 82

Kubo J. M., Stebbins A., Annis J., Dell'Antonio I. P., Lin H., Khiabanian H., Frieman J. A., 2007, ApJ, 671, 1466

Lara-López M. A. et al., 2010, A&A, 521, L53

Larson R. B., Tinsley B. M., Caldwell C. N., 1980, ApJ, 237, 692

Leggett S. K., Brand P. W. J. L., Mountain C. M., 1987a, MNRAS, 228, 11P

Leggett S. K., Clowes R. G., Kalafi M., MacGillivray H. T., Puxley P. J., Savage A., Wolstencroft R. D., 1987b, MNRAS, 227, 563

Lequeux J., Peimbert M., Rayo J. F., Serrano A., Torres-Peimbert S., 1979, A&A, 80, 155

Lintott C. J. et al., 2008, MNRAS, 389, 1179

López-Caniego M., 2014, ArXiv:1401.4683

Magrini L. et al., 2011, A&A, 535, A13

Marsden G. et al., 2009, ApJ, 707, 1729

Meyer D. M., Jura M., Cardelli J. A., 1998, ApJ, 493, 222

Mihos J. C., 2004, Clusters of Galaxies: Probes of Cosmological Structure and Galaxy Evolution, 277

Mobasher B. et al., 2001, ApJS, 137, 279

Morgan H. L., Edmunds M. G., 2003, MNRAS, 343, 427

Morgan W. W., 1961, Proceedings of the National Academy of Science, 47, 905

Neugebauer G. et al., 1984, ApJ, 278, L1

Oemler, Jr. A., 1974, ApJ, 194, 1

Panter B., Jimenez R., Heavens A. F., Charlot S., 2007, MNRAS, 378, 1550

Pappalardo C. et al., 2012, A&A, 545, A75

Paturel G., Petit C., Prugniel P., Theureau G., Rousseau J., Brouty M., Dubois P., Cambrésy L., 2003, A&A, 412, 45

Pilbratt G. L. et al., 2010, A&A, 518, L1

Plutarch, 2006, The complete works Volume 3 : essays and miscellanies. Echo Library, Middlesex, England

Poglitsch A. et al., 2010, A&A, 518, L2

Pohlen M. et al., 2010, A&A, 518, L72

Prugniel P., Heraudeau P., 1998, A&AS, 128, 299

Ramella M., Geller M. J., Huchra J. P., 1989, ApJ, 344, 57

Rengarajan T. N., Iyengar K. V. K., 1992, MNRAS, 259, 559

Roussel H., 2013, PASP, 125, 1126

Schröder A., Drinkwater M. J., Richter O.-G., 2001, A&A, 376, 98

Shang C., Scharf C., 2009, ApJ, 690, 879

Shimakawa R., Kodama T., Tadaki K.-i., Hayashi M., Koyama Y., Tanaka I., 2014, ArXiv e-prints

Smith M. W. L. et al., 2012, ApJ, 748, 123

Smith M. W. L. et al., 2010, A&A, 518, L51

Soifer B. T., Neugebauer G., Houck J. R., 1987, ARA&A, 25, 187

Stickel M., Klaas U., Lemke D., Mattila K., 2002, A&A, 383, 367

Strauss M. A. et al., 2002, AJ, 124, 1810

Taylor R., Davies J. I., Auld R., Minchin R. F., 2012, ArXiv e-prints

The L. S., White S. D. M., 1986, AJ, 92, 1248

Thomas D., Maraston C., Bender R., Mendes de Oliveira C., 2005, ApJ, 621, 673

Tremonti C. A. et al., 2004, ApJ, 613, 898

Verstappen J. et al., 2013, A&A, 556, A54

Vila-Costas M. B., Edmunds M. G., 1992, MNRAS, 259, 121

Vlahakis C., Dunne L., Eales S., 2005, MNRAS, 364, 1253

Vogelsberger M. et al., 2014, Nature, 509, 177

Wang G., Leggett S. K., Clowes R. G., MacGillivray H. T., Savage A., 1991, MNRAS, 248, 112

Werner M. W. et al., 2004, ApJS, 154, 1

Whittet D., 1992, Dust in the galactic environment, Adam Hilger graduate series in astronomy. Institute of Physics

Yin J., Hou J. L., Prantzos N., Boissier S., Chang R. X., Shen S. Y., Zhang B., 2009, A&A, 505, 497

Zwicky F., 1937, ApJ, 86, 217

Zwicky F., 1951, PASP, 63, 61